

MECHATRONIC MATERIALS AND SYSTEMS

FINAL REPORT FOR:

DISTRIBUTION STATEMENT A

Approved for Public Release
Distribution Unlimited

**DR. STEPHEN FISHMAN
OFFICE OF NAVAL RESEARCH
BALLSTON TOWER ONE
800 NO. QUINCY STREET
ARLINGTON, VA 22217-5660**

FROM

**UNIVERSITY OF CALIFORNIA, SANTA BARBARA
HARVARD UNIVERSITY
UNIVERSITY OF VIRGINIA
CAMBRIDGE UNIVERSITY**

**ANTHONY G. EVANS
PRINCIPAL INVESTIGATOR**

20050928 054

TABLE OF CONTENTS

	Page
Executive Summary	1
Part I: Design and demonstration of a high authority shape morphing structure	2
Part II: The load capacity of a kagome based high authority shape morphing structure	26
Part III: Actuator placement optimization in a kagome based high authority shape morphing structure	33
Part IV: Twisting of a high authority morphing structure	41
Part V: Performance of sandwich plates with truss cores	84
Part VI: Sandwich plates actuated by a kagome planar truss	99
Part VII: Kagome plate structures for actuation	111
Part VIII: Minimum weight design of a high authority flexural actuator based on electroelastomers	124
Part IX: Actuation of the kagome double layer grid. Part 1: Prediction of performance of the perfect structure	164
Part X: Actuation of the kagome double layer grid. Part 2: Effect of imperfections on the measured and predicted actuation stiffness	198

DESIGN AND DEMONSTRATION OF A HIGH AUTHORITY SHAPE MORPHING STRUCTURES

EXECUTIVE SUMMARY

A concept for a high authority shape morphing plate is described and demonstrated. The design incorporates an active back-plane comprising a Kagome truss, capable of changing the shape of a solid face, connected to the back-plane by means of a tetrahedral truss core. The two shape deformations to be demonstrated consist of hinging and twisting. The design is performed by a combination of analytic estimation and numerical simulation, guided by previous assessments of the Kagome configuration. It is shown that, while the structure is capable of sustaining large passive loads at low weight, the demonstrable authority is actuator-limited. A protocol for optimizing is described. A first version assesses the required geometric dimensions and actuator specifications in order to maximize the permissible shape changes and load capacity. The critical external loads for all failure mechanisms of the individual components are calculated and used as constraints. The resistance of the structure to actuation is presented as an additional constraint. The ensuing relations are subsequently used to choose the best material for a given application. In a second version, the placement of the trusses to achieve the desired deformation, subject to the load capacity of the individual actuators, is ascertained. A two level scheme is used comprising a heuristic algorithm with a simplex-based optimization providing the cost function. It is shown that methods capable of avoiding entrapment in local minima, such as simulated annealing and genetic algorithm, give good results. The report is presented in three parts covering each of the important aspects of the design and implementation.

**Part 1: Design and demonstration
of a high authority shape morphing structure**



Design and demonstration of a high authority shape morphing structure

S.L. dos Santos e Lucato ^{*}, J. Wang, P. Maxwell, R.M. McMeeking, A.G. Evans

Materials Department, Mechanical Engineering Department, University of California at Santa Barbara, Santa Barbara, CA 93106, USA

Received 25 July 2003; received in revised form 27 January 2004

Available online 12 March 2004

Abstract

A concept for a high authority shape morphing plate is described and demonstrated. The design incorporates an active back-plane comprising a Kagome truss, capable of changing the shape of a solid face, connected to the back-plane by means of a tetrahedral truss core. The two shape deformations to be demonstrated consist of hinging and twisting. The design is performed by a combination of analytic estimation and numerical simulation, guided by previous assessments of the Kagome configuration. It is shown that, while the structure is capable of sustaining large passive loads at low weight, the demonstrable authority is actuator-limited. The full potential of the system can only be realized by developing and incorporating superior actuators.

An optimization has been used to ascertain the largest displacements achievable within the force capability of the actuators. These displacements have been demonstrated and shown to correspond with values predicted by numerical simulation. The consistency between measured and calculated responses has allowed objectives to be set for alternative materials, as well as structural and actuator enhancements.

© 2004 Elsevier Ltd. All rights reserved.

Keywords: Shape morphing; Sandwich panels; Actuator; Optimization; Failure mechanisms

1. Introduction

One of the goals in shape morphing technology is to cause surfaces to displace even when resisted by large pressure loads (or heavy weights). The challenges become especially demanding when minimum weight requirements and power budgets are imposed. This challenge can be addressed by seeking structures that are simultaneously statically determinate, yet stiff. A two-dimensional manifestation consists of a corrugated structure that can bend and hinge with much higher authority than bimorphs and other competing approaches (Lu et al., 2001). Another manifestation is the Kagome structure depicted on Fig. 1 (Hutchinson et al., 2003; Hyun and Torquato, 2002), having the attribute that it can be actuated into intricate surface shapes, ranging from bending to twisting to undulating (Fig. 2). The basic mechanics have

^{*} Corresponding author. Tel.: +1-805-8934341; fax: +1-805-8938486.

E-mail address: lucato@engineering.ucsb.edu (S.L. dos Santos e Lucato).

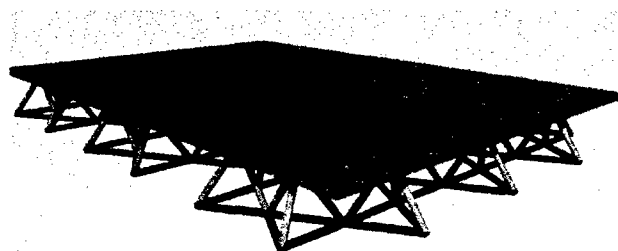


Fig. 1. Schematic representation of the Kagome-structure. The face-sheet is shown in blue, the core in green and the Kagome back-face is red.

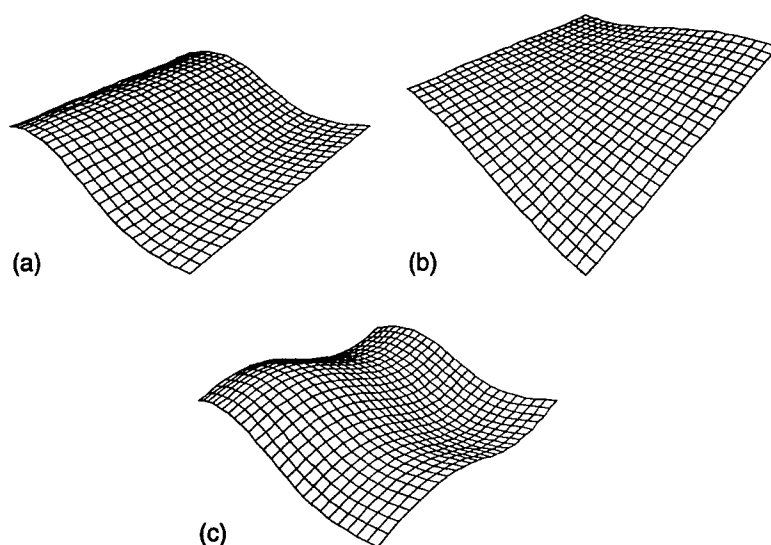


Fig. 2. Target surface shapes ranging from bending (a) to twisting (b) to undulating (c).

been elucidated elsewhere (Hutchinson et al., 2003). The intent of the study is to provide an experimental assessment of the concept with associated analysis. For this initial demonstration, hinging and twisting will be explored. The more complex contours depicted on Fig. 2 will be demonstrated in future assessments. The design process selects the geometry and the preferred materials. It ascertains the stresses, relative to the failure envelope, and ascertains the actuator authority needed to maximize the load capacity as a function of the designated displacements.

The basic structural design is depicted on Fig. 3. It consists of a solid face-sheet with a Kagome back-plane and a tetrahedral core. A related design based on two Kagome faces and a tetrahedral core is described elsewhere (Symons et al., 2003). The length of the panel is chosen to include six hexagonal units of the Kagome plate, while the width incorporates four units with member length, $L = 5.1$ cm. Along the sides, to avert degradation of the buckling resistance, patch trusses are used. For initial demonstration, the back-plane and core members have the same length and cross-section. Future demonstrations will use selected members with differing cross-section. The configuration is rigidly supported at one end. Replacing various truss elements in the back-plane with linear actuators enables the shape of the solid face to be changed. To achieve smooth contour changes and low structural weight, the solid face and the back-plane are stiffness matched (Christensen, 2000, Wicks, 2003). For the actual demonstration, the length of the panel is chosen

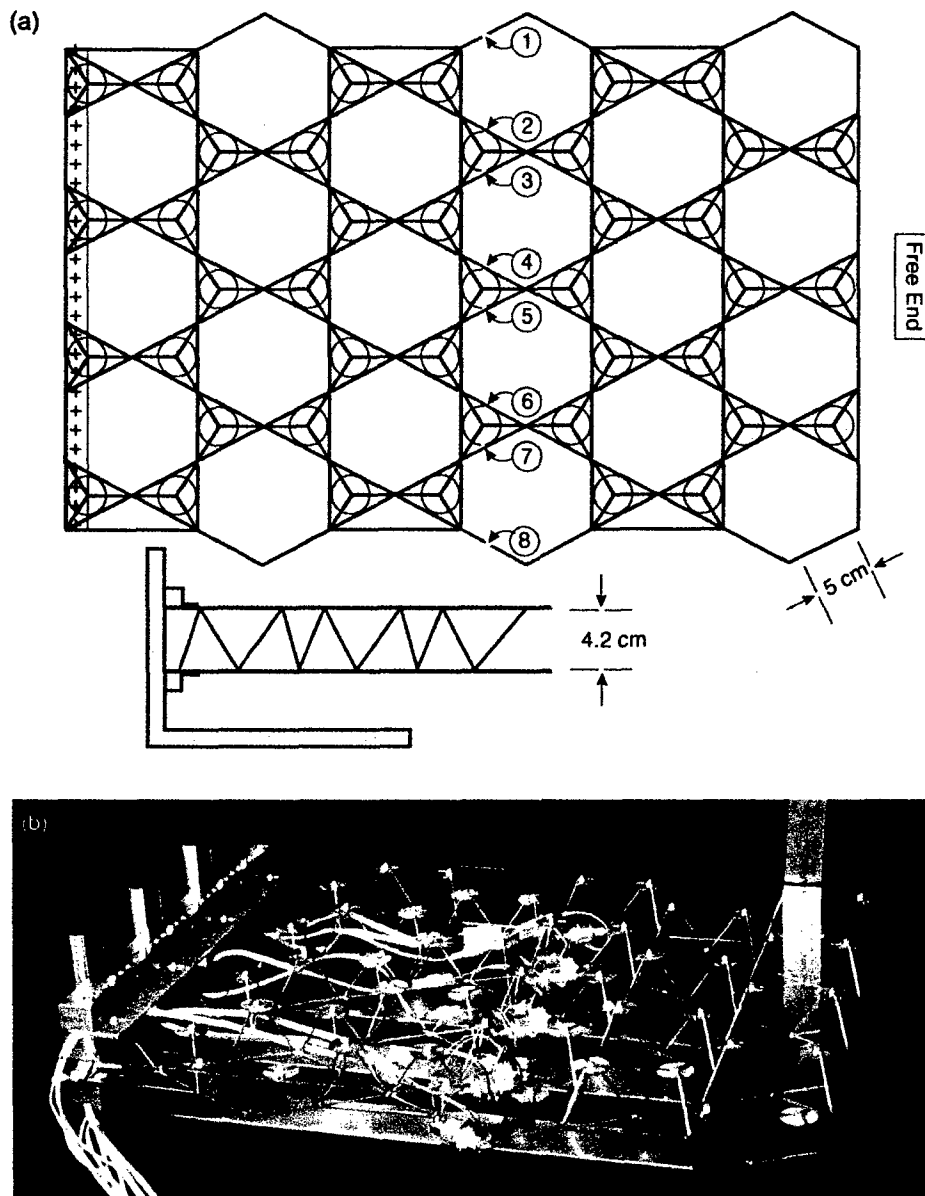


Fig. 3. Final assembly of Kagome-structure with actuator positions highlighted. Design (a) including the fixture and photo (b).

to include six hexagonal units of the Kagome plate, while the width incorporates four units. The truss aspect ratio has been chosen to maximize the displacement without failure, as described below. The objectives are to demonstrate hinging and twisting displacements, subject to large pressures and static end loads.

To facilitate fabrication, the Kagome and tetrahedral structures are fabricated from 304 stainless steel by laser cutting, followed by bending, as described elsewhere (Maxwell et al., 2003). This material choice limits the shape morphing performance because of its low yield strain, $\epsilon_Y = 10^{-3}$, and high density. The enhanced performance to be realized upon using Ti or Al alloys (having higher yield strain and lower density) will be emphasized. The core members incorporate circular pads, which facilitate attachment to the solid face. The

attachment is performed by welding, but could be created by transient liquid phase (TLP) bonding or, in the case of Ti, by diffusion bonding.

For morphing purposes, various truss elements are replaced by linear actuators. The replacements are made in pairs (Fig. 3), to minimize local distortions. A commercial linear, stepper actuator (Haydon Switch, model Z 26443) is used. This actuator can extend to strains $>10\%$, but can only displace loads of 50 N at a stepping rate of 50/s decaying linearly to 1 N at 700/s. This operating characteristic limits the passive loads that can be supported, as elaborated below, highlighting the need for a higher authority actuator. Accordingly, the test results and the analysis will be used for two additional purposes.

- (i) Evaluate the loads on the actuator that could be lifted upon incorporating actuators with superior force capability.
- (ii) Define the actuator capabilities that would be needed to create a structure-limited rather than actuator-limited system.

The design is achieved by a combination of analytic approximations with more detailed finite element results. The procedure has two steps. *Step I.* Analytic results for the stresses caused by passive loads are derived using beam and plate theory. These results are used to estimate dimensions and to assess the scaling. They are augmented by selected finite element calculations. *Step II.* The stresses and displacements induced during actuation are determined using finite elements, with emphasis on the core and face members adjacent to the actuators. The same calculations are used to evaluate the forces on the actuators as a function of the displacements. At this stage, the dimensions are adjusted and the load capacity re-evaluated to assure that there is no cyclic yielding (indicative of fatigue) or buckling.

Numerical simulations depicted on Fig. 4 illustrate the shape changes to be explored.

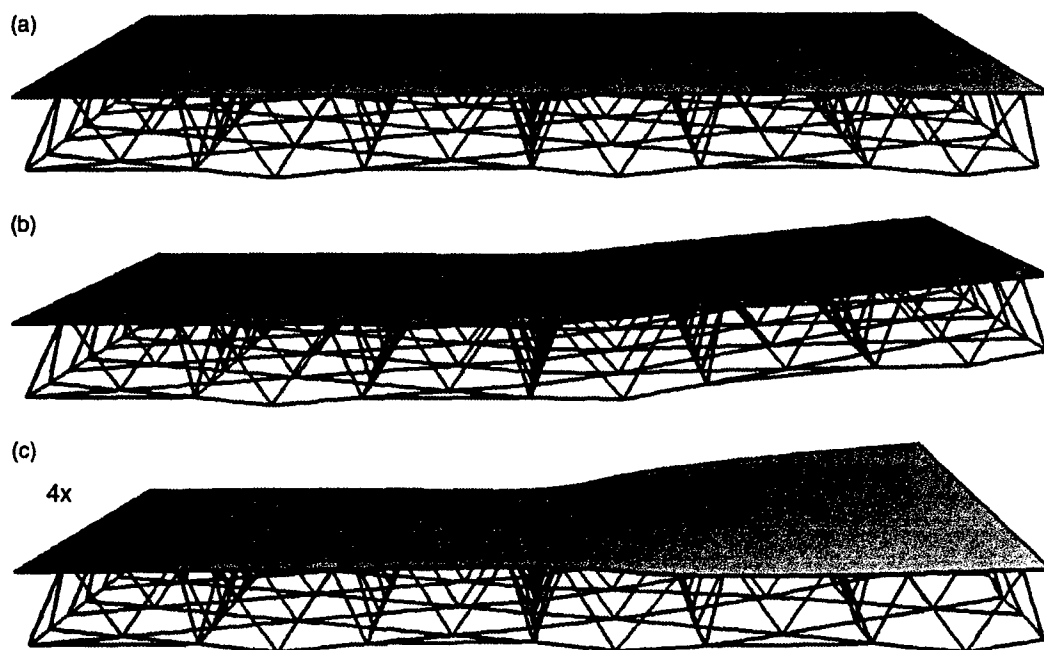


Fig. 4. Numerical results for hinging and twisting modes of the Kagome structure. (a) Initial configuration. Resulting shapes of hinging (b) and twisting (c) modes.

2. Numerical procedures

A finite element method has been used for several purposes:

- (i) To generate results that can be compared with analytic solutions governing the passive loads.
- (ii) To calculate the stresses induced by actuation, for twisting and hinging deformations, and to ascertain the forces on the actuators.
- (iii) To determine the actuator displacements that achieve a prescribed displacement of the solid face sheet, consistent with a minimum in the largest load experienced by any of the actuators.

The calculations are conducted at two different levels, by using the finite element package ABAQUS. *To simulate the complete system*, the core and the Kagome face members are modeled using linear Timoshenko-type beams, while the solid face sheet is discretized using general-purpose shell elements. A total of 10 elements are used per member to capture bending and buckling. The actuators are incorporated into the model by means of truss elements, with representative cross-sectional area. One side of the structure is clamped. Actuation is achieved by changing the temperature of the truss elements representing the actuators. The passive response is assessed by applying a line load along the outer edge of the solid face sheet.

A full *elastic/plastic analysis is performed on the following two sub-systems* by using 3D solid elements. (a) The in-plane performance of the Kagome is evaluated and compared with existing results. Imperfections are introduced into the truss members to assure that elastic and plastic buckling effects are captured. (b) The core tetrahedron above the actuators is found to be most susceptible to cyclic yielding during actuation. To find materials and configurations that obviate this potential problem, a single tetrahedron is modeled. For this purpose, two of the members are clamped and cyclic displacements imposed on the third member with amplitude ascertained from the system-level model.

3. Passive load capacity

3.1. The back-plane design

The Kagome back-plane is designed by balancing the in-plane failure mechanisms, using the unit cell loci depicted on Fig. 5. The non-dimensional coordinates characterizing yielding are (Hutchinson et al., 2003)

$$\begin{aligned}\Pi_{11} &\equiv N_{11}L_f/A_f\sigma_Y, \\ \Pi_{22} &\equiv N_{22}L_f/A_f\sigma_Y,\end{aligned}\tag{1}$$

where N_{ii} refers to the in-plane load per unit length, L_f is the length of the truss members, A_f is their cross-sectional area and σ_Y is the yield strength of the material to be used. The present demonstration uses trusses with square cross-section, d_f ($A_f = d_f^2$). To characterize buckling, the additional non-dimensional parameter is (Hutchinson et al., 2003)

$$\Sigma = \sqrt{I_f/A_f/L_f\sqrt{\varepsilon_Y}},\tag{2}$$

where I_f is the moment of area of the truss members and ε_Y is their yield strain. Each buckling contour on Fig. 5 refers to a particular choice of Σ .

Since the optimal performance of structures often occurs at the confluence of failure mechanisms (Ashby et al., 2000), it is assumed that the maximum actuation displacement without failure occurs when the slenderness ratio of the trusses in the Kagome face is coincident with simultaneous failure by buckling and yielding (see Fig. 8). A more complete assessment is described elsewhere (Wicks and Hutchinson, 2001; Hutchinson et al., 2003). For the uni-axial deformations envisaged in the current demonstration ($N_{22} = 0$), the failure mechanisms are simultaneous when (Fig. 5)

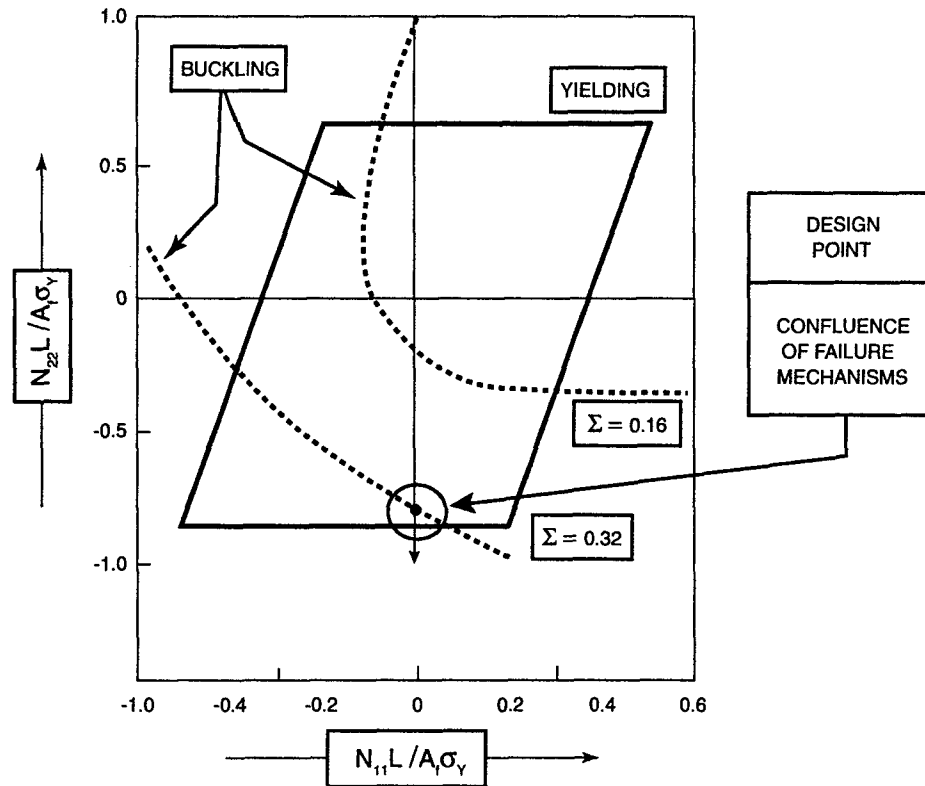


Fig. 5. In-plane failure mechanisms of the Kagome back-plane. Loads exceeding the shaded region result in failure by yielding. The dashed curves represent the load-limits established by buckling.

$$\Sigma \approx 0.32, \quad (3a)$$

$$\Pi_{11} = 0.866. \quad (3b)$$

As elaborated below, the patched topology (Fig. 3) has a greater buckling resistance than implied by Fig. 5. Accordingly, imposing condition (3) causes failure by yielding in preference to buckling. Future demonstrations will take account of this extra buckling resistance.

Condition (3a) determines the aspect ratio of the trusses as (Hutchinson et al., 2003)

$$d_f/L_f = 1.1\sqrt{\varepsilon_Y}. \quad (4)$$

Evidently, the design depends on the choice of alloy, through ε_Y . For the present demonstration, performed using 304 stainless steel ($\sigma_Y = 200$ MPa, $\varepsilon_Y = 10^{-3}$), the preferred truss aspect ratio is: $L_f/d_f = 29$. Such a design would be yield-limited as noted above. The corresponding ratio for alloys with higher yield strain would be smaller: for example, a structure made using a Ti-6V-4Al alloy ($\sigma_Y = 800$ MPa, $\varepsilon_Y = 6.10^{-3}$), would correspond to an aspect ratio: $L_f/d_f \approx 13$. Additional considerations based on the overall weight might change this choice of aspect ratio.

The maximum value of the nominal in-plane stress ($\sigma_{11} = N_{11}/d_f$) that can be sustained by the trusses is obtained from (3b) and (4) as

$$\Sigma^{\max} \equiv \sigma_{11}^{\max}/\sigma_Y = 0.866(d_f/L_f) \equiv 0.95\sqrt{\varepsilon_Y}. \quad (5)$$

Now the benefits of the Ti alloy over stainless steel become especially apparent. For stainless steel, $\Sigma^{\max} = 3.48 \times 10^{-3}$ and $\sigma_{11}^{\max} = 0.7$ MPa. For Ti alloys, these loads are much larger: $\Sigma^{\max} = 7.78 \times 10^{-3}$ and

$\sigma_{11}^{\max} = 6.2$ MPa. The stress σ_{11}^{\max} provides a bound on the passive load that can be realized, as well as bounding the largest allowable actuation strain.

Selected numerical results for the response of the Kagome are summarized on Figs. 6 and 8. They refer to responses induced when displacements are imposed in the one-direction. The calculations are performed with and without imperfections and assessed with and without yielding. They are conducted in accordance with stress/strain characteristics representative of 304 stainless steel. Results are presented for two cases: yield control (Fig. 6(a)), and buckling control (Fig. 6(b)). When yielding is preceded by buckling (Fig. 6(b)), it occurs in strict accordance with Fig. 5. In the presence of imperfections, it is immediately followed by plastic buckling, with rapid softening, attributed to the slenderness of the truss members. When susceptible to elastic buckling (Fig. 6(b)), and when imperfections are present, bending of the truss members once they buckle, causes them to yield, with resultant softening. In the presence of patches, the effective stress at buckling (Fig. 7) exceeds that expected from the periodic model (Fig. 5). Omitting the patches reduces the buckling stress to a level below that in Fig. 5, highlighting the beneficial role of patch members in governing the overall performance.

3.2. The load capacity

The magnitudes of the passive loads that can be supported without failure are derived for a cantilever plate with a line load, P (per unit width) imposed at the free-end (Fig. 3). Emphasis is placed on analytic formula that can be used to select materials and to assess the scaling. A complete analysis, presented elsewhere (Wicks and Hutchinson, 2001) (Fig. 8), reveals that when optimized, this design is as good as the best available truss structures and competitive with honeycomb core panels. In loadings that cause the solid face to experience compression, it fails by local buckling, requiring that this face be relatively thick. The consequence is a minimum weight design comparable to that for the octet truss (Deshpande and Fleck, 2001). For loads that allow the face to remain in tension, as in the present demonstration, the structure is lighter, with weight comparable to that for a fully optimized sandwich panel (Wicks and Hutchinson, 2001). Moreover, when optimized, the face has about the same stiffness as the active Kagome face. Failure occurs by simultaneous yielding and buckling of both the Kagome face and the core.

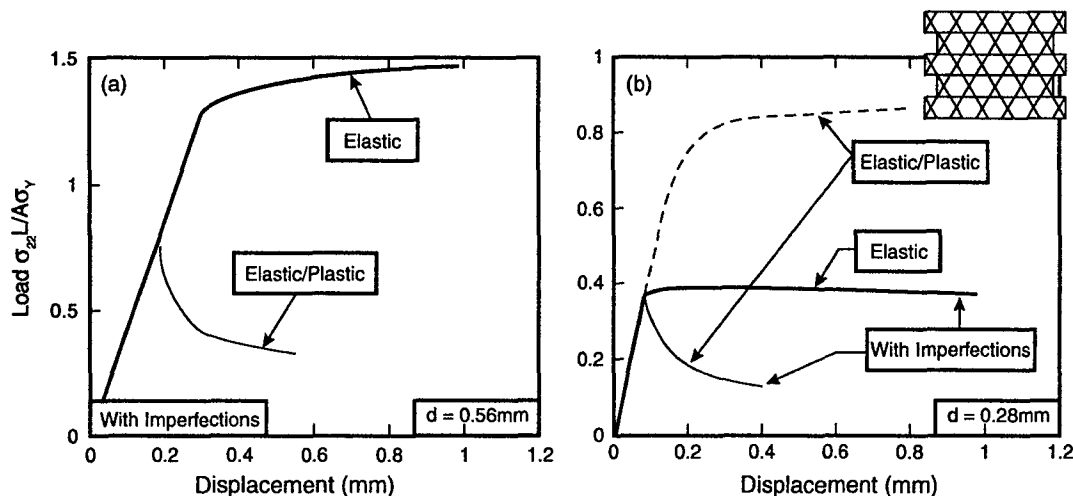


Fig. 6. Numerical results for the load-displacement responses of the Kagome back-plane subject to uniaxial in-plane straining. Results are presented for two cases: one wherein the structure is expected to be yield-controlled (a) and another when buckling-controlled (b).

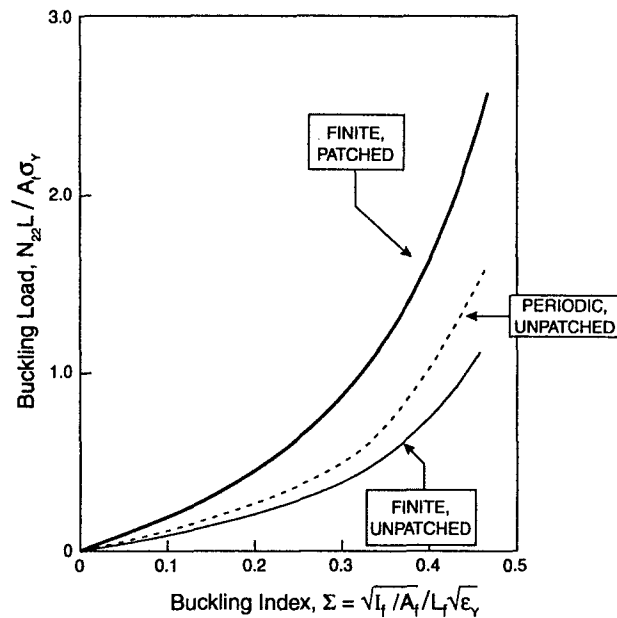


Fig. 7. In-plane buckling load of the Kagome back-plane depicted for an infinite, periodic structure, compared with a finite, unpatched structure, as well as a finite, patched structure.

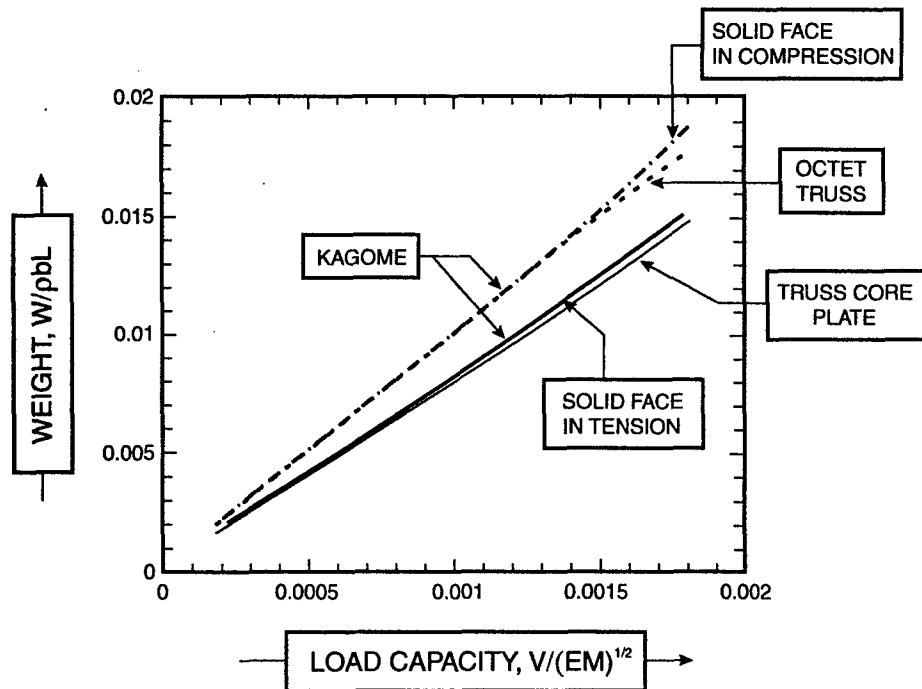


Fig. 8. Minimum weight as a function of the load-capacity for several sandwich panel geometries (Wicks, 2003). Note that the Kagome structure performs as well as the best available truss structures.

- (i) *The back-plane load capacity.* The Kagome back-plane and the solid face must sustain the bending moment. Since these faces are stiffness matched, the nominal stress induced in the back-plane is related to the bending moment, M , by (Ashby et al., 2000)

$$\sigma_{11} = M/d_f H_c, \quad (6a)$$

where H_c is the core thickness. For the present case, wherein the core and face truss members have the same dimensions (this will be a variable in future assessments), $L_c = L_f$, (6a) becomes

$$\sigma_{11} = \sqrt{3/2} P s / d_f L_f, \quad (6b)$$

where s is the span (Fig. 3). Since the aspect ratio has been chosen to assure failure by yielding rather than buckling, equating σ_{11} to σ_{11}^{\max} (5) gives the end load that can be supported without failing the faces by yielding as

$$P_M \leq 0.866 \sqrt{2/3} \frac{d_f^2}{s} \sigma_Y. \quad (7)$$

- (ii) *Passive face.* When the passive face is stiffness matched to the back-plane, its thickness, d_{pf} would be

$$\frac{d_{pf}}{d_f} = \frac{E}{E_{pf}} \frac{d_f}{\sqrt{3} L_f} \equiv \frac{1.1 \sqrt{\varepsilon_Y}}{\sqrt{3}} \frac{E}{E_{pf}}, \quad (8)$$

where E_{pf} is the Young's modulus of the face. For the present demonstration, polycarbonate is used for the face ($E_{pf} = 4$ GPa), whereupon, $d_{pf} \approx d_f$. Much smaller face thickness would be required when a metal face is used. For example, an Al alloy face would require that, $d_{pf}/d_f = 0.13$.

The load that can be supported by the faces prior to yield, in a stiffness-matched system, is given by (Wicks and Hutchinson, 2001)

$$P_M^f \leq \sqrt{2/3} \sigma_Y^f d_{pf} L_f / s, \quad (9)$$

where σ_Y^f is the yield strength of the face. The ratio of the loads that can be sustained by the face and the back-plane is thus

$$\frac{P_M^f}{P_M} = 0.67 \frac{\varepsilon_Y^f}{\varepsilon_Y}. \quad (10)$$

For a polycarbonate face ($\varepsilon_Y^f \approx 1.5 \times 10^{-2}$) and stainless steel back-plane ($\varepsilon_Y \approx 10^{-3}$), the load capacity is limited by yielding of the back-plane. When the passive face and the back-plane are made from the same material, the structure would be limited by face yielding. Small thickness adjustments would change this tendency.

In normal operation, the passive loads place the faces in tension. However, should the design require the face to experience compression, it would be susceptible to wrinkling, which would occur in accordance with

$$P_{Mw}^f \leq \sqrt{3/2} \times 2.24 E_{pf} \frac{d_{pf}^3}{L_f}. \quad (11)$$

The ratio of the wrinkling load to the yield load is

$$\frac{P_{Mw}^f}{P_M^f} = \frac{3.36}{\varepsilon_Y^f} \left(\frac{d_{pf}^3}{d_f L_f^2} \right). \quad (12)$$

This ratio reveals that face failure will occur preferentially by wrinkling, which accounts for the effects of loading direction expressed in Fig. 8.

- (iii) *Load supported by the core.* The tetrahedral core must sustain the shear force without yielding or buckling. The end load that can be supported by core members with square cross-section, before yielding, is given by (Wicks and Hutchinson, 2001)

$$P_v \leq \frac{1}{\sqrt{6}} \frac{d_c^2}{L_c} \sigma_Y. \quad (13)$$

(Note that this core has half the number of tetrahedral element as a truss core sandwich panel (Hutchinson et al., 2003)). The equivalent result for elastic buckling is

$$P_{vb} \leq \pi \frac{k E_c d_c^4}{4 \sqrt{6} L_c^3}, \quad (14)$$

where E_c is Young's modulus and k is a coefficient that depends on the end constraints (typically, $k \approx 1$). Comparing (13) and (14) and by using (4) for the aspect ratio of the core members, the ratio of the yielding and buckling loads becomes

$$\frac{P_v}{P_{vb}} = \frac{4}{1.2 k \pi}. \quad (15)$$

Accordingly, when $k \approx 1$, the core is essentially at the transition between yielding and buckling, which is desirable from a minimum weight perspective (Fig. 8) (Wicks and Hutchinson, 2001). A design with a core member thickness slightly larger than the face member thickness would assure failure by yielding.

- (iv) *Overall load capacity.* When the core is yield-controlled (13), the ratio of the load capacity of the core and the back-plane is

$$\chi_c \equiv \frac{P_M}{P_V} = 1.74 \left(\frac{d_f}{d_c} \right)^2 \frac{L_c}{s}. \quad (16)$$

At the optimum, $\chi_c \approx 1$ (Wicks, 2003). The present design ($s/L_c = 5.3$), with back-plane and core members having the same cross-section, is sub-optimal ($\chi_c \approx 0.32$): whereupon the loads are limited by yielding of the back-plane. Accordingly, (7) can be used to estimate the passive load capacity as, $P_M \approx 1.2$ kN/m (equivalent to a load of 20 kg). Note that, replacing stainless steel with a Ti alloy ($\sigma_Y = 800$ MPa) should increase the load capacity by a factor four: $P_M \rightarrow 4.8$ kN/m.

4. Actuation

Because of the bonded nature of the structure (Fig. 3), forces are induced upon imposing an actuation strain that can cause the system to be actuator-limited, rather than structure-limited. Before embarking on a shape morphing demonstration, it is essential to evaluate these forces and compare them with the operating characteristics of the actuator. Results are presented for actuators placed along the mid-section, half way between the support and the free end of the cantilever (Fig. 3), for the two scenarios outlined above. For hinging, all of the actuators are imparted the same extension (Fig. 4(b)). For twisting, different extensions are imposed on each actuator in the sequence described below (Fig. 4(c)).

4.1. Hinging

Resistance of the structure. Preliminary results for hinging displacements (Fig. 9) provide an indication of the resistance of the structure to actuation, expressed through the magnitudes of the forces on the actu-

ators, F_A , relative to those associated with the passive loads. The calculations also reveal that F_A is largely governed by the bending deformations induced in the core members and the face-plate immediately above the actuators. Accordingly, the scaling should have the form presented in Appendix A, which can be generalized as

$$\Sigma = \frac{1 + A(E_{pf}/E_c)\alpha + B(E_{pf}/E_c)^2\alpha^2}{C + D(E_{pf}/E_c)\alpha}, \quad (17a)$$

where Σ is the non-dimensional force

$$\Sigma = \frac{F_A L_c^3}{E_c \Delta d_c^4}, \quad (17b)$$

and α is a slenderness index

$$\alpha = \left(\frac{d_{pf}}{d_c} \right)^3 \frac{w}{d_c}. \quad (17c)$$

Here Δ is the actuator displacement, w is the width of the panel and A, B, C, D represent non-dimensional coefficients. The fidelity of this representation is ascertained by performing full numerical calculations of F_A for realistic ranges of the dimensions, with representative elastic properties (stainless steel, Ti and Al) and displacements (an actuation strain up to 10%). Results are obtained for steel and PMMA face sheets.

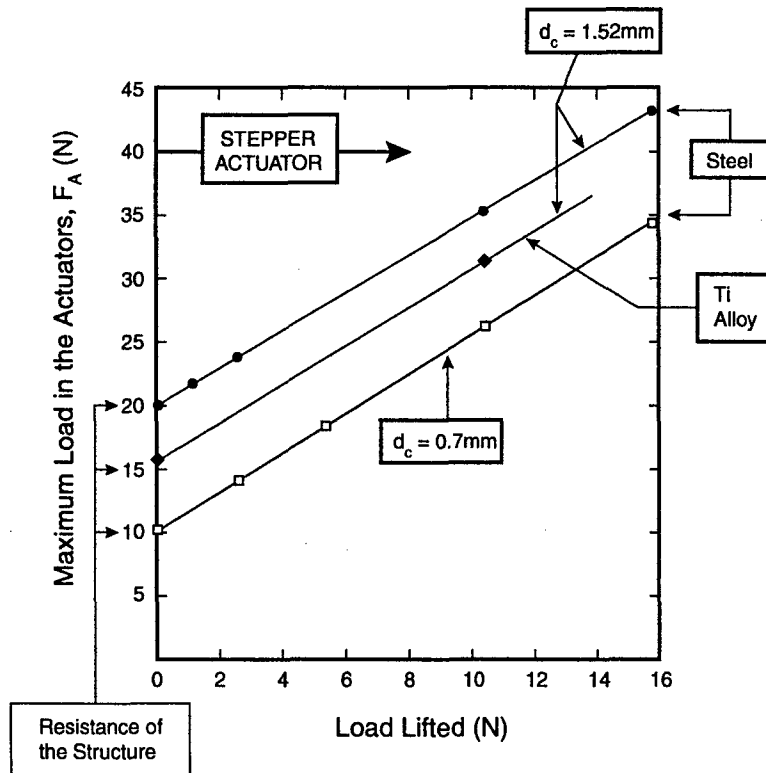


Fig. 9. Force on the actuators as function of the externally applied load. The resistance of the structure to actuation is obtained at zero external load.

To assess the relevant range, the dimensions that arise when the Kagome back-plane and the solid face are stiffness matched is determined as

$$\frac{d_c^2}{d_{pf} L_c} \frac{E_c}{E_{pf}} = \sqrt{3}. \quad (18)$$

Please note that the length and cross-section of the core members and the Kagome back-plane members are identical in this analysis. This implies that, for demonstrations similar to that in this article, for steel face sheets, $0 < \alpha < 0.02$, while for polycarbonate, $0 < \alpha < 2500$. Results have been obtained in these ranges (Fig. 10(a)–(d)) for core and Kagome face members having the same dimensions. The results for steel faces with *bonded joints* can be expressed as ($E_{pf} = E_c$)

$$\Sigma \approx 0.2 - 0.8\alpha + 13\alpha^2. \quad (19a)$$

The corresponding result when *the joints are pinned* is

$$\Sigma \approx 0.03\alpha. \quad (19b)$$

The result for polycarbonate faces bonded to the core ($E_c/E_{pf} = 1/200$) is

$$\Sigma \approx 0.22 + 6.2 \times 10^{-4}\alpha - 7.8 \times 10^{-8}\alpha^2. \quad (19c)$$

The large difference between (19a) and (19b) reinforces the major benefits of a pin-jointed design. Note that (19a) is relatively insensitive to α , signifying that the *steel faces* exert a minor contribution to F_A : where-upon, to a reasonable approximation, for bonded joints

$$F_A \approx 0.2E_c d_c (d_c/L_c)^3 \Delta. \quad (19d)$$

The crucial influence of the slenderness of the core members on F_A is apparent. Conversely, when *polycarbonate faces* are used, there is a strong α influence, such that the force on the actuator can be approximated by

$$F_A \approx 6.2 \times 10^{-4} E_c w (d_{pf}/L_c)^3 \Delta. \quad (19e)$$

That is, the force is dominated by the faces, so that reducing the core member thickness has a much smaller effect, as apparent from Fig. 9. The force on the actuator can thus be affected by the choice of face sheet material, with the non-intuitive trend that the *higher the material modulus, the lower the force* (because stiffness matching has been imposed). This finding is made explicit on Fig. 10(d), which compares actual values of F_A for steel and polycarbonate faces for two different assumptions. In one case the face and core members have the same thickness, consistent with Fig. 10(a)–(c). In the other, only the core member thickness is changed, consistent with Fig. 9. The latter demonstrates the large difference in F_A between the steel and polycarbonate faces, especially for slender cores.

The force on the actuators induced by the passive load, F_A^* can be obtained directly from (5) and (6) upon noting that the stress at the location of the actuators is half that at the supports

$$F_A^* = 0.58 \sqrt{3/2} P_M s. \quad (20)$$

These two forces are additive, giving the result plotted on Fig. 9 for the present demonstration. It is apparent from these formulae and from Fig. 9 that the *forces on the actuators when the passive loads attain their maximum realizable magnitudes (7) far exceed the loads associated with the resistance of the structure*. To enable the system to become actuator dominated, the force capacity of the actuators would need to be increased to, $F_A \approx 300$ N for a steel system and, $F_A \approx 1200$ N for a Ti system.

Fatigue of the core members. The bending of the core members just above the actuators suggests that these may be susceptible to fatigue. To assess this possibility, a cyclic FEM analysis has been performed using the mesh depicted on Fig. 11(a). The analysis has been performed using stress/strain behaviors

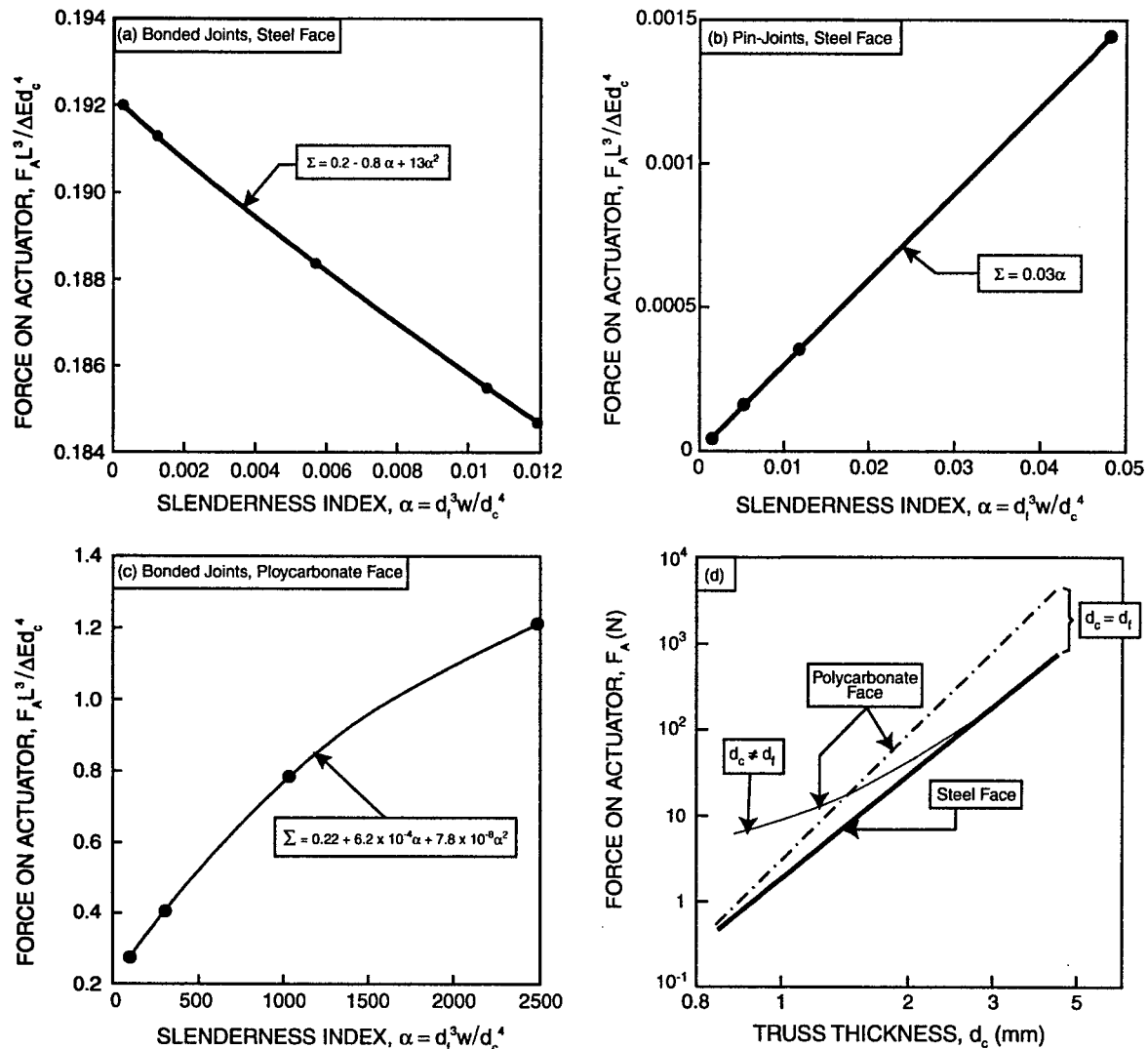


Fig. 10. The non-dimensional force on the actuators as function of the member slenderness. Results for a steel face are plotted for bonded joints (a) as well as flexible joints (b). Results for a polycarbonate face are plotted for bonded joints (c). Absolute values of the forces for steel and polycarbonate faces are compared (d) for several choices of the core member dimensions.

representative of both 304 stainless steel and Ti-6V-4Al. The calculations are performed by imposing prescribed displacements on the ends of the truss members ascertained from the full panel-scale model, actuated by a strain of 10%. The tab is allowed to displace freely in the vertical and horizontal directions. The first calculations have been performed for core members having the same slenderness as the face members. The largest bending stresses are located in the truss members adjacent to the tabs (Fig. 11(b)). For stainless steel, these stresses exceed the yield strength (Fig. 12(a)) resulting in cyclic plastic straining. While after about 40 cycles the system becomes elastic, indicative of shakedown, the response suggests a susceptibility to low cycle fatigue (LCF). In an attempt to obviate this problem, calculations have been

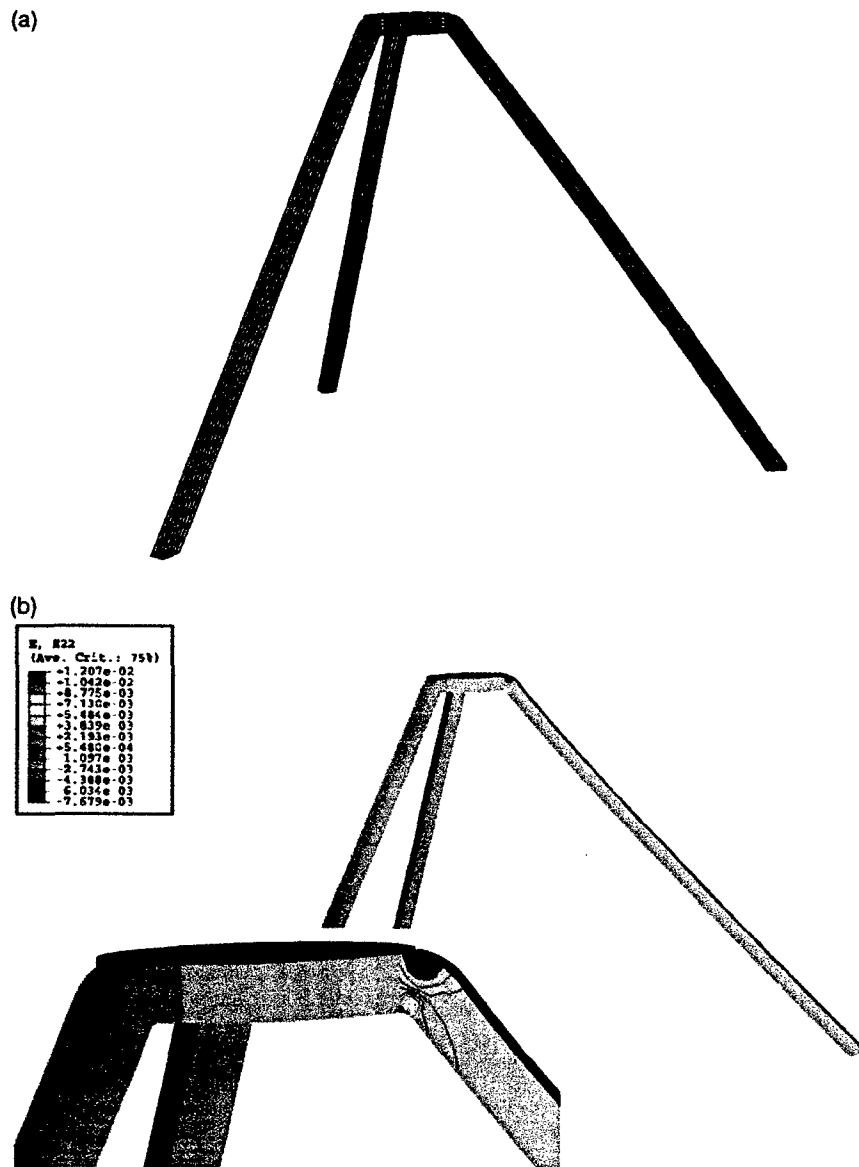


Fig. 11. Detailed fatigue study of a single core member. (a) FEA mesh. (b) Strains in the core member after 12 cycles.

performed for more slender core members: exemplified by the result for $d_c = 0.75$ mm (Fig. 12(b)). The modified results indicate that, when $d_c < 0.8$ mm, shakedown occurs after the first cycle (Fig. 12(b)) enabling the core members to be LCF resistant. To completely eliminate plastic deformation, further calculations reveal that the truss members need to be in the range, $d_c < 0.35$ mm. Such small values would diminish the passive load capacity, because of core buckling. The results for the Ti alloy (Fig. 12(c)) demonstrate the major advantages of this material, relative to stainless steel. Note that, even when the members are relatively thick, $d_c = 3$ mm, they remain elastic, eliminating LCF and alleviating high cycle fatigue (HCF).

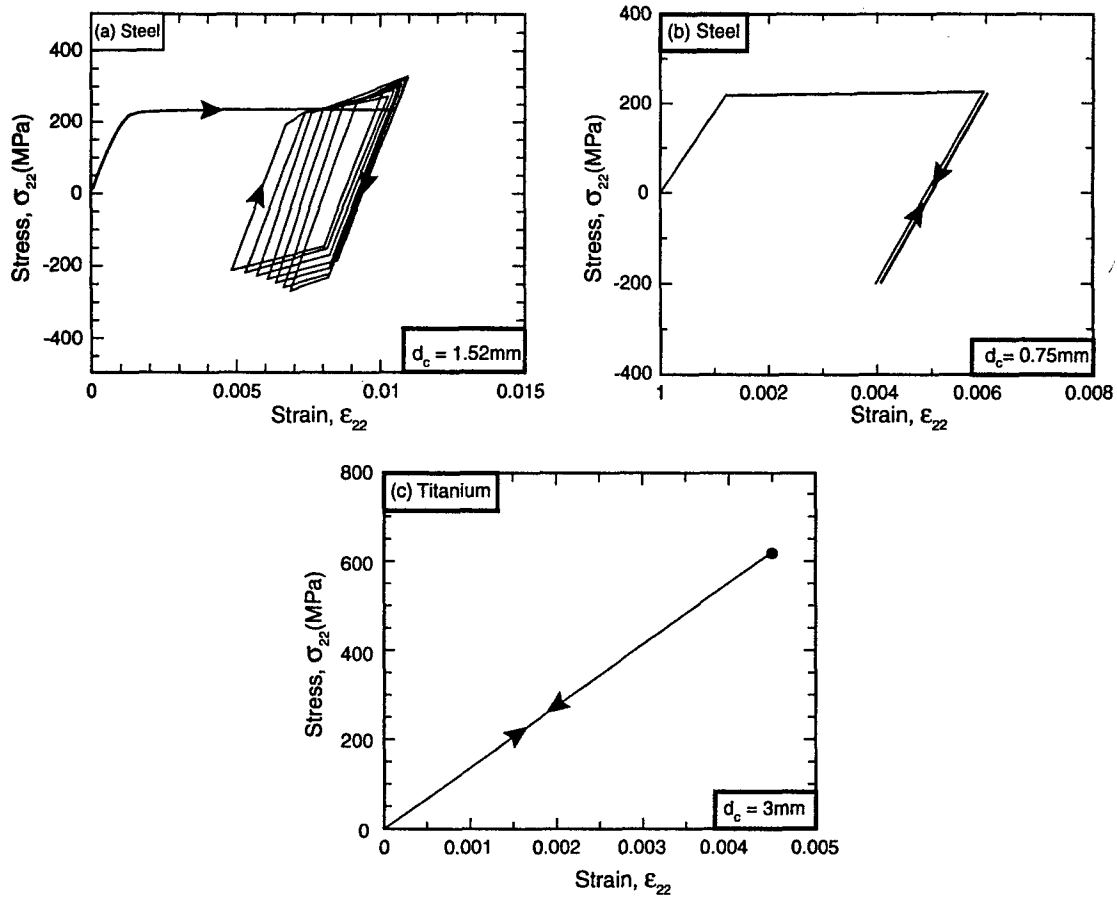


Fig. 12. Cyclic stress-strain curves at the maximum strain location calculated for core members fabricated from steel and titanium. Steel cores with a cross-section of $1.54 \times 1.54 \text{ mm}$ (a) and $0.7 \times 0.7 \text{ mm}$ (b); titanium core with a cross-section of $3 \times 3 \text{ mm}$ (c). Note that the titanium core members are 60 mm long while the steel core members are 51 mm in length.

4.2. Twisting

Achieving and maximizing the twist. The objective is to actuate the structure so that the free edge twists but remains straight. For this purpose, n points are identified along the edge. The vertical displacement, v_i , $i = 1, n$, of each is to be controlled and maximized by selecting actuator strains ϵ_j , $j = 1, m$, for m independent actuators, where $m > n$. The redundancy among the actuators will be used to optimize the twist of the edge, within the force capabilities of the actuators: a crucial requirement for *actuator-limited* structures. From analysis or measurement of the actuation of the structure without passive loading, a matrix A of influence coefficients can be constructed such that

$$v_i = \sum_{j=1}^m A_{ij} \epsilon_j. \quad (21)$$

Thus, A is an n by m matrix, with rank n . In some cases, the rank of A will be $r < n$, which implies that only r of the n controlled displacements will be linearly independent. This situation is undesirable, since the

displacements cannot be controlled independently and cannot be guaranteed to form a straight line upon twisting. In this case, control points should be dropped and n reduced until $r \rightarrow n$.

The null-space of the matrix A has dimension $m - n$ and consists of combinations of actuator strains that give rise to zero displacements at the control points along the edge to be twisted (Luenberger, 1973). An ortho-normal basis for the null-space is the set of $m - n$ vectors ε_j^k , $k = 1, m - n$, such that

$$\sum_{j=1}^m A_{ij} \varepsilon_j^k = 0. \quad (22)$$

These basis vectors ε_j^k can be found from Eq. (22) by standard matrix manipulations (Kreyszig, 1999). Now calculate

$$w^k = \sum_{j=1}^m \varepsilon_j^k \varepsilon_j, \quad (23)$$

which are projections of the actuator strain array into the null-space of A . Therefore, w_k , $k = 1, m - n$, represent the degrees of freedom that lead to zero displacements of the control points. Now introduce a matrix B defined as

$$B_{ij} = \begin{cases} A_{ij}, & i = 1, n \\ \varepsilon_j^{i-n}, & i = n + 1, m \end{cases}. \quad (24)$$

Thus, B is m by m with the matrix A forming its first n rows and ε_j^k forming its lower $m - n$ rows. It follows from Eq. (24) that

$$\sum_{j=1}^m B_{ij} \varepsilon_j = \begin{cases} v_i, & i = 1, n \\ w^{i-n}, & i = n + 1, m \end{cases}. \quad (25)$$

Since all its rows are linearly independent, the matrix B is non-singular and inversion of Eq. (25) provides

$$\varepsilon_j = \sum_{i=1}^n B_{ji}^{-1} v_i + \sum_{i=n+1}^m B_{ji}^{-1} w^{i-n}. \quad (26)$$

The structure of Eq. (26) shows that a required twist can be achieved by specifying the n displacements v_i for the control points, plus any values for the remaining $m - n$ parameters w^k , because the latter do not affect on the control point displacements.

Now maximize the twist of the edge without exceeding the force limits of the actuators. Through analysis (or measurement) without passive loads, the relationship between the actuator forces P_k , $k = 1, q$, and the actuator strains ε_i , $i = 1, m$ can be established as

$$P_k = \sum_{i=1}^m C_{ki} \varepsilon_i. \quad (27)$$

Thus C is a q by m matrix with $q \geq m$. Note that q may be larger than m because actuators may be operated in pairs or sets to have the same actuator strain, but each actuator in general experiences different force levels, even when paired or put together in sets. Combining Eqs. (26) and (27) gives

$$P_k = \sum_{j=1}^m C_{kj} \left(\sum_{i=1}^n B_{ji}^{-1} v_i + \sum_{i=n+1}^m B_{ji}^{-1} w^{i-n} \right). \quad (28)$$

Expressing the control point displacements in terms of a single degree of freedom, ϕ , that represents the amount of twisting

$$v_i = \phi \bar{v}_i, \quad (29)$$

where \bar{v}_i are simply the displacements of the control points for unit value of ϕ . As a result, Eq. (28) becomes

$$P_k = \beta_k \phi + \sum_{i=1}^{m-n} D_{ki} w^i, \quad (30)$$

where

$$\beta_k = \sum_{j=1}^m \sum_{i=1}^n C_{kj} B_{ji}^{-1} \bar{v}_i, \quad (31)$$

and D is a m by $m - n$ matrix given by

$$D_{ki} = \sum_{j=1}^m C_{kj} B_{ji+n}^{-1}. \quad (32)$$

The remaining task is to maximize ϕ in Eq. (30) subject to minimum and maximum constraints on the actuator forces P_k . This is a straightforward linear programming problem (Luenberger, 1973) to find the $m - n$ coordinates w^i . Once solved, the resulting values of ϕ and w^i are inserted into Eqs. (29) and (26) to compute the required actuator strains that produce the maximum possible twisting within the actuator force constraints.

Illustrations relevant to the current demonstration. The demonstration structure has eight independently operated actuators (Fig. 3). Five points are chosen on the actuated edge as control points (thus $n = 5$ and $m = 8$). Finite element calculations have provided the following results for the matrix A with the displacement of the control points measured in mm:

$$[A] = \begin{pmatrix} 15.60 & -17.76 & 168.32 & 26.76 & 93.32 & -9.17 & 56.33 & -8.03 \\ 2.73 & 4.27 & 111.99 & 24.70 & 112.99 & 19.97 & 50.00 & -1.22 \\ 2.95 & 69.66 & 49.66 & 41.33 & 41.33 & 48.66 & 69.66 & 2.93 \\ -1.22 & 50.00 & 19.93 & 112.66 & 24.80 & 112.32 & 4.23 & 2.68 \\ -8.13 & 56.33 & -9.20 & 92.99 & 26.90 & 168.65 & -17.66 & 15.50 \end{pmatrix}, \quad (33)$$

which has rank 5 as required. The null space of A has dimension 3 and its base vectors are

$$\begin{aligned} \{\varepsilon^1\}^T &= \{36.10 \quad -0.68 \quad -6.18 \quad -0.35 \quad 5.17 \quad 1.00 \quad 0.00 \quad 0.00\}, \\ \{\varepsilon^2\}^T &= \{-0.07 \quad -0.99 \quad -0.35 \quad 0.14 \quad -0.15 \quad 0.36 \quad 1.00 \quad 0.00\}, \\ \{\varepsilon^3\}^T &= \{0.01 \quad -0.03 \quad 0.01 \quad 0.15 \quad -0.01 \quad -0.16 \quad 0.01 \quad 1.00\}. \end{aligned} \quad (34)$$

Note that these expressions have not been normalized, so strictly, ε_j^i do not form an ortho-normal basis. However, the two basis vectors are orthogonal, which suffices for our purposes. The matrix B then becomes

$$[B] = \begin{pmatrix} 15.60 & -17.76 & 168.32 & 26.76 & 93.32 & -9.17 & 56.33 & -8.03 \\ 2.73 & 4.27 & 111.99 & 24.70 & 112.99 & 19.97 & 50.00 & -1.22 \\ 2.95 & 69.66 & 49.66 & 41.33 & 41.33 & 48.66 & 69.66 & 2.93 \\ -1.22 & 50.00 & 19.93 & 112.66 & 24.80 & 112.32 & 4.23 & 2.68 \\ -8.13 & 56.33 & -9.20 & 92.99 & 26.90 & 168.65 & -17.66 & 15.50 \\ 36.10 & -0.68 & -6.18 & -0.35 & 5.17 & 1.00 & 0.00 & 0.00 \\ -0.07 & -0.99 & -0.35 & 0.14 & -0.15 & 0.36 & 1.00 & 0.00 \\ 0.01 & -0.03 & 0.01 & 0.15 & -0.01 & -0.16 & 0.01 & 1.00 \end{pmatrix}, \quad (35)$$

and its inverse is

$$[B]^{-1} = \begin{pmatrix} 4.23 & -5.17 & 1.09 & -1.18 & 1.23 & 26.36 & -29.37 & 8.61 \\ -2.89 & -0.99 & 9.06 & -0.92 & -1.14 & -0.50 & -434.19 & -20.87 \\ 14.59 & -12.77 & 1.65 & -6.51 & 6.54 & -4.51 & -154.95 & 12.92 \\ -4.65 & 4.29 & -5.13 & 22.35 & -14.16 & -2.55 & 59.44 & 142.36 \\ -14.04 & 22.24 & -5.13 & 4.31 & -4.68 & 3.78 & -64.10 & -9.71 \\ 6.53 & -6.50 & 1.60 & -12.75 & 14.59 & 0.73 & 158.47 & -152.17 \\ -1.21 & -0.83 & 9.00 & -1.08 & -2.78 & 0.00 & 437.97 & 8.86 \\ 1.28 & -1.26 & 1.15 & -5.25 & 4.29 & 0.00 & 0.00 & 953.00 \end{pmatrix} \times 10^3. \quad (36)$$

There are a total of eight actuators so that $q = 8$. The matrix C was determined by finite element analysis to be

$$[C] = \begin{pmatrix} -27.50 & 14.06 & 25.53 & 11.33 & -13.20 & -9.47 & 6.10 & -9.33 \\ 13.97 & -320.97 & 98.66 & 123.65 & -18.26 & 56.99 & 36.00 & 6.00 \\ 24.70 & 97.99 & -295.64 & -14.60 & 202.31 & -70.67 & 55.99 & -10.20 \\ 10.57 & 122.99 & -14.50 & -343.30 & 44.00 & 202.31 & -18.56 & -13.87 \\ -13.97 & -18.93 & 202.65 & 44.00 & -343.30 & -14.10 & 122.65 & 10.43 \\ -10.30 & 55.99 & -70.66 & 201.98 & -14.17 & -295.30 & 97.66 & 24.46 \\ 5.97 & 36.00 & 56.66 & -17.93 & 123.32 & 98.32 & -320.30 & 13.93 \\ -9.33 & 6.13 & -9.33 & -13.10 & 11.20 & 25.30 & 14.03 & -27.36 \end{pmatrix}, \quad (37)$$

where the load is measured in MPa. Thus the inner product of C and B^{-1} is

$$[C][B]^{-1} = \begin{pmatrix} 0.27 & -0.37 & 0.18 & 0.21 & -0.18 & -0.91 & -6.57 & -6.00 \\ 2.44 & -1.30 & -2.85 & 1.52 & 0.12 & 0.02 & 156.98 & 26.45 \\ -7.81 & 8.41 & -0.16 & 3.24 & -3.98 & 2.65 & 2.03 & -9.15 \\ 1.78 & -1.77 & 2.78 & -10.00 & 7.38 & 0.68 & -50.76 & -97.36 \\ 7.34 & -9.96 & 2.78 & -1.79 & 1.81 & -2.59 & 53.33 & 25.85 \\ -3.99 & 3.26 & -0.15 & 8.40 & -7.81 & -0.30 & -4.18 & 95.28 \\ 0.15 & 1.48 & -2.82 & -1.26 & 2.40 & 0.43 & -158.25 & -8.60 \\ -0.18 & 0.21 & 0.18 & 0.37 & 0.27 & -0.14 & 7.72 & -32.17 \end{pmatrix}. \quad (38)$$

The optimization as carried out for a twisting motion defined by

$$\begin{pmatrix} v_1 \\ v_2 \\ v_3 \\ v_4 \\ v_5 \end{pmatrix} = \phi \begin{pmatrix} 0.00 \\ 0.25 \\ 0.50 \\ 0.75 \\ 1.00 \end{pmatrix}, \quad (39)$$

so that one corner moves upward and the other downwards. With this motion

$$\{\beta\}^T = \{0.409 \quad 0.0471 \quad 0.148 \quad -0.339 \quad 0.344 \quad -0.345 \quad -0.154 \quad -0.392\}, \quad (40)$$

and D is the 8 by 3 matrix formed by the three rightmost columns of Eq. (38). The constraints on the actuators are that the stress carried by each must lie between -0.4 and 0.4 MPa. With these restrictions, optimization of ϕ using Mathematica provides the results

$$\begin{pmatrix} w_1 \\ w_2 \\ w_3 \end{pmatrix} = \begin{pmatrix} -1.002 \\ 0.131 \\ 0.0464 \end{pmatrix}, \quad (41)$$

with $\phi = 6.64$ mm. Thus, within the limits of the actuators, the optimized twisting involves a motion in which one corner is displaced by 6.8 mm relative to the other. Twisting is more limited than hinging because of the associated stretching of the solid face sheet. Note, however, that the realizable twist scales linearly with the force capacity of the actuator (provided that the face does not yield). Accordingly, incorporation of an actuator with factor 6 higher capacity (to achieve the structure-limited hinging described above) would allow a twist of almost 7 cm.

5. The demonstration

5.1. Assembly

A detailed description of the processes used to manufacture the foregoing structure (Fig. 3(a)) is provided elsewhere (Maxwell et al., 2003). The Kagome face members have square cross-section (1.5×1.5 mm), while the core members are rectangular (0.75×1.5 mm), with unit length 51 mm. Stainless steel 304 was used for the Kagome back-plane and the core. The stiffness-matched solid face comprised polycarbonate, thickness 1.5 mm. After assembly, eight of the Kagome members were removed and replaced with the linear stepper motors. The entire assembly was rigidly attached to three heavy L-shaped stainless steel supports. The polycarbonate face was reinforced with an aluminum stripe. The fully assembled structure is shown in Fig. 3(b).

A computer based system is devised to control the actuators. Every actuator is connected to a drive card (Haydon Switch, model 39105) which distributes the power from an attached DC power supply to the motors in the correct stepping sequence. All drive cards are connected through a digital interface (Keithley KPCI-3102) to the control computer. The drive cards are controlled by two digital signals, determining the direction of the actuation and the stepping. A custom designed program stores the position of every actuator and coordinates the actuators to obtain the desired shape by generating the direction and the stepping signals.

5.2. Comparison with model

To demonstrate hinging subject to a small (1 kg) restraining load, all actuators were extended simultaneously by 7% (equivalent to 281 steps at $12.7 \mu\text{m}/\text{step}$). A 23 mm tip displacement was realized, in good agreement with the FEM simulation (26 mm). The present actuators have a load limit of ~ 50 N at a stepping rate of 50/s, resulting in the maximum allowable load capacity summarized on Fig. 9. Verification of this estimate was performed by sequentially elevating the load on the free edge by 0.5 kg until the actuators ceased operation. This procedure revealed that the actuation became erratic (but did not cease entirely) at loads exceeding 3.0 kg. This load capacity compares well with the calculated value of 2.5 kg. Recall that a load of 30 kg could be lifted if the system were not actuator limited. Measurement repeated with a 50 μm thick Al alloy face sheet did not change the results.

Demonstration of the twisting mode was based on the actuator strains provided by the optimization procedure described in Section 4.2. These strains were, respectively, -2.91% , 0.97% , -0.17% , 1.50% , 0.52% , 2.22% , 1.08% and 4.83% for the eight actuators. The maximum twist that could be corresponded to a 6.5 mm height difference between the two edges, in close agreeing the predicted value (6.8 mm). Recall that larger twist angles would be possible with superior actuators. The final shapes of the demonstration structure for the hinging and twisting modes are shown in Fig. 13.

This comparison has achieved two primary objectives:

- (i) It has affirmed that the structure in its present form is actuator-limited, highlighting the need for superior actuators that allow the system to realize its potential. Assessments of alternative actuators are in progress.

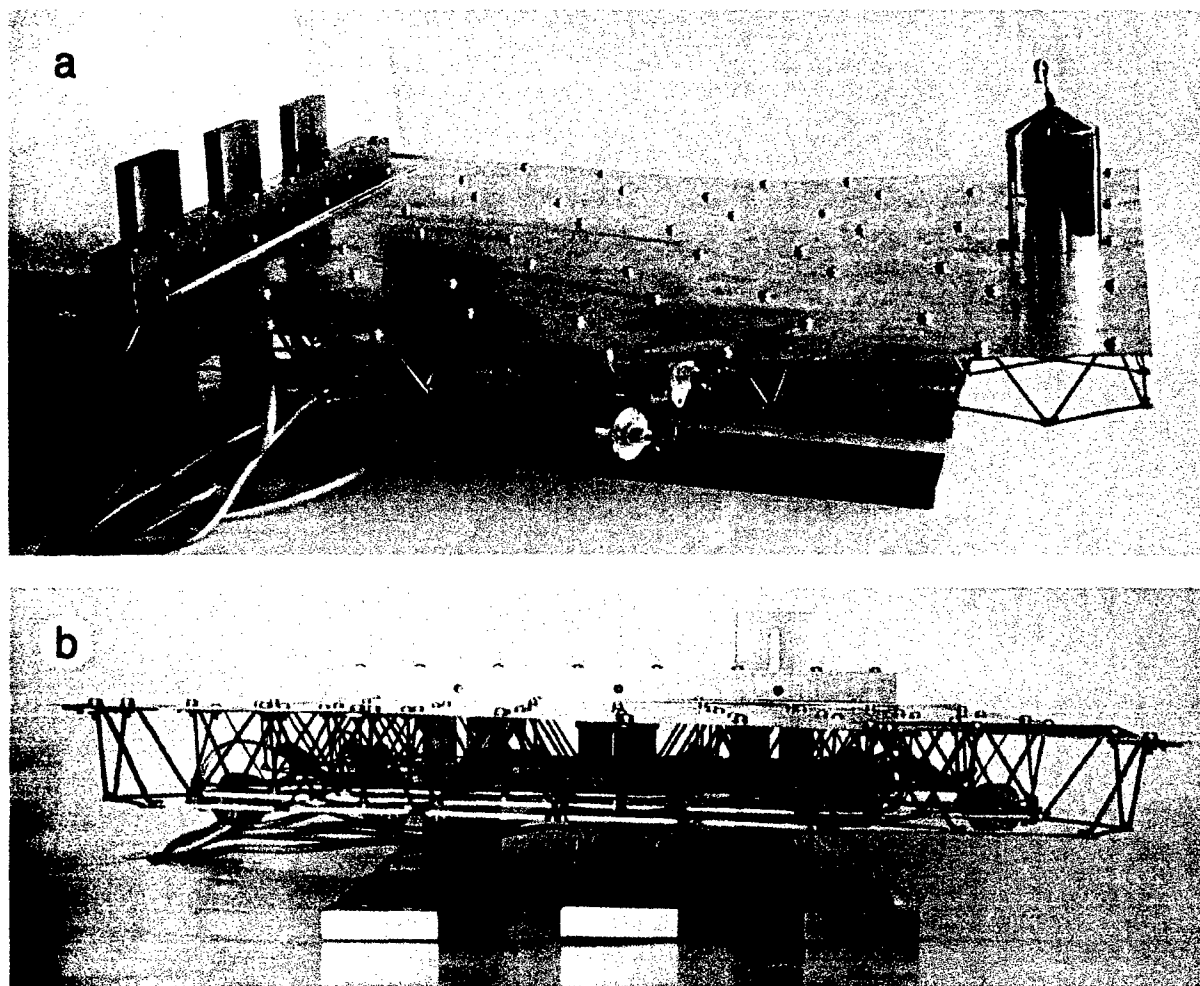


Fig. 13. Demonstration of the hinging and twisting modes when an Al alloy face sheet is used.

- (ii) The agreement between measured and calculated displacements and load capacities has provided confidence in the numerical method, allowing the method to be used to set objectives for ongoing activities related to alternative materials, as well as structural and actuator enhancements.

6. Concluding remarks

A combination of analytical and numerical assessments has been used to guide the design of a high authority shape morphing structure, based on the attributes of a Kagome active plane. A version of the structure has been manufactured using a stainless steel active face and core, with a polycarbonate passive face, and commercially available linear stepper actuators. Hinging and twisting has been demonstrated. It has not been possible to demonstrate the full capabilities of the system because of the limitations imposed by the actuators. These limitations have been characterized in a consistent manner, using both measurements and simulations, allowing the numerical method to be used to set the objectives that need to be realized to demonstrate the full potential.

The scaling used in conjunction with numerical simulations has identified the following objectives.

- (i) Among potential material candidates, Ti–6V–4Al appears to be the best choice, because of its high yield strain and relatively low density. The replacement of steel by this alloy will eliminate fatigue in hinging actuations and allow the passive load capacity to increase to 4.8 kN/m at lower overall weight. It will also slightly increase the load that can be lifted by the present actuators and increase the realizable twisting angle. Such a system is being fabricated by diffusion bonding.
- (ii) New capability is needed for linear actuators that allow the system to become structure-limited. For a Ti system, to realize the full authority potential in a hinging mode, the maximum force capacity would need to be increased to 1200 N (compared with 50 N for the present actuators), while still capable of strains of order 10% at acceptable frequencies. Such a capacity would also permit extensive twisting. New developments in piezoelectric and ferromagnetic shape memory systems will provide the much greater authority needed to obviate these limitations (Karaca et al., 2003).
- (iii) The incorporation of fully flexible joints at the core members encompassing the actuation sites would reduce the forces on the actuators and eliminate any tendency for fatigue.

It will be important to compare and contrast the performance of the present structure with that comprising two Kagome faces and a tetrahedral core (Symons et al., 2003). This comparison will establish the circumstances governing the choice between these complementary designs.

Appendix A. Scaling of the actuation resistance to hinging

The scaling of the actuation resistance of the demonstration structure (Fig. 3) can be ascertained from analysis of the two-dimensional structure shown in Fig. 14(a). The configuration consists of a face sheet having elastic bending stiffness $E_{\text{pr}}I_{\text{pr}}$ (where I_{pr} is the second moment of area of its cross-section), bonded to symmetrically triangulated core members with bending stiffness E_cI_c . An actuator (not shown), attached to the structure by pin-joints, applies a force F_A to each apex of the core members. The ensuing displacement, $\Delta/2$, is a measure of the actuation resistance of the structure, $k = F_A/\Delta$. The response is dominated by elastic bending of both the face sheet and the core members. Elastic extension of each component leads only to a negligible, higher order, correction. Accordingly, the stiffness in local coordinates of a core member, with nodes A and B (Fig. 14(b)) is (Thomson and Dahleh, 1998):

$$\begin{Bmatrix} F_2^A \\ M^A \\ F_2^B \\ M^B \end{Bmatrix} = \frac{E_c I_c}{L^3} \begin{bmatrix} 12 & 6L & -12 & 6L \\ 6L & 4L^2 & -6L & 2L^2 \\ -12 & -6L & 12 & -6L \\ 6L & 2L^2 & -6L & 4L^2 \end{bmatrix} \begin{Bmatrix} u_2^A \\ \theta^A \\ u_2^B \\ \theta^B \end{Bmatrix}, \quad (\text{A.1})$$

where u_i^N , $i = 1, 2$, $N = A, B$, are the displacement components of the nodes, θ^N , $N = A, B$, are the anti-clockwise nodal rotations, F_i^N , $i = 1, 2$, $N = A, B$, are the applied force components at the nodes and M^N , $N = A, B$, are the applied nodal moments, positive when anti-clockwise. Equilibrium requires that

$$F_1^A + F_1^B = 0, \quad (\text{A.2})$$

and inextensibility provides

$$u_1^B = u_1^A. \quad (\text{A.3})$$

Equivalent relationships are valid for a face sheet member with E_cI_c and L in Eq. (A.1) replaced by $E_{\text{pr}}I_{\text{pr}}$ and $\sqrt{2}L$, respectively.

The solution procedure seeks three equilibrium equations that contain the load, F_A , the bending moments, M , and shear forces, V , by eliminating the member tensions, T (Fig. 14(c)):

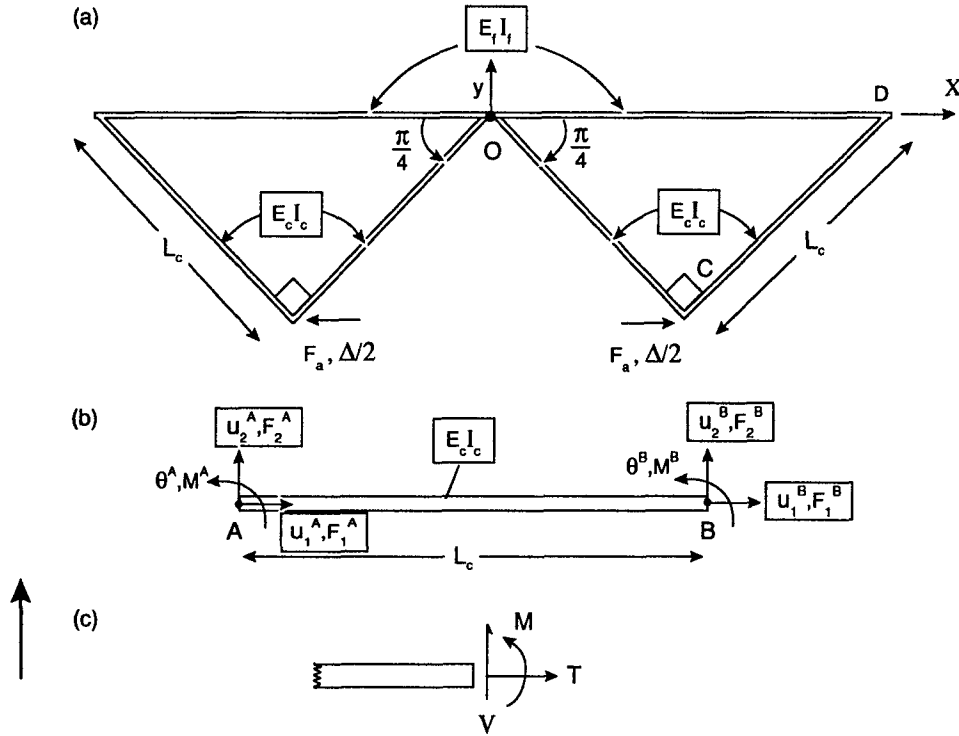


Fig. 14. Two-dimensional structure used to determine the actuation resistance. (a) Full model consisting of the face sheet and two core units. (b and c) Nomenclature describing the core members.

$$\begin{aligned}
 M_{CD} + M_{OD} &= 0, \\
 M_{OC} - M_{CD} - V_{CD}L &= 0, \\
 F_A &= \sqrt{2}(V_{OC} + V_{CD}) + 2V_{OD},
 \end{aligned}
 \tag{A.4}$$

where M_{AB} and V_{AB} are the bending moment and shear force, respectively, at the right-hand end of member AB (Fig. 14(b)).

Since the point O at the origin (Fig. 14(a)) neither displaces nor rotates, it can be deduced from inextensibility that joint C moves a distance $\Delta/\sqrt{2}$ towards point D and joint D moves a distance Δ in the direction parallel to the positive y-axis. Use of Eq. (A.1) for the relevant members then provides

$$\begin{aligned}
 M_{OC} &= \frac{E_c I_c}{L^3} \left(4L^2 \theta_C - \frac{6L}{\sqrt{2}} \Delta \right), \\
 V_{OC} &= \frac{E_c I_c}{L^3} \left(6\sqrt{2} \Delta - 6L \theta_C \right), \\
 M_{CD} &= \frac{E_c I_c}{L^3} \left(2L^2 \theta_C + 4L^2 \theta_D - \frac{6L}{\sqrt{2}} \Delta \right), \\
 V_{CD} &= \frac{E_c I_c}{L^3} \left(6\sqrt{2} \Delta - 6L \theta_C - 6L \theta_D \right), \\
 M_{OD} &= \frac{E_{pf} I_{pf}}{L^3} \left(2\sqrt{2} L^2 \theta_D - 3L \Delta \right), \\
 V_{OD} &= \frac{E_{pf} I_{pf}}{L^3} \left(3\sqrt{2} \Delta - 3L \theta_D \right),
 \end{aligned}
 \tag{A.5}$$

where θ_C and θ_D are the anti-clockwise rotations of joints C and D, respectively.

The first two of equations of (A.4) give

$$\theta_C = \frac{9(\sqrt{2}E_c I_c + E_{pf} I_{pf})\Delta}{2(7E_c I_c + 4\sqrt{2}E_{pf} I_{pf})L}, \quad (\text{A.6})$$

and

$$\theta_D = \frac{3\sqrt{2}(E_c I_c + \sqrt{2}E_{pf} I_{pf})\Delta}{(7E_c I_c + 4\sqrt{2}E_{pf} I_{pf})L}. \quad (\text{A.7})$$

These two results are inserted into the first of Eq. (A.4) to provide the actuation resistance

$$k = \frac{F_A}{\Delta} = \frac{6\sqrt{2}(E_c I_c + \sqrt{2}E_{pf} I_{pf})(2\sqrt{2}E_c I_c + E_{pf} I_{pf})}{(7E_c I_c + 4\sqrt{2}E_{pf} I_{pf})L^3}. \quad (\text{A.8})$$

For a system, width w , with n core members

$$I_c = \frac{n}{12} d_c^4, \quad (\text{A.9})$$

and

$$I_f = \frac{w}{12} d_{pf}^3, \quad (\text{A.10})$$

such that Σ (as defined in Eq. (17b)) becomes

$$\Sigma = \frac{\left(n + \sqrt{2} \frac{E_{pf}}{E_c} \alpha\right) \left(2\sqrt{2}n + \frac{E_{pf}}{E_c} \alpha\right) \left(\frac{L_c}{L}\right)^3}{\sqrt{2} \left(7n + 4\sqrt{2} \frac{E_{pf}}{E_c} \alpha\right)}. \quad (\text{A.11})$$

Generalization to account for the three-dimensionality of the demonstration structure and its heterogeneity in elastic properties yields Eq. (17a).

References

- Ashby et al., 2000. *Metal Foams: A Design Guide*. Butterworth-Heinemann, Boston.
- Christensen, R.M., 2000. Mechanics of cellular and other low-density materials. *Int. J. Solids Struct.* 37, 93–104.
- Deshpande, V., Fleck, N.A., 2001. *Int. J. Solids Struct.* 38, 62–75.
- Hutchinson, R.G., Wicks, N., Evans, A.G., Fleck, N.A., Hutchinson, J.W., 2003. Kagome plate structures for actuation. *Int. J. Solids Struct.* 40, 6969–6980.
- Hyun, S., Torquato, S., 2002. Optimal and manufacturable two-dimensional, Kagomé-like cellular solids. *J. Mater. Res.* 17, 137–144.
- Karaca, H.E., Karaman, I., Lagoudas, D.C., Maier, H.J., Chumlyakov, Y.I., 2003. Recoverable stress-induced martensitic transformation in a ferromagnetic CoNiAl alloy. *Scripta Mater.* 49, 831–836.
- Kreyszig, E., 1999. *Advanced Engineering Mathematics*, eighth ed. Wiley, New York.
- Luenberger, D.G., 1973. *Linear and Nonlinear Programming*, second ed. Addison-Wesley, Reading, MA.
- Lu, T.J., Hutchinson, J.W., Evans, A.G., 2001. Optimal design of a flexural actuator. *J. Mech. Phys. Solids* 49, 2071–2093.
- Maxwell, P., dos Santos e Lucato, S.L., Evans, A.G., 2003. Fabrication of a high-authority Kagome actuator, to be submitted.
- Symons, D., Hutchinson, R.G., Fleck, N.A., 2003. Actuation performance of the Kagome Double Layer Grid. Submitted to *J. Mech. Phys. Solids*.
- Thomson, W.T., Dillon Dahleh, M., 1998. *Theory of Vibration with Applications*, fifth ed. Prentice-Hall, Englewood Cliffs, NJ.
- Wicks, N., 2003. Optimization and actuation of truss structures. Ph.D. Thesis, Engineering Sciences, Harvard University, Cambridge, Massachusetts.
- Wicks, N., Hutchinson, J.W., 2001. Optimal truss plates. *Int. J. Solids Struct.* 38, 5165–5183.

Part II: The load capacity of a kagome based high authority shape morphing structure

The Load Capacity of a Kagome Based High Authority Shape Morphing Structure

S. L. dos Santos e Lucato

A. G. Evans

Materials Department, University of California,
Santa Barbara, CA 93106-5050

A protocol for optimizing a high authority shape morphing plate is described. The design incorporates an active Kagome back-plane capable of changing the shape of a solid face by transmitting loads through a tetrahedral truss core. The optimization assesses the required geometric dimensions and actuator specifications in order to maximize the permissible shape changes and load capacity. The critical external loads for all failure mechanisms of the individual components are calculated and used as constraints in the optimization. Resistance of the structure to actuation is presented as an additional constraint. The ensuing relations are subsequently used to choose the best material for a given application. Numerical examples of the procedure are given for a defined structure. [DOI: 10.1115/1.2042482]

1 Introduction

Shape morphing structures are designed to displace surfaces while resisted by large pressure loads (or heavy weights). An approach for addressing this challenge is to seek structures that are simultaneously statically determinate yet stiff [1–6]. One manifestation is the Kagome structure (Fig. 1) [2,3,6] which can be actuated into relatively intricate surface shapes. The structure consists of a solid face sheet with a Kagome, active back-plane and a tetrahedral core. Replacing various truss elements in the back-plane with linear actuators enables the shape of the solid face to be changed. A preliminary demonstration structure has been constructed and used to reveal the practical potential (Fig. 2) [6]. To facilitate fabrication, this structure was made using 304 stainless steel. The length of the panel was chosen to include six hexagonal units of the Kagome plate, while the width incorporated four. Hinging and twisting have been demonstrated and shown to be consistent with linear models [6]. To achieve smooth contour changes at low structural weight, the solid face and the back-plane were stiffness matched. Multiple virtual control points define the shape change [4–6]. The demonstration structure was found to be actuator limited, because the actuators ceased to function at loads much lower than the passive load capacity of the structure.

The intent of the present article is to provide a exploration of the authority space for this structure. It will embrace a broad range of material properties and assume actuators having load capacity substantially superior to those used in the preliminary demonstration. A corollary will be an optimization protocol. For tractability and clarity of presentation, the present assessment is limited to simple hinging of the demonstration structure (Fig. 2). Yet, the approach has much wider applicability and its implementation for the attainment of more complex shape changes will be presented in a forthcoming article. The procedure ascertains the stresses, relative to the failure envelope, and determines the actuator authority needed to maximize the load capacity as a function of designated displacements.

2 Passive Load Capability

The passive loads that can be supported without failure have been derived for a cantilever plate subject to a line load, P , imposed at the free end (Fig. 1) [7]. When optimized for loadings that cause the solid face to experience compression, its structural efficiency is competitive with truss and honeycomb core panels [5]. The basic results needed for optimization will be presented with the assumption that the Kagome members are connected by pin joints. Relative to bonded joints this choice allows a fully analytical investigation. It does so without affecting the yield loads, while providing a conservative assessment of the buckling loads.

In the ensuing analysis, the subscripts k , c , and f refer to the Kagome back-plane, core, and solid face, respectively. All truss members have a square cross section, thickness d_x , and a length L_x (Fig. 1). The solid face has thickness d_f . The width and span of the structure are denoted w and s , respectively. The lengths of the Kagome and core members are equal ($L=L_k=L_c$), ensuring maximum resistance to core shear [5]. The Young's modulus is designated E , and yield strength σ_Y . Failure loads are denoted P_{XZ} , with subscript X referring to the component and Z to the failure mode: Y for yielding and B for buckling/wrinkling. The actuator is considered to cease functioning at axial load P_{ACT} .

Kagome back-plane. Initially, the stiffness of the solid face is chosen to match that for the back-plane (by adjusting its thickness). Under this assumption, the nominal stress induced in the back-plane is related to the bending moment, $M=Ps$, and the core height, $H_c=\sqrt{3}/2L$, by [8]

$$\sigma_{11} = \sqrt{\frac{3}{2}} \frac{Ps}{d_f w L} \quad (1a)$$

Modifications that arise when the system is not stiffness matched are presented in the Appendix. There are three Kagome truss orientations (Fig. 1): one parallel to the width (truss A) and the others at $\pm 30^\circ$ to the span (truss B). For the present loading state, the latter two are equivalent. The nominal stress σ_{11} is related to that on a truss member σ_{truss} by [2]

$$\sigma_{11} = -\sqrt{3} \frac{d_f}{L} \sigma_{truss} \text{ (truss A)} \quad \text{and} \quad \sigma_{11} = \frac{\sqrt{3} d_f}{2 L} \sigma_{truss} \text{ (truss B)} \quad (1b)$$

If the back-plane is loaded in compression, trusses in orientation A are in tension and those in orientation B are in compression and

Contributed by the Applied Mechanics Division of THE AMERICAN SOCIETY OF MECHANICAL ENGINEERS for publication in the ASME JOURNAL OF APPLIED MECHANICS. Manuscript received by the Applied Mechanics Division, July 23, 2004; final revision, February 14, 2004. Review conducted by Z. Suo. Discussion on the paper should be addressed to the Editor, Prof. Robert M. McMeeking, Journal of Applied Mechanics, Department of Mechanical and Environmental Engineering, University of California—Santa Barbara, Santa Barbara, CA 93105-5070, and will be accepted until four months after final publication in the paper itself in the ASME JOURNAL OF APPLIED MECHANICS.

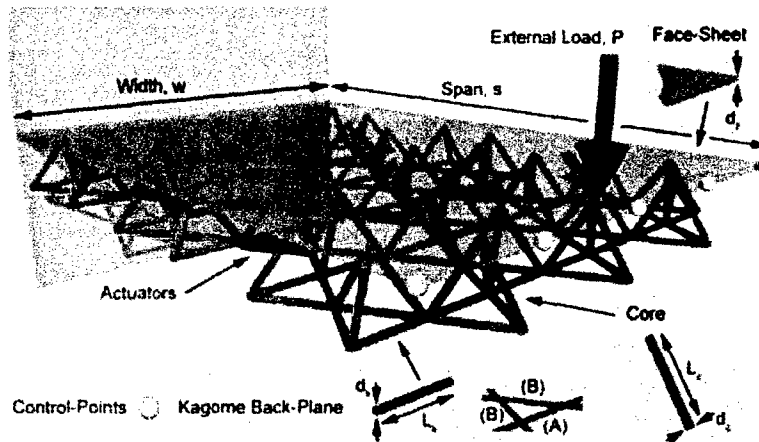


Fig. 1 (Color) Schematic representation of the Kagome-structure. The face sheet is shown in blue, the core in green, and the Kagome back-plane is red. Actuators are placed in lieu of the Kagome members. The control points are used to define the target deformation.

vice versa. Equating $|\sigma_{truss}|$ to the yield strength, σ_Y , gives the end load that can be supported without failure by yielding as

$$P_{KY} \leq \sqrt{2} \frac{w d_k^2}{s} \sigma_{Yk} \text{ (truss A)} \quad \text{and} \quad P_{KY} \leq \frac{1}{\sqrt{2}} \frac{w d_k^2}{s} \sigma_{Yk} \text{ (truss B).} \quad (2)$$

The permissible load is always smaller for trusses in orientation B.

The treatment of buckling is slightly more complex, since the direction of the external load has to be considered. The load that can be supported without buckling if the solid face is in tension (Kagome in compression, i.e., only trusses in B orientation can buckle) is

$$P_{KB} \leq \frac{\pi^2}{12\sqrt{2}} \frac{w d_k^4}{L^2 s} E_k \quad (3)$$

Core. The tetrahedral core must sustain the shear force. The end load supported before yielding is [7]

$$P_{CY} \leq \frac{1}{\sqrt{6}} \frac{w d_c^2}{L} \sigma_{Yc}. \quad (4)$$

(Note that this core has half the number of tetrahedral element as a truss core sandwich panel [2].) The equivalent result for elastic buckling is

$$P_{CB} \leq \frac{\pi}{4\sqrt{6}} \frac{w d_c^4}{L^3} E_c. \quad (5)$$

Solid Face. The solid face has thickness

$$d_f = \lambda_{sm} \frac{E_k}{E_f} \frac{d_k^2}{\sqrt{3} L_k} \quad (6)$$

The scaling factor λ_{sm} is unity when the face is stiffness matched (solid face sheet has the same linear elastic load-deflection behavior as the Kagome back-plane when loaded in tension): $\lambda_{sm} > 1$ signifies a solid face stiffer than the back-plane and vice versa. In this analysis the face sheet stiffness for a given material combi-

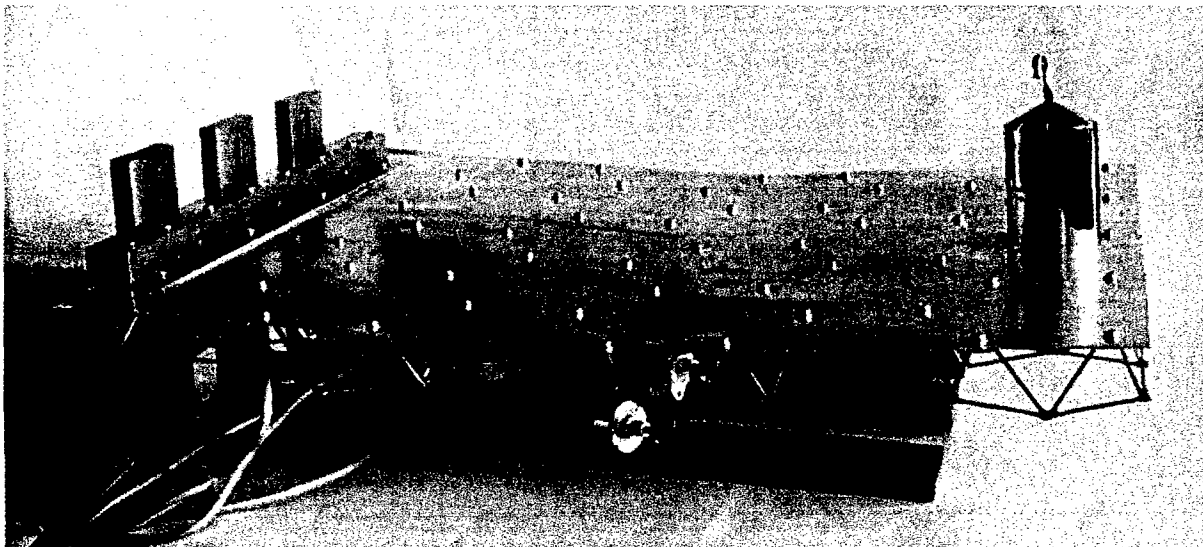


Fig. 2 (Color) Photo of the actual demo structure. The aluminum solid face sheet is used. Actuators are placed along the middle section and extended by 10%.

nation is varied by changing the thickness of the solid face sheet. For example, $\lambda_{sm}=1$ for a stainless steel back-plane ($E_k=200$ GPa) and a polycarbonate ($E_f=4$ GPa) solid face requires both faces to have the same thickness $d_f \approx d_k$. For designs with $d_f \ll H_c$, the load that can be supported is obtained from 1(a) by equating σ_{11} to σ_{Yf} :

$$P_{FY} \leq \sqrt{\frac{2}{3}} \frac{w d_f L}{s} \sigma_{Yf} \quad (7)$$

3 Actuation Resistance

When an actuation strain is imposed, the structure induces forces on the actuator, F_{ACT} [6,9]. These forces must be evaluated and compared with the operating characteristics of the actuator. To illustrate the procedure, results are presented for actuators placed along the mid-section, half way between the support and the free end of the cantilever (Fig. 2). For hinging, all actuators experience the same extension and the resistance of the structure scales as [6]

$$\Sigma = \frac{1 + A(E_f/E_c)\alpha + B(E_f/E_c)^2\alpha^2}{C + D(E_f/E_c)\alpha} \quad (8)$$

where Σ is the nondimensional resistance,

$$\Sigma = \frac{F_{ACT} L^3}{E_c \Delta d_c^4} \quad (9)$$

and α is a stubbiness index,

$$\alpha = \left(\frac{d_f}{d_c} \right)^3 \frac{w}{d_c} \quad (10)$$

Here Δ is the actuator displacement and A, B, C, D are nondimensional coefficients. When $E_f = E_c$, Eq. (8) reduces to

$$\frac{F_{ACT} L^3}{E_c \Delta d_c^4} = 0.2 - 0.8\alpha + 13\alpha^2 \quad (11)$$

The passive load induces another force F_{EXT} on the actuators, obtained from (1b) as

$$F_{EXT} = \frac{0.58\sqrt{3}s}{\sqrt{2}} P_{ACT} \quad (12)$$

Since the two forces are additive, the total force on the actuators is

$$F_{TOT} = F_{EXT} + F_{ACT}$$

Equating to the load capacity of the actuator, F_{ACT}^{max} , the maximum permissible external load becomes

$$P_{ACT} = (F_{ACT}^{max} - F_{ACT}) \frac{\sqrt{2}}{0.58s\sqrt{3}} \quad (13)$$

4 Geometric Optimization

The objectives are to ascertain geometries that satisfy various design criteria, subject to the avoidance of all failure mechanisms. Throughout, the solid face sheet is assumed to be stiffness matched to the back-plane ($\lambda_{sm}=1$). The three criteria are as follows:

(i) Maximize the externally applied load by identifying the first subsystem to fail:

$$P_{ext}^{max} = \min(P_{KY}, P_{KB}, P_{CY}, P_{CB}, P_{FY}, P_{FB}, P_{ACT}) \quad (14)$$

(ii) Maximize the displacement exerted by the actuators without causing failure of any other subsystem:

$$P_{ext}^{passive} = \min(P_{KY}, P_{KB}, P_{CY}, P_{CB}, P_{FY}, P_{FB}) \quad (15a)$$

$$\Delta^{max} = \left(F_{ACT}^{max} - P_{ext}^{passive} \frac{0.58s\sqrt{3}}{\sqrt{2}} \right) \frac{L^3}{\Sigma E_c d_c^4} \quad (15b)$$

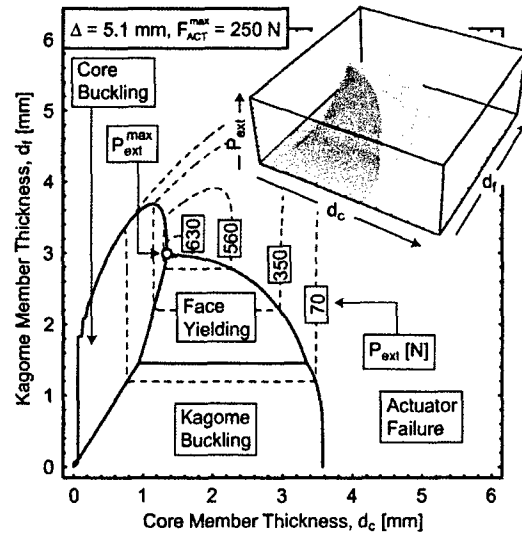


Fig. 3 Maximum load capability for a given actuator capacity and extension. All structure failure mechanisms except face wrinkling are included.

(iii) Determine the actuator load capacity needed to lift a specified passive load:

$$F_{ACT}^{required} = P_{ext}^{passive} \frac{0.58s\sqrt{3}}{\sqrt{2}} + F_{ACT} \quad (16)$$

The variables are the thicknesses of the back-plane d_k and the core members d_c . In an application environment the truss length must coincide with the size of the actuators and is not a variable. For simplicity of presentation (as already noted), the other parameters are those applicable to the demonstration structure [6] [$L=L_k=L_c=5.1$ cm, $s=0.53$ m, $w=0.41$ m, $E_c=E_k=E_f=200$ GPa, $\sigma_{Yc}=\sigma_{Yk}=\sigma_{Yf}=200$ MPa (304 stainless steel)].

The load capacity at specified mass is typically the important engineering metric. To ascertain this quantity, note that the mass of the structure is

$$m = 24 \left[6 \left(L_k - \frac{1}{\sqrt{3}} d_k \right) d_k^2 \rho_k + \left(\frac{\sqrt{3}}{2} + 6L_c \right) d_c^2 \rho_c + 2\sqrt{3} L_k^2 d_f \rho_f \right] \quad (17)$$

with ρ_k, ρ_c, ρ_f being the densities of the Kagome, core, and solid face sheet materials, respectively. Invoking (14), the specific load capacity becomes

$$\bar{P} = \frac{P_{ext}^{max}}{m} \quad (18)$$

5 Load Capability

The maximum load capability is limited either by structural failure [Eqs. (2)–(5) and (7)] or by the actuator capacity [Eq. (13)]. A failure map calculated using (14) is presented as a surface in three-dimensional space comprising the coordinates, P_{ext}, d_c, d_k (Fig. 3, inset), with the truss thickness, d_c and d_k , as variables. Four failure domains are apparent. For very thin members, failure is dominated by buckling of either the core or the Kagome members. As the members become stubbier the failure mode transitions to face yielding. Eventually (for even greater stubbiness), the load becomes actuator limited. The maximal passive load capability is always at the confluence of the actuator limit and one (or more) of the structural limits. Note that, for a system with a 250 N actuator

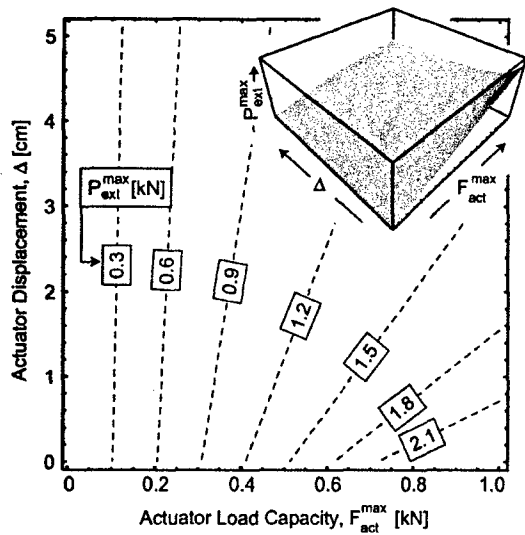


Fig. 4 Maximum load capability as a function of actuator capacity and actuator

subject to 10% extension, the maximum load capability is 640 N, achieved with core and Kagome cross sections $d_c=1.4$ mm and $d_t=3.0$ mm, respectively.

This geometry is only optimal for one material and one actuator. Every other combination will exhibit another point. The *maximum permissible load capability for all possible actuators* is computed using a nonlinear optimization with Mathematica [10]. A typical result (Fig. 4) reveals that the load capability increases monotonically with increasing actuator capacity but decreases with increasing deformation. Since the latter is the limiting feature, Fig. 4 can be used to determine the actuator load capacity required to realize a specified load capability.

The maximum displacement that can be achieved (16) for an actuator capacity of 250 N is plotted in Fig. 5. To avoid the abrupt load drops when failure occurs by buckling, the dimensions of the members have been chosen to reside in the face yield regime. The requirements on the actuator capacity (for 10% extension) are shown on Fig. 6. To assure failure by face yielding, the capacity

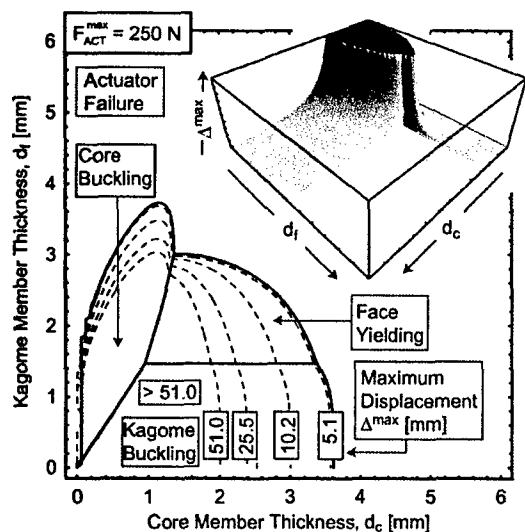


Fig. 5 Contour of actuator extension for a given actuator capacity of 250 N. The plot has been truncated at $\Delta^{\max}=51$ mm.

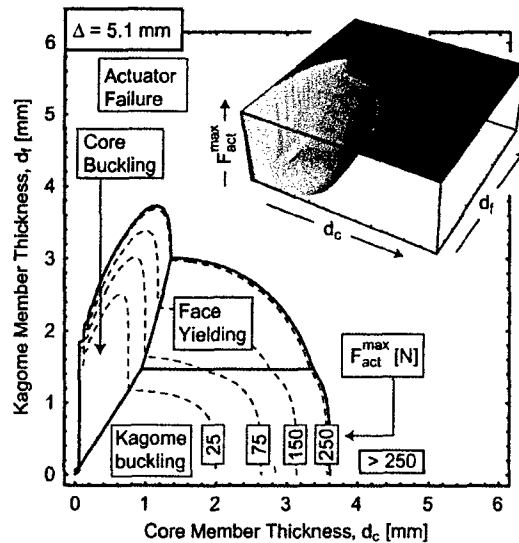


Fig. 6 Required actuator capacity for a given actuator extension of 10%. The plot has been truncated at $F_{ACT}^{\max}=250$ N.

must be $F_{act}^{\max} > 75$ N. Corresponding plots for other values of actuator capacity and displacement can be readily generated.

6 Influence of Material Properties

The previous assessments have been performed for fixed values of the material properties, E and σ_Y . The role of these properties is now explored by optimizing for ranges of Young's modulus (1–300 GPa) and yield strength (50–900 MPa). Many different failure maps have been generated (not shown for conciseness). The results are summarized in Fig. 7, which plots trends with face thickness for five cases. It is apparent that when the face is in tension (no wrinkling) materials with high yield strength ($\sigma_Y > 200$ MPa) provide the greatest load capacity. This maximum occurs for small relative face thickness, $1 < \lambda_{sm} < 3$. The modulus is relatively unimportant in this range. Low modulus only exerts an adverse influence at larger λ_{sm} where the load capacity is sub-optimal. Materials with lower yield strength ($\sigma_Y \leq 50$ MPa) are clearly inferior (they permit appreciably lower load capability for all λ_{sm}).

The effect of varying the actuator capacity on the *load capability per unit mass* [Eq. (18)] is plotted in Fig. 8 for various engi-

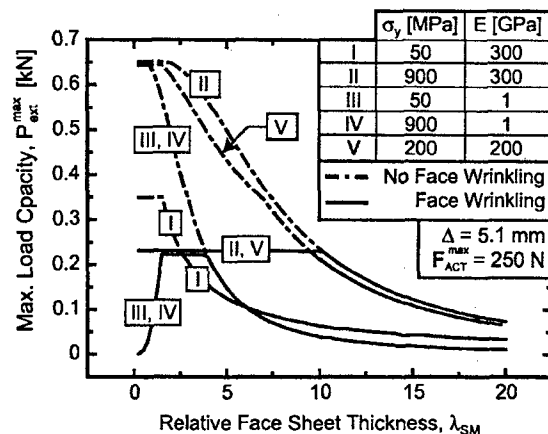


Fig. 7 Effect of variation of face thickness on load capacity for various materials

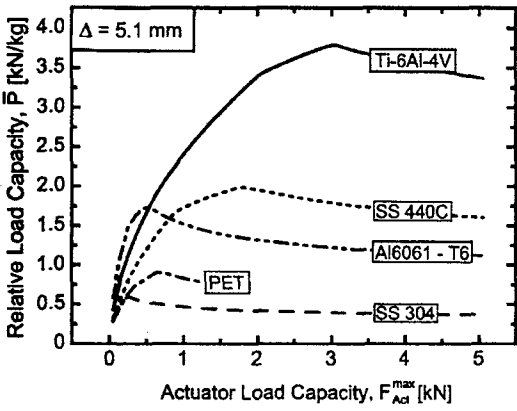


Fig. 8 Specific external load capacity as a function of the actuator load capacity for various engineering materials

neering materials. These materials include a titanium alloy (Ti-6Al-4V), an aluminum alloy (Al 6061-T6), two stainless steels (304 and 440C), and a polymer (PET). Every location on this figure represents a nonlinear optimization with the specified material parameters and actuator capacity. The calculations are based on a 10% actuator extension. For each material, there is a peak specific load capacity and associated actuator capacity. The decrease at large actuator capacity arises because stiffer trusses and a thicker face are needed to support the larger loads, causing the weight to increase more rapidly than the rise in load capability. Note that, when only low capacity actuators are available, Al alloys are preferred. Conversely, when actuator capacity is unlimited, Ti alloys provide a much greater load capability per unit mass than all other materials.

7 Concluding Remarks

An assessment of the requirements and properties of a Kagome based shape morphing structure has been conducted. The fully optimized structure always resides at the confluence of the actuator limit and one (or more) structural failure mechanism. The most robust design is located just within the actuator-limited domain. Designs within the buckling domain should be avoided, because of the drop in load capacity. Those located in yield domains might be acceptable, since strain hardening provides some safety margin.

The load capability scales almost linearly with the actuator capacity but decreases at large deformations. When the passive face is loaded in tension, materials with high yield strength provide the greatest load capacity. The modulus is relatively unimportant. The load capability per unit mass exhibits a maximum. When the actuator capacity is unlimited, Ti alloys provide the greatest load capability per unit mass. Also the greatest load capacity is obtained with solid face sheet thickness of one to three times that of the stiffness matched thickness. Thicker faces increase the resistance against actuation without increasing the overall load capacity of the passive structure.

Since the constraint equations are quite general (except that the length of the Kagome and core members must be equal) other actuator locations and shape changes can be readily introduced by changing Eqs. (11) and (12).

Nomenclature

- d_k, d_c, d_f = thickness of Kagome members, core members, solid face sheet
- L_k, L_c = length of Kagome members, core members
- L = length of Kagome and core members ($L_k=L_c$ required)

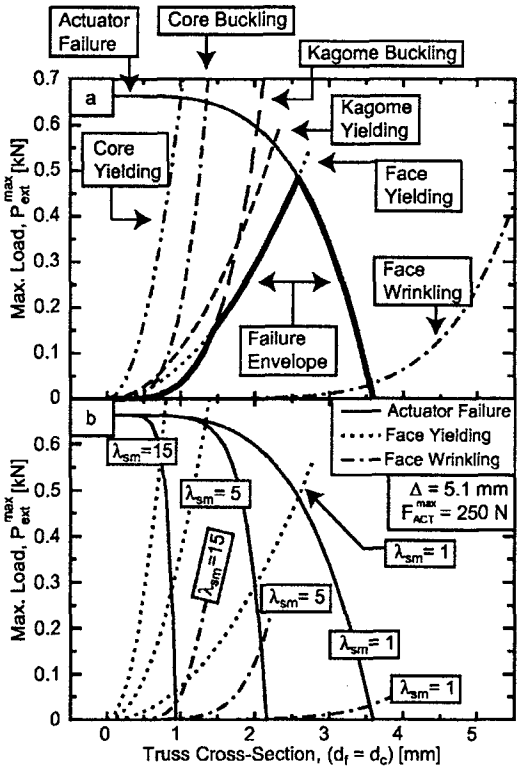


Fig. 9 Variation of the face thickness and comparison of face wrinkling to face yielding. (a) Face thickness fixed at $\lambda_{sm}=1$. (b) Face thickness fixed varied $\lambda_{sm}=1, 5$ and 15 .

- w, s, H_c = width and span of the structure, height of the core
- λ_{sm} = solid face thickness scaling factor
- E_k, E_c, E_f = Young's modulus of Kagome, core, and solid face
- $\sigma_{Yk}, \sigma_{Yc}, \sigma_{Yf}$ = yield strength of Kagome, core, and solid face
- ρ_k, ρ_c, ρ_f = Density of the Kagome, core, and solid face sheet
- P_{KY}, P_{CY}, P_{FY} = external load to yield Kagome, core, and solid face
- P_{KB}, P_{CB}, P_{FB} = external load to buckle Kagome, core, and solid face
- P_{ACT} = external load to cease actuator function
- F_{ACT}, F_{EXT} = force on actuators due to structural resistance and external load
- F_{ACT}^{max} = load limit of actuator
- P_{ext}, Δ = permissible external load, displacement of actuator
- $P_{ext}^{max}, \Delta^{max}$ = maximum permissible external load and actuator displacement

Appendix: Solid Face in Compression

In normal operation, the passive loads place the solid face in tension. Should the design require the face to experience compression, it would be susceptible to wrinkling at the load:

$$P_{FH} \leq \frac{2.24\sqrt{3} d_f^3 E_f}{\sqrt{2} L} \quad (A1)$$

The ratio of the loads that cause failure by yielding and wrinkling is given by combining Eqs. (7) and (A1):

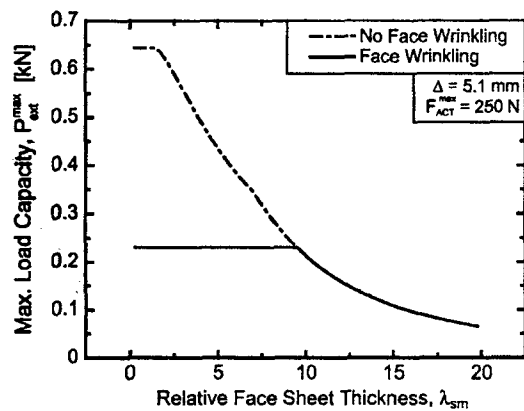


Fig. 10 Maximum load capability as a function of the solid face sheet thickness with and without face wrinkling

$$\frac{P_{FY}}{P_{FB}} = \frac{1}{3.36} \frac{wL^2}{s_d^2} \varepsilon_{YF} \quad (A2)$$

where $\varepsilon_{YF} = \sigma_{YF}/E_F$ is the yield strain of the solid face. The trends for a stiffness-matched system ($\lambda_{sm}=1$) are shown in Fig. 9(a); while those for systems with different λ_{sm} are shown on Fig. 9(b). For clearance of visualization only a cut along the $d_k=d_c$ plane is shown. When stiffness matched and loaded in tension, the maximum load capacity [Fig. 9(a)] occurs at the confluence of face yielding and actuator failure: with load capability, $P_{ext}^{max} \approx 0.5$ kN. However, when loaded in compression, failure is limited by wrinkling and occurs at a much lower load, $P_{ext}^{max} \approx 30$ N. Increasing the face thickness ($\lambda_{sm} > 1$) dramatically increases the wrinkling

resistance [Fig. 9(b)]; but the benefits are offset by a corresponding increase in actuation resistance. The highest load capability in compression is $P_{ext}^{max} \approx 150$ N when $\lambda_{sm} \approx 5$. Note that the load capability can be increased by lifting the restriction $d_k=d_c$.

The trends in maximum load capability with relative face thickness obtained using Mathematica are plotted in Fig. 10. Thicker faces have no benefit when in tension: they only serve to increase the actuation resistance. When in compression, while thicker faces resist wrinkling, they also increase the actuation resistance. Upon optimizing, these effects compensate at thickness $\lambda_{sm} \sim 9$. For even thicker faces, wrinkling is no longer an active constraint and the structure always fails by Kagome buckling.

References

- [1] Lu, T. J., Hutchinson, J. W., and Evans, A. G., 2001, "Optimal Design of a Flexural Actuator," *J. Mech. Phys. Solids*, **49**, pp. 2071–2093.
- [2] Hutchinson, R. G., Wicks, N., Evans, A. G., Fleck, N. A., and Hutchinson, J. W., 2003, "Kagome Plate Structures for Actuation," *Int. J. Solids Struct.*, **40**, pp. 6969–6980.
- [3] Hyun, S., and Torquato, S., 2002, "Optimal and Manufacturable Two-Dimensional, Kagome-Like Cellular Solids," *J. Mater. Res.*, **17**, pp. 137–144.
- [4] Christensen, R. M., 2000, "Mechanics of Cellular and Other Low-Density Materials," *Int. J. Solids Struct.*, **37**, pp. 93–104.
- [5] Wicks, N., 2003, "Optimization and Actuation of Truss Structures," Ph.D. thesis, Engineering Sciences, Harvard University, Cambridge, MA.
- [6] Dos Santos e Lucaro, S. L., Wang, J., McMeeking, R. M., and Evans, A. G., 2004, "Design and Demonstration of a High Authority Shape Morphing Structure," *Int. J. Solids Struct.*, **41**, pp. 3521–3543.
- [7] Wicks, N., and Hutchinson, J. W., 2001, "Optimal Truss Plates," *Int. J. Solids Struct.*, **38**, pp. 5165–5183.
- [8] Ashby, M. et al., 2000, *Metal Foams: A Design Guide*, Butterworth-Heinemann, Boston.
- [9] Symons, D. D., Hutchinson, R. G., and Fleck, N. A., 2004, "Actuation Performance of the Kagome Double Layer Grid," *J. Mech. Phys. Solids*, **52**, pp. 1111–1121.
- [10] Mathematica 5.0, 2003, www.wolfram.com, Wolfram Research, Champaign, IL, USA.

Part III: Actuator placement optimization in a kagome based high authority shape morphing structure

Actuator placement optimization in a Kagome based high authority shape morphing structure

S L dos Santos e Lucato, R M McMeeking and A G Evans

Materials Department, University of California, Santa Barbara, CA 93106-5050, USA

Received 19 August 2004, in final form 11 January 2005

Published 28 July 2005

Online at stacks.iop.org/SMS/14/869

Abstract

An optimization protocol for a high authority shape morphing plate is described. The shape morphing design incorporates an active back-plane comprising a Kagome truss, capable of changing the shape of a solid face, connected to the back-plane by means of a tetrahedral truss core. Several members of the Kagome truss are replaced by actuators, enabling the structure to deform. The trusses to be replaced depend on the desired deformation, subject to the load capacity of the individual actuators. A two-level scheme is used comprising a heuristic algorithm with a simplex based optimization providing the cost function. It is shown that methods capable of avoiding entrapment in local minima, such as simulated annealing and the genetic algorithm, give good results.

(Some figures in this article are in colour only in the electronic version)

1. Introduction

Shape morphing structures are designed to displace surfaces while being resisted by large pressure loads (or heavy weights) [1–6]. One approach for addressing this challenge is to use the Kagome structure depicted in figure 1 [2, 3, 6]. The basic structure consists of a solid face-sheet with a Kagome back-plane and a tetrahedral core. The configuration is rigidly supported at one end. Replacing various truss elements in the back-plane with linear actuators enables the shape of the solid face to be changed.

While this structure can undergo a wide range of deformations, it is limited by yielding and buckling failure of the passive structure as well as the load specification of the actuators. Previous investigations concluded that the deformations are limited by the incorporated actuators rather than by the structure itself [6–8]. Structural failure, if it is the limiting factor, can easily and cheaply be remedied by making it sturdier. The inherent increase in weight and resistance against actuation is small compared to the increase in load capacity of the structure [7]. In contrast, incorporation of more actuators or higher authority actuators to overcome actuation as the limiting factor usually results in a significant increase in weight and system complexity. It is therefore desirable to reduce the number of actuators to limit the overall cost and

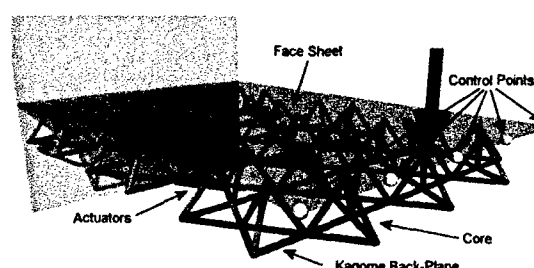


Figure 1. Schematic representation of the Kagome structure consisting of the face-sheet, the core and the Kagome back-plane. Actuators are placed in lieu of the Kagome members. The control points are used to define the target deformation.

complexity of the system. Placement of a limited number of actuators becomes a crucial design aspect.

The objective of the present study is to find actuator configurations that maximize the deformation. The procedure selects configurations of actuators and ascertains the quality of every configuration by a second (local) optimization. The results of the latter are used as cost functions for the global optimization that determines the best configuration for a limited number of actuators. Some key characteristics required for the optimization are calculated by means of a finite element

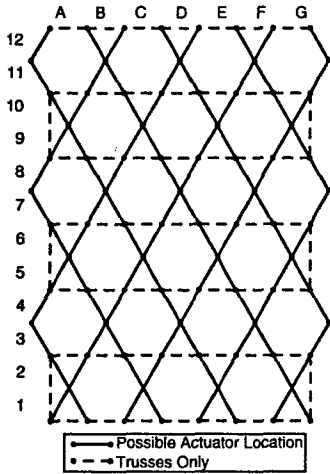


Figure 2. Kagome layer of the structure used in this study. Possible locations of actuators in the Kagome layer are shown as solid lines.

analysis. Here, the length of the panel was chosen to include six hexagonal units of the Kagome plate, while the width incorporated four, resulting in 96 possible actuator locations (figure 2). Multiple virtual control points define the shape change to be achieved [6].

The search space for global optimization is discrete and unordered, excluding the use of gradient based algorithms. Moreover, probing the entire search space is prohibitive. Optimization problems of this nature have been solved with heuristic methods, such as simulated annealing and genetic algorithms [9, 10]. The purpose of this study is to assess the performance of these algorithms in actuator placement optimization with the objective of actuating the structure to a final shape as close as possible to a predefined shape.

2. Local optimization and the cost function

The *local optimization* is devised to find the largest possible deformation for a given set of actuators subject to external constraints, e.g. the load limit of the actuators. For local optimization, n points are identified along the solid face (figures 1, 3). The vertical displacement ($v_i, i = 1, \dots, n$) of each point is controlled and maximized by selecting actuator strains ($\varepsilon_j, j = 1, \dots, m$) for m independent actuators (where $m > n$). The redundancy will be used to optimize the

deformation within the force capabilities of the actuators: a crucial requirement for *actuator-limited* structures [6]. For the unloaded structure, a matrix A of influence coefficients can be constructed such that

$$v_i = \sum_{j=1}^m A_{ij} \varepsilon_j. \quad (1)$$

The null-space of the matrix A has dimension $m - n$ and consists of combinations of actuator strains giving rise to zero displacements at the control points along the edge to be twisted [11]. One orthonormal basis for the null-space is the set of $m - n$ vectors $\varepsilon_j^k, k = 1, \dots, m - n$, such that

$$\sum_{j=1}^m A_{ij} \varepsilon_j^k = 0. \quad (2)$$

These basis vectors ε_j^k can be found from equation (2) by standard matrix manipulations [12]. Now calculate projections of the actuator strain array into the null-space of A :

$$w^k = \sum_{j=1}^m \varepsilon_j^k \varepsilon_j. \quad (3)$$

Therefore, $w^k, k = 1, \dots, m - n$, represent the degrees of freedom for zero displacement of the control points. Now introduce a matrix B defined as

$$B_{ij} = \begin{cases} A_{ij}, & i = 1, \dots, n \\ \varepsilon_j^{i-n}, & i = n + 1, \dots, m \end{cases}. \quad (4)$$

It follows that

$$\sum_{j=1}^m B_{ij} \varepsilon_j = \begin{cases} v_i, & i = 1, \dots, n \\ w^{i-n}, & i = n + 1, \dots, m \end{cases}. \quad (5)$$

Since all its rows are linearly independent, the matrix B is non-singular and inversion of equation (5) provides

$$\varepsilon_j = \sum_{i=1}^n B_{ji}^{-1} v_i + \sum_{i=n+1}^m B_{ji}^{-1} w^{i-n}. \quad (6)$$

The structure of (6) shows that a deformation can be achieved by specifying the n displacements, v_i , for the control points, plus any values for the remaining $m - n$ parameters, w_k , because the latter do not affect the control point displacements.

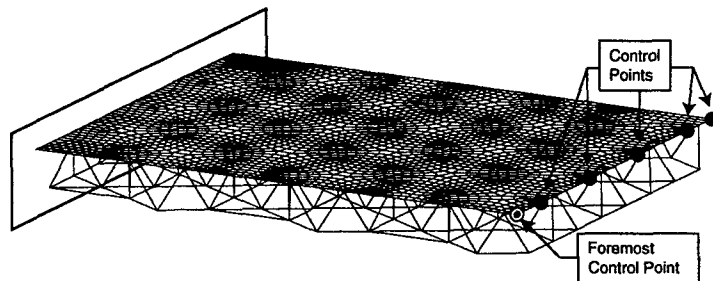


Figure 3. Finite element model of the Kagome structure. Six control points used in this study are highlighted. The foremost open control point is used to discuss the quality of the results.

Now maximize the deformation without exceeding the force limits of the actuators. In the absence of a load, the relationship between the actuator forces P_k , $k = 1, \dots, q$, and the actuator strains ε_i , $i = 1, \dots, m$, can be established as

$$P_k = \sum_{i=1}^m C_{ki} \varepsilon_i. \quad (7)$$

Note that q may be larger than m because actuators may be operated in pairs or sets to have the same actuator strain, but each actuator in general experiences different force levels, even when they are paired or put together in sets. That is, replacing two adjacent truss members with actuators being actuated to exactly the same strain results in such a scenario. Combining (6) and (7) gives

$$P_k = \sum_{j=1}^m C_{kj} \left(\sum_{i=1}^n B_{ji}^{-1} v_i + \sum_{i=n+1}^m B_{ji}^{-1} w^{i-n} \right). \quad (8)$$

The control point displacements can be expressed in terms of a single degree of freedom, ϕ , representing the deformation:

$$v_i = \phi u_i \quad (9)$$

where u_i are the displacements for unit value of ϕ . As a result, (9) becomes

$$P_k = \beta_k \phi + \sum_{i=1}^{m-n} D_{ki} w^i \quad (10a)$$

where

$$\beta_k = \sum_{j=1}^m \sum_{i=1}^n C_{kj} B_{ji}^{-1} u_i \quad \text{and} \quad D_{ki} = \sum_{j=1}^m C_{kj} B_{ji+n}^{-1}. \quad (10b)$$

The remaining task is to maximize ϕ in (10a) subject to minimum and maximum constraints on the actuator forces P_k . It is a straightforward linear programming problem [11] to find the $m - n$ coordinates of w^i . Once solved, the resulting values of ϕ and w^i are inserted into (9) and (10a) to compute the actuator strains that produce the maximum possible deformation within the actuator force constraints.

2.1. The cost function

The global optimization routines in the present work base their actuator selection criteria on some measure of the quality of the present actuator configuration. Therefore they require an externally computed cost function for assessing the quality of any given actuator configuration. In the present study the quality measure, i.e. the cost function, accounts for the difference between the optimized deformation and the desired deformation.

The above local optimization algorithm calculates the largest possible deformation for a single actuator configuration, e.g. the present one. The resulting deformation parameter ϕ as calculated using (10a) increases with increasing deformation and would provide a good measure of the achievable deformation. However, in our present computer implementation of the local algorithm, the deformation vector v_i is extended by w^i to form a generalized deformation vector as shown on the right-hand side of equation (5). Therefore ϕ

cannot be used directly because it depends on the null-space of A and hence the actual actuator set. Instead the root mean square of the difference between the defined target deformation u_i and the optimized deformation v_i is used as an absolute measure:

$$f = \sqrt{\sum_{i=1}^n (u_i - v_i)^2}. \quad (11)$$

This cost function measures the quality of the optimized deformation relative to the target deformation. Note that with this choice of cost function, the target deformation should be chosen sufficiently large, since a penalty is imposed on solutions yielding a deformation larger than that defined. Although this is not a problem per se, it reduces the safety margin of the final assembly by requiring it to operate at its limit.

2.2. Finite element analysis

The matrices A and C are calculated by a finite element analysis. The mesh, depicted in figure 3, consists of linear beams and linear four-point shell elements. The calculations have been performed with the commercial FEA package ANSYS. The actuator displacements have been modeled by thermally expanding the beam elements by 1%. One FE calculation was performed for every possible (active) actuator position. Only one actuator was active in each run, resulting in 96 calculations. The stresses on all members are transposed to a file. Additionally, the displacements at 60 separate locations along the solid face were transposed. The control points for the local optimization were chosen from among those locations. The ANSYS script language APDL was used to automate the task.

3. Global optimization algorithms

In this section, several algorithms are used to determine the best possible placement of a limited number of actuators, based on a prescribed set of target deformations. The load limits of the actuators are incorporated into the optimization by means of the local routine. All possible actuator locations are numbered (shown as solid lines in figure 2). The following algorithms invoke one (or more) actuator sets, each consisting of m actuators. The number m is predetermined and is not part of the optimization. The following steps are common. The number of actuators and the desired target deformations are defined before the analysis is started. To calculate the cost function for a specific set of actuators, the matrices A and C for the active set are assembled and passed to the local optimizer. Only the active control points and the active actuators are included. Completeness of the original files is required since any actuator position may become active during the optimization. All global and local algorithms are implemented in a custom program written in Borland Delphi.

3.1. The random algorithm

The random algorithm is used as a benchmark. All m actuators are chosen randomly in every step. The best solution is the only information retained from previous steps (figure 4). After the

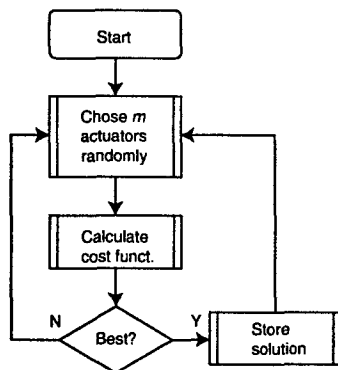


Figure 4. Flow diagram of the random search algorithm.

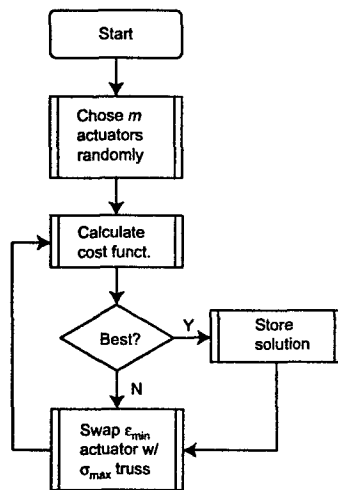


Figure 5. Flow diagram of the iterative replacement algorithm.

actuators are chosen, the cost function is calculated. If the cost is lower than that of the best previous solution, it is stored.

3.2. Iterative replacement

This algorithm utilizes some information inherent to the structure in addition to the cost function. The passive member subject to the highest stress is determined, along with the actuator that undergoes the least extension. Reasoning that the former position is most likely to benefit from being extended and the latter the least amenable to actuation, the two positions are interchanged. The new configuration is transitioned onto the local optimizer and the procedure repeated. After every pass, the new configuration is stored if more favorable than the previous best solution (figure 5).

3.3. Simulated annealing

This algorithm is amongst the most widely used algorithms when little knowledge of the objective function is available [13], especially when the search space is unordered. To overcome local optima, the method permits some higher

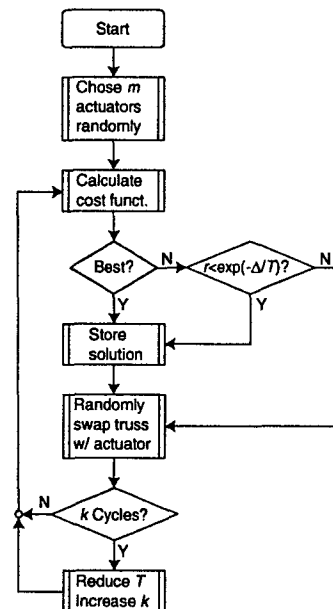


Figure 6. Flow diagram of the simulated annealing algorithm.

cost steps to proceed. After the cost function has been calculated with the local optimization algorithm, one randomly chosen actuator in the set is swapped with a randomly chosen truss member and the fitness of the new set is determined. If the new set is superior to the old one, it is accepted. Moreover, if the new set has a higher cost than the old, it is still accepted provided that

$$r \leq \exp(-\Delta/T), \quad (12)$$

where r is a random number ($0 \leq r < 1$), T is the annealing temperature and $\Delta (=f_{\text{new}} - f_{\text{old}})$ is the difference in cost between the new and the old solutions. If equation (12) is satisfied, the new set is stored and the cycle restarted (figure 6).

The annealing temperature T has to be adapted during optimization. Various methods have been devised for determining the initial values and the subsequent cooling [13]. In the present study, a simple cooling schedule is used. That is, after a predetermined number of cycles (k), T is reduced to αT ($0 < \alpha < 1$). Simultaneously, the number of cycles to be completed is increased to βk ($1 < \beta$). Initially, T is chosen to accept almost all bad sets and slowly lowered ($0.8 < \alpha < 1$). The parameters are $\alpha = 0.9$, $\beta = 1.1$ and an initial cycle length $k = 100$.

3.4. The genetic algorithm

This algorithm is a technique that 'converges' to the best possible solution [14, 15]. Similar to simulated annealing, it is suitable when no prior knowledge is available regarding the optimum and especially where the search space is unordered. The genetic algorithm works with ℓ sets of m actuators simultaneously. Each set of actuators is mapped into a chromosome. Each actuator corresponds to a particular position in a chromosome. The chromosome length depends on the number of actuators in a set. A binary representation of the location number with 7 bits/actuator was chosen for

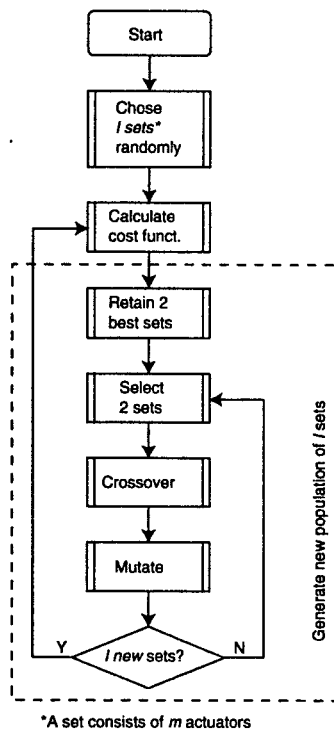


Figure 7. Flow diagram of the genetic algorithm.

this study: bits 1–7 represent the first actuator, bits 8–14 the second etc. The chromosomes are grouped into a population of ℓ chromosomes, with population size determined by the length of each chromosome [16]. In the present study a population size of 20 satisfies the minimum requirements.

The initial population is chosen randomly and the cost function, also known as the fitness, is calculated. The cost of every individual chromosome is obtained by decoding, resulting in a set of location numbers. The maximum realizable deformation is calculated for every set using the local optimization routine. Finally, the population is sorted by cost, starting with the best. A new population is generated. In order to retain the best solutions so far, the two best chromosomes are copied to the new population (known as 'elitism'). The remainder of the new population is filled by selecting chromosomes from the previous population ('selection'), exchanging information between them ('crossover') and randomly changing bits ('mutation') to introduce new information. Once the new population is filled, the fitness is calculated and the cycle restarted (figure 7).

Several variations have been defined [15, 16]. The simplest selection procedure is to choose two chromosomes randomly. This method does not rely on information about the cost of the individual chromosomes. Other methods such as 'roulette-wheel' or 'rank' selection base the probability of selecting a chromosome on its cost, giving the best chromosomes the highest chance of passing their information onto the next generation. The crossover procedure exchanges information between two selected chromosomes mimicking

sexual reproduction. This is performed by cutting the parent chromosomes into several pieces at the same randomly selected locations. The number of cuts is reflected in the name (a single cut is a one-point crossover etc). A four-point crossover with a probability of 95% and rank selection provides consistent results in the present study. The new chromosomes are assembled by alternating pieces from the two parents. The last step is the mutation of the newly formed chromosomes, conducted by randomly flipping some bits with a preset probability. In the present study a probability of 5% gives the best results.

4. Scenarios and results

4.1. Scenarios

The four algorithms are used to optimize the actuator placement for four different scenarios: hinging and twisting, both using 8 and 16 actuators. Hinging refers to uniform lifting of the free edge, while twisting raises one side of the free edge while simultaneously lowering the other, while maintaining the free edge in a straight line. Note that there are 10^{11} and 10^{17} combinations for placing 8 and 16 actuators, respectively, on 96 possible locations. All optimizations are performed using six control points located along the outer edge (figure 3).

All algorithms are continued for 10 000 cycles for each scenario. Every scenario is optimized 10 times to reduce the effect of an unfavorable initial choice. The commonest actuators of the 10 runs are manually selected and passed through the local optimizer. If the cost of the manual selection is worse than the best optimization result, a new manual set (replacing some of the less common positions) is rerun. Improvements were always found using fewer than five manual runs.

4.2. Optimization results

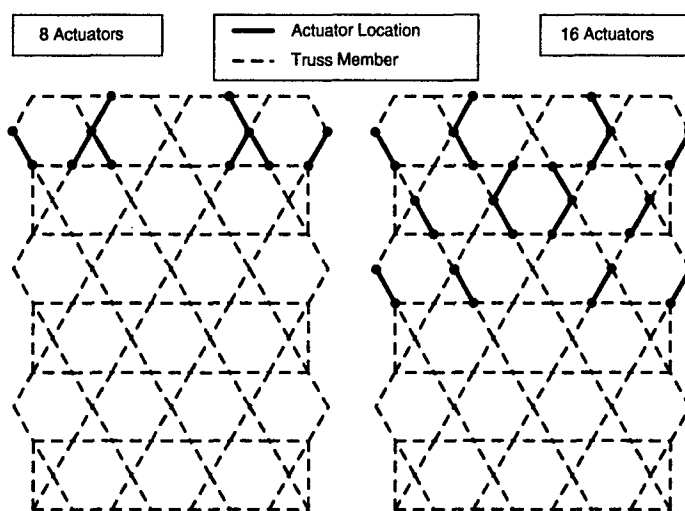
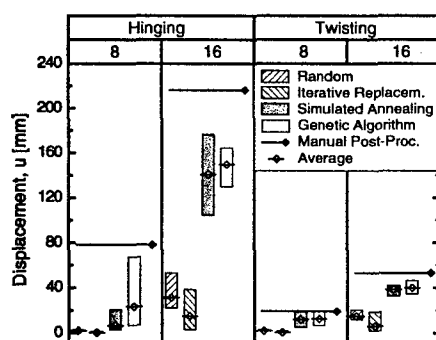
These comprise the locations of the actuators as well as the predicted displacement of every control point and the required displacement of every actuator. The placement of actuators for hinging is relatively simple. For 8 and 16 actuators, filling all positions along row 3 and along rows 3 and 4, respectively, maximizes the achievable deformation. Twisting is more intricate (figure 8), but symmetric with respect to the central axis.

The displacement at the control point on the edge is used to illustrate the quality of the results (figure 3, open control point), assembled in table 1 and visualized in figure 9. The iterative replacement algorithm performs well in the first few cycles but is then trapped in a local optimum. Conversely, the simulated annealing and genetic algorithms perform well because they accept some inferior solutions that inhibit trapping at a local minimum. The difference in their performance is within one standard deviation (table 1) and statistically insignificant.

Note that hinging yields higher deformations, because twisting stretches the solid face, increasing the actuation resistance. Doubling the number of actuators from 8 to 16 triples the achievable hinging (from 78 to 216 mm) and doubles the twisting (from 19 to 53 mm). The results have been verified by FE analysis (figure 10) with actuators at the locations revealed by the optimization. The predicted displacements are exactly reproduced.

Table 1. Examples of the worst, average and best results, as well as the standard deviation. The best results from manual post-processing as well as from the FEM verification are included. The displacement of the top left edge has been used.

Min/avg/max (mm) Std deviation (mm)	Hinge		Twist	
	8 actuators	16 actuators	8 actuators	16 actuators
Random	1.7/2.2/2.6 0.4	22.2/31.3/53.3 9.0	1.9/2.1/2.8 0.3	12.1/15.0/20.4 2.6
Iterative replacement	0.1/0.5/1.3 0.3	3.0/14.1/38.5 12.1	0.2/0.7/2.0 0.6	2.0/6.1/18.5 4.8
Simulated annealing	3.2/6.7/20.8 5.3	104.4/140.8/176.6 21.5	5.2/13.1/19.3 5.8	32.5/38.6/42.0 3.2
Genetic algorithm	7.2/23.7/67.3 15.3	129.8/149.6/164.5 11.1	6.9/12.6/19.3 4.2	34.4/39.9/46.3 4.2
Manual post-processing	78.1	216.2	19.3	53.3
FEM verification	78.1	216.2	19.3	53.3

**Figure 8.** Optimized locations of the actuators for twisting with 8 and 16 actuators.**Figure 9.** Optimized deformation result for all scenarios and algorithms. The span is marked by boxes with the average highlighted by an open diamond. Closed diamonds represent the result of the manual post-processing.

5. Concluding remarks

A heuristic global optimization routine combined with a fast local optimization algorithm is efficient in assessing the best

placement of actuators in a Kagome morphing structure. Because of the large, unordered search space, methods that accept inferior cost moves must be used to avoid trapping at a local minimum—such as simulated annealing and a genetic algorithm. The two methods yield results of equal quality. Given their random nature, repeating the runs and manually assembling the common features increases the quality of the results.

While all optimizations have been performed for only one target shape, it is straightforward to implement an optimization for multiple deformations. In that case, the local algorithm would be run for every target deformation and the results stored in a local cost vector. The global cost would be determined from the local cost vector by means of an appropriate norm. This method would allow simultaneous optimization for more than one objective. For example, active vibration damping could be explored, with some Kagome members replaced with sensors and high frequency actuators. The resulting vibration amplitude could be calculated by a modal FE analysis and used as a second cost function.

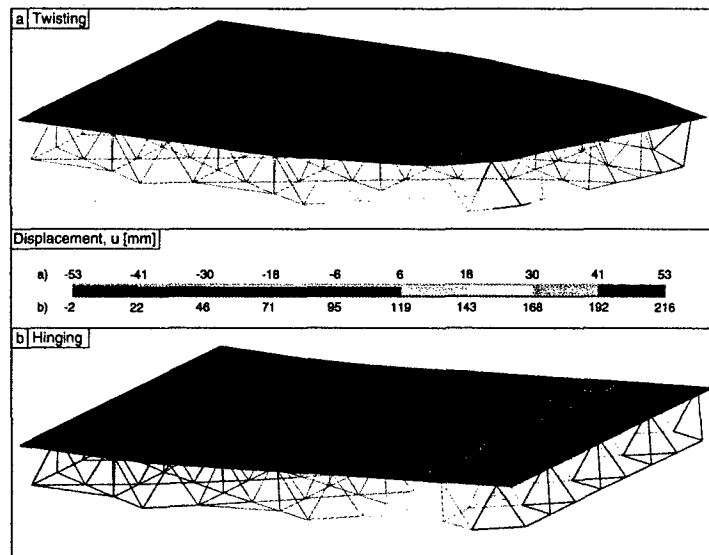


Figure 10. Result of the FEM verification of the optimization results for twisting and hinging using 16 actuators.

Acknowledgments

The authors would like to thank John Hutchinson from Harvard University and Simon Guest from Cambridge University for very valuable discussions and input to this study.

References

- [1] Lu T J, Hutchinson J W and Evans A G 2001 Optimal design of a flexural actuator *J. Mech. Phys. Solids* **49** 2071–93
- [2] Hutchinson R G, Wicks N, Evans A G, Fleck N A and Hutchinson J W 2003 Kagome plate structures for actuation *Int. J. Solids Struct.* **40** 6969–80
- [3] Hyun S and Torquato S 2002 Optimal and manufacturable two-dimensional, Kagome-like cellular solids *J. Mater. Res.* **17** 137–44
- [4] Christensen R M 2000 Mechanics of cellular and other low-density materials *Int. J. Solids Struct.* **37** 93–104
- [5] Wicks N 2003 Optimization and actuation of truss structures *PhD Thesis* Engineering Sciences, Harvard University, Cambridge, MA
- [6] Dos Santos e Lucato S L, Wang J, McMeeking R M and Evans A G 2004 Design and demonstration of a high authority shape morphing structure *Int. J. Solids Struct.* **41** 3521–43
- [7] Dos Santos e Lucato S L and Evans A G 2005 The load capacity of a Kagome based high authority shape morphing structure *J. Appl. Mech.* at press
- [8] Wicks N and Hutchinson J W 2004 Sandwich plates actuated by a Kagome planar truss *J. Appl. Mech.* **71** 652–62
- [9] Sadri A M, Wright J R and Wynne R J 1999 Modelling and optimal placement of piezoelectric actuators in isotropic plates using genetic algorithms *Smart Mater. Struct.* **8** 490–8
- [10] Mir M and Hasan Imam M 1996 Analytic annealing for macrocell placement optimization *Comput. Electr. Eng.* **22** 169–77
- [11] Luenberger D G 1973 *Linear and Nonlinear Programming* 2nd edn (Reading, MA: Addison-Wesley)
- [12] Kreyszig E 1999 *Advanced Engineering Mathematics* 8th edn (New York: Wiley)
- [13] Sait M S and Youssef H 1999 *Iterative Computer Algorithms with Applications in Engineering* (Los Alamitos, CA: IEEE Computer Society)
- [14] Goldberg D 1989 *Genetic Algorithms in Search, Optimization, and Machine Learning* (Reading, MA: Addison-Wesley)
- [15] Holland J H 1975 *Adaptation in Natural and Artificial Systems* (Ann Arbor, MI: University of Michigan Press)
- [16] Reeves C and Rowe J 2003 *Genetic Algorithms—Principles and Perspectives* (Boston, MA: Kluwer Academic)

Part IV: Twisting of a high authority morphing structure

Part IV: Twisting of a high authority morphing structure

TWISTING OF A HIGH AUTHORITY MORPHING STRUCTURE

J. Wang, A. Nausieda, S.L. dos Santos e Lucato,
A.G. Evans

*Materials Department,
University of California at Santa Barbara,
CA 93106, USA*

ABSTRACT

The twisting of a high authority shape morphing plate is described. The design incorporates an active Kagome back-plane capable of changing the shape of a solid face by transmitting loads through a tetrahedral core. The objective is to ascertain designs that provide the maximum edge twist subject to specified passive load. Non-linear effects, such as face wrinkling, have been probed by using a finite element method and the fidelity of the results assessed through comparison with measurements. The numerical results have been used to validate a dimensional analysis of trends in the actuation resistance of the structure with geometry, as well as the passive load capacity. The forces determined by such analysis have been combined with the failure mechanisms for all sub-systems to establish the constraints. The important domains have been visualized using mechanism maps. An optimization has been used to generate load capacity maps that guide geometric design and provide actuator capacity requirements.

LIST OF SYMBOLS

d	Thickness of Kagome and core members
d_f	Thickness of solid face sheet
d_{fw}	Minimum face thickness to suppress face wrinkling
d_{sm}	Stiffness matched face thickness
E	Young's modulus of the material
F_{ACT}	Force on actuators due to structural resistance
F_{ACT}^{max}	Load capacity of actuator
F_c	Force in core due to external load
F_{EXT}	Force on actuators due to external load

\bar{F}_R	Force in core (\bar{F}_c) and Kagome (\bar{F}_k) due to structure resistance
J	Work done by actuators
J_c	Strain energy stored in core when actuated
J_f	Strain energy stored in solid face when actuated
J_k	Strain energy stored in Kagome when actuated
H_c	Height of the core
L	Length of Kagome and core members
P_{ACT}	External load to cease actuator function
P_{CB}	External load to buckle core
P_{CY}	External load to yield core
P_{EXT}^{max}	Maximum permissible external load
P_{FB}	External load to buckle face
P_{FY}	External load to yield face
P_{KB}	External load to buckle Kagome, core and solid face
P_{KY}	External load to yield Kagome, core and solid face
P_{PAS}	External passive load
s	Span of the structure
w	Width of the structure
ϵ_Y	Yield strain of the material
ρ	Density of the material
$\bar{\sigma}_f$	Stress in solid face due to structural resistance
σ_f	Stress in solid face due to external load
σ_{truss}^{max}	Stress in Kagome due to external load
σ_Y	Yielding stress of the material
Δ	Twist displacement
Δ_{max}	Maximum Permissible twist displacement

1. INTRODUCTION

A class of high authority shape morphing plate structure has been identified and partially characterized [1-8]. One manifestation is the Kagome structure [2, 3, 6-10] that can be actuated into relatively intricate surface shapes. The basic design consists of a solid face-sheet with an active Kagome back-plane and a tetrahedral core (figure 1). In order to induce hinging and twisting, specific trusses in the Kagome-plane are replaced by linear actuators [6]. The authority of the structure (product of load supported and displacement) has been examined in the hinging mode, with accompanying experimental validation [6]. This assessment has included the placement of the actuators and the preferred materials. While many of the desired shape changes can be

achieved by hinging along the three equivalent directions provided by the Kagome structure (figure 1), twisting is indispensable in some instances. The primary objective of this article is to establish the twisting characteristics.

A preliminary examination of twisting displacements has been conducted by using a linear formulation of the induced forces [6]. This investigation used a genetic algorithm to ascertain the placement of the actuators [7]. It focused on the demonstration structure depicted on figure 1. It ascertained the largest displacements that can be realized subject to the avoidance of structural failure by either buckling or yielding (of both the truss members and the solid face), within the load capacity of representative actuators. It remains to verify these characteristics by pursuing a more detailed numerical analysis, accompanied by the design and conduct of critical experiments. In this article, such an assessment is performed on the same demonstration structure, followed by a generalization that illustrates trends with materials and dimensions.

The article is organized in the following manner. Initially, the features of the demonstration structure are described, as well as the actuator placements. Preliminary calculations are used to probe aspects of the response that impose a practical limit on the achievable twisting: yielding and buckling of the core and Kagome members as well as face wrinkling. Thereafter, numerical parameter studies are used to find trends in displacement and to ascertain designs that inhibit the undesirable responses. The trends are used for optimization studies of the type previously conducted for hinging [8].

2. STRUCTURE

The basic structure (figure 1) comprises a solid face, a Kagome active-plane and tetrahedral core. Based on the preference for Ti alloys elucidated in a previous study [8], most of the assessments are made using Ti-6Al-4V as the material of choice. However, because of fabrication limitations, the experimental assessment uses a combination of a high strength Al alloy (6061-T6) face with a truss system made from 304 stainless steel. To achieve the target shapes, some members of the Kagome are replaced by linear stepper motors (or turnbuckles). The structure may be fully or partially patched to gain structural capability. The demonstration panel is partially-patched [6] (Appendix I). It includes 6 hexagonal units of the Kagome in the longitudinal dimension and 4 for the width. Since the failure

modes are affected by the slenderness of the members (length to diameter, L/d) [2], two different choices have been made: one susceptible to buckling ($L/d = 33$) and the other to yield or fatigue ($L/d = 20$). The truss lengths, L , have been chosen to accommodate commercially available linear stepper motors: $L = 5.1\text{cm}$ [6]. The face thickness, d_f , has been chosen with the expectation that minimum weight designs arise when the face is stiffness matched to the Kagome plane, $d_f = d_{sm}$ [4]. In practice, the choices are constrained by the thickness of commercially available sheet materials.

Two placement schemes are used, assuming 8 actuators in both cases.

- (i) For benchmarking of the response, an entire row at the center of the plate is replaced by actuators (figure 2a). These locations are globally sub-optimal from the perspective of the edge twist [6]. However, the overall shape may be more desirable in some circumstances, as discussed below.
- (ii) To assess the best possible edge twist response, the actuators are placed at the optimal location suggested by a previous assessment [7] (figure 2b).

3. NUMERICAL PROCEDURES

The calculations are conducted using a finite element method with the commercial code ABAQUS. To simulate the complete actuation system, the core and Kagome members are modeled using linear Timoshenko-type beams, while the solid face sheet is discretized using general-purpose quadrilateral shell elements. A total of 10 beam elements are used per member to capture bending and buckling. The actuators are incorporated into the model by means of truss elements, with representative cross-sectional area. Actuation is achieved by thermal expansion of these truss elements. One side of the structure is fully clamped, while the other is free to displace.

As in prior assessments [6-8], elastic analysis is used to ascertain the actuation resistance and the effects of the passive load. The ensuing structural determination is conducted by comparing the loads and stresses with failure criteria based on buckling and yielding. The calculations are conducted in two circumstances.

- (a) A small-displacement method is used with an optimization routine to assess the maximum twist displacements for specified actuator load capacity [6]. The method also determines the strains required in the actuators.
- (b) To characterize the failure modes such as face wrinkling and buckling of the Kagome and core members, a large-displacement method is used. It generates wrinkling patterns that can be compared with experimental observations.

The latter are used to assess the response to the passive load and to determine the resistance of the structure to twisting.

4. INITIAL ASSESSMENT

To gain preliminary insight into responses that limit the achievable twisting, a series of preliminary calculations have been conducted. The emphasis has been on the co-linear actuator configuration, which is expected to exacerbate the detrimental responses. The most relevant are summarized in this section. Initially, a linear analysis (no yielding or buckling) has been used to establish the ranges of the actuation strains needed to realize large displacements while maintaining the straightness of the edge (figure 1), subject to a maximum allowable force on the actuators, F_{Act}^{max} . The results are summarized on table I. The consequences of imposing these strains are ascertained by the subsequent conduct of a non-linear elastic analysis (yielding suppressed). This analysis is performed without imperfections because the structure (even when partially-patched) is relatively imperfection insensitive (Appendix I).

Upon imposing the strains from table I, the demonstration panel is found to exhibit appreciable *face wrinkling* (figure 3). The implication is that this undesirable feature must be suppressed by thickening the face, even though the accompanying increase in actuation resistance must diminish the realizable twisting. The goal will be to find the minimum face thickness needed to achieve the required displacement while avoiding face wrinkling. This thickness is denoted, d_{fw} . Establishing trends in d_{fw} will be one of the objectives of this article.

An assessment of the elastic energy stored in the three sub-elements of the structure (core, face and Kagome), summarized on table II, indicates that the

actuation resistance is provided largely by the Kagome plane, but with significant contributions from the core and the face. This feature of twisting differs markedly from that for hinging [6], wherein essentially all of the resistance was provided by the core members above the actuators (table II). The deformation of the Kagome members at maximum twist (figure 4) affirms that they experience bending. This characteristic provides some appreciation for the trends in achievable twisting with the relative dimensions of the truss members and the face, discussed next.

5. ACTUATION RESISTANCE

A series of calculations has been performed for the all Ti-alloy system, in which the face thickness has been varied systematically for two values of the truss slenderness ($L/d = 20$ and 33), and two disparate values of the actuator capacity, F_{ACT}^{max} (40 and 400N). Results have been obtained for both of the actuator placements. The displacements attained are plotted as a function of face thickness on figure 5. Major effects of F_{ACT}^{max} and L/d on the achievable twist displacements are evident. Note that, as expected, much larger displacements can be realized when the actuators are placed in the optimal configuration rather than co-linear. Examples of the associated deformations are illustrated on figure 6, revealing the combinations susceptible to wrinkling. The latter allows d_{fw} to be ascertained and superposed on the displacements (figure 5). The fidelity of these results is assessed by experimental measurements described in Appendix II.

The elastic energies stored within each of the three sub-elements, normalized by the work done by the actuators, J , are plotted on figure 7. For the co-linear configuration, (figure 7a) most of the energy is stored in the Kagome plane, due to member bending (figure 4), consistent with the results in table II. Conversely, for the optimal placement (figure 7b), especially when the faces are thick enough to avoid wrinkling,, the largest contribution is from face stretching. The consequences on achievable twist will be elaborated next.

Unification of the twist results, Δ_{max} , can be pursued by invoking results ascertained from the hinging investigation [6]. This analysis indicated that, for a material with Young's modulus, E , the resistance to actuation caused by bending is governed by the non-dimensional parameter:

$$\Phi_{bend} = \frac{\Delta_{max} EL}{F_{ACT}} \left[\frac{d}{L} \right]^4 \quad (1a)$$

The analogous parameter for face stretching is:

$$\Phi_{stretch} = \frac{\Delta_{max} EL}{F_{ACT}} \left[\frac{d_f}{L} \right] \quad (1b)$$

In these formulae, F_{ACT} is the maximum load induced on any of the actuators by the twisting structure. By assuming that the total force is the sum of the resistances caused by member bending and face stretching then:

$$\frac{F_{ACT}}{EL\Delta_{max}} = A_a \left(\frac{d}{L} \right)^4 + B_a \left(\frac{d_f}{L} \right) \quad (1c)$$

where A_a and B_a are quantities to be obtained by fitting to the finite element results.

To assess the merit of this premise, the numerical results are plotted using logarithmic coordinates based on these non-dimensional parameters. The results are plotted on figure 8. The correspondence evident in the figures signifies that (1) has fidelity adequate for present purposes. The fit for the co-linear actuators gives (table III): $A_a = 1.0$, $B_a = 2.10^{-4}$. The corresponding results for the optimal configuration are: $A_a = 0.15$, $B_a = 7.10^{-5}$.

These magnitudes affirm the large (order of magnitude) reduction in the resistance when the actuators are optimally placed for edge twist. They also reveal that, for the latter, face stretching becomes the dominant contribution to the resistance, especially when the face is thick enough to avoid wrinkling. This effect accounts for the linear downward trend in achievable twist displacement as the face thickens (figure 5).

6. ACTUATION INDUCED FORCES

The forces and stresses induced by actuation in the different subsystems of the structure have been ascertained from the numerical results. In accordance with the forces on the actuators, they also comprise member bending and face stretching contributions and thus fit a formula essentially the same as (1c). Namely, the largest forces induced on the members, \bar{F}_R , satisfy:

$$\frac{\bar{F}_R}{EL\Delta_{max}} = A_R \left(\frac{d}{L} \right)^4 + B_R \left(\frac{d_f}{L} \right). \quad (2a)$$

The magnitudes of the coefficients (A_R, B_R) for each of the members are summarized on table III. Within each category (optimal or co-linear), one set of results refers to the maximum compressive force, pertinent to failure by buckling. The other is the absolute maximum (whether tension or compression), used to ascertain the incidence of yielding. An example of the correspondence between (2a) and the detailed numerical calculations is demonstrated on figure 9.

The corresponding result for the average stresses induced in the faces between neighboring core supports is:

$$\frac{\bar{\sigma}_f L}{E\Delta_{\max}} = C_f \left(\frac{d}{L} \right)^4 + D_f \left(\frac{d_f}{L} \right) . \quad (2b)$$

The coefficients are given in table III. The correspondence is illustrated on figure 9.

7. PASSIVE LOAD CAPACITY

The passive loads that can be sustained without failure have been derived by assuming a cantilever plate, span s , and width w , subject to a line load, P_{PAS} [11]. This load induces a force F_{EXT} on the actuators: [6]

$$F_{EXT} = \Theta \frac{s}{w} P_{PAS} \quad (3)$$

The coefficient Θ differs for the two actuator placements: $\Theta_c = 0.58\sqrt{3/2}$ for co-linear and $\Theta_o = 0.58\sqrt{1/6}$ for optimal [2]. The nominal stress induced in the Kagome back-plane is related to the bending moment, $M = P_{PAS}s$, and the core height $H_c = \sqrt{3/2}L$, by [11]:

$$\sigma_N = \sqrt{\frac{3}{2}} \frac{P_{PAS}s}{dwL} \quad (4a)$$

This stress is related to the actual stress on a truss member σ_{truss} by [2]:

$$\begin{aligned} \sigma_N &= -\sqrt{3} \frac{d_f}{L} \sigma_{truss} \quad (\text{truss X}) \\ \sigma_N &= \frac{\sqrt{3}}{2} \frac{d_f}{L} \sigma_{truss} \quad (\text{truss Y}) \end{aligned} \quad (4b)$$

where trusses X are parallel to the width and Y at $\pm 30^\circ$ to the span. The maximum stress in the Kagome trusses is thus:

$$\sigma_{truss}^{max} = \frac{P_{PAS}}{d^2 w} \quad (4c)$$

The corresponding maximum stress in the face sheets and the maximum force in the core members are, respectively: [12]

$$\sigma_f = \frac{P_{PAS}}{d H_c}, \quad (5a)$$

and

$$F_c = \frac{\sqrt{3} P_{PAS} L \sqrt{L^2 - H_c^2}}{w H_c} \quad (5b)$$

8. MECHANISM MAPS

The forces induced in the actuators due to the twisting resistance of the structure and the passive load are additive: $F_{TOT} = F_{EXT} + F_{ACT}$. By equating this force to be the load capacity of the actuator, F_{ACT}^{max} , the maximum permissible external load (based on the actuator constraint) can be ascertained as:

$$P_{ACT} \leq \frac{E \Delta_{max} L}{\Theta_S} \left\{ \frac{F_{ACT}^{max}}{E \Delta_{max} L} - \left[A_a \left(\frac{d}{L} \right)^4 + B_a \left(\frac{d_f}{L} \right) \right] \right\}. \quad (6a)$$

The forces induced in the subsystems are also additive. They lead to the following constraints.

Avoidance of failure by yielding (at stress, σ_y): for the Kagome members:

$$P_{KY} \leq \frac{w d^2}{\sqrt{2} s} E \left\{ \varepsilon_y - \frac{L \Delta_{max}}{d^2} \left[A_R \left(\frac{d}{L} \right)^4 + B_R \left(\frac{d_f}{L} \right) \right] \right\}, \quad (7a)$$

for the core members:

$$P_{CY} \leq \sqrt{\frac{2}{3}} \frac{w d^2}{L} E \left\{ \varepsilon_y - \frac{L \Delta_{max}}{d^2} \left[A_R \left(\frac{d}{L} \right)^4 + B_R \left(\frac{d_f}{L} \right) \right] \right\}, \quad (7b)$$

and for the face:

$$P_{FY} \leq \sqrt{\frac{2}{3}} \frac{w d_f L}{s} E \left\{ \varepsilon_y - \frac{\Delta_{max}}{L} \left[C_f \left(\frac{d}{L} \right)^4 + D_f \left(\frac{d_f}{L} \right) \right] \right\}. \quad (7c)$$

Avoidance of member buckling: for the Kagome members:

$$P_{KB} \leq \frac{w d^4}{\sqrt{2} s L^2} E \left\{ \frac{\pi^2}{12} - \frac{L^3 \Delta_{max}}{d^4} \left[A_R \left(\frac{d}{L} \right)^4 + B_R \left(\frac{d_f}{L} \right) \right] \right\}, \quad (8a)$$

and for the core members:

$$P_{CB} \leq \frac{wd^4}{\sqrt{3}L^3} E \left\{ \frac{\pi^2}{4\sqrt{2}} - \sqrt{2} \frac{L^3 \Delta_{\max}}{d^4} \left[A_R \left(\frac{d}{L} \right)^4 + B_R \left(\frac{d_f}{L} \right) \right] \right\}. \quad (8b)$$

Avoidance of face wrinkling:

$$P_{FB} \leq \sqrt{\frac{2}{3}} \frac{wd_f^3}{sL} E \left\{ \frac{49\pi^2}{144(1-\nu^2)} - \frac{L\Delta_{\max}}{d_f^2} \left[C_f \left(\frac{d}{L} \right)^4 + D_f \left(\frac{d_f}{L} \right) \right] \right\}. \quad (9)$$

These results can be used to construct mechanism maps, using procedures described elsewhere [8]. Detailed results are presented for actuators with optimal placement (figure 10 and table IV). This exercise reveals three different response modes, dependent on the actuator load capacity, F_{ACT}^{\max} .

- (i) *Low load actuators*, $F_{ACT}^{\max} < 3kN$ (figure 10a). In this case, the maximum load capacity is at the confluence of actuator failure, Kagome member buckling and face wrinkling.
- (ii) *Intermediate load actuators*, $6kN > F_{ACT}^{\max} > 3kN$ (figure 10b). Now the maximum is at the confluence of actuator failure, Kagome yielding and face wrinkling. This change occurs because the stubbiness of the members has been increased to retain compatibility with the higher loads on the actuators.
- (iii) *High load actuators*, $F_{ACT}^{\max} > 6kN$ (figure 10c). In this case, the design is no longer actuator limited. Instead the load capacity is dictated entirely by structural considerations.

These different domains will become apparent when the system is optimized, as discussed next.

9. OPTIMIZATION

The objective of the optimization is to seek the topology and the actuator capacity that realize a specified twist while supporting the largest possible external load or pressure. Ascertaining the maximum requires that the first subsystem to fail be identified by using:

$$P_{EXT}^{\max} = \min(P_{KY}, P_{KB}, P_{CY}, P_{CB}, P_{FY}, P_{FB}, P_{ACT}). \quad (10)$$

The load capacity at specified mass is typically the important engineering metric. The mass of the structure is [8]:

$$m = 24 \left\{ 6 \left[L - \frac{1}{\sqrt{3}} d \right] d^2 \rho + \left[\frac{\sqrt{3}}{2} + 6L \right] d^2 \rho + 2\sqrt{3} L^2 d \rho \right\}, \quad (11)$$

with ρ being the density of the material. The relative load capacity thus becomes: $\bar{P} = P_{EXT}^{max} / m$.

The effect of varying the actuator capacity on \bar{P} is plotted on figure 11. Every point represents a non-linear optimization with the specified F_{ACT}^{max} . Note the three domains anticipated by the mechanism maps. At low actuator capacity, the load capability increases rapidly as the actuators improve because the concomitant increase in the Kagome member stubbiness inhibits buckling. Once the actuators become sufficiently strong, these members transition to failure by yielding, causing a diminished rate of change of \bar{P} with actuator capacity. Finally, when the design becomes structure-limited, F_{ACT}^{max} has no further effect (the decrease in \bar{P} on figure 11 at largest F_{ACT}^{max} is a consequence of increasing the stubbiness to support stronger actuators, causing the design to translate away from the structural optimum).

Since the preceding results are optimal for only one twist displacement, the load capacity for a wide range of displacements has been computed by using a non-linear optimization with Mathematica [13]. The result (figure 12) reveals the actuator and structure-limited domains. In the former, \bar{P} increases with F_{ACT}^{max} . This diagram allows the selection of actuators capable of providing specified levels of edge twist and load capacity.

10. CONCLUSION

Analytic and numerical assessments have been used to guide and characterize the design of a high authority shape morphing structure for twisting, based on the attributes of a Kagome active back-plane. Two different actuator placement schemes have been explored. Optimal placement renders the maximum achievable edge twist displacement. A co-linear placement induces a more gradual shape change but at reduced edge twist.

Non-linear responses of the structure to actuation have been simulated numerically. Trends in the elastic energy stored in the subsystems indicate that face stretching and truss bending are the major contributions to the actuation resistance. Analytic models have been derived for the geometric

scaling and their fidelity established by comparison with numerical results. A large reduction in the resistance when the actuators are optimally placed is consistent with the larger achievable edge twist.

The forces associated with the actuation resistance and those induced by passive loads have been derived and combined with the failure mechanisms to create mechanism maps. These maps reveal that, at low actuator capacity, the optimal design resides at the confluence of the actuator limit and two structural failure mechanisms: while at high actuator capacity, the optimal is at the confluence of three structural failure mechanisms. A design diagram has been constructed that allows determination of the actuator capacity needed to attain specified edge twist while supporting a required load.

APPENDIX I. Structural Assessment of the Kagome Plane

The passive load capacity of the Kagome plane has been evaluated with emphasis on the role of imperfections. Both partially and fully-patched designs are pursued [6] (figure A1). The measurements are performed on panels laser cut from 304 stainless steel and from Ti-6Al-4V. Before embarking on calculations an eigenvalue analysis was used to establish the natural mode shapes. The first modes (figures A2), activated at the lowest load, are used to analyze the role of imperfections (relative amplitude, ξ). The load/deflection responses calculated for the *partially-patched* panels (figures A3) and the deformed shapes (figures A2) reveal that the responses become imperfection sensitive when $\xi \geq 10^{-3}$. Note that the peak load for the stainless steel structure involve plastic buckling at loads significantly above yield, while the Ti alloy panel fails by elastic buckling. The change from failure by plastic to elastic buckling is consistent with expectations [2, 6]. Prior to attainment of the load maximum, the central row of trusses rotate. This rotation triggers collapse of the un-patched rows in a pattern reminiscent of the mechanism that operates in the pin-jointed Kagome (figure A4) [9,10]. The corresponding results for the *fully-patched* designs (figure A5) indicate that the load/deflection responses are much less imperfection sensitive and that the rotation-induced collapse mechanism is suppressed.

Compression tests were conducted by using thick glass constraining plates to eliminate out-of-plane displacements. To minimize frictional drag, the plates were separated by spacers incorporated at the bolted joints, 50 μ m thicker

than the specimen. The load-displacement results (figure A6) indicate that the Ti alloy structures fail by elastic buckling at a load, $P_{\max} = 5.2\text{kN}$; while the steel structures failed by plastic buckling at $P_{\max} = 3.3\text{kN}$. Note that the load capacities measured for both materials are within the calculated range assuming small imperfections, $\xi \leq 10^{-4}$ (figure A6). This imperfection size corresponds to actual amplitude of approximately 0.05mm, similar to the dimensional tolerance for precision laser cutting systems [16]. *The important implication is that the imperfections caused by laser cutting are in a range where the imperfection sensitivity is minimal.* A pursuant implication is that there is no particular load capacity detriment to using the partially patched design used in the present study [6].

Finally, images of specimens strained well beyond failure are summarized on figure A7. At ~0.5% strain, the truss pairs near the right edge of row 4 distort and buckle, causing the adjacent nodes to rotate, and a truss pair near the right edge of row 5 to buckle. This failure differs from the finite element results, which predict symmetric collapse of row 5. This disparity is attributed to the slight loading asymmetry in the experiments.

APPENDIX II: Experimental Validation of Face Wrinkling

A series of experiments has been conducted using the demonstration structure with a Kagome plane and a core made from 304 stainless steel and a face made from a high strength Al alloy. To emphasize face wrinkling, this structure is tested with the co-linear actuator array. To guide the experiments, numerical simulations have been conducted for an actuator load capacity, $F_{ACT}^{\max} = 40\text{N}$. The realizable twisting is plotted on figure B1. The twisted configurations are also indicated on the figure. Note that, for this case, the simulations predict, $d_{fw} = 0.30\text{mm}$.

Based on commercial availability, aluminum sheets with three different thickness were chosen that bound d_{fw} : these were, $d_f = 0.15, 0.30, 0.53\text{mm}$. Turnbuckles were used to impose the displacements indicated on table I, assuring that the loads never exceed 40N. Images of the panels at the maximum twist are shown in figure B2. Consistent with the calculations, the result for the thinnest panel ($d_f/d_{fw} = 0.5$) reveals dramatic wrinkling. Moreover, the wrinkling pattern is remarkably similar to that found in the calculations (figure B1). Also in accordance with the calculations, the assembly with the thickest face ($d_f/d_{fw} = 1.8$) displayed a smooth twist. The

intermediate panel ($d_f/d_{fw}=1$) did not wrinkle but exhibited some face distortion. All of the twist displacements are comparable to the calculated values (table V). *We conclude that the numerical procedure captures the incidence of face wrinkling with high fidelity.*

FIGURES

Fig. 1: Schematic of the Kagome demonstration structure. The solid face is shown in blue, the core in green and the Kagome back-plane in red. Actuators are placed in-lieu of the Kagome-members. The control points are used to define the target deformation.

Fig. 2: Two different placement schemes of the actuators: (a) co-linear (sub-optimal for an edge twist perspective); (b) optimal.

Fig. 3: Wrinkling in the solid face upon actuation. This assembly has Al alloy face with stainless steel core and Kagome back-plane: (a) Finite element simulation; (b) Experimental result.

Fig. 4: The bending of the Kagome members when the structure with co-linear actuators is twisted. (Deformation scale factor is 7).

Fig. 5: Maximum twisting displacements attained for two different aspect ratios ($L/d = 20, 33$) and two different actuator force capacity ($F_{ACT}^{max} = 40N, 400N$): (a) Co-linear placement of the actuators; (b) Optimal placement of the actuators. The vertical arrows indicate the face wrinkling transitions at, d_{fw} .

Fig. 6: Deformations upon maximum twist for the two different actuator placements ($L/d = 33, d_f = d_{fw}$).

Fig. 7: Elastic energy stored in the three sub-elements: Kagome back-plane, tetrahedral core and solid face-sheet. The symbols give the actual results. The shaded bands are used to highlight the trends. (a) Co-linear placement: note that most energy is stored in the Kagome plane due to member bending. (b) Optimal placement: now most of the energy is either in the core, due to member bending (small face thickness) or in the face (large face thickness), due to face stretching.

Fig. 8: The forces induced by the structure on the actuators: a comparison of results ascertained numerically (symbols) and the analytic formulae (lines): (a) Co-linear; (b) Optimal.

Fig. 9: The forces induced by the structure on the Kagome members: a comparison of results ascertained numerically (symbols) and the analytic formulae (lines): (a) Co-linear; (b) Optimal.

Fig. 10: Mechanism maps and maximum load capacity for three actuator capacities: (a) 1kN; (b) 4kN; (c) 7kN.

Fig. 11: External load capability as function of actuator load capacity.

Fig. 12: A map of the maximum load capability as function of actuator capacity and twist displacement.

Fig. A1: Two different geometries of the Kagome plane: (a) Partially patched; (b) Fully patched.

Fig. A2: Shapes of the first three modes: (a) First; (b) Second; (c) Third, as well as the deformed shape near the load maximum.

Fig. A3: Load/displacement curves for the partially-patched panels for a range of imperfection amplitudes: (a) 304 stainless steel; (b) Ti-6Al-4V.

Fig. A4: characteristic deformation pattern of truss rotation for pinned (left) and bonded joints.

Fig. A5: Load/displacement curves for fully patched Ti alloy panels for a range of imperfection amplitudes.

Fig. A6: Trend in the peak load with imperfection amplitude for partially and fully-patched panels: stainless steel and Ti alloy. The measured peak loads are superposed.

Fig. A7: Deformed partially patched specimens tested in compression: (a) stainless steel and (b) Ti alloy.

Fig. B1: The maximum twist displacement realizable for different face thickness and the wrinkling patterns of the solid face-sheets.

Fig. B2: Face wrinkling suppressed by increasing the face-sheet thickness: (a) $d_f = 0.15\text{mm}$, below critical face-sheet thickness d_{fw} , dramatic face wrinkling observed; (b) $d_f = 0.30\text{mm}$, critical face-sheet thickness d_{fw} , face distortion observed; (c) $d_f = 0.53\text{mm}$, above critical face-sheet thickness d_{fw} , smooth twist without face wrinkling.

TABLES

Table I: Maximum twist displacements obtained for different assemblies and the strains in the actuators to realize them, subject to an actuator load capacity of 40N.

Table II: Elastic energy stored in the sub-systems for hinging and twisting with actuators at co-linear arrangement. The assembly is the demonstration structure.

Table III: The coefficients for the numerically fitted equations defining the maximum forces or stresses induced in the actuators and sub-systems by actuation.

Table IV: The maximal passive load and geometric dimensions needed to achieve a twist displacement of 5.1mm within different actuator capacities.

Table V: Comparison of the achieved twist displacements between numerical simulation and test. Δ_{up} is the upward displacement of one corner and Δ_{down} the downward displacement of the other.

REFERENCES

- [1] Lu, T. J., Hutchinson, J. W., Evans, A. G., 2001. Optimal Design of a Flexural Actuator. *J. Mech. Phys. Solids* 49, 2071-2093.
- [2] Hutchinson, R. G., Wicks, N., Evans, A. G., Fleck, N. A., Hutchinson, J. W., 2003. Kagome Plate Structures for Actuation. *Int. J. Solids Struct.* 40, 6969-6980.
- [3] Hyun, S. Torquato, S., 2002. Optimal and Manufacturable Two-dimensional Kagome-like Cellular Solids. *J. Mater. Res.* 17, 137-144.
- [4] Christensen, R. M., 2000. Mechanics of Cellular and Other Low-density Materials. *Int. J. Solids Struct.* 37, 93-104.
- [5] Wicks, N., 2003. Optimization and Actuation of Truss Structures. Ph.D Thesis, Engineering Sciences, Harvard University, Cambridge, Massachusetts.
- [6] dos Santos e Lucato, S.L., Wang, J., Maxwell, P., McMeeking, R.M., Evans, A.G., 2004. Design and demonstration of a high authority shape morphing structure. *Int. J. Solids Struct.* 41, 3521-3543.
- [7] dos Santos e Lucato, S.L., McMeeking, R.M., Evans, A.G., 2004. Actuator Placement Optimization in a Kagome Based High Authority Shape Morphing Structure. Submitted to *Smart Materials and Structures*.
- [8] dos Santos e Lucato, Evans, A.G., 2004. The Load Capacity of a Kagome Based High Authority Shape Morphing Structure. Submitted to *J. Appl. Mech.*
- [9] Symons, D.D., Hutchinson, R.G., Fleck, N.A., 2005. Actuation of the Kagome Double Layer Grid. Part 1 prediction of performance of the perfect structure. Submitted to *J. Mech. Phys. Solids*.

- [10] Symons, D.D., Shiel, J., Fleck, N.A., 2005. Actuation of the Kagome Double Layer Grid. Part 2: effect of imperfections on the measured and predicted actuation stiffness. Submitted to J. Mech. Phys. Solids.
- [11] Ashby et al., 2000. Metal Foams: A Design Guide. Butterworth-Heinemann, Boston.
- [12] Wicks, N., Hutchinson, J.W., 2001. Optimal truss plates. Int. J. Solids Struct. 38, 5165-5183.
- [13] Mathematica 5.0, 2003. www.wolfram.com , Wolfram Research, Champaign, IL, USA.
- [14] ABAQUS Theory Manual, 1998. Hibbitt, Karlsson and Sorensen Inc., Pawtucket, R.I.
- [15] Hutchinson, J.W., 1974. Plastic buckling. In Chia-Shun Yih, editor, Advances in Applied Mechanics 14, 67-144.
- [16] J. Furphy & Sons Pty Ltd. Laser Cutting Technology.
<<http://www.furphys.com.au/lasertech.html>>

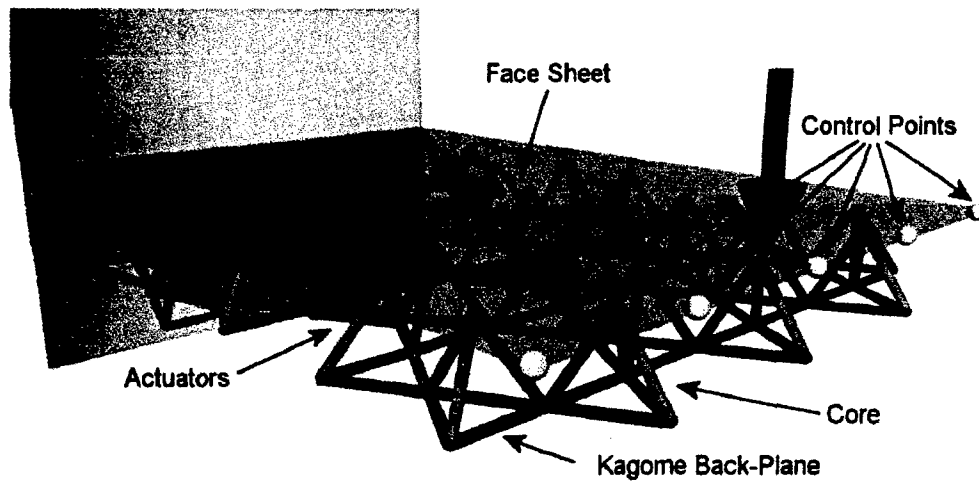


Fig. 1: Schematic of the Kagome demonstration structure. The solid face is shown in blue, the core in green and the Kagome back-plane in red. Actuators are placed in-lieu of the Kagome-members. The control points are used to define the target deformation.

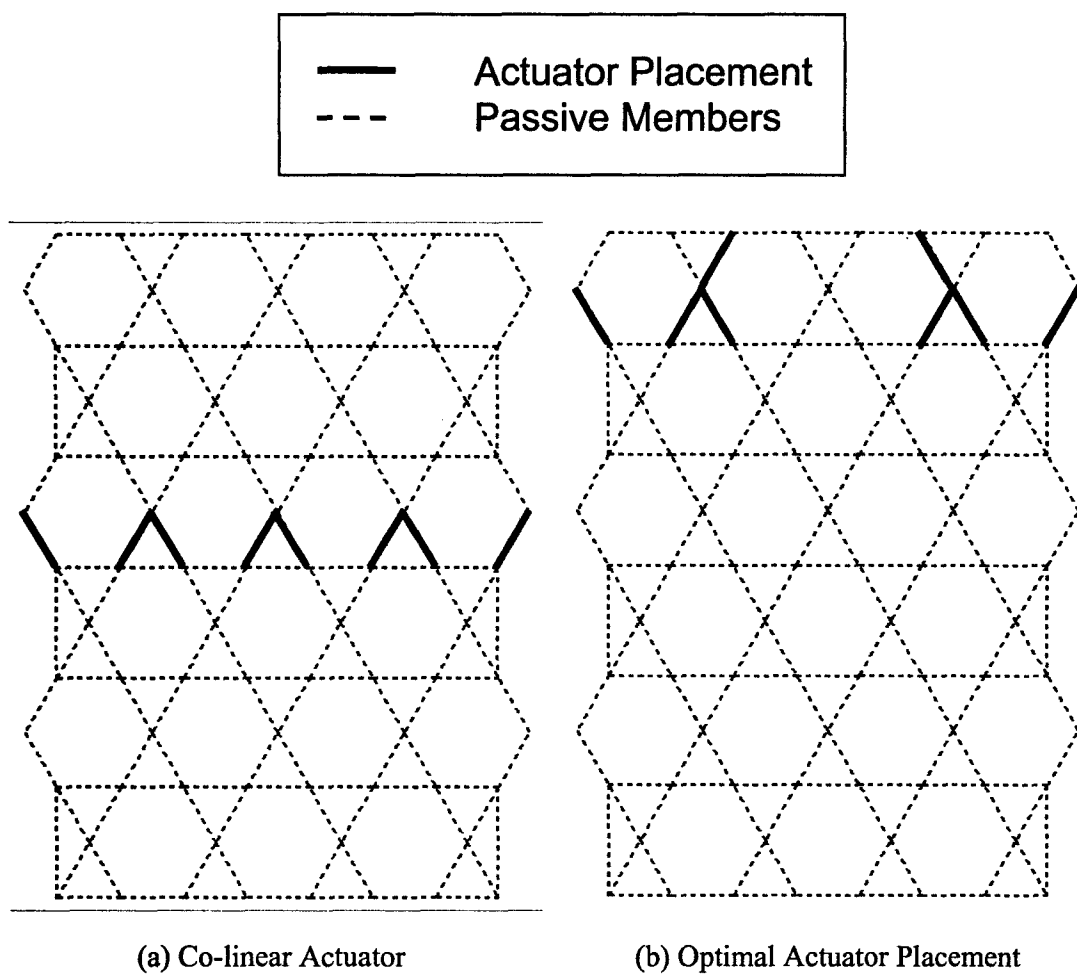


Fig. 2: Two different placement schemes of the actuators: (a) co-linear (sub-optimal for an edge twist perspective); (b) optimal.

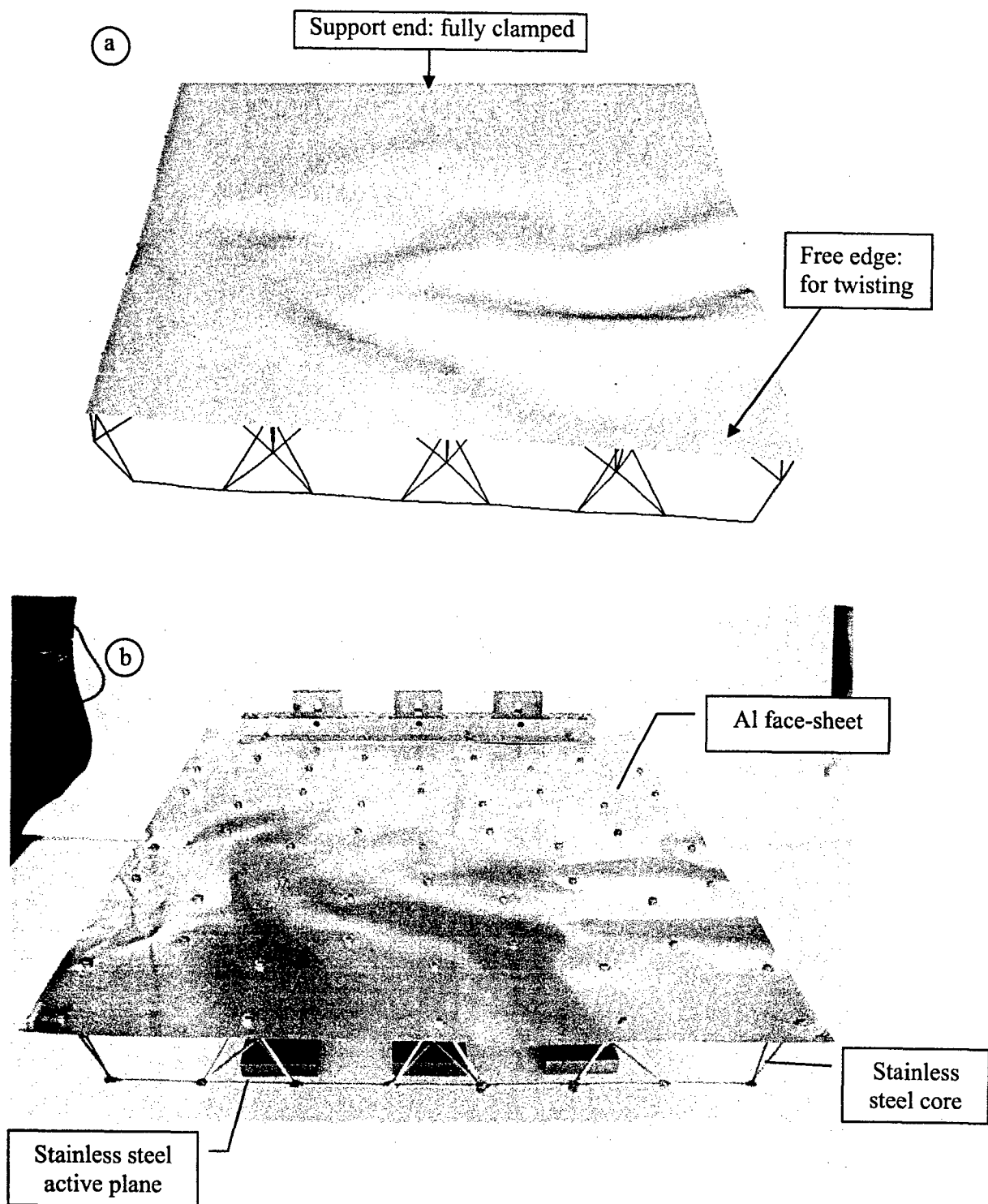
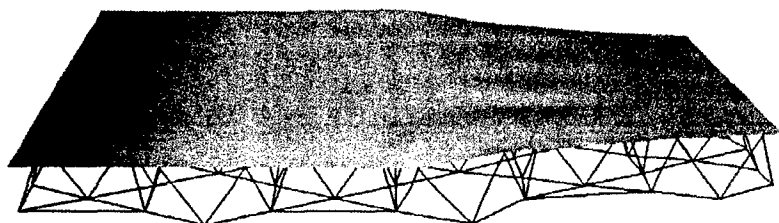
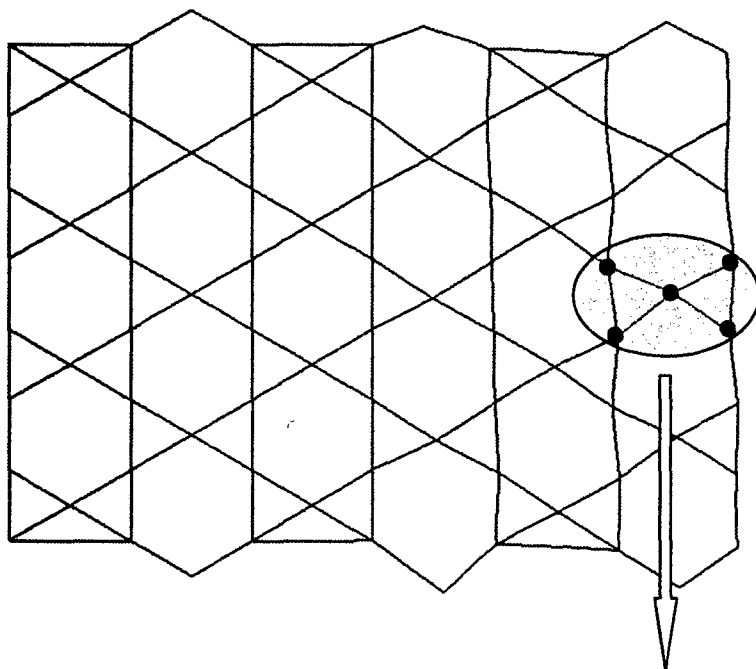


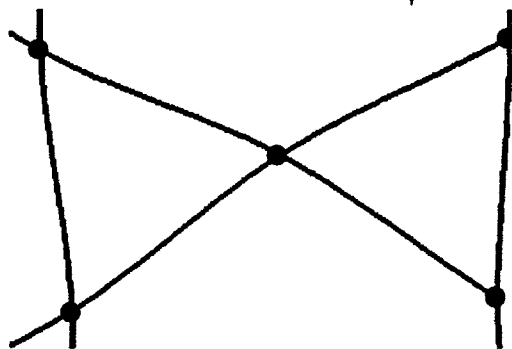
Fig. 3: Wrinkling in the solid face upon actuation. This assembly has Al alloy face with stainless steel core and Kagome back-plane: (a) Finite element simulation; (b) Experimental result.



Side View



Plan View



Representation
Element

Fig. 4: The bending of the Kagome members when the structure with co-linear actuators is twisted. (Deformation scale factor is 7).

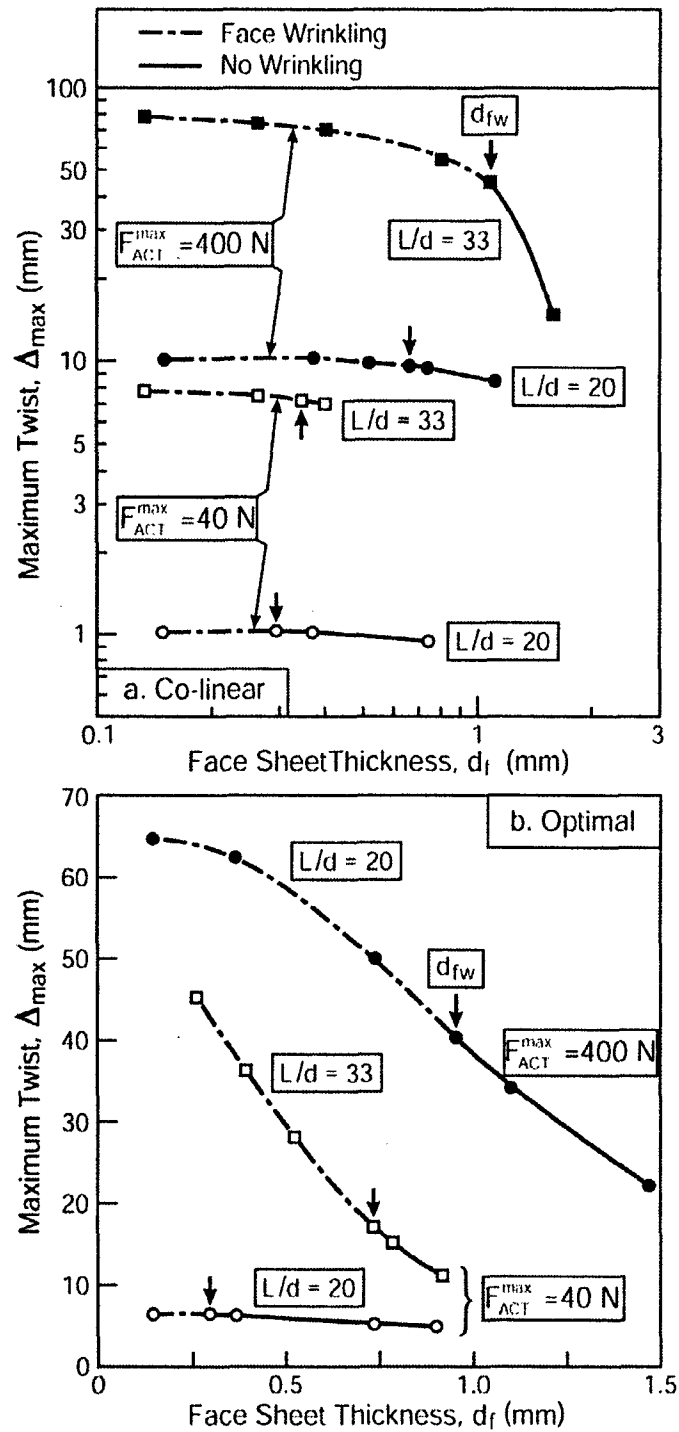
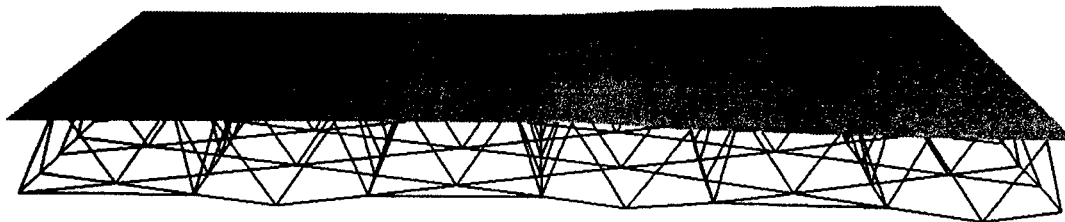
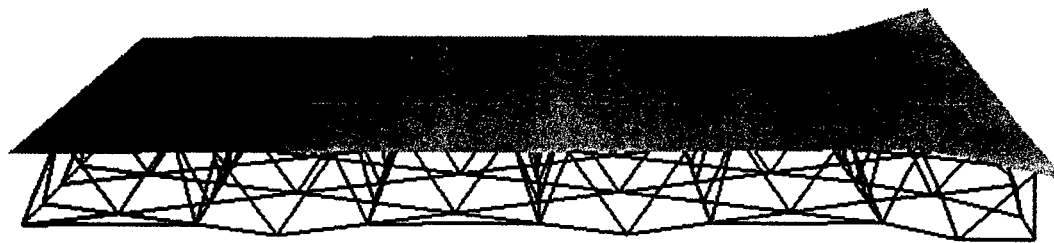


Fig. 5: Maximum twisting displacements attained for two different aspect ratios ($L/d = 20, 33$) and two different actuator force capacity ($F_{ACT}^{\max} = 40\text{N}, 400\text{N}$): (a) Co-linear placement of the actuators; (b) Optimal placement of the actuators. The vertical arrows indicate the face wrinkling transitions at, d_{fw} .

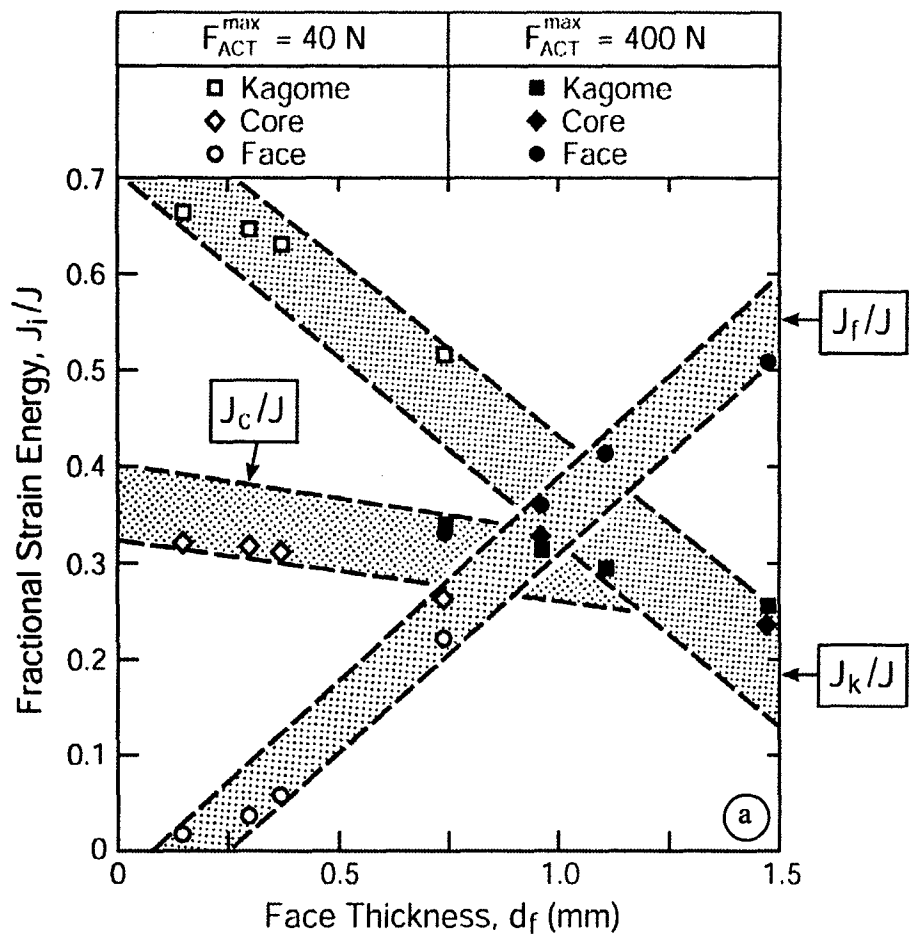


(a)



(b)

Fig. 6: Deformations upon maximum twist for the two different actuator placements ($L/d = 33$, $d_f = d_{fw}$).



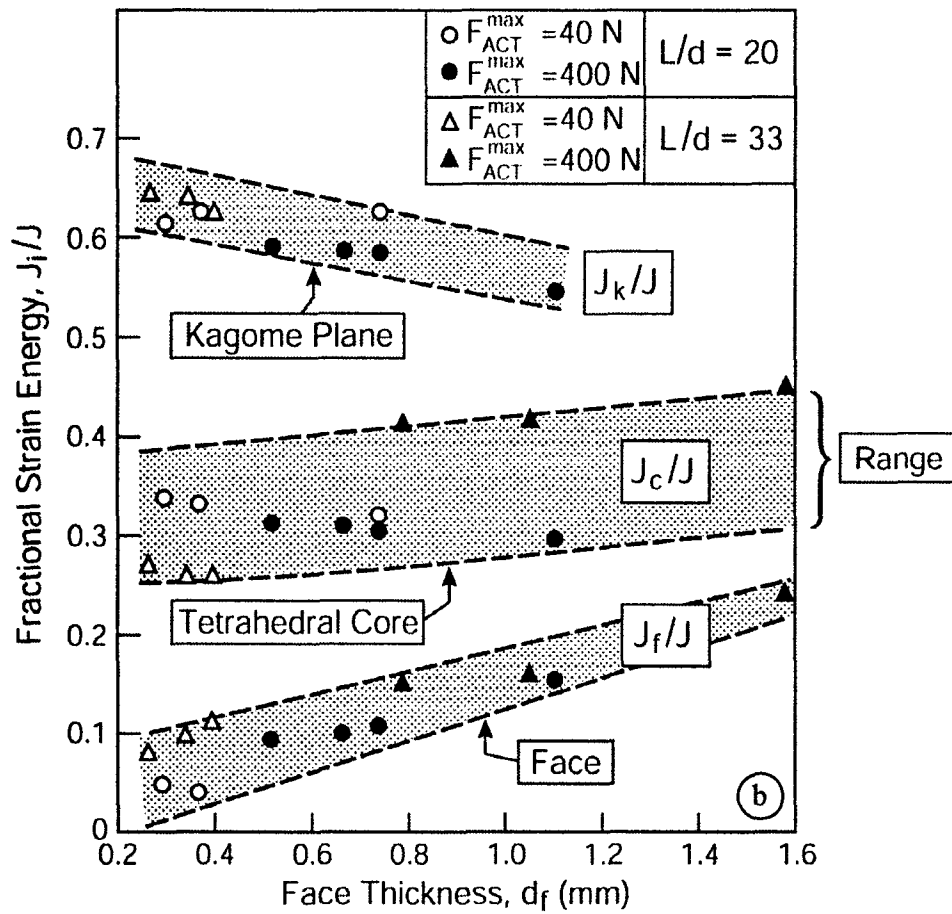


Fig. 7: Elastic energy stored in the three sub-elements: Kagome back-plane, tetrahedral core and solid face-sheet. The symbols give the actual results. The shaded bands are used to highlight the trends. (a) Co-linear placement: note that most energy is stored in the Kagome plane due to member bending. (b) Optimal placement: now most of the energy is either in the core, due to member bending (small face thickness) or in the face (large face thickness), due to face stretching.

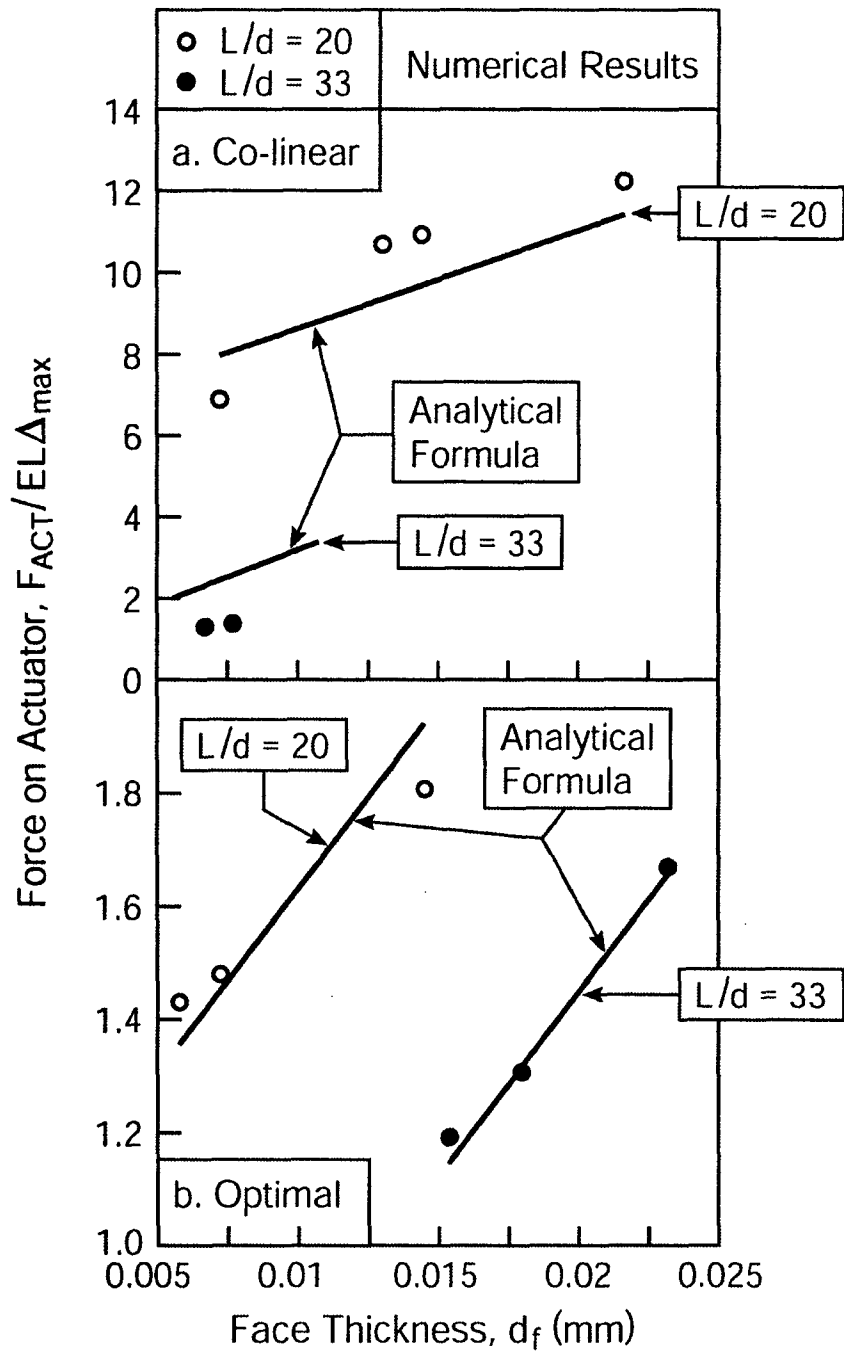


Fig. 8: The forces induced by the structure on the actuators: a comparison of results ascertained numerically (symbols) and the analytic formulae (lines): (a) Co-linear:

$$\frac{F_{ACT}}{EL\Delta_{max}} = 1.0 \left(\frac{d}{L} \right)^4 + 2.3 \times 10^{-4} \left(\frac{d_f}{L} \right); \text{ (b) Optimal: } \frac{F_{ACT}}{EL\Delta_{max}} = 0.16 \left(\frac{d}{L} \right)^4 + 6.6 \times 10^{-5} \left(\frac{d_f}{L} \right)$$

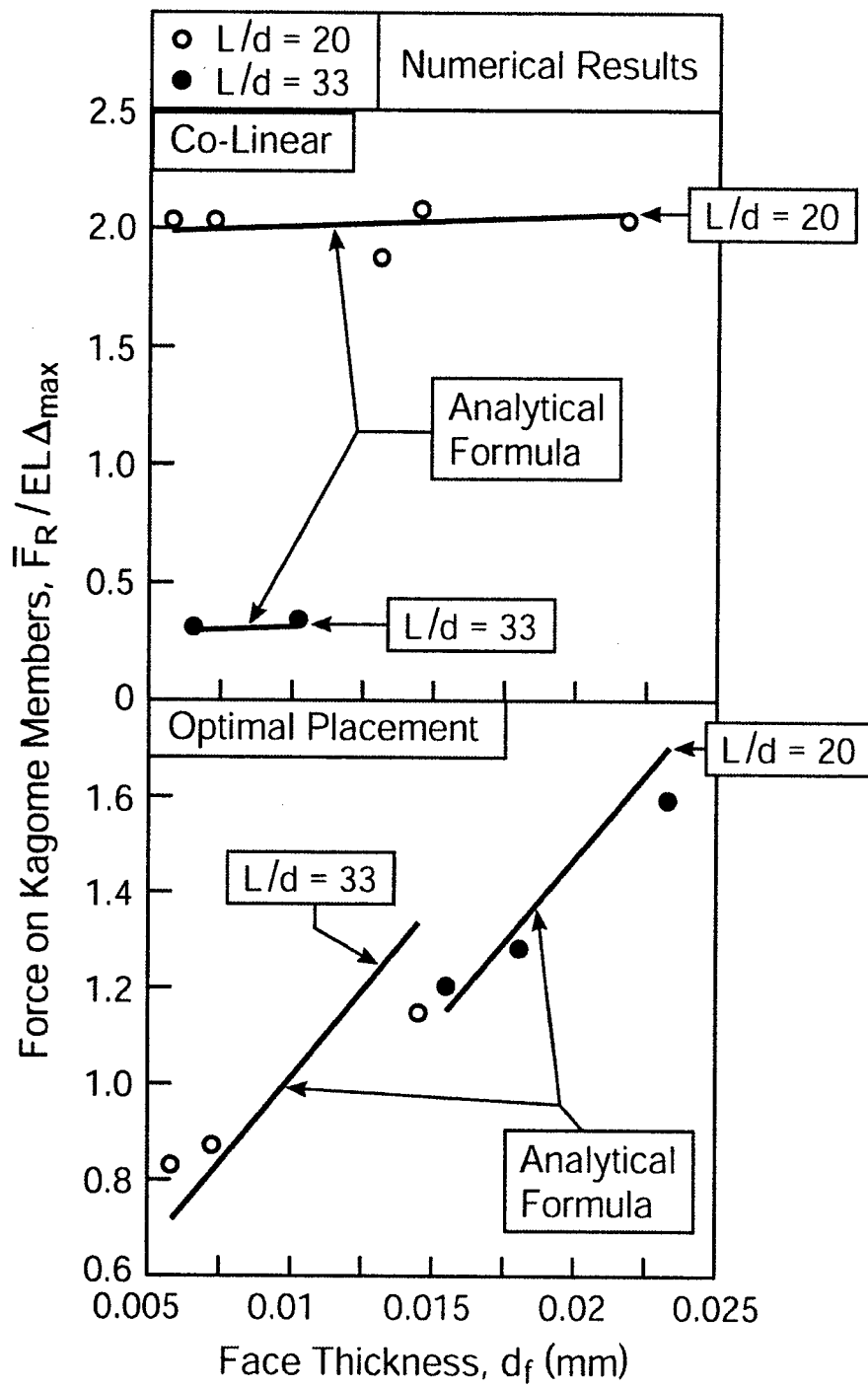


Fig. 9: The forces induced by the structure on the Kagome members: a comparison of result ascertained numerically (symbols) and the analytic formulae (lines): (a) Co-linear:

$$\frac{\bar{F}_K}{EL\Delta_{\max}} = 3.2 \left(\frac{d}{L} \right)^4 + 4.6 \times 10^{-5} \left(\frac{d_f}{L} \right); \text{ (b) Optimal } \frac{\bar{F}_c}{EL\Delta_{\max}} = 0.048 \left(\frac{d}{L} \right)^4 + 7.2 \times 10^{-5} \left(\frac{d_f}{L} \right)$$

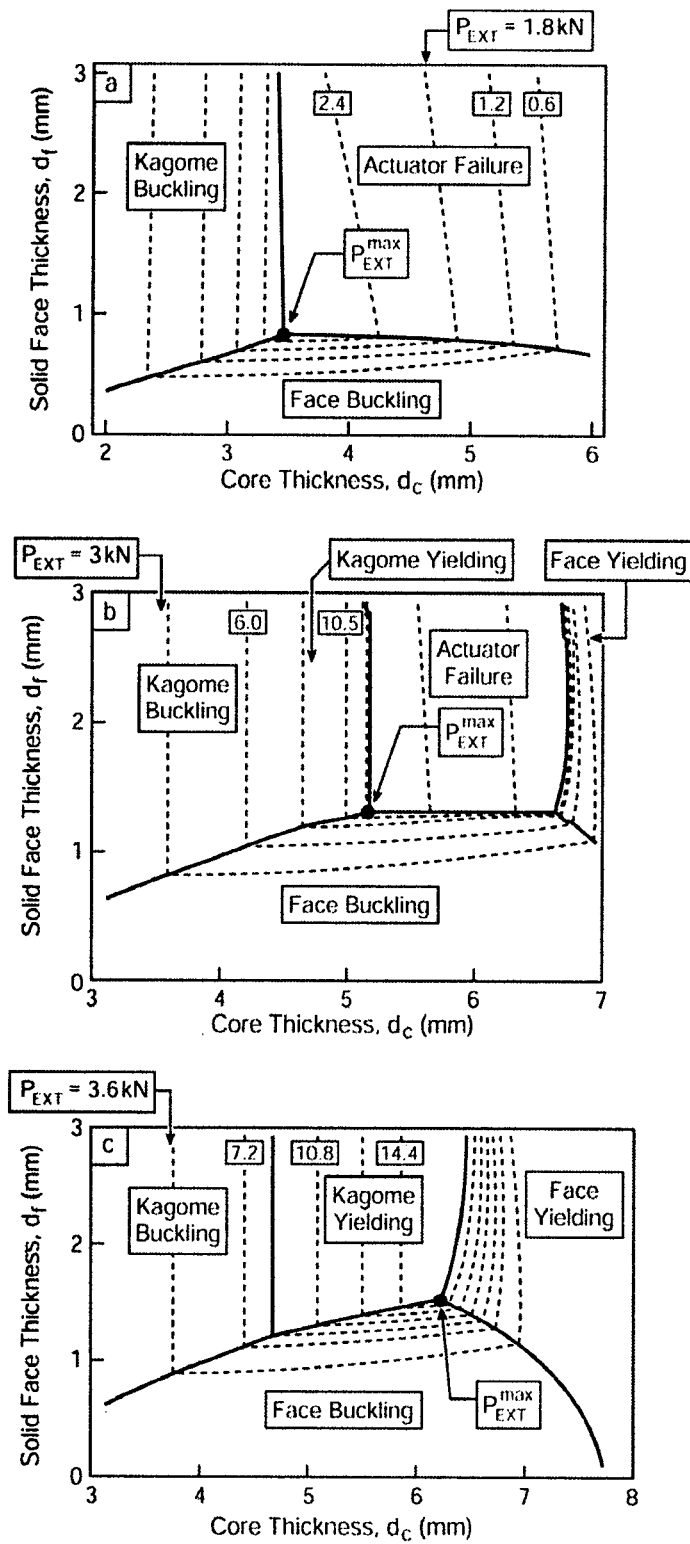


Fig. 10: Mechanism maps and maximum load capacity for three actuator capacities: (a) 1kN; (b) 4kN; (c) 7kN.

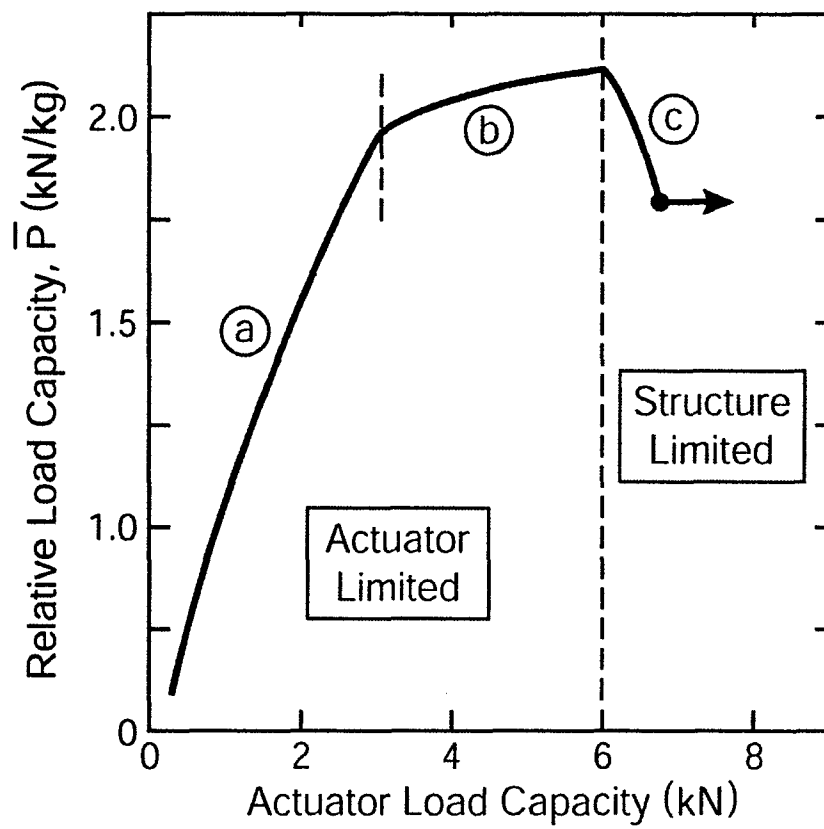


Fig. 11: External load capability as function of actuator load capacity.

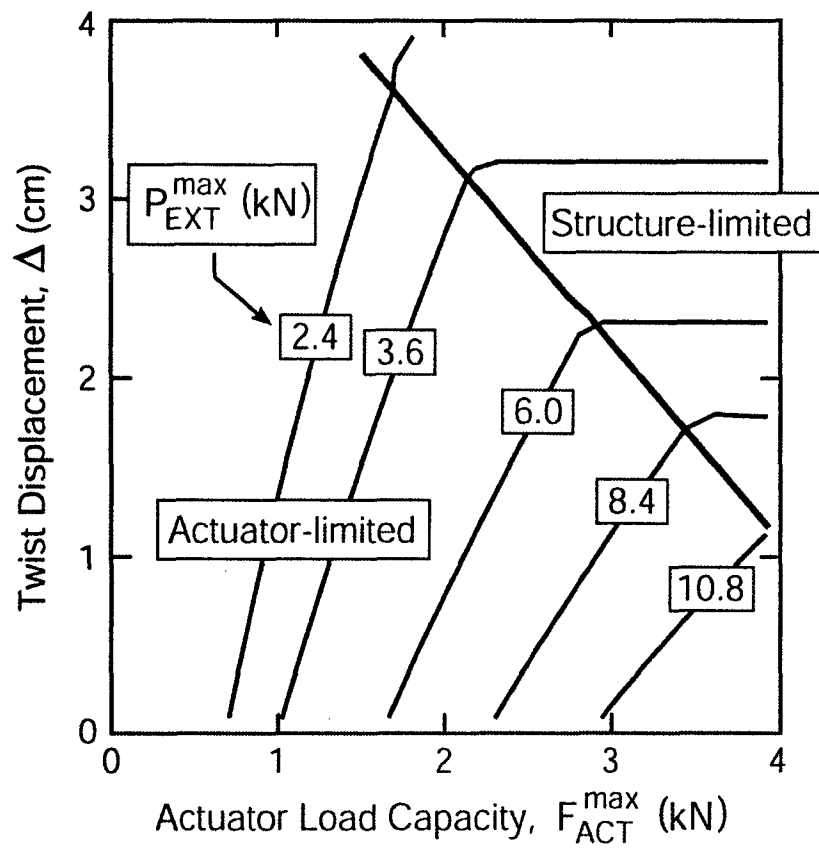


Fig. 12: A map of the maximum load capability as function of actuator capacity and twist displacement.

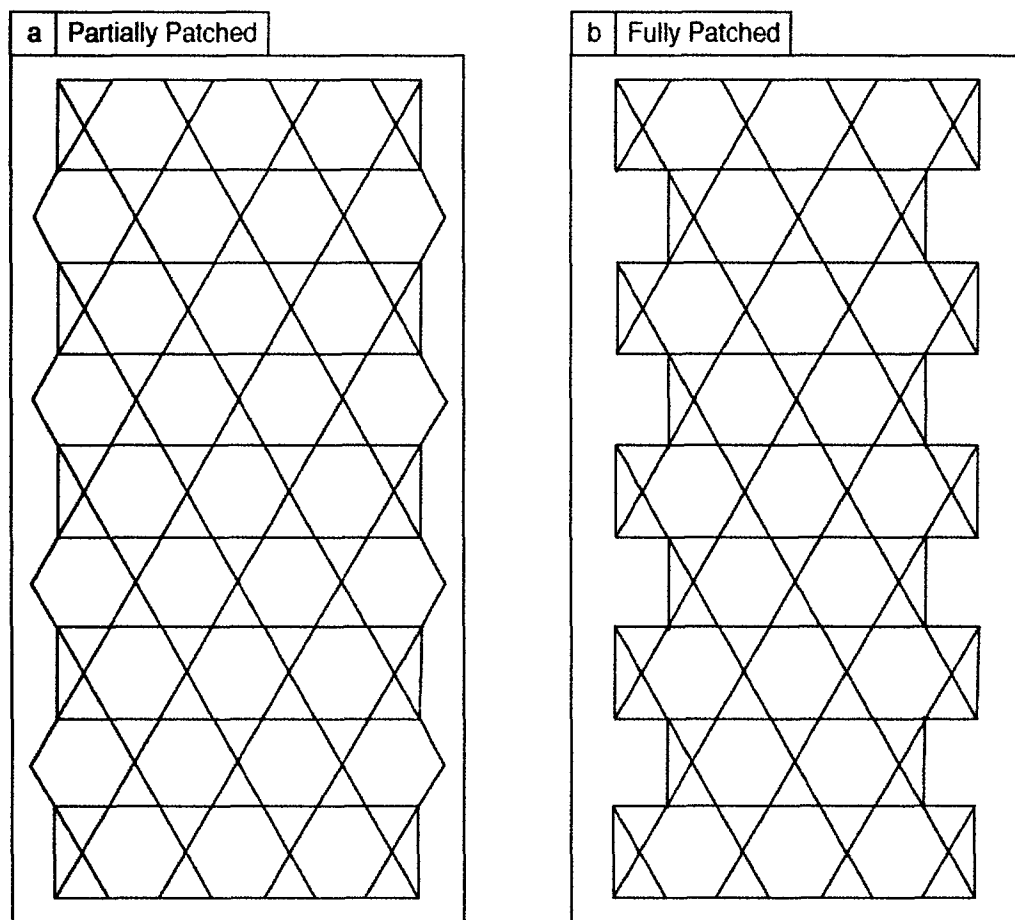


Fig. A1: Two different geometries of the Kagome plane: (a) Partially patched; (b) Fully patched.

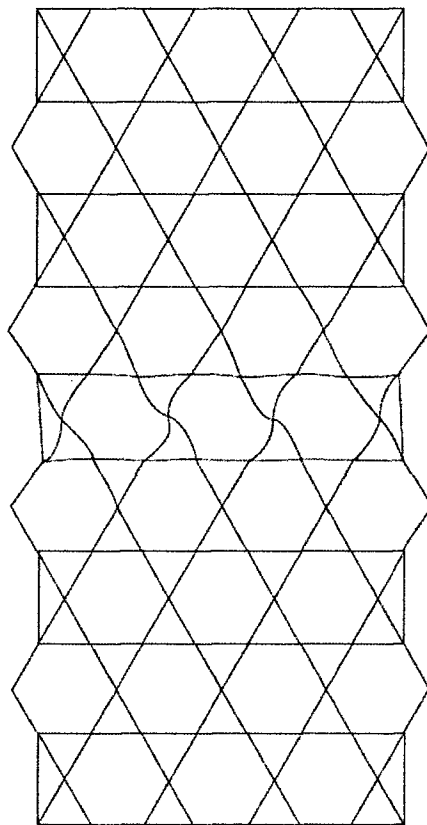
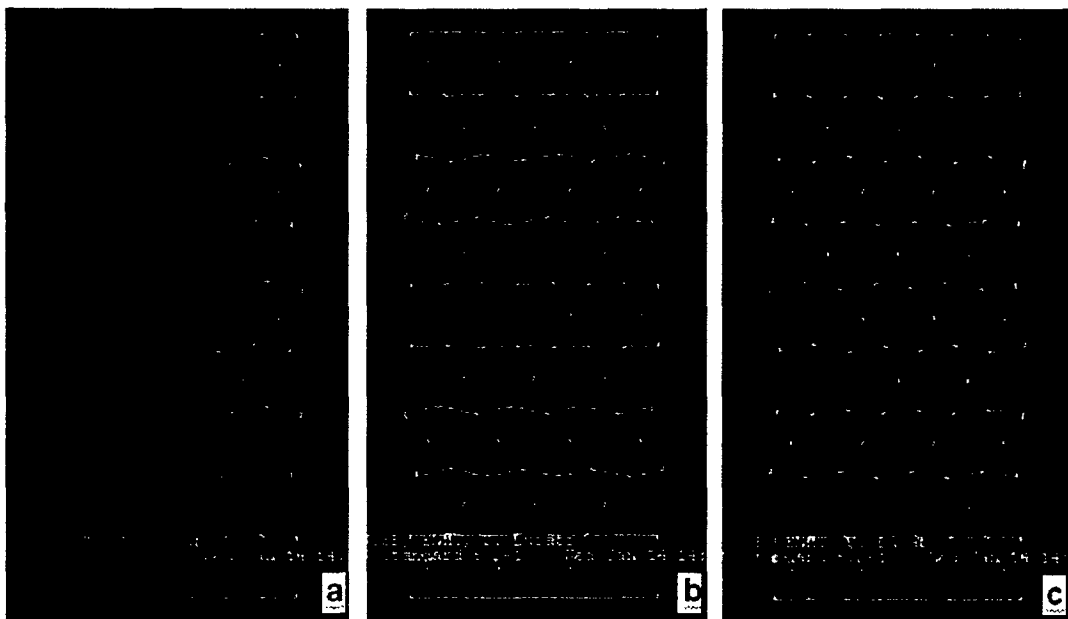


Fig. A2: Shapes of the first three modes: (a) First; (b) Second; (c) Third, as well as the deformed shape near the load maximum.

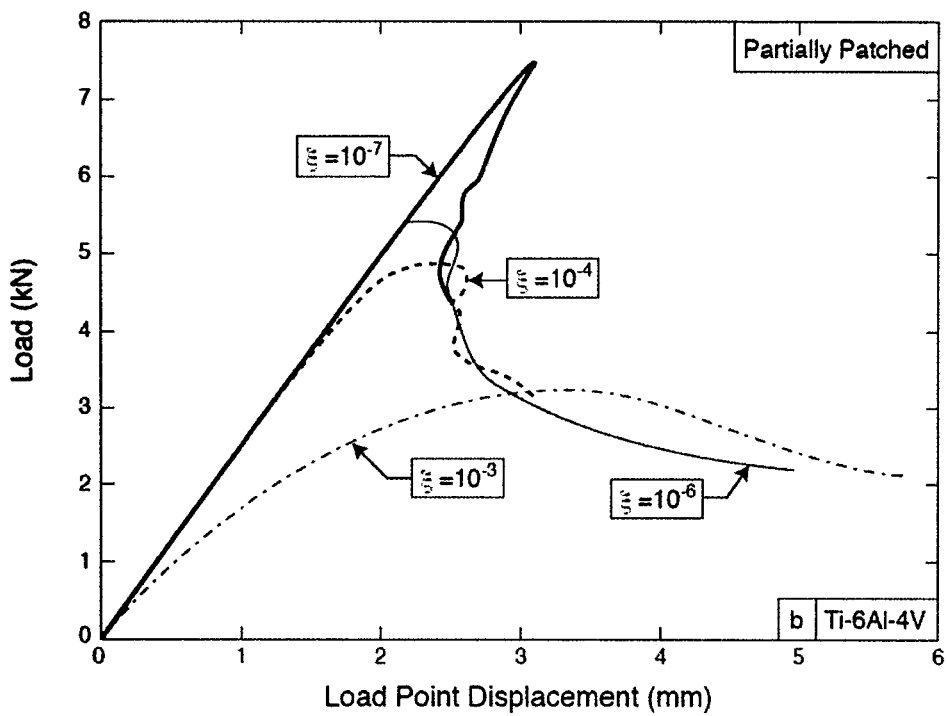
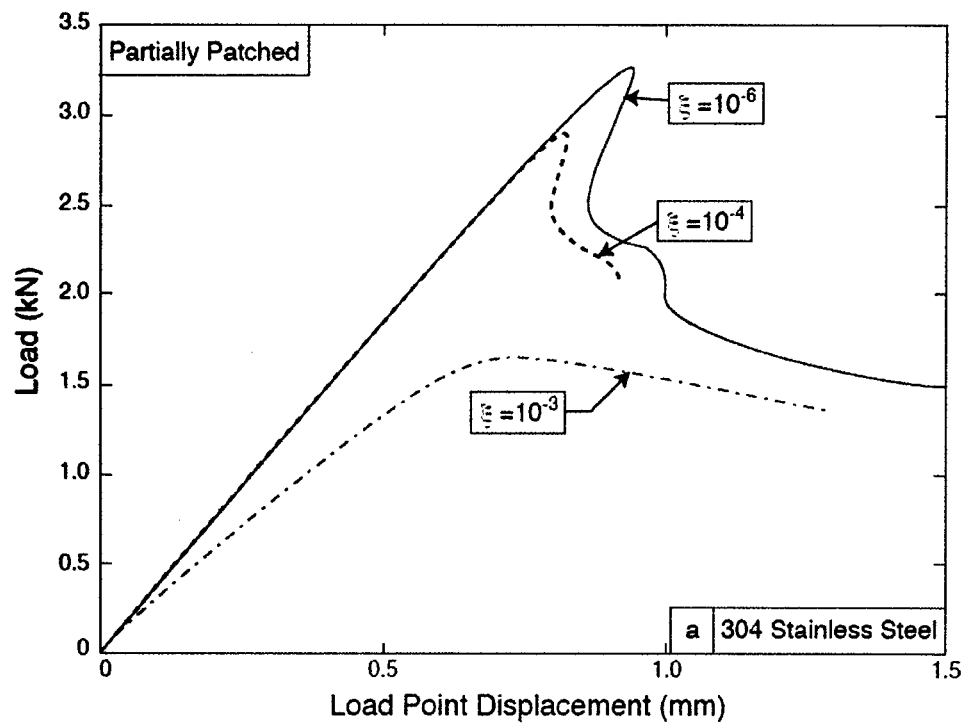


Fig. A3: Load/displacement curves for the partially-patched panels for a range of imperfection amplitudes: (a) 304 stainless steel; (b) Ti-6Al-4V.

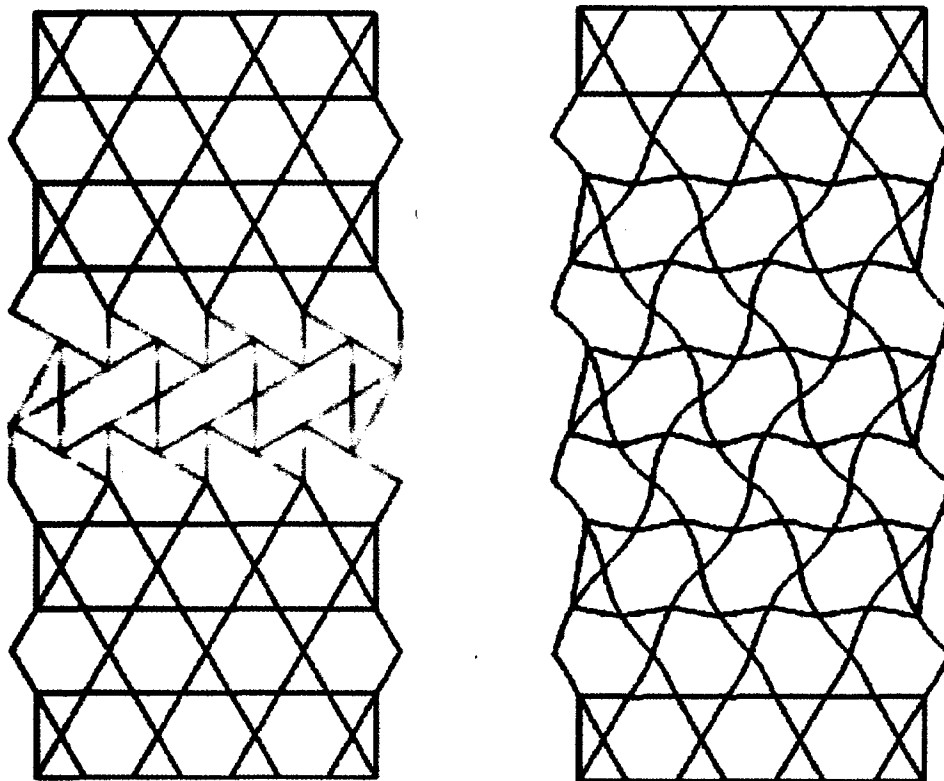


Fig. A4: characteristic deformation pattern of truss rotation for pinned (left) and bonded joints.

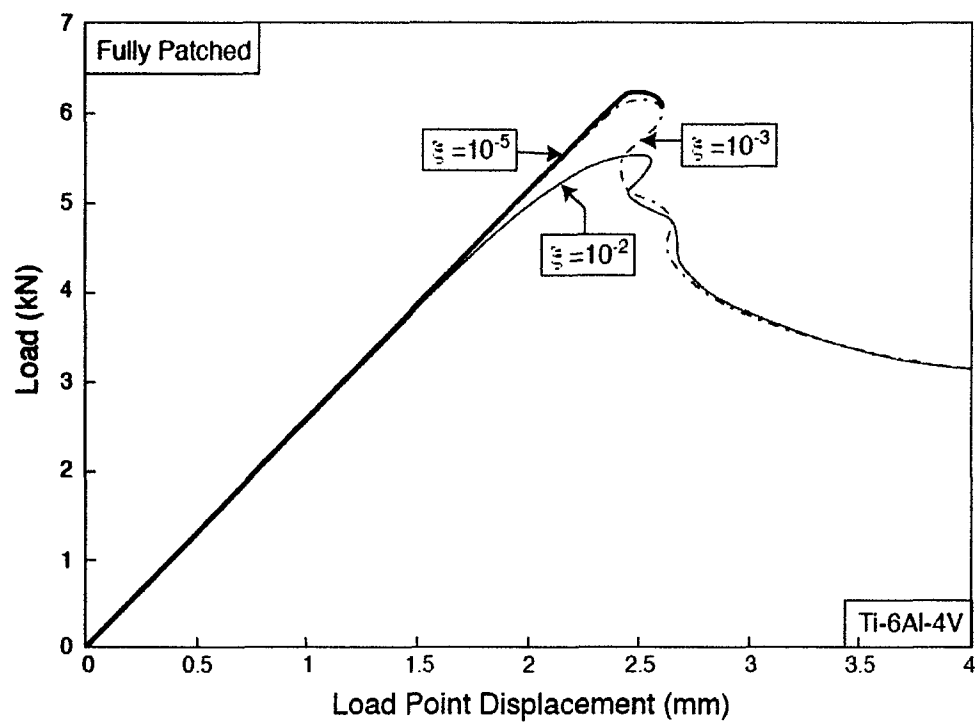


Fig. A5: Load/displacement curves for fully patched Ti alloy panels for a range of imperfection amplitudes.

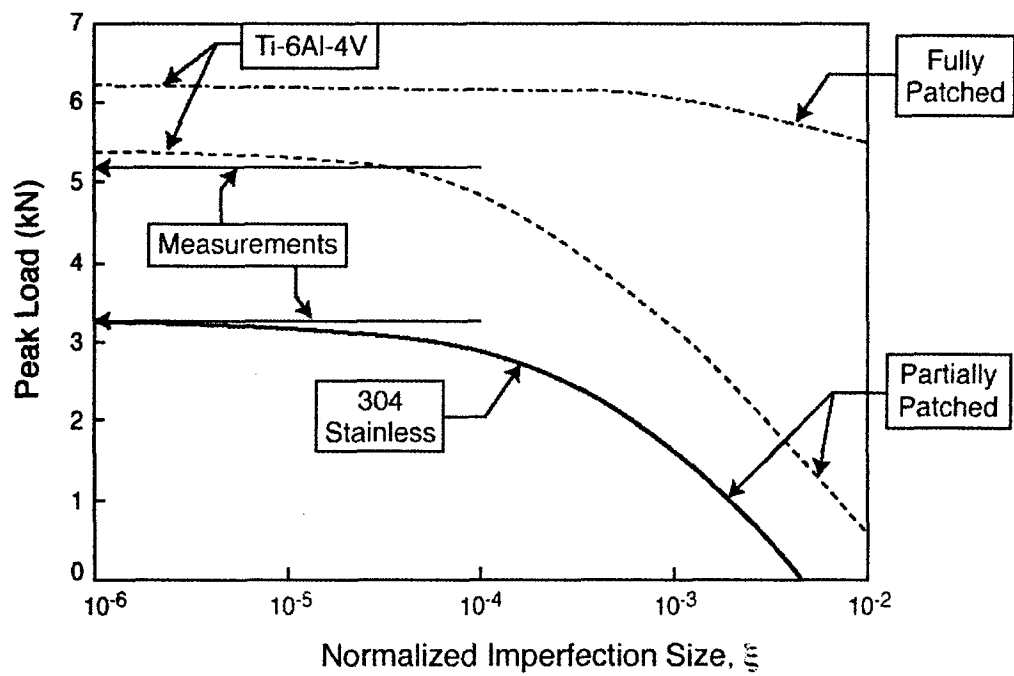


Fig. A6: Trend in the peak load with imperfection amplitude for partially and fully-patched panels: stainless steel and Ti alloy. The measured peak loads are superposed.

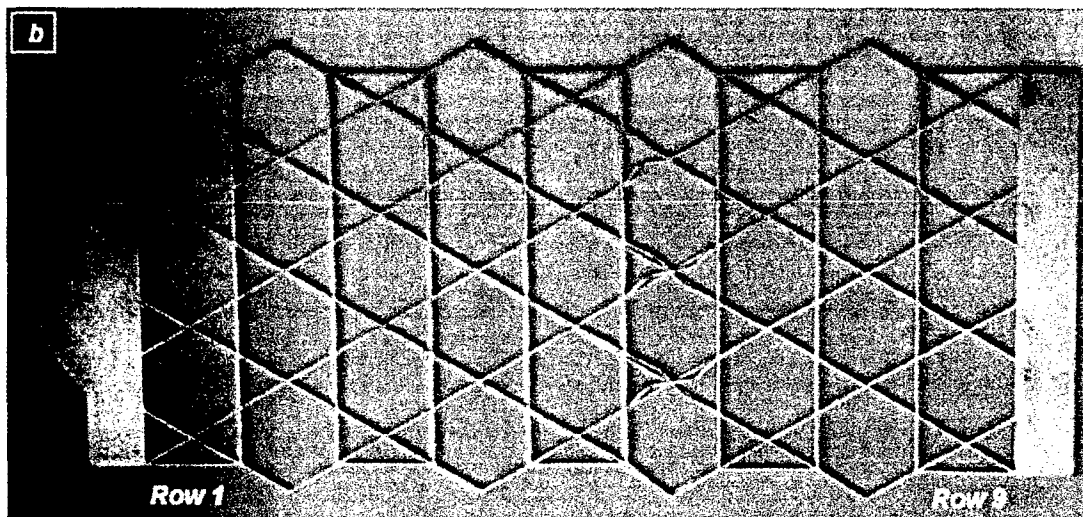
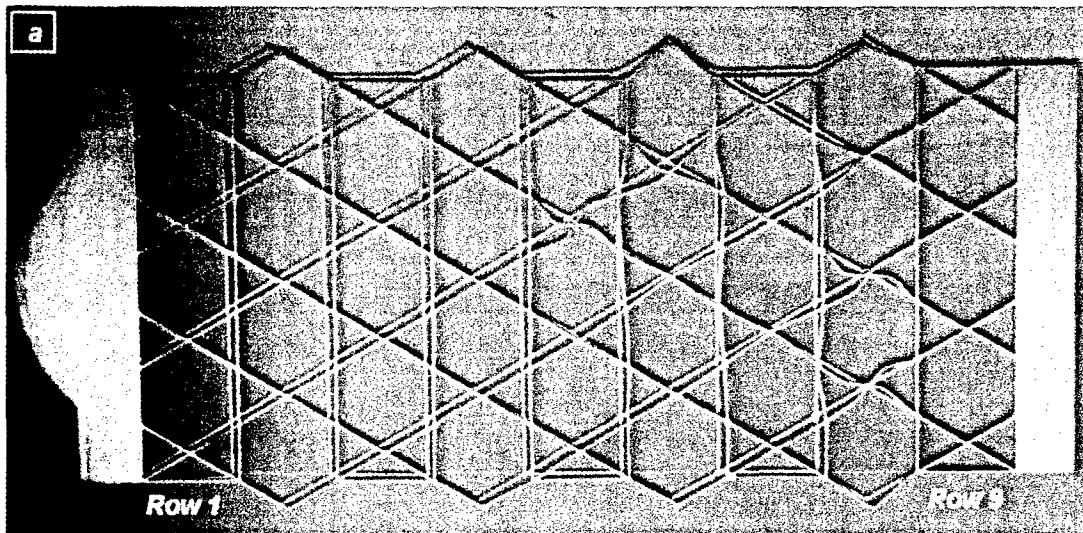
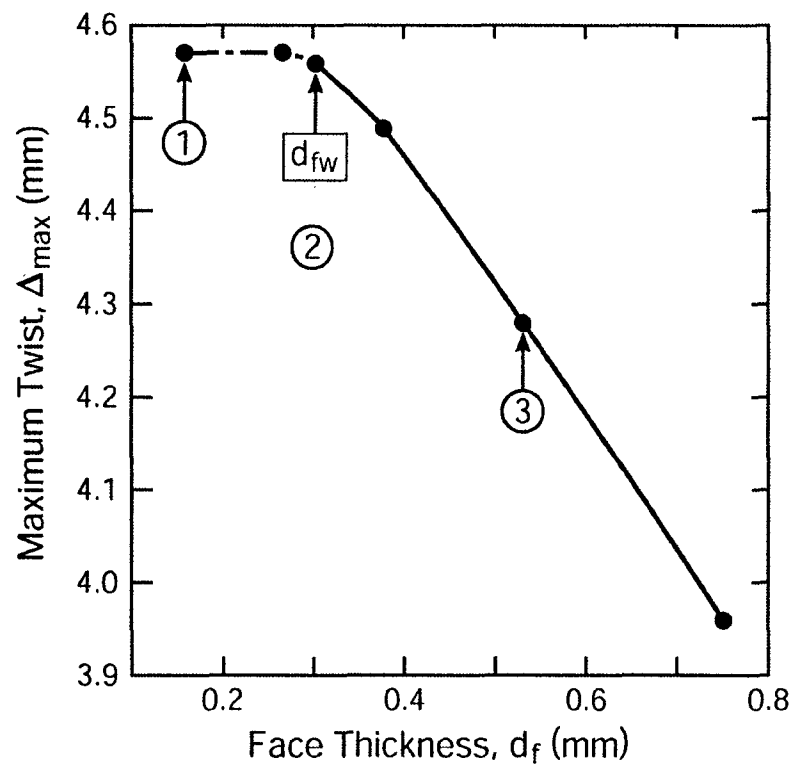


Fig. A7: Deformed partially patched specimens tested in compression: (a) stainless steel and (b) Ti alloy.



①

②

③

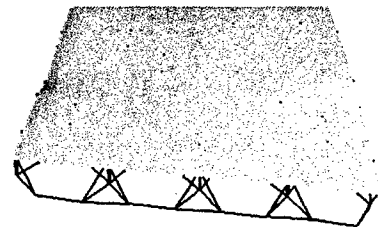
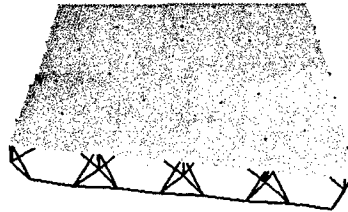
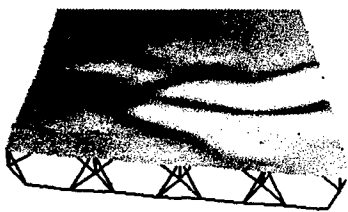


Fig. B1: The maximum twist displacement realizable for different face thickness and the wrinkling patterns of the solid face-sheets.

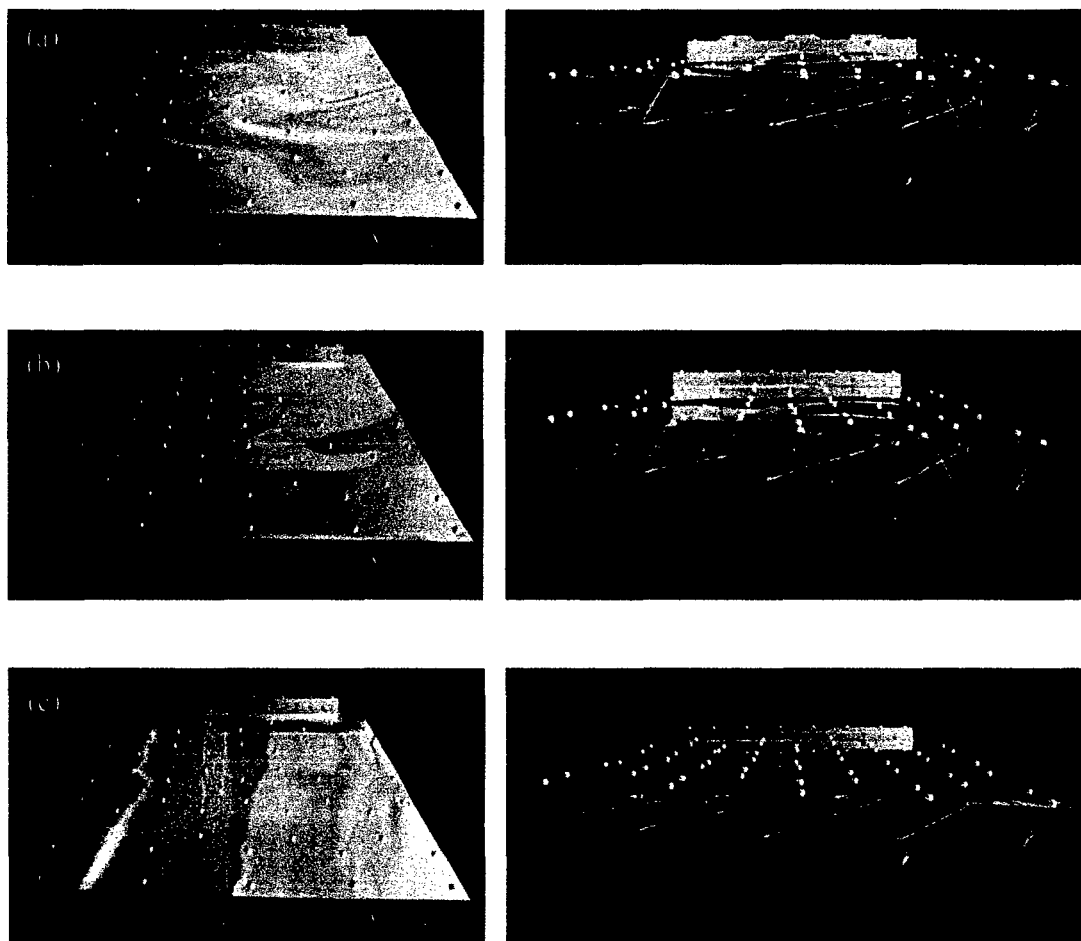


Fig. B2: Face wrinkling suppressed by increasing the face-sheet thickness: (a) $d_f = 0.15\text{mm}$, below critical face-sheet thickness d_{fw} , dramatic face wrinkling observed; (b) $d_f = 0.30\text{mm}$, critical face-sheet thickness d_{fw} , face distortion observed; (c) $d_f = 0.53\text{mm}$, above critical face-sheet thickness d_{fw} , smooth twist without face wrinkling.

Table I: Maximum twist displacements obtained for different assemblies and the strains in the actuators to realize them, subject to an actuator load capacity of 40N.

Assembly (face/core/ Kagome)	Truss thickness (mm)	Face Thickness (mm)	Maximum Twist (mm)	Actuation Strains in the 8 Actuators
Al Alloy/SS/SS	1.52	0.152	7.8	{-0.080, -0.0019, -0.028, 0.011, -0.011, 0.028, 0.0019, 0.080}
Ti/Ti/Ti	1.52	0.132	7.8	{-0.068, -0.0017, -0.024, 0.0097, -0.0097, 0.024, 0.0017, 0.068}

Table II: Elastic energy stored in the sub-systems for hinging and twisting with actuators at co-linear arrangement. The assembly is the demonstration structure.

Strain Energy (J)	Face Sheet	Core	Kagome Back-Plane
Twisting	41×10^{-3}	28×10^{-3}	36×10^{-3}
Hinging	230×10^{-6}	11×10^{-3}	131×10^{-9}

Table III: The coefficients for the numerically fitted equations defining the maximum forces or stresses induced in the actuators and sub-systems by actuation.

	Co-linear	Optimal
A_a	1.0	0.16
B_a	2.3×10^{-4}	6.6×10^{-5}
$(A_K)_{\text{Compressive}}$	3.2	0.17
$(B_K)_{\text{Compressive}}$	4.6×10^{-5}	6.1×10^{-5}
A_K	3.2	0.18
B_K	1.2×10^{-4}	6.1×10^{-5}
$(A_C)_{\text{Compressive}}$	2.1	4.8×10^{-2}
$(B_C)_{\text{Compressive}}$	7.8×10^{-3}	7.2×10^{-5}
A_C	2.1	4.8×10^{-2}
B_C	8.7×10^{-3}	7.6×10^{-5}
$(C_f)_{\text{Compressive}}$	215	30
$(D_f)_{\text{Compressive}}$	-1.6×10^{-3}	4.1×10^{-2}
C_f	2.9×10^3	150
D_f	-0.23	0.22

Table IV: The maximal passive load and geometric dimensions needed to achieve a twist displacement of 5.1mm within different actuator capacities.

$F_{ACT}^{max} (kN)$	$P_{EXT}^{max} (kN)$	$d(mm)$	$d_f(mm)$
1.0	2.9	3.5	0.85
4.0	11	5.2	1.3
6.3	17	6.3	1.5
7.0	17	6.4	1.6

Table V: Comparison of the achieved twist displacements between numerical simulation and test. Δ_{up} is the upward displacement of one corner and Δ_{down} the downward displacement of the other.

Face-sheet Thickness (mm)	Twist at the edge			
	FEA		Test	
	Δ_{down}	Δ_{up}	Δ_{down}	Δ_{up}
0.15	-1.41	5.76	-2.3	6.2
0.30	-4.56	4.56	-4.8	5.5
0.53	-4.35	4.28	-4.7	5.3

**Part V: Performance of sandwich plates
with truss cores**



Performance of sandwich plates with truss cores

Nathan Wicks *, John W. Hutchinson

Division of Engineering and Applied Sciences, Harvard University, Cambridge, MA 02138, USA

Received 15 July 2002; received in revised form 30 January 2003

Abstract

Sandwich plates with truss cores fashioned from straight struts have distinct advantages relative to other constructions, including those with honeycomb cores. In addition to opportunities afforded by their open architecture, the truss core sandwich plates meet or exceed the load carrying capacity of other competitive constructions. The weight of truss core sandwich plates subject to a crushing stress and arbitrary combinations of bending and transverse shear are optimized subject to buckling and plastic yielding constraints and then compared with the weight performance of other types of optimized plates. Several issues central to the optimization process are addressed by a fundamental model study. These include the relation of designs based on a pure moment loading to those based on combined moment and transverse shear and the accuracy needed to model the various modes of buckling that must be taken into account in the design process.

© 2003 Elsevier Ltd. All rights reserved.

Keywords: Sandwich plates; Truss cores; Optimal design; Buckling; Plastic yielding

1. Introduction

New focus on sandwich plates with truss cores has been motivated by potential multifunctional applications that exploit their open architecture as well as their apparent superior strength and stiffness (Evans et al., 2001). Moreover, new methods have been devised which permit “micro” plates with truss cores to be manufactured (Brittain et al., 2001). In the present context the terminology “truss core” refers to a core constructed from beam elements but not folded plates, as is sometimes implied. A preliminary study (Wicks and Hutchinson, 2001) has revealed that the perfor-

mance of optimized sandwich plates with truss cores is competitive with more widely used constructions, including sandwich plates with honeycomb cores and stringer stiffened plates. A more extensive study of the performance of optimized truss core sandwich plates is undertaken in the present paper. We begin by investigating the optimal design of a model of a two-dimensional truss structure subject to pure bending (see Fig. 1). The various buckling modes of this structure can be analyzed exactly, providing insights into the validity of the approximations that are usually invoked in the optimal design of more complicated structures such as truss core sandwich plates. The model problem also reveals the connection between an optimal configuration designed to carry a pure moment and its counterpart designed to carry

* Corresponding author.

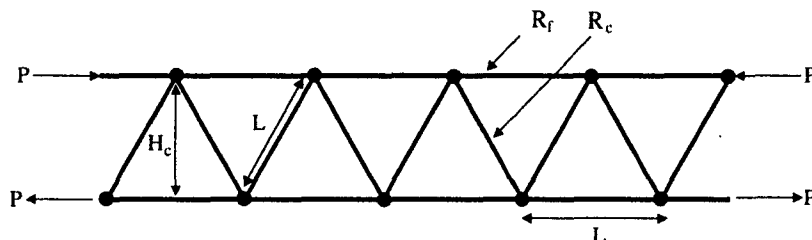


Fig. 1. Geometry of the two-dimensional infinite model truss.

a combination of moment and transverse shear force. The second part of the paper specifically addresses the optimization of sandwich plates with truss cores subject to a crushing stress, bending, and transverse shear. The optimal configurations are compared to optimized plates with honeycomb cores.

2. A two-dimensional truss under pure moment

The infinite truss shown in Fig. 1 carries a moment $M = PH_c$. Each member is taken to have a solid circular cross section, with radius R_f for the horizontal members and radius R_c for the inclined core members. All members are made from the same material whose Young's modulus is E and initial yield stress in tension is σ_Y . All members have length L such that each triangular group is equilateral and $H_c = \sqrt{3}L/2$. Individual truss members are assumed to be slender (i.e. $R/L \ll 1$) and they are regarded as beam columns. At the joints, the members are assumed rigidly connected to one another such that ends of each member meeting at a joint undergo the same displacements and rotation. Only in-plane deformations are considered.

2.1. Bifurcation buckling analysis: exact formulation

The analysis reveals all possible bifurcation buckling modes of the truss and the associated critical moments. Two distinct modes of importance emerge: a mode with sinusoidal half-wavelength equal to the member length wherein compressed members buckle between their joints and a longer wavelength mode.

As is customary in investigations of this kind, the pre-buckling load is approximated as being carried entirely by the horizontal members. This is an excellent approximation since the axial forces in the core members are zero and the elastic energy induced by bending in the pre-buckling response is extremely small. The bifurcation buckling analysis is given in Appendix A. Each member is represented as a beam column, and its deformation is expressed in terms of the displacement components and rotation at its ends where it connects to adjoining members. The eigenvalue problem for the bifurcation mode is formulated exactly as an infinite set of finite difference equations involving the joint displacements and rotations. The equations admit sinusoidal solutions with a wavelength λ . With $M_c(\lambda)$ denoting the minimum eigenvalue at a given λ , the critical moment governing bifurcation is the lowest value of $M_c(\lambda)$ over the entire spectrum of λ . The full spectrum of eigenvalues is spanned for the range of wavelengths, $1 \leq \lambda/(2L) < \infty$, as discussed in Appendix A.

Examples of the eigenvalue spectrum are plotted in Fig. 2. In the example with the larger ratio, R_c/R_f , the lowest eigenvalue is associated with the short wave mode ($\lambda = 2L$), corresponding to buckling of the compressed horizontal members between their joints, as depicted. The other eigenvalue spectrum shown is for very slender core members relative to the horizontal members. In this example, the lowest eigenvalue is associated with a longer wave mode ($\lambda \approx 3.6L$). This longer wave mode appears when the ratio, R_c/R_f , is very small, as will be quantified in the next section. The result from the approximate formula for the short wave eigenvalue that is presented in Section 2.2 very accurately predicts the value plotted at $\lambda = 2L$ for both of the R_c/R_f values shown in Fig. 2.

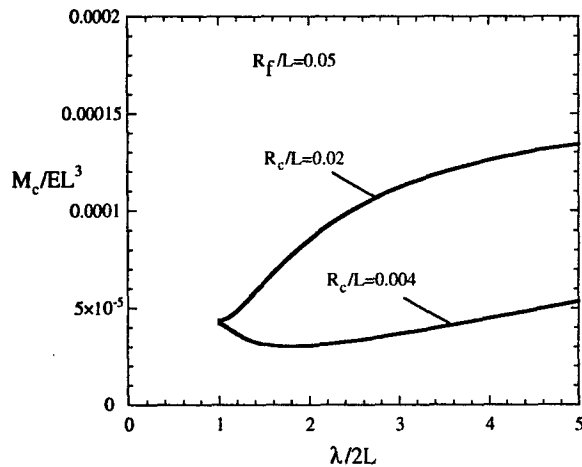


Fig. 2. Eigenvalue spectrum, $M_c(\lambda)$, for $R_f/L = 0.05$, for two core radius values ($R_c/L = 0.02$ and $R_c/L = 0.004$).

2.2. Approximate results for short and longer wavelength buckling modes

The model problem is sufficiently simple such that it is possible to use results from the exact

analysis to carry out an optimal design of the truss, and this will be done. The primary aim in conducting the model study, however, is to make use of the exact solution to assess the validity of using approximate formulas for the two buckling modes highlighted above. Optimal design of more complex structures under more general loads will generally employ approximate formulas of the type that will be introduced below. Thus, the present model problem affords an opportunity to quantitatively evaluate the accuracy of optimal configurations obtained using approximate buckling formulas.

The scheme for estimating the constraining effect of the lower portion of the structure on the buckling of the horizontal members in the *short wavelength mode* is depicted in Fig. 3a. The top compression member is constrained to have zero deflection at each joint and its rotation is constrained by a torsional spring. The spring constant is determined from the problem depicted in Fig. 3b where a moments of equal magnitude but alternating sign act on the remaining part of the truss. If the effect of the tensile load P on the bottom

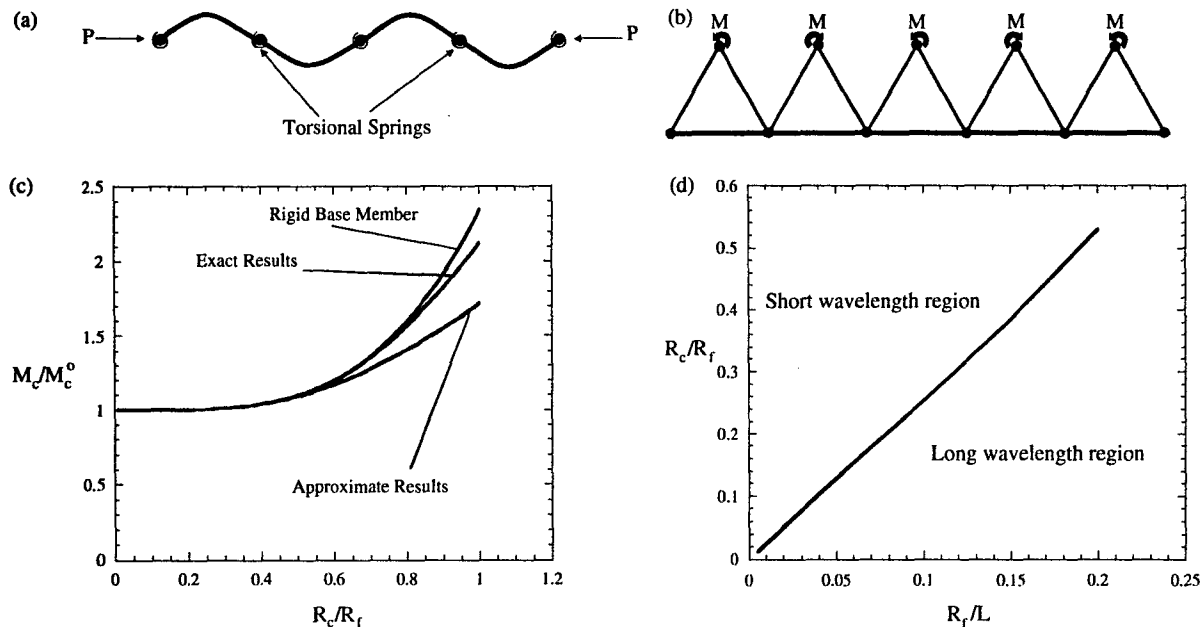


Fig. 3. Approximate analysis of the short wavelength buckling mode (a)–(c) and the border between the long and short wavelength buckling (d).

horizontal member is neglected, the torsional spring constant can be determined exactly as

$$K = M/\theta = \frac{8EI_c}{L} \left\{ 1 + \frac{16}{3}q^2 + \frac{8}{3}\frac{I_c}{I_f} \left(\frac{3}{4} - q \right)^2 \right\}^{-1}$$

$$q = \frac{3I_c}{8I_f + 4I_c} \quad (1)$$

where $I_f = \pi R_f^4/4$ and $I_c = \pi R_c^4/4$. If the horizontal members are much thicker than the core members such that $q \cong 0$, then $K = 8EI_c/L$, and this is identical to the case where the core members are attached to a rigid foundation. The eigenvalue equation for the critical load P for an infinite beam having zero deflection and constrained by the above torsional spring at equally spaced distances L is

$$\sqrt{\frac{P}{EI_f}} \frac{L}{2} \cot \left(\sqrt{\frac{P}{EI_f}} \frac{L}{2} \right) = -\frac{KL}{4EI_f} \quad (2)$$

By expanding (2) in a Taylor series about $\sqrt{P/EI_f}L = \pi$ (appropriate for sufficiently small KL/EI_f) and retaining up to and including terms of second order, one obtains the explicit approximation for the short wavelength buckling load

$$\sqrt{\frac{P}{EI_f}} \frac{L}{2} = \frac{\pi}{4} + \sqrt{\left(\frac{\pi}{4} \right)^2 + \frac{KL}{4EI_f}} \quad (3)$$

Results for the critical buckling moment from the exact analysis are compared in Fig. 3c with results from (3) for the full expression (1) for K , and the two sets are in good agreement for values of R_c/R_f up to about 0.5. In this figure, M_c^0 denotes the critical moment with $K = 0$ corresponding to simple support of a beam of length L . An even better approximation is seen to pertain for the case where the base horizontal members are taken to be rigid, i.e. $K = 8EI_c/L$.

The lowest eigenvalue is associated with a “long” wavelength mode only when R_c/R_f becomes smaller than a transitional value. Fig. 3d is a plot of the transition value of R_c/R_f as a function of R_f/L at which the long wavelength mode has the same eigenvalue (buckling moment) as the short wavelength mode ($\lambda = 2L$). The condition that ensures that the short wavelength mode is critical is well approximated by

$$\frac{R_c}{R_f} \geq -0.00313 + 2.62 \frac{R_f}{L} \quad (4)$$

An approximate approach to estimating the critical load associated with the “long” wavelength mode has the compressed beam resting on an elastic foundation where the spring constant for normal displacement is obtained for triangular core elements rigidly supported at the bottom beam. The critical load from such an analysis is $P = 2\sqrt{EI_f S}$, where the spring constant is $S = 2H^2 R_c^2 \pi E / L^4$. Equating this critical load with the short wavelength critical load based on simple support at the nodes gives the approximation to the transition as $R_c/R_f = \pi^2 R_f / 2\sqrt{6}L = 2.01 R_f / L$. The error in this result compared to the transition (4) is due to the fact that the so-called long wavelength mode, in fact, is not really long compared to the member length.

In the optimization described below for a pure moment loading, condition (4) will be invoked as a constraint on the design. It is conceivable that a lighter weight design might be attained if R_c/R_f were allowed to become even smaller. However, as we shall see, the inclusion of any realistic level transverse shear in the design process ensures that R_c/R_f is well above the transition ensuring that short wavelength buckling is critical.

2.3. Optimization of the two-dimensional truss subject to pure moment

The dimensions of the truss members, R_c , R_f and L , are now identified that give the lightest weight given that the truss must support a prescribed moment M such that the force carried by the horizontal members is $P = 2M/\sqrt{3}L$. With w as the weight per unit volume of the material comprising the members, the weight per unit length of the truss is $W = 2\pi w(R_c^2 + R_f^2)$. The horizontal members must not exceed yield requiring, $\sqrt{3}\pi\sigma_Y R_f^2 L/2 \geq M$, while the short wavelength (3) and long wavelength (4) buckling conditions provide the respective constraints

$$\frac{\sqrt{3}}{2} \pi \left(\frac{\pi}{4} + \sqrt{\left(\frac{\pi}{4} \right)^2 + \frac{KL}{4EI_f}} \right)^2 \frac{ER_f^4}{L} \geq M$$

and

$$\frac{R_c}{R_f} \geq -0.00313 + 2.62 \frac{R_f}{L}$$

Plastic buckling of the horizontal members is not explicitly considered since it is excluded by the constraint on plastic yielding. The yielding constraint could be replaced by a constraint on plastic buckling, but this would have relatively little influence on the optimal design. Except for materials with very high strain hardening, the plastic buckling load is only slightly higher than the load at plastic yield and for this reason the constraint on plastic yielding is only slightly conservative.

The only length quantity other than unknown member dimensions is $(M/E)^{1/3}$. To put the optimization problem in non-dimensional form, introduce dimensionless member variables as $\vec{x} \equiv (x_1, x_2, x_3) = (R_f, R_c, L)/(M/E)^{1/3}$. The dimensionless optimization problem requires that the dimensionless weight, $W/[w(M/E)^{2/3}] = 2\pi(x_1^2 + x_2^2)$, be minimized with respect to \vec{x} subject to the three constraints noted above, i.e.

$$\begin{aligned} \frac{\sqrt{3}\pi}{2} \varepsilon_Y x_1^2 x_3 &\geq 1 \\ \frac{\sqrt{3}\pi^3}{8} \left(\frac{1}{2} + \sqrt{\frac{1}{4} + k} \right)^2 x_1^4 x_3^{-1} &\geq 1 \\ \frac{x_2}{x_1} &\geq -0.00313 + 2.62 \frac{x_1}{x_3} \end{aligned} \quad (5)$$

Here, $\varepsilon_Y = \sigma_Y/E$ is the yield strain and k is

$$k = \frac{KL}{\pi^2 EI_f} = \frac{4}{\pi^2} (x_2/x_1)^4 \frac{(x_2/x_1)^4 + 2}{2(x_2/x_1)^4 + 1}$$

The yield strain is the only parameter in the dimensionless optimization problem. For a numerical example, take $\varepsilon_Y = 0.007$ corresponding to a high strength aluminum considered in the earlier study (Wicks and Hutchinson, 2001). The solution to the optimization problem is

$$\begin{aligned} x_1 &= 1.4088, \quad x_2 = 0.19249 \\ x_3 &= 26.457, \quad W/[w(M/E)^{2/3}] = 12.703 \end{aligned} \quad (6)$$

All three constraints in (5) are active for the solution.

3. The optimal two-dimensional truss subject to both moment and transverse shear force

Now suppose the same truss at its most severely loaded section carries a moment M and a shear force V . Let $\ell = M/V$ and assume that $\ell \gg L$, which necessarily holds if the truss contains multiple sections. (A cantilever beam of length ℓ loaded with a force V at its free end experiences the moment $M = V\ell$ at its supported end.) The most heavily loaded core members are subject to forces $\pm 2V/\sqrt{3}$, depending on their inclination and the direction of the shear force, while the most heavily loaded horizontal members are subject to $2M/(\sqrt{3}L)$.

With M and V prescribed, the truss weight is to be minimized by selecting R_c , R_f and L subject to the three constraints imposed in Section 2.3 (long and short wavelength buckling and yield of the horizontal members) plus an additional two constraints: buckling and yield of the core members. The prior discussion of plastic buckling being excluded by the constraint on plastic yielding applies here as well. Now, the long and short wavelength buckling conditions for the compressed horizontal members are clearly approximate because the moment and, therefore the axial load, vary from member to member. As is customary in optimization studies, the conditions are nevertheless assumed to apply “locally”. This approach is appropriate for a slender structure with $\ell \gg L$ for which the axial forces will change by a small amount from member to member. Since the design is based on the maximum moment carried by the structure, this approach will underestimate the buckling loads and lead to a conservative design. A set of dimensionless variables different from that employed above is used: $\vec{x} \equiv (x_1, x_2, x_3) = (R_f, R_c, L)/\ell$. With this choice, $W/(w\ell^2) = 2\pi(x_1^2 + x_2^2)$ must be minimized with respect to \vec{x} subject to the five constraints

$$\begin{aligned} \frac{\sqrt{3}\pi^3}{8} \left(\frac{1}{2} + \sqrt{\frac{1}{4} + k} \right)^2 x_1^4 x_3^{-1} &\geq \Omega \\ \text{(short wavelength buckling)} \\ \frac{x_2}{x_1} &\geq -0.00313 + 2.62 \frac{x_1}{x_3} \\ \text{(long wavelength buckling)} \end{aligned}$$

$$\begin{aligned} \frac{\sqrt{3}\pi}{2} \varepsilon_Y x_1^2 x_3 &\geq \Omega \quad (\text{face sheet yielding}) \\ \frac{\sqrt{3}\pi^3}{2} x_2^4 x_3^{-2} &\geq \Omega \quad (\text{core buckling}) \\ \frac{\sqrt{3}\pi}{2} \varepsilon_Y x_2^2 &\geq \Omega \quad (\text{core yielding}) \end{aligned} \quad (7)$$

Now there are two dimensionless parameters in the problem, ε_Y and the dimensionless load combination, $\Omega = V^3/(EM^2)$. The core members are taken as clamped at the ends in evaluating their elastic buckling loads, consistent with the optimal outcome wherein the truss has face members which are more than twice as thick as the core members.

The solution to the optimization problem can be determined with a nonlinear optimization routine such as that available in the IMSL Library for numerical analysis. For $\varepsilon_Y = 0.007$, the dimensionless weight of the optimal truss is plotted against $V/(EM^2)^{1/3}$ in Fig. 4a, while the member dimensions for the optimal truss are shown in Fig. 4b, c and d. This plot spans the entire range of loading for which the truss can be regarded as being a relatively slender beam. Note that at the largest value of $V/(EM^2)^{1/3}$ shown, L/ℓ is 0.20. The constraints active over the entire range plotted are short wavelength buckling, yield of faces, and elastic buckling of the core members. The aspect ratio of the core members is such that the long

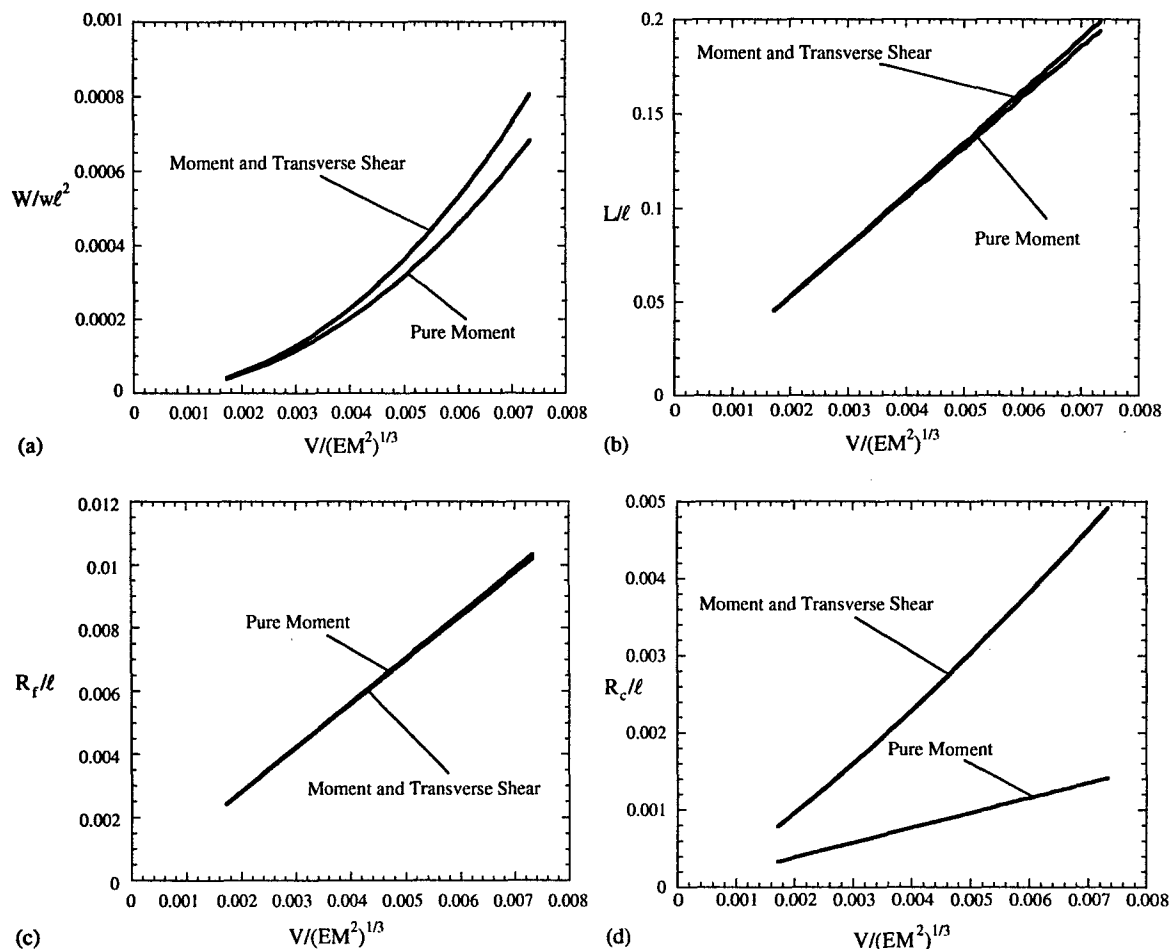


Fig. 4. Weight per unit length (a) and member dimensions (b)–(d) for optimally designed two-dimensional truss carrying moment M and shear force V for $\varepsilon_Y = 0.007$. The results for the truss designed to carry a pure moment M are also included for comparison.

wavelength buckling mode is not at issue (i.e. the left hand side of second constraint in (7) greatly exceeds the right hand side).

The dimensionless results for the pure moment problem in (6) can be re-expressed in terms of the non-dimensional variables used in (7) and in Fig. 4 as

$$\frac{W}{w\ell^2} = \Omega^{2/3} \frac{W}{w(M/E)^{2/3}} \quad (8)$$

$$(R_f, R_c, L)/\ell = \Omega^{1/3} (R_f, R_c, L)/(M/E)^{1/3}$$

In this form, V is an inessential parameter that appears in the normalization on both sides of the equations in the same manner. Thus, the results for the truss optimized under a pure moment can be directly compared with the optimal truss designed to carry both moment and transverse shear force, and that comparison is included in the several parts of Fig. 4. Even when the shear force is very small, the pure moment design always underestimates the weight of a truss designed to carry both moment and shear force, although the error in weight is not very large. More significantly, the member dimensions of the truss designed to carry only a pure moment are very different from those based on the combined load design. While the optimal dimensions for L/ℓ and R_f/ℓ are comparable for the two cases, the pure moment analysis underestimates R_c/ℓ by as much as 400% compared to the combined load analysis over the load range plotted.

The optimal values of R_c/R_f for the combined moment and transverse shear case are all well within the range where the short wave buckling mode is the lowest buckling eigenvalue, as already emphasized. A lower weight design under pure moment optimization might exist if the constraint requiring the short wavelength mode to be critical were relaxed. This would hardly be worth pursuing given that essentially any transverse load applied to the structure excludes the possibility of the long wavelength mode. Sizing the core members to carry the transverse shear ensures that they are sufficiently substantial such that the long wavelength mode does not occur. For the two-dimensional truss beam, at least, a optimal design based on a pure moment appears to lead to a structure

which is inadequate even when very small transverse shear loads are applied.

4. Optimization of sandwich plates with truss and honeycomb cores

Optimizations of sandwich plates with truss cores and with honeycomb cores have been performed previously (Wicks and Hutchinson, 2001). In this section we optimize sandwich plates with truss cores subject to bending, transverse shear, and a crushing stress, as shown in Fig. 5. A more accurate approximation for the critical buckling stress of the face sheets than that employed earlier is introduced in this paper. A similar optimization is also performed for a honeycomb core sandwich plate to provide a weight performance comparison.

As in the examples discussed above, the design focuses on uniform plates even though for specific load distributions a tapered plate might be more weight efficient. The objective in this paper is to uncover the relative performance of truss core sandwich plates relative to honeycomb construction. More efficient designs might also make use of distinct materials for the core and faces. Here, to limit the possibilities, we restrict attention to a common material with weight density w for all core members and face sheets. The tetragonal truss core is comprised of tripods whose members all have length L_c and a solid circular cross-section of

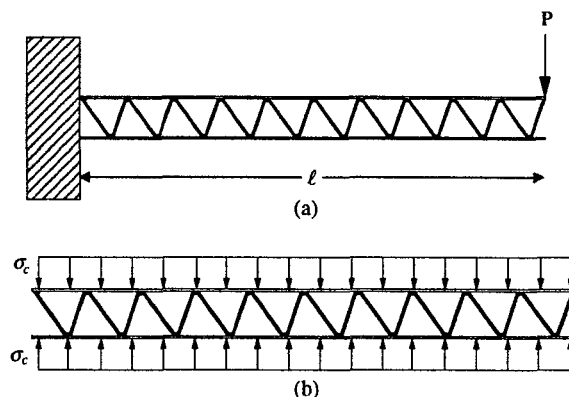


Fig. 5. Loading situation for panels under transverse loading (a) and crushing stress (b).

radius R_c . The weight per unit area of a plate with truss core and solid face sheets is

$$W = 2w \left[t_f + \frac{\pi}{\sqrt{3}} \frac{L_c R_c^2}{L_c^2 - H_c^2} \right] \quad (9)$$

with t_f as the face sheet thickness and H_c as the core thickness. Conventions for the tetragonal core structure are shown in Fig. 6a and b. The honeycomb core is a regular hexagon with height H_c (the core thickness), web thickness t_c , and web length L_c . The weight per unit area of sandwich plate with the honeycomb core is

$$W = 2w \left[t_f + \frac{H_c t_c}{\sqrt{3} L_c} \right] \quad (10)$$

where t_f is the thickness of each face sheet. The conventions for the honeycomb cores are shown in Fig. 6c.

The performance of tetragonal and honeycomb cores under shear and compression are of particular interest in sandwich plate design. Key design

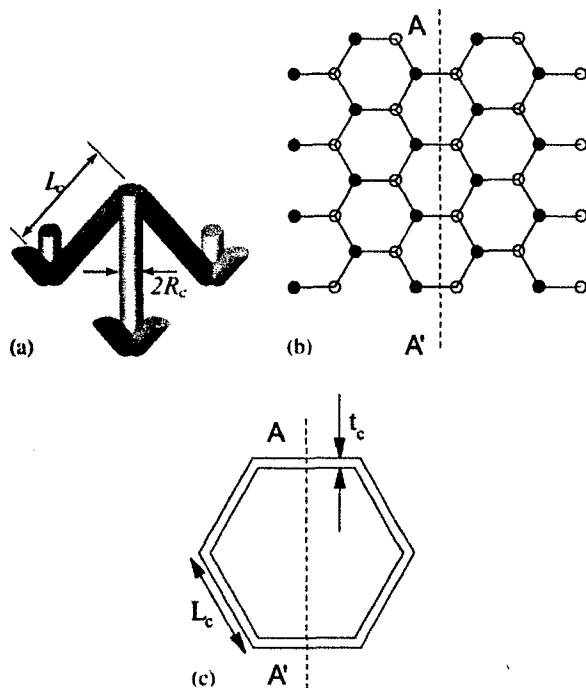


Fig. 6. Conventions for tetragonal (a)–(b) and honeycomb (c) core structures. Transverse load lines are parallel to $A - A'$. In (b) solid core nodes are at the upper face sheet, and open nodes are at the lower sheet.

properties of the two cores are the elastic shear modulus, the crushing strength (both yield and elastic buckling), and shear strength (again, both yield and elastic buckling). These properties are tabulated in Fig. 7a, expressed in terms of the relative density (ρ_c) of the core defined as the volume of core material per volume of core. The properties in Fig. 7a are for a regular tetragonal core (“regular” meaning that the distance between nearest nodes on the face sheets is the same as the core member length, or $H_c/L_c = \sqrt{2/3}$). Of particular relevance is the scaling of the elastic buckling properties of these cores. For the tetragonal core, the buckling strength scales with the core relative density squared. For the honeycomb core, the buckling strength scales with the core relative

	Tetragonal Core	Honeycomb core
Elastic shear modulus	$\bar{G} = \frac{1}{9} E \rho_c$	$\bar{G} = \frac{1}{3(1-\nu^2)} E \rho_c$
Crushing strength (plastic yield)	$\bar{\sigma} = \frac{2}{3} \sigma_Y \rho_c$	$\bar{\sigma} = \sigma_Y \rho_c$
Crushing strength (elastic buckling)	$\bar{\sigma} = \frac{\sqrt{2}\pi}{9} E \rho_c^2$	$\bar{\sigma} = \frac{\pi^2}{4(1-\nu^2)} E \rho_c^3$
Shear strength (plastic yield)	$\bar{\tau} = \frac{1}{3\sqrt{2}} \sigma_Y \rho_c$	$\bar{\tau} = \frac{2}{3\sqrt{3}} \sigma_Y \rho_c$
Shear strength (elastic buckling)	$\bar{\tau} = \frac{1}{18} E \rho_c^2$	$\bar{\tau} = \frac{\pi^2 k_t}{24(1-\nu^2)} E \rho_c^3$

(a)

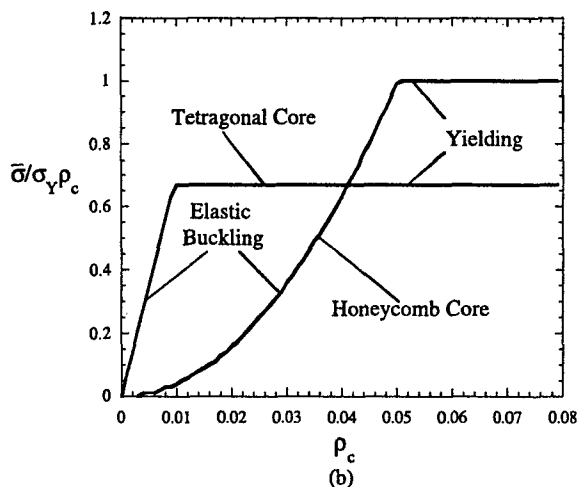


Fig. 7. Table of properties of regular tetragonal and honeycomb core sandwich panels (a). Crushing strength of regular tetragonal and honeycomb core sandwich panels as a function of relative density (b).

density cubed. To illustrate the importance of this factor, the crushing strength properties of both cores as a function of core relative density have been plotted for a representative yield strain of 0.007 in Fig. 7b. For low density cores, typical of those used in sandwich plates, the tetragonal core is significantly stronger. This observation points to the potential advantage of tetragonal core structures for use in sandwich panels.

4.1. Sandwich plate with truss or honeycomb core

The general situation envisioned is again that of a uniform, infinitely wide plate subject to a maximum moment per unit length M and a maximum transverse shear force per unit length V . Bending occurs only about the direction parallel to the loading line. A wide plate under three-point loading with force per unit length $2P$ at the center is a prototypical example. Each half of the plate carries a uniform transverse shear load per length, $V = P$, and a maximum moment per length, $M = P\ell$, at the center, where ℓ is the half-length of the plate. In this example, the maximum moment and the maximum shear transverse force are attained at the same point, but that is not essential nor to be expected. In the general situation, the ratio of the maximum moment to the maximum transverse force (both per unit length),

$$\ell \equiv \frac{M}{V}$$

defines a quantity with dimensions of length which is central in the analysis. The study is limited to relatively thin plates in the sense that the thickness, H_c , is assumed to be small compared to ℓ . Thus, L_c , the core member length, will also be small compared to ℓ .

The four constraints in the optimization under moment and transverse shear are face sheet yielding, face sheet buckling/wrinkling, core member yield, and core member buckling. In this study, a constraint on crushing strength is also included because sandwich plates optimized without this constraint tend to be susceptible to crushing. This is especially true for honeycomb core plates. Consider a plate subject to a uniform crushing stress σ_c , as shown in Fig. 5. The tetragonal core

member forces due to this crushing stress are $\sqrt{3}\sigma_c L_c d^2 / 2H_c$ where $d = \sqrt{L_c^2 - H_c^2}$.

This crushing stress adds two more strength constraints to the optimization—core member yielding and buckling under crushing stress. The six constraints are thus

$$\frac{M}{t_f H_c} \leq \sigma_Y \quad (\text{face sheet yielding})$$

$$\frac{M}{t_f H_c} \leq \frac{4E}{27(1-\nu^2)} \left(\frac{t_f}{d} \right)^2 \left(\frac{\pi}{4} + \sqrt{\left(\frac{\pi}{4} \right)^2 + \frac{9(1-\nu^2)d}{4Et_f^3}} \kappa \right)^2$$

(face sheet buckling)

$$\text{where } \kappa = \frac{\pi ER_c^4}{4\sqrt{3}L_c d} \left(12 - \frac{6d^2}{L_c^2} \right) + \frac{\pi GR_c^4}{4\sqrt{3}L_c d} \left(\frac{3d^2}{L_c^2} \right)$$

$$\frac{\sqrt{3}VdL_c}{H_c \pi R_c^2} \leq \sigma_Y \quad (\text{core member yielding})$$

$$\frac{\sqrt{3}VdL_c}{H_c \pi R_c^2} \leq \frac{\pi^2 ER_c^2}{L_c^2} \quad (\text{core member buckling})$$

$$\sigma_c \leq \frac{2\sigma_Y \pi R_c^2 H_c}{\sqrt{3}L_c d^2} \quad (\text{core member crushing yield})$$

$$\sigma_c \leq \frac{2\pi^3 ER_c^4 H_c}{\sqrt{3}L_c^3 d^2} \quad (\text{core member crushing buckle})$$

(11)

The elastic buckling stress of the compressed face sheet is associated with a sinusoidal mode varying only in the compression direction with nodes at the lines where the joints of the core tripods are attached to the face sheets. The κ factor above is used to model the rotational resistance of the core tripods on the face sheets at the nodes. This factor assumes that these tripods are clamped at the lower (tensile) face, based on the accuracy of the equivalent assumption in the earlier 2D problem (see Fig. 3b). No “long wavelength” constraint is present due to the results of the earlier 2D problem—the other core constraints (core yield and buckling) size the core members such that the long wavelength modes are suppressed. These buckling constraints for the core members are valid for members assumed to be clamped at the face sheets.

The weight per unit area and constraints are written in dimensionless form using $\ell = M/V$ and the four design variables $\vec{x} = (t_f/\ell, R_c/\ell, H_c/\ell, d/\ell)$.

The normalized weight per unit area, $W/w\ell$, and the six dimensionless constraints involve only the parameters: σ_Y/E (taken as 0.007 in the calculations), ν (taken as 1/3 in the calculations), V/\sqrt{EM} , and the normalized crushing strength, σ_c/σ_Y . The solution to this optimization problem was again found using an IMSL subroutine. The details of the honeycomb core analysis can be found in the earlier study on this topic (Wicks and Hutchinson, 2001).

4.2. Optimization with no constraint on the crushing stress

The fully optimized (minimum weight) results for these structures in the absence of any constraint on crushing stress is shown in Fig. 8a. The plots are terminated at $V/\sqrt{EM} \cong 0.0018$, as larger values of V/\sqrt{EM} generate plates that would not be considered thin, and thus the range of V/\sqrt{EM} for which the results have been presented comprise the full range of relevance. The estimate of the face sheet buckling condition for the tetragonal truss core is more accurate than in the earlier study (Wicks and Hutchinson, 2001). However, there is little difference between the earlier results and those presented here. As before, the full honeycomb optimization results in plate thickness H_c of more than 0.10ℓ which is unrealistically thick. Here optimal results are shown both for the case where H_c/ℓ for the honeycomb core is constrained to be less than 0.10 and where H_c/ℓ is constrained to be identical to that of the optimal tetragonal core structure at the same V/\sqrt{EM} . Thus, with no crushing stress, the optimal honeycomb core structure is the lighter weight design, over the entire range of transverse shear load parameter, although the relative advantage is not large especially when the two cores have the same thickness.

In Fig. 8b the crushing strength of these optimal structures are plotted. Clearly the optimal tetragonal core structure is far superior in this regard. Indeed, it is seen that the honeycomb core is unusually vulnerable to crushing. The superiority of the tetragonal core is due to two effects—its inherent advantage at low densities, as illustrated in Fig. 7b and the fact that the optimal tetragonal

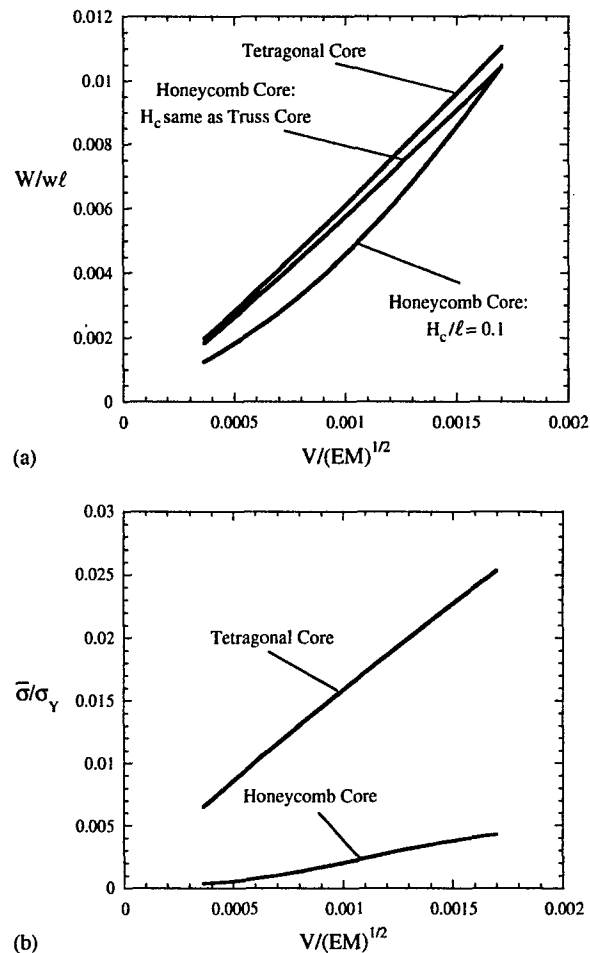


Fig. 8. Normalized weight per unit area of optimized tetragonal and honeycomb core sandwich panels subject to transverse shear and moment (a). Two cases of honeycomb panels have been considered: the core thickness fixed at $H_c/\ell = 0.1$; and the core thickness taken equal to that of the sandwich plate with truss core at the same value of V/\sqrt{EM} . Crushing strength of the optimized tetragonal and honeycomb core structures (b). The honeycomb panel results are for the core thickness fixed at $H_c/\ell = 0.1$ ($\varepsilon_Y = 0.007$).

core plate has somewhat higher core density than the optimized honeycomb core plate.

4.3. Optimization with a crushing stress constraint

To illustrate the effect of the crushing stress constraints, the optimization was run at a mid-range load combination corresponding to $V/\sqrt{EM} = 0.001$, over a range of crushing stress from

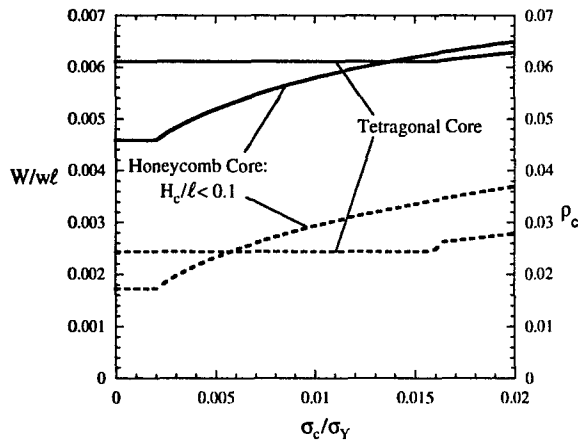


Fig. 9. Top solid lines are minimum weights for tetragonal and honeycomb core structures subject to crushing stress as well as normalized transverse load value $V/\sqrt{EM} = 0.001$. Bottom dashed lines are the core relative densities for these optimized structures ($\varepsilon_Y = 0.007$).

0% to 2% of the material yield stress, σ_Y . The results from this optimization are shown in Fig. 9. Both the minimum weight and the core relative densities are plotted. At the higher values of prescribed crushing stress (above about 1.4% of the material yield stress), the optimized tetragonal core is the lighter of the two structures. The honeycomb structure has a higher core density at the higher levels of crushing stress in order to counteract its inferior crushing resistance properties.

For the tetragonal core structures, face member yield and buckle are active constraints throughout the load range plotted. At low values of crushing stress (below about 1.5% of the yield stress), core member buckle (from the transverse loads) is an active constraint. At higher values of crushing stress, core member crush buckling becomes active. The core members of the optimized tetragonal core have $H_c > \sqrt{2/3}L_c$ corresponding to members oriented closer to the perpendicular to the face sheet than is the case for a regular tetrahedron. This orientation increases both the crushing strength of the core and the ability of the core to resist face sheet buckling (by decreasing the wavelength of the buckle).

The full honeycomb optimization results in plate thickness H_c of more than 0.10ℓ over the low end of the loading range. This is not a thin plate

and such a design would most likely not be considered in an application. In order to make a meaningful comparison between the plates with honeycomb and truss cores, H_c/ℓ for the honeycomb was constrained to be less than 0.10 over the entire optimization. With no crushing stress, the active constraints for the honeycomb plate are face yield, face buckle, and core web buckle. Above low levels of crushing stress (as low as 0.2% of the yield stress), the active constraints switch to face yield and core member crush buckling. These constraints remain active throughout the higher crushing stress levels shown in Fig. 9.

One final optimization comparison is shown in Fig. 10. In this example, the crushing stress is fixed at 2% of the yield stress of the material, while the V/\sqrt{EM} load combination varies over the same range previously plotted. In the presence of this crushing stress, the optimal tetragonal core structure is actually lighter than the optimal honeycomb core structure over the entire range plotted, although the difference between the weights of the two designs is small. A design constraint requiring a crushing strength of 2% of the base material yield stress is not unreasonable. Constraints for certain applications might dictate even larger crushing strengths.

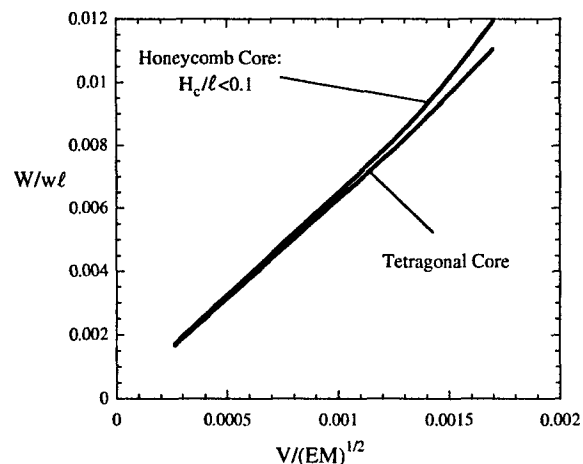


Fig. 10. Normalized weight per unit area of optimized tetragonal and honeycomb core sandwich panels subject to a crushing stress of $\sigma_c/\sigma_Y = 0.02$, as well as transverse shear and moment. Here the honeycomb core thickness has been constrained such that $H_c/\ell \leq 0.1$ ($\varepsilon_Y = 0.007$).

5. Conclusions

Truss core construction appears to be as efficient as honeycomb core construction for sandwich plates optimally designed to carry prescribed combinations of moment and transverse force when a realistic minimum crushing strength is imposed. If the constraint on the crushing strength is relaxed, optimized honeycomb core plates have a slight weight advantage, but their crushing strength is exceptionally low. By contrast, the truss core has an inherent crushing advantage at the low core densities typical of most sandwich plate designs. It is this advantage that wins the day when a design constraint on crushing strength becomes important. Given the very close competition between the two methods of construction from a weight perspective, the advantage outcome is likely to hinge on other issues such as ease of manufacture, vulnerability to delamination or moisture, and multi-functional capabilities. In each of these categories, truss core sandwich construction has distinct possibilities that may tilt the advantage in its favor.

Acknowledgements

This work was supported in part by the Office of Naval Research and in part by the Division of Engineering and Applied Sciences, Harvard University. Nathan Wicks acknowledges the fellowship support of the National Defense Science and Engineering Graduate Fellowship Program.

Appendix A. Bifurcation buckling analysis of the planar truss under pure moment

Fig. 11 shows the unit cell for the finite difference analysis. In the j th cell, there are two types of nodes and four types of members. The force and displacement quantities are expanded in perturbation series about the pre-buckling state in the usual way i.e. $N_j^3 = -P + \xi \tilde{N}_j^3 + \dots$, $N_j^4 = P + \xi \tilde{N}_j^4 + \dots$, $w_j^k = \xi \tilde{w}_j^k + \dots$, etc. The six equations of perturbed nodal equilibrium (force balance in two directions and moment balance, at each node type) can then be written in matrix form:

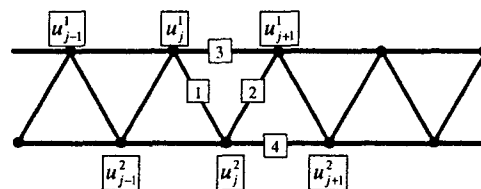


Fig. 11. Unit cell for exact 2D finite difference buckling analysis.

$$K_{ij}F_j = 0$$

where \vec{F} is a vector of the 22 force-like quantities which enter into the perturbed equilibrium equations. (N_j^k , V_j^k , M_j^k are the axial force, shear force, and moment respectively in the k th member of the j th unit and u_j^k , w_j^k , θ_j^k are the displacements and rotation of the k th type node of the j th unit.) Thus, K is a 6 by 22 matrix.

Treating each member as a beam column, the force quantities are related to the displacement components and rotations at the ends of the members:

$$F_i = B_{ij}U_j$$

where \vec{U} is a vector of the 18 displacements and rotations at the j th joints and the joints adjacent to these joints. B is a 22 by 18 matrix relating these quantities. These relations for a beam of length L with a compressive axial force P are:

$$N(0) = N(L) = -\frac{EA}{L}[u(L) - u(0)]$$

$$M(0) = -\frac{2EI}{L} \left[2C_{10}\theta(0) + C_{20}\theta(L) - \frac{3C_{30}}{L}(w(L) - w(0)) \right]$$

$$M(L) = \frac{2EI}{L} \left[2C_{10}\theta(L) + C_{20}\theta(0) - \frac{3C_{30}}{L}(w(L) - w(0)) \right]$$

$$V(0) = V(L)$$

$$= \frac{6EI}{L^2} \left[C_{30}(\theta(0) + \theta(L)) - \frac{2C_{40}}{L}(w(L) - w(0)) \right]$$

where A is the member cross-sectional area and C_{10} , C_{20} , C_{30} , and C_{40} are the stability functions (Bleich, 1952) defined as:

$$C_{10} = \frac{\bar{P}(\sin \bar{P} - \bar{P} \cos \bar{P})}{4(2 - 2 \cos \bar{P} - \bar{P} \sin \bar{P})}$$

$$C_{30} = \frac{\bar{P}^2(1 - \cos \bar{P})}{6(2 - 2 \cos \bar{P} - \bar{P} \sin \bar{P})}$$

$$C_{20} = \frac{\bar{P}(\bar{P} - \sin \bar{P})}{2(2 - 2 \cos \bar{P} - \bar{P} \sin \bar{P})}$$

$$C_{40} = \frac{\bar{P}^3 \sin \bar{P}}{12(2 - 2 \cos \bar{P} - \bar{P} \sin \bar{P})}$$

where $\bar{P} = (PL^2/EI)^{1/2}$ is the dimensionless load parameter used in the beam analysis. These relations can be analytically continued to cases with tensile or zero axial load.

Solutions are assumed of the periodic form $u_j^1 = e^{i\mu j} C_1$, $w_j^1 = e^{i\mu j} C_2$, etc. Displacement quantities are then expressed as:

$$U_k = e^{i\mu j} D_{km} C_m$$

where the C_m are six complex constants that determine the buckling mode. The set of equilibrium equations can then be written:

$$K_{ij} B_{jk} D_{km} C_m = 0$$

In order to find bifurcation solutions, the matrix $K_{ij} B_{jk} D_{km}$ must be singular. In dimensionless form, this matrix is a function of the dimensionless quantities μ , R_f/L , R_c/L , and M/EL^3 . Physically, these quantities are the wave-number of the peri-

odic solution, the slenderness ratios of the horizontal and core members, and the dimensionless buckling moment (the eigenvalue of the system).

Computations were performed to calculate the lowest eigenvalue (M/EL^3) for a given set of (μ , R_f/L , R_c/L). The determinant of the matrix is non-negative, dropping to zero at the eigenvalues and then increasing again. This is due to the fact that in this complex formulation the eigenvalues are double-roots. In the numerical computations, the eigenvalues were found by looking for zero-crossings of the derivative of the matrix determinant.

References

- Bleich, F., 1952. Buckling Strength of Metal Structures. McGraw-Hill, New York. pp. 210–211.
- Brittain, S., Sugimura, Y., Schueller, O.J.A., Evans, A.G., Whitesides, G.M., 2001. Fabrication and mechanical performance of a mesoscale, space-filling truss system. *JMEMS* 10, 113–120.
- Evans, A.G., Hutchinson, J.W., Fleck, N.A., Ashby, M.F., Wadley, H.N.G., 2001. The topological design of multifunctional cellular metals. *Progress in Materials Science* 46, 309–327.
- Wicks, N., Hutchinson, J.W., 2001. Optimal truss plates. *International Journal of Solids and Structures* 38, 5165–5183.

**Part VI: Sandwich plates actuated by a
kagome planar truss**

Sandwich Plates Actuated by a Kagome Planar Truss

N. Wicks

J. W. Hutchinson

Division of Engineering and Applied Sciences,
Harvard University,
Cambridge, MA 02138

Kagome truss plates have properties that suggest they should be uniquely effective as an actuation plane for sandwich plates: a Kagome truss plate has in-plane isotropy, optimal stiffness and strength, and its truss members can be actuated with minimal internal resistance. In this paper, sandwich plates are studied that are comprised of one solid face sheet and one actuated Kagome face sheet joined by a pyramidal truss core. Various aspects of the actuation behavior of these plates are investigated, including internal resistance and strains resulting from actuation and efficiency of actuation. Single and double curvature actuation modes are investigated. Contact is made with analytic results for actuation modes with long wavelength. [DOI: 10.1115/1.1778720]

1 Introduction

Recent studies of planar trusses based on the ancient Kagome basket weave pattern have shown that these truss plates have many properties that make them desirable for actuation planes of sandwich plates, [1,2]. In this study, we begin by analyzing the actuation characteristics of a single Kagome truss plate (Fig. 1) and follow with an actuation analysis of a sandwich plate comprised of one solid face sheet and one actuated Kagome face sheet joined by a pyramidal truss core (Fig. 2).

The single Kagome truss plate can be constructed from the unit cell shown in Fig. 1(b). The 120 deg symmetry of the structure ensures in-plane elastic isotropy assuming all the truss members are identical. Here, only solid circular members are considered, of length L and radius R . The Kagome-backed solid skin plate can be constructed from the unit cell depicted in Fig. 2(c). In the present study we limit consideration to plates with identical solid circular truss members of length L and radius R both for the Kagome face and the core. The solid skin thickness is denoted by t . In addition, to further limit the number of parameters in the system, we consider only plates in which both face sheets and the core members are constructed of the same material with Young's modulus E , Poisson's ratio ν and yield stress σ_Y . The Kagome-backed sandwich plate in Fig. 2 has isotropic bending and stretching stiffness.

The feature of the planar Kagome truss in Fig. 1 that makes it most advantageous for actuation is the ability to actuate members to achieve arbitrary in-plane nodal displacements with minimal internal resistance. Among infinite isotropic planar truss structures, a pin jointed planar Kagome truss is optimally stiff and strong to overall stressing. Although it has kinematic mechanisms, it is nevertheless able to carry arbitrary states of overall stress. Members of a pin jointed Kagome truss can be actuated (i.e., elongated or shortened) with no internal resistance, or equivalently, with no redundant stresses. When joints are welded, as will be assumed throughout this paper, actuation of a member does encounter internal resistance, but minimally so as will be shown. Welded joints also suppress the kinematic mechanisms and result in a structure with substantial in-plane buckling resistance. These and other aspects of the Kagome structure are explored elsewhere, [1–5].

In this study, we aim to explore the details of actuation of the planar Kagome truss and the Kagome-backed sandwich plate.

Contributed by the Applied Mechanics Division of THE AMERICAN SOCIETY OF MECHANICAL ENGINEERS for publication in the ASME JOURNAL OF APPLIED MECHANICS. Manuscript received by the ASME Applied Mechanics Division, October 15, 2003; final revision, January 14, 2004. Associate Editor: R. M. McMeeking. Discussion on the paper should be addressed to the Editor, Prof. Robert M. McMeeking, Journal of Applied Mechanics, Department of Mechanical and Environmental Engineering, University of California–Santa Barbara, Santa Barbara, CA 93106-5070, and will be accepted until four months after final publication of the paper itself in the ASME JOURNAL OF APPLIED MECHANICS.

Simulations of various periodic actuation modes of these infinite Kagome structures have been performed for a range of member aspect ratios. In its most general form, the approach is numerical. A calculation requires the formulation of a “super element” representing a unit cell followed by the assembly of the complete structure as a union of the super elements. The scaling of the energy required for actuating the unloaded structure with aspect ratio of the truss members is investigated. Bending and stretching strains in the members induced by actuation are also determined. For actuation modes with wavelengths long compared to the member length, the response computed with the numerical approach is compared to actuation predicted by an analytical long wavelength approximation outlined in a previous study, [1].

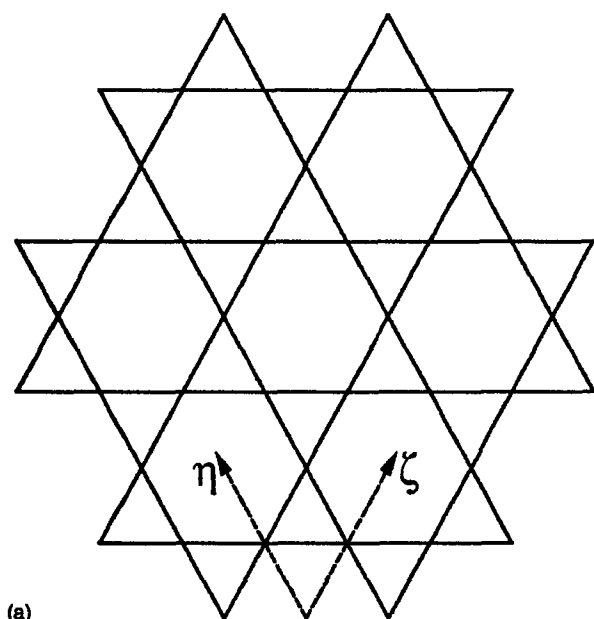
2 Planar Kagome Structure

2.1 The Planar Kagome Structure. Consider the infinite planar Kagome structure shown in Fig. 1(a) having members of length L and solid circular cross-sections of radius R and undergoing in-plane displacements. The unit cell of such a structure is shown in Fig. 1(b). The members are modeled as Euler-Bernoulli beams, with clamped conditions at each node representing welded joints (i.e., the displacement and rotational degrees-of-freedom are the same for all beams meeting at a given node). Actuation of any member comprises an elongation or contraction of the member by a strain e if the member were unconstrained. In other words, the actuation strain e is equivalent to a stress-free transformation strain.

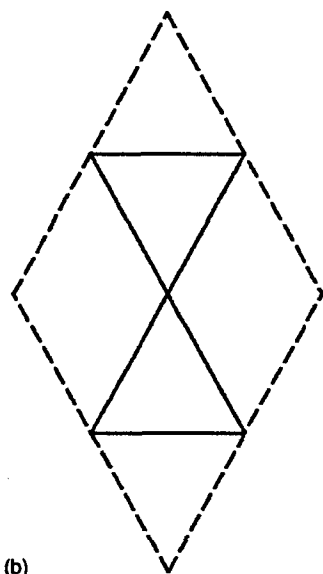
2.2 Actuation Methodology. The actuation of beam members is modeled via the so-called cut-stress-reweld scheme employed by Eshelby in his study of the transformation strains in ellipsoidal inclusions, [6]. To actuate a given member, envision the following steps:

1. Remove the actuating member from the structure.
2. Allow the member to actuate (elongate or contract) freely by strain e .
3. Place equal and opposite forces $-E\pi R^2 e$ on the ends of the member to deform it back to its original configuration.
4. Place the member back into the structure and “weld” it in place.
5. Release the forces from the ends of the member by applying equal and opposite forces $E\pi R^2 e$ to the joints at the member ends.

Thus, the cut-stress-reweld procedure is equivalent to analyzing the complete truss subject to equal and opposite actuation forces of magnitude $E\pi R^2 e$ applied to the joints at the ends of the respective member.



(a)



(b)

Fig. 1 (a) The Kagome planar truss. (b) The unit cell used for the Kagome planar truss analysis. The dashed lines are the outline of the cell. The solid lines are truss members of the unit cell.

2.3 Enforcement of Periodicity. Our goal is to simulate periodic actuations of an infinite structure by modeling the behavior of just one periodic cell subject to periodic boundary conditions. Consider the potential energy functional for a periodic cell:

$$\Phi = \frac{1}{2} K_{ij} u_i u_j - k_j^0 u_j \quad (1)$$

where K is the conventional stiffness matrix of the structure, u is the vector of displacements and rotations at the nodes of the structure, and k^0 is the vector of applied nodal forces and moments (in this situation these correspond to the virtual actuation forces described earlier). If the structure were isolated and unconstrained

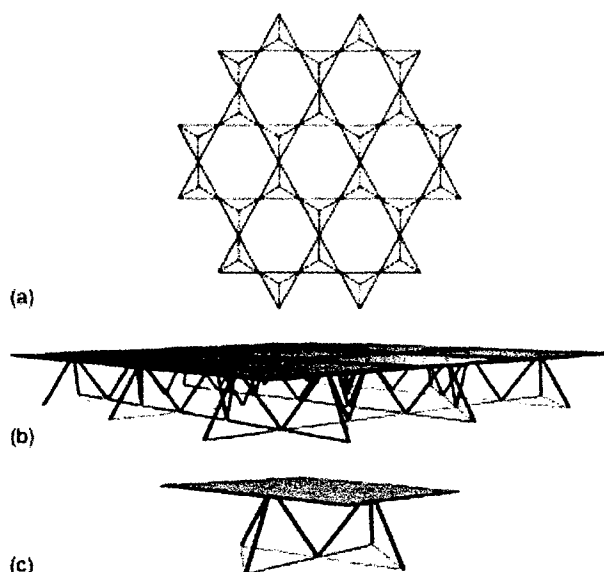


Fig. 2 (a) The Kagome plane and tetrahedral core of the Kagome plate structure. The solid members are the Kagome face members, and the dashed members the tetrahedral core members. (b) The Kagome plate structure. (c) The unit cell used for the Kagome plate analysis.

(apart from rigid-body motion), the problem would be solved in the usual manner by solving the system of equations represented by

$$K_{ij} u_j = k_i^0 \quad (2)$$

Now consider periodic boundary conditions represented by constraints of the form

$$a_{ij} u_j = 0 \quad (3)$$

The details of the actual periodic boundary conditions imposed for in-plane nodal displacements and rotations are included in the Appendix. It is important to note that once the appropriate periodic boundary conditions are imposed on the *displacements/rotations*, periodicity of *forces/moments* is satisfied by the solution. For the periodic cell in Fig. 3, the forces acting on a node along one edge of the periodic cell (corresponding to internal forces in the structure) will be equal and opposite to those acting on the equivalent node on the opposite edge, for a displacement field which satisfies the periodic conditions outlined in the Appendix. The displacements themselves are not, in general, periodic—we consider, for example, a displacement field corresponding to a constant strain. Thus, there are some cases for which the strains, forces and moments, will be periodic, but not the displacements.

To impose these additional conditions, Lagrangian multipliers are employed. The modified energy functional now takes the form:

$$\Phi = \frac{1}{2} K_{ij} u_i u_j - k_j^0 u_j - \lambda_i a_{ij} u_j \quad (4)$$

The systems of equations resulting from minimization of the energy functional with respect to displacements u_i and the Lagrangian multipliers λ_i are

$$K_{ij} u_j = k_i^0 + \lambda_j a_{ji} \quad (5)$$

$$a_{ij} u_j = 0 \quad (6)$$

Now consider periodic actuations of the infinite structure. The actuation forces exert no net force or moment on the structure.

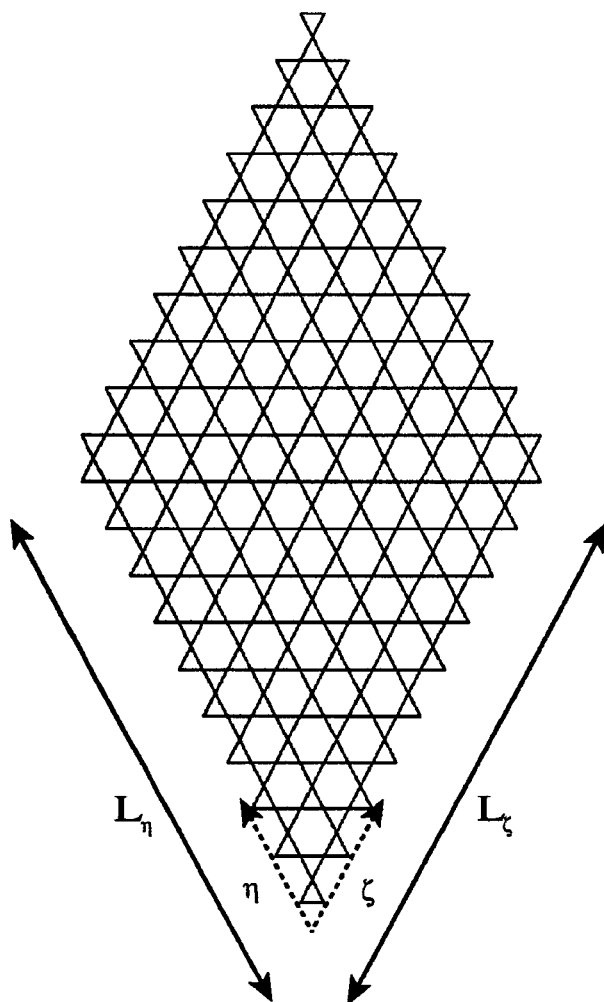


Fig. 3 The periodic cell used for the planar Kagome truss simulations

This means that if the energy functional given by (4) above is minimized over the periodic cell, the energy of the infinite structure is also minimized. Thus, it is possible to simulate the behavior of the infinite structure by modeling just the periodic cell with the appropriate boundary conditions.

2.4 Calculation of Actuators. The objective is to probe how effectively the planar Kagome structure can achieve arbitrary in-plane deformations through actuation of its members. To this end, periodic actuation of the structure is simulated as described in previous sections for actuation of each member in the periodic cell, tracking the nodal displacements in a matrix of influence coefficients, A . The ij th component of this matrix is the i th displacement resulting from the actuation of the j th member. To generate this matrix, displacements are calculated at each of the nodes in the periodic cell resulting from a unit actuation of each member in that cell.

As this simulation is linear, once the matrix of influence coefficients, A , has been constructed, the displacements of the nodes from actuation of any combination of members is easily computed as

$$u_i = A_{ij} e_j \quad (7)$$

where e is a vector of member actuators.

Now consider a target field of in-plane nodal displacements u^d . The aim is to determine how well this field can be recreated by actuating members of the Kagome structure. Calculate elongations \tilde{e} and displacements \tilde{u} via the relations:

$$\tilde{e}_i = A_{ij}^+ u_j^d \quad (8)$$

$$\tilde{u}_i = A_{ij} \tilde{e}_j \quad (9)$$

where A^+ is the Moore-Penrose generalized inverse of A , also called the pseudo-inverse of A , [7]. Then, \tilde{e} is the vector of member actuators which minimize the squared error between \tilde{u} and u^d . If there exist multiple vectors of actuators that minimize this squared error, \tilde{e} is such a vector of minimal length (i.e., $|\tilde{e}|$ is minimized).

2.5 Example Target Displacement Fields. The simulations outlined above were run for several target displacement fields. The objective is to assess the ability of the structure to achieve specific actuators and to determine the associated energy required and stresses induced. The periodic cell used for these simulations is shown in Fig. 3. It contains a total of 100 unit cells. The axes used for describing the displacements fields described here are the ζ -axis and the η -axis shown in Fig. 3. It is important to note that the target displacement fields are all consistent with the periodic displacement boundary conditions.

The first target displacement field is described by

$$u^d = A_0 e_\zeta \sin\left(\frac{\pi \zeta}{L_\zeta}\right) \quad (10)$$

Here, A_0 is an amplitude factor, e_ζ is a unit vector aligned with the ζ -axis, and L_ζ the length of the periodic cell in the ζ -direction. This target field is a displacement in the ζ -direction that is everywhere positive except along the edges $\zeta=0$ and $\zeta=L_\zeta$ of the periodic cell where it is zero and reaches a maximum of $A_0 e_\zeta$ along the line $\zeta=L_\zeta/2$ of each periodic cell. In this case, the displacement field is repeated in every periodic cell. This target field is depicted in Fig. 4. The Moore-Penrose best-fit actuators for this displacement field are calculated as described above. For this periodic cell, the number of nodal displacements in the target field is 640, while the number of members actuated is 600. One would expect some error between the target and achievable fields, however the actual displacements differ from the target displacements by less than 1% of the maximum target displacement. The actuators are quite close to the actuators predicted by the long wavelength approximation outlined in previous work, [1]. In this long wavelength theory, the actuation strain, ϵ^T , of a member connecting neighboring nodes I and J is $\epsilon^T = (u_\alpha^d(x^I) - u_\alpha^d(x^J)) t_\alpha / L$ where t_α is the unit vector parallel to the member and directed from J to I and u_α is the displacement derived from the target displacement field.

A second target displacement field is described by:

$$u^d = A_0 (e_\zeta + e_\eta) \sin\left(\frac{\pi \zeta}{L_\zeta}\right) \sin\left(\frac{\pi \eta}{L_\eta}\right) \quad (11)$$

Here, e_η is a unit vector aligned with the η -axis and L_η the length of the unit cell in the η direction. This displacement is zero along all of the edges of the periodic cell and reaches a maximum of $A_0 (e_\zeta + e_\eta)$ at the center ($\eta=L_\eta/2, \zeta=L_\zeta/2$) of each periodic cell. The target displacement field can be seen in Fig. 5. The Moore-Penrose best-fit actuators are predicted quite well by the long wavelength approximation. In this example, the maximum discrepancy between the actual displacements of the nodes and the target displacements is less than 2% of the maximum target displacement. For simulations run for a target displacement field in the same direction, but with a wavelength half of that of (11) (in both the ζ and η directions), this maximum discrepancy is less than 10^{-7} . The critical difference between the two sets of target displacement fields is that the field described by (11) with the full wavelength has a jump in slope across the boundaries between

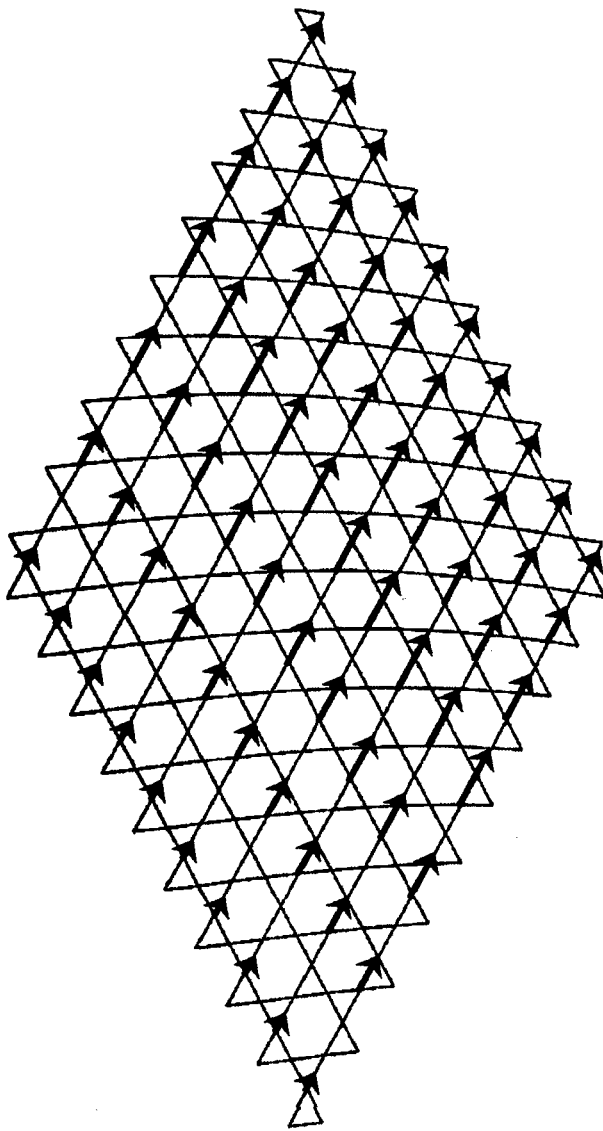


Fig. 4 The target field described by $u^d = A_0 e_\zeta \sin(\pi \eta / L_\eta)$. The arrows show the displacement vectors of the nodes.

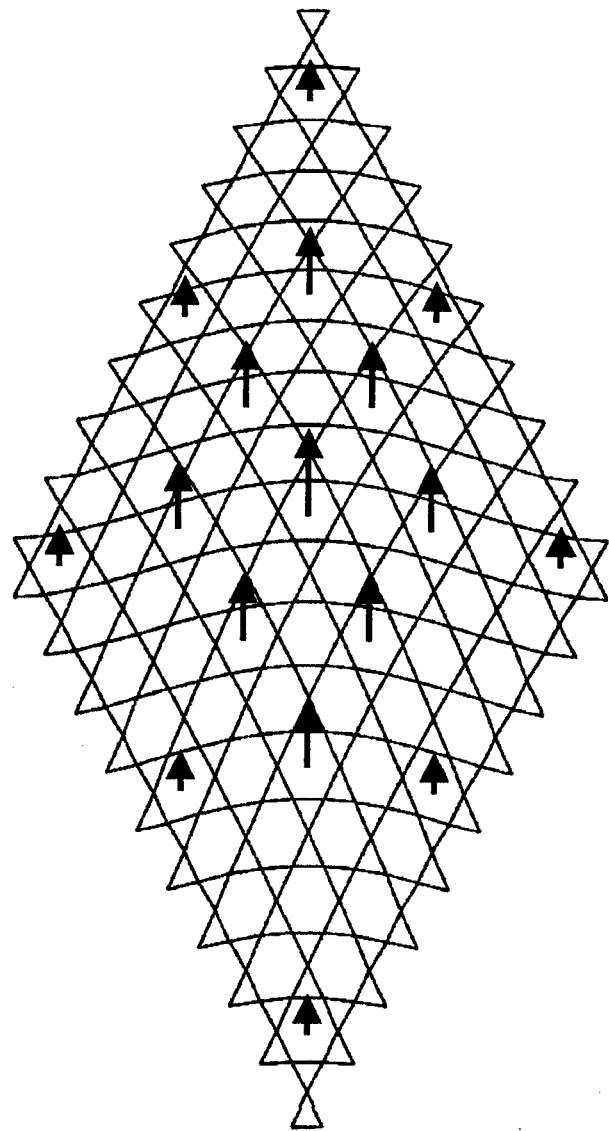


Fig. 5 The target displacement field described by $u^d = A_0 (e_\zeta + e_\eta) \sin(\pi \zeta / L_\zeta) \sin(\pi \eta / L_\eta)$. The arrows show the displacement vectors of the nodes.

periodic cells (and, as a result, a jump in actuation). For the displacement field with the half-wavelength, the slope of displacement is continuous across periodic cell boundaries.

A final target displacement field of interest is described by

$$u_d = A_0 \zeta e_\zeta. \quad (12)$$

This corresponds to a constant strain of A_0 in the ζ direction. This field is shown in Fig. 6. In this example, the actual displacements of the nodes match the target displacements almost perfectly—the maximum discrepancy is less than 10^{-7} of the maximum target displacement. Note that for this displacement field, the slope of displacement is again continuous across periodic cell boundaries.

2.6 Actuation of Selected Kagome Members. In practical applications it will generally be desirable to manufacture structures in which only a small subset of the members will be actuated. The Moore-Penrose actuation scheme can be applied in a similar manner in such cases. This procedure is outlined in Section 4.4 for the Kagome plate structure. Given a restriction on the number of members to be actuated, systematic procedures for

identifying the “best” subset of actuation members remain to be established. The behavior of planar Kagome structures with limited numbers of actuation members will be considered in subsequent work.

3 Energy of Actuation of Planar Kagome Structure

3.1 Energy of Actuation. One of the motivations behind the selection of the Kagome structure for actuation is the desire to find a structure that can be actuated with minimal internal resistance to actuation. Here, we present the total strain energy stored in the planar Kagome structure actuated to achieve the target displacement fields described above. In the limit of a pin-jointed Kagome structure, actuations can be achieved with no internal resistance, although mechanisms will also exist, [1]. For the Kagome structures considered here, simulated with Euler-Bernoulli beams welded together at their ends, the energy of actuation is expected to be due primarily to elastic bending of the beams.

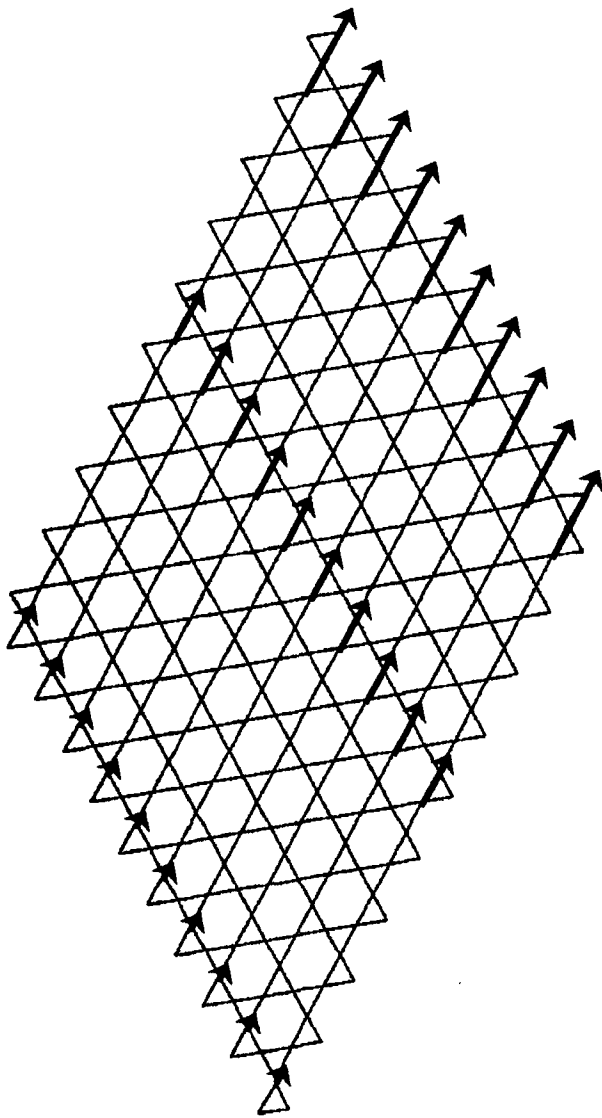


Fig. 6 The target displacement field described by $u_d = A_0 \zeta e_\zeta$

The strain energy of actuation is calculated in a straightforward manner depicted in Fig. 7. Consider an actuating member of length L , cross-sectional area A , and Young's modulus E . The imposed actuation strain of ϵ^T is the strain the member would undergo if the member were free to actuate (if the structure offered no resistance). As the structure will have some resistance to the actuation, the member will undergo some elastic strain that we denote ϵ^e . The axial force F experienced by the member is then easily calculated as $F = \epsilon^e EA$. The work done by the actuator (acting on the structure) is the work of this axial force acting through the actuation strain ϵ^T , $-1/2 \epsilon^e \epsilon^T EAL$, and it is stored as elastic strain energy in the structure.

3.2 Reference Energy. Now consider the work done by the same actuator, undergoing the same actuation strain ϵ^T , but in this case consider the structure to be rigid—that is, consider a structure that will completely resist the actuation. This corresponds to fixing both ends of the member as it is actuated. In this situation, the total strain of the member is zero, so $\epsilon^e + \epsilon^T = 0$. The energy

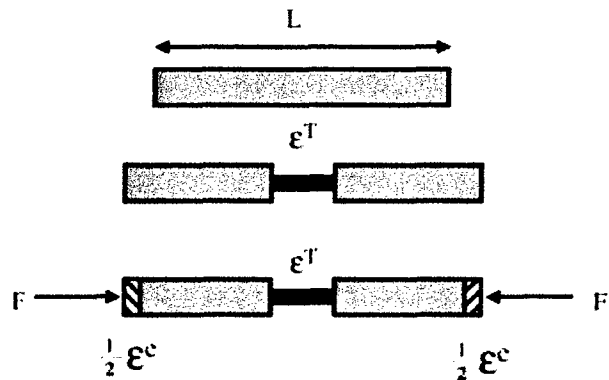


Fig. 7 The energy of actuation of a beam. The rest of the structure resists the imposed actuation strain ϵ^T , generating an elastic strain of ϵ^e and an internal force $F = \epsilon^e EA$.

of actuation in this case is therefore $1/2(\epsilon^T)^2 EAL$, and this is chosen as the reference energy for each member in the energy calculations and comparisons below.

Actuation of multiple members does not pose any energy accounting difficulties—the total energy of actuation can be calculated by adding up the contributions from each individual member, with the elastic strain of each member calculated in response to all the actuations. In some circumstances, the work done by an individual member may be negative—the actuations of other members may result in the structure actually assisting, not resisting, an actuation. However, the overall energy of actuation will of course always be positive. Thus, the relevant energy ratio calculated for energy comparisons is

$$\hat{W} = \frac{\sum_{i=1}^{\text{#members}} -\frac{1}{2} \epsilon_i^e \epsilon_i^T E_i A_i L_i}{\sum_{i=1}^{\text{#members}} \frac{1}{2} (\epsilon_i^T)^2 E_i A_i L_i} \quad (13)$$

This energy ratio \hat{W} is plotted for several slenderness ratios in Fig. 8 for the target displacement fields shown above. For a structure with energy storage dominated by bending energy, \hat{W} can be

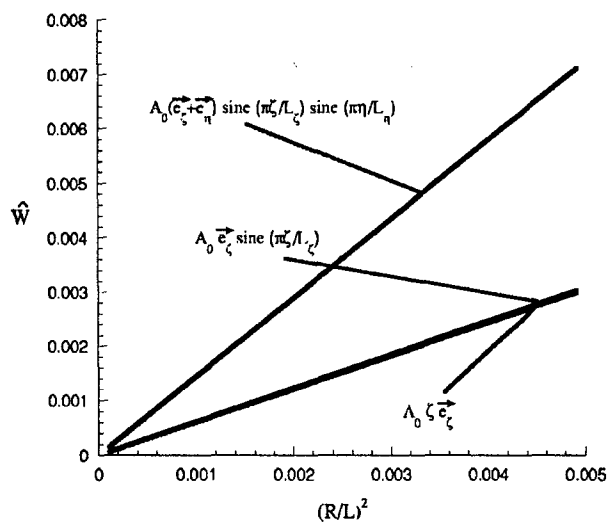


Fig. 8 Normalized actuation energy for the target displacement fields, as a function of $(R/L)^2$

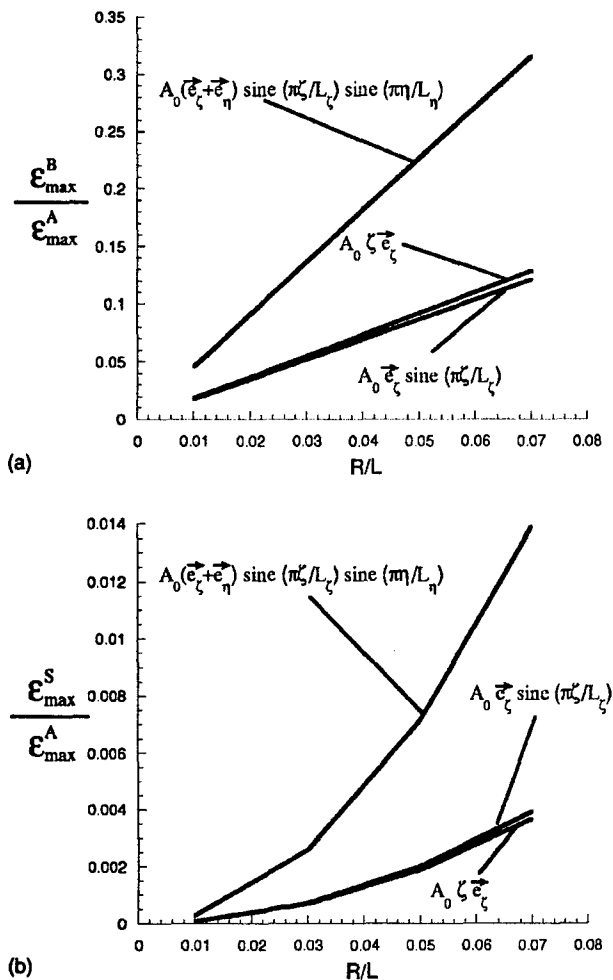


Fig. 9 (a) Maximum bending strain normalized by maximum actuation strain for the target displacement fields, as a function of R/L . (b) Maximum stretching strain normalized by maximum actuation strain for the target displacement fields, as a function of R/L .

shown to scale with the slenderness ratio squared, $(R/L)^2$, while for a statically overdetermined structure, such as a fully triangulated sheet, \hat{W} is expected to be of order unity, independent of the slenderness ratio and whether pin jointed or weld jointed. The energy associated with actuation of the Kagome structure is clearly much smaller than that energy of a fully triangulated truss grid. The energy associated with actuation of an isolated beam in a Kagome structure is investigated in work by Wicks and Guest [5]. For such actuations, \hat{W} scales linearly with slenderness, with energy equally partitioned between stretching and bending. However, for the target fields considered here, \hat{W} clearly scales as the square of the slenderness.

3.3 Strain Levels Induced by Actuation. As the structures will generally undergo cyclic actuations, investigation of strain levels for fatigue design is also required. One quantity of interest is the maximum stretching strain occurring in the structure divided by the maximum actuation strain. For a bending controlled structure, this ratio is also expected to scale with slenderness ratio squared. Of more interest is the ratio of maximum bending strain to maximum actuation strain—which is expected to scale linearly with the slenderness ratio for bending controlled structures. These trends are seen to hold in Fig. 9 where the normalized maximum

bending and stretching strains are plotted as a function of slenderness ratio for the target displacement fields described above. The maximum actuation strain, ϵ_{\max}^A , is used to normalize the induced bending and stretching strains. The relatively larger bending strains will restrict the levels of actuation due to fatigue.

4 Kagome Plate Structure

4.1 The Kagome Plate Structure. Consider a solid face sheet of thickness t , backed by a planar Kagome structure. Core members attach to the face sheet and Kagome plane to form tetrahedral units, as shown in Fig. 2. The Kagome planar members and the core members have solid circular cross sections of radius R and are all of the same length L . As a result, the core thickness is $H_c = \sqrt{273}L$. While in some applications it may be desirable to use solid face sheets and Kagome planar sheets of different materials, for the purposes of this study we restrict the structure to be of one single isotropic material of Young's Modulus E and with a Poisson's ratio of $\nu = 1/3$. The unit cell used in this analysis is shown in Fig. 2(c).

The stiffness matrix of the unit cell (Fig. 2(c)) of the Kagome plate structure is simulated through the use of a composite element comprised of beam and shell elements. We model the Kagome planar and core members as three-dimensional Euler-Bernoulli beams, with six degrees-of-freedom at each node. The behavior of the solid plate is simulated via linear shell elements in the commercial finite element package ABAQUS [8]. The in-plane behavior of these elements is plane stress, while the out-of-plane behavior corresponds with linear plate theory, [9], as these are flat shell elements.

Since the sandwich plate will generally be subject to applied transverse loads, the Kagome planar truss in its role as a face sheet must carry substantial in-plane loads in addition to undergoing actuation. For the sandwich plate to carry transverse loads efficiently, it is desirable for the solid and Kagome plane face sheets to have comparable in-plane stiffness. The in-plane stiffness of the Kagome planar truss is isotropic, with the relation between average in-plane strains and the overall stress resultants given by

$$\begin{aligned} \epsilon_{11} &= S^{-1}(N_{11} - \nu N_{22}), & \epsilon_{22} &= S^{-1}(N_{22} - \nu N_{11}), \\ \epsilon_{12} &= S^{-1}(1 + \nu)N_{12} \end{aligned} \quad (14)$$

with $S = EA/(\sqrt{3}L)$ and $\nu = 1/3$. Equating the in-plane stiffness of the solid sheet and that of the Kagome sheet described by (14) leads to the following relation between the face sheet thickness and member radius:

$$\frac{t}{L} = \frac{\pi}{\sqrt{3}} \left(\frac{R}{L} \right)^2. \quad (15)$$

This relation will be used to specify the face sheet thickness for the various member radii used in the examples detailed below.

4.2 Actuation and Periodicity of the Infinite Kagome Plate. First consider an infinite Kagome plate structure. The objective of this section is to probe how well the shape of the solid face sheet can be controlled by periodic actuations of the members of the planar Kagome face sheet. Actuation is simulated via the same cut-stress-reweld scheme outlined in Section 2.2. For the infinite plate, periodic target and actuation fields are considered and a corresponding periodic cell is adopted for performing the computations. The details of the periodic boundary conditions for out of plane behavior are given in the Appendix. The periodic boundary conditions, in addition to those suppressing rigid-body motions, are imposed via the use of Lagrangian multipliers, as shown in Section 2.3, resulting in solutions that show periodicity of the forces and moments exerted on the boundaries of the periodic cell.

As in the planar Kagome case, a simulation is run for a unit elongation of every member of the Kagome plane. Core members



Fig. 10 Periodic cell used for Kagome plate simulation

are not actuated. In this case, the vertical displacements of the nodes of the solid face sheet are assembled into a matrix of influence coefficients B . The ij th component of B is the vertical displacement of the i th node of the solid face sheet resulting from a unit elongation of the j th member of the Kagome plane.

The linearity of the theory allows the displacements of the nodes from arbitrary actuation (elongation or contraction) of any combination of members to be calculated easily once B is assembled:

$$w_i = B_{ij} e_j \quad (16)$$

where e is the vector of member actuations and w the vector of vertical displacements of solid face sheet nodes.

Now consider a target field of the vertical displacements of the solid face sheet displacement field w^d . We wish to determine how well this field can be recreated by actuating members of the Kagome plane. The Moore-Penrose generalized inverse is employed in a similar manner as before to calculate elongations \tilde{e} and displacements \tilde{w} via the relations

$$\tilde{e}_i = B_{ij}^\dagger w_j^d \quad (17)$$

$$\tilde{w}_i = B_{ij} \tilde{e}_j \quad (18)$$

where B^\dagger is the Moore-Penrose generalized inverse of B . Here, \tilde{e} is the vector of member actuations which minimize the squared error between \tilde{w} and w^d . As before, if there exist multiple vectors of actuations which minimize this squared error, \tilde{e} is such a vector of minimal length.

4.3 Example Target Displacement Fields. The simulations outlined above were run for several target displacement fields. The periodic cell used for these simulations is shown in Fig. 10. It contains a total of 64 unit cells. The axes used for describing the displacements fields described here are the same ζ -axis and η -axis used in the planar Kagome examples. It is important to note that the target displacement fields imposed are all consistent with the periodic displacement boundary conditions described in the Appendix. As in the planar Kagome examples, the displacements themselves are not, in general, periodic, while the stresses, strains and curvatures are periodic. Here we consider, for example, a displacement field corresponding to a constant curvature—the internal forces are periodic (with periodicity size of the periodic cell), while the displacements are clearly not periodic.

The first target displacement field is described by

$$w^d = A_0 \zeta^2 e_z \quad (19)$$

Here, the displacement corresponds to the vertical displacement of the nodes of the solid face sheet corresponding to a state of constant curvature of $\kappa_{\zeta\zeta} = 2A_0$ with A_0 with A_0 as the amplitude factor and e_z the unit vector perpendicular to the plate (aligned with the z -axis). The Moore-Penrose best-fit actuations for this displacement field are calculated as described above. The achievable displacement field is shown in Fig. 11—only the achievable field is shown, as it is indistinguishable from the target field. There are 384 members that are actuated in this simulation and only 209 target nodal displacements. However, the rank of B is only 194, so it is interesting that the achievable field is so close to the target field. Actuation energy and strains will be discussed in Section 5.

The second target displacement field is

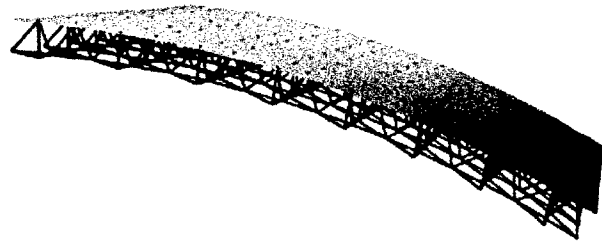


Fig. 11 Best-fit displacement field calculated using Moore-Penrose analysis for target field $w^d = A_0 \zeta^2 e_z$

$$w^d = A_0 e_z \sin\left(\frac{2\pi\zeta}{L_\zeta}\right) \quad (20)$$

where L_ζ is the length of the unit cell in the ζ -direction. This displacement field has zero displacement along two edges of the periodic cell, corresponding to $\zeta=0$ and $\zeta=L_\zeta$. Along these same edges, the slope in the ζ -direction takes the value of $2\pi A_0/L_\zeta$. This displacement field takes on a maximum value of $\pm A_0 e_z$ at $\zeta=L_\zeta/4$ and $\zeta=3L_\zeta/4$. The achievable displacement field shown in Fig. 12 again matches the target field.

One final target displacement field of interest is described by

$$w^d = A_0 e_z \sin\left(\frac{2\pi\zeta}{L_\zeta}\right) \sin\left(\frac{2\pi\eta}{L_\eta}\right) \quad (21)$$

Note that, unlike the previous target displacement fields, this field involves a nonzero Gaussian curvature of the solid face sheet. The achievable field shown in Fig. 13 also matches the target field.

4.4 Comparison With Long Wavelength Theory. The best-fit actuations for the displacement fields described above have been compared with the actuations predicted by the long wavelength approximation outlined in previous work, [1]. In this long wavelength theory, the extensional strain, ϵ^T , of a member is $\epsilon^T = -H \kappa_{\alpha\beta}^d t_\alpha t_\beta$ where κ^d is the curvature tensor associated with w^d ($\kappa_{\alpha\beta}^d = w_{,\alpha\beta}^d$) and t_α is the unit vector specifying the orientation of the member.

Member actuations calculated via the Moore-Penrose analysis for the case of constant curvature agree well with actuations predicted by the long wavelength theory. As this is a displacement field with infinite wavelength, the agreement is not surprising. Actuations for the simulation corresponding to the sinusoidal dis-



Fig. 12 Best-fit displacement field calculated using Moore-Penrose analysis for target field $w^d = A_0 e_z \sin(2\pi \zeta / L_\zeta)$

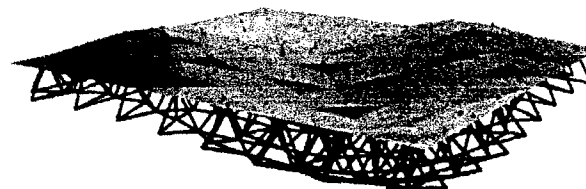


Fig. 13 Best-fit displacement field calculated using Moore-Penrose analysis for target field $w^d = A_0 e_z \sin(2\pi \zeta / L_\zeta) \times \sin(2\pi \eta / L_\eta)$. The faceting of the solid sheet is an artifact of the plotting—the actual shape of the solid sheet is smooth.

placement field (20) are also predicted well by the long wavelength theory. This displacement field has a wavelength of eight unit cells. Actuations were also calculated for a sinusoidal displacement field with a wavelength of only four unit cells:

$$\mathbf{w}^d = A_0 \mathbf{e}_z \sin\left(\frac{4\pi\zeta}{L_\zeta}\right). \quad (22)$$

The actuations predicted by the long wavelength theory show more discrepancy in this case, as would be expected, but the largest actuation strains are not in major disagreement.

4.5 Actuation of Selected Kagome Members. As a practical matter, it will usually be the case that only a small subset of the Kagome face members will be actuated. The Moore-Penrose actuation scheme described previously can still be used to probe how well such structures can achieve the target displacement fields.

Consider there are only M members which have been identified for actuation. The matrix B contains the displacements of the solid face sheet nodes corresponding to all member actuations. Thus, we can construct a new matrix B^* that contains only the M columns corresponding to the members to be actuated. Then the vertical displacements of the face sheet nodes are again easily calculated according to

$$\mathbf{w}_i = B_{ij}^* \mathbf{e}_j^* \quad (23)$$

where now \mathbf{e}^* is the vector of actuations of those members that can be actuated.

Consider a target displacement field \mathbf{w}^d . The minimum length, minimum squared error set of actuations for the M members is

$$\tilde{\mathbf{e}}_i^* = B_{ij}^{*+} \mathbf{w}_j^d. \quad (24)$$

Here, B^{*+} is the Moore-Penrose generalized inverse of B^* . The vertical displacements of the solid face nodes are also easily calculated:

$$\tilde{\mathbf{w}}_i = B_{ij}^* \tilde{\mathbf{e}}_j^*. \quad (25)$$

Reconsider the target displacement field that corresponds to constant curvature:

$$\mathbf{w}^d = A_0 \zeta^2 \mathbf{e}_z. \quad (26)$$

Now, however, assume that only members of the Kagome plane in the row corresponding to $\zeta \approx L_\zeta/2$ can actuate. These members are located in the middle of the periodic cell, as shown in Fig. 14(a). The Moore-Penrose best-fit displacement field is shown in Fig. 15. Note that the structure displays only local curvature along the line $\zeta = L_\zeta/2$.

Reconsider also the target sinusoidal displacement field:

$$\mathbf{w}^d = A_0 \mathbf{e}_z \sin\left(\frac{2\pi\zeta}{L_\zeta}\right). \quad (27)$$

Here, however, assume that only the selected members of the Kagome plane are actuated corresponding to those aligned in rows having $\zeta \approx L_\zeta/4$ and $\zeta \approx 3L_\zeta/4$, as shown in Fig. 14(b). These members lie within the zones of maximum curvature magnitude of the target displacement field. When the Moore-Penrose analysis is run under these conditions, the resulting displacement field is displayed in Fig. 16. While the shape looks very similar to that in Fig. 12 achieved by activating all the members of the Kagome face, the curvature in Fig. 16 is nevertheless limited to regions where members are actuating along $\zeta \approx L_\zeta/4$ and $\zeta \approx 3L_\zeta/4$.

5 Energy of Actuation of Kagome Plate Structure

5.1 Energy of Actuation. The strain energy of actuation is again calculated in the manner depicted in Fig. 7 and the work done by each actuator is $-1/2 \epsilon^T \epsilon^T EAL$ where ϵ^T is its actuation strain and ϵ^c is the elastic strain it experiences as a consequence of all actuations. This work is stored as elastic strain energy in the

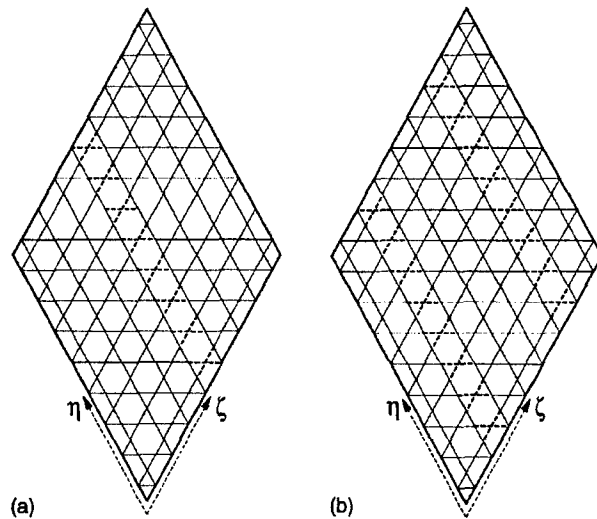


Fig. 14 The members which are allowed to actuate in the analysis of actuation of selected Kagome members. Only the Kagome plane is shown. The dashed members are the members selected to actuate.

structure. The work done by the same actuator, undergoing the same actuation strain ϵ^T , in a perfectly stiff structure is, as before, $1/2(\epsilon^T)^2 EAL$. This energy is taken as the reference energy for the energy calculations presented below. As with the planar Kagome truss, actuation of multiple members does not pose any energy accounting difficulties—the total energy of actuation can be calculated by adding up the contributions from each individual member. The relevant energy ratio calculated for energy comparisons is again given by (13) where ϵ_i^c are computed for each specific set of actuations ϵ_i^T .

As noted earlier, for a structure with energy storage dominated by bending energy in the beam members, the energy ratio \hat{W} can be shown to scale with the slenderness ratio squared, $(R/L)^2$. It is important to note that the sandwich plate comprised of the Kagome face with a solid face sheet is indeterminate—not only are the joints welded, but a solid face is intrinsically indeterminate. It can be anticipated that this indeterminacy will result in

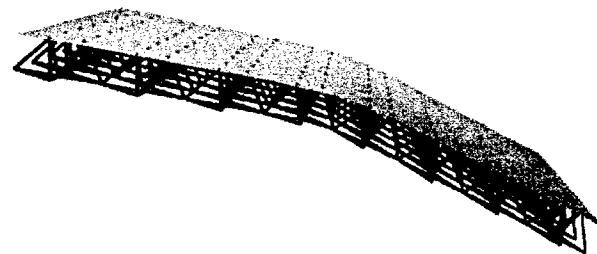


Fig. 15 The best-fit displacement field when limited members are allowed to actuate for the target displacement field $\mathbf{w}^d = A_0 \zeta^2 \mathbf{e}_z$



Fig. 16 The best-fit displacement field when limited members are allowed to actuate for the target displacement field $\mathbf{w}^d = A_0 \mathbf{e}_z \sin(2\pi\zeta/L_\zeta)$

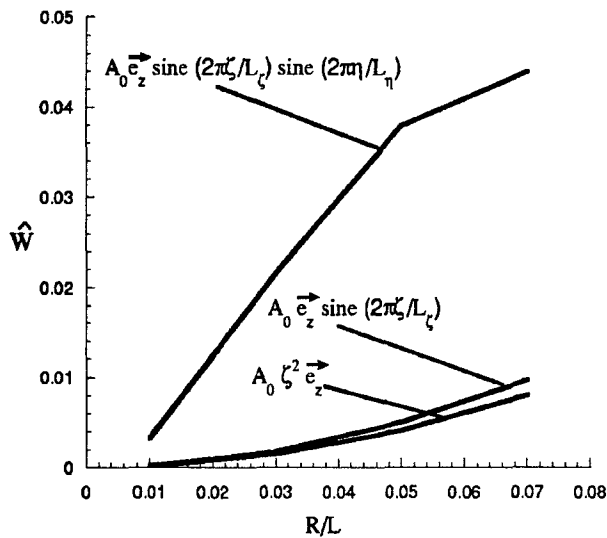


Fig. 17 Normalized actuation energy for the target displacement fields, as a function of R/L

somewhat larger actuation energies than those predicted for bending dominated structures. The energy ratio \hat{W} is plotted against the slenderness ratio for the truss members in Fig. 17 for the three target periodic displacement fields described above. It is clear from this plot that the Kagome-backed sandwich plate offers considerably more resistance to actuation for modes with curvature in two directions than to actuations that bend the plate solely in one direction. Nevertheless, compared to the reference energy, the actuation energy is still small. A more meaningful interpretation of the actuation energy will be given in Section 5.2. Similar trends are seen in Figs. 18 and 19, where the maximum bending and stretching strain quantities for these displacement fields are plotted as a function of slenderness ratio.

Plates actuated to produce double curvature will necessarily be limited to smaller actuation strains (and thus displacements) to ensure they do not undergo plastic yield. It is important to note that the results here for the double curvature plate have been computed using linear theory. Large resistance will arise for suffi-

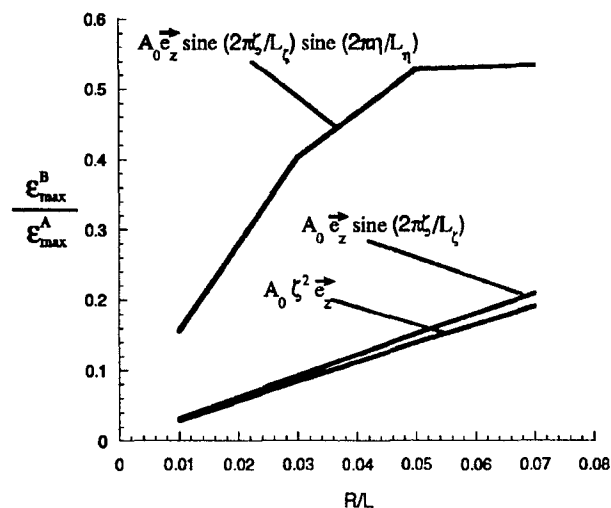


Fig. 18 Maximum bending strain normalized by maximum actuation strain for the target displacement fields, as a function of R/L

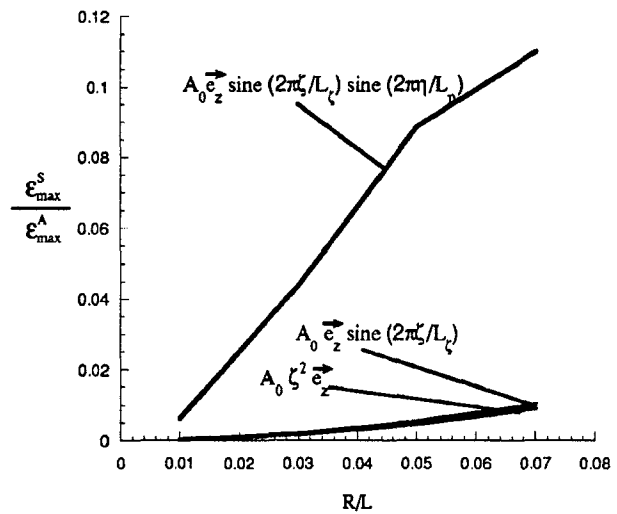


Fig. 19 Maximum stretching strain normalized by maximum actuation strain for the target displacement fields, as a function of R/L

ciently large deflections due to nonlinear coupling between bending and stretching in the solid face sheet whenever shapes with nonzero Gaussian curvature are actuated. This nonlinear effect is not considered in this paper. Thus, the results for doubly curved shapes presented here are restricted to small deflections.

5.2 Comparison of Two Energy Quantities. In most applications, a multifunctional role of these actuating structures is anticipated where the structures will be required to both change shape and carry and lift significant loads. Here an approximate calculation is presented of the relative energies to perform these two different functions, highlighting the significance of structures with low resistance to actuation.

For specificity, consider a cantilevered Kagome plate structure of length ℓ subjected to a load per unit length P at free end. Now imagine that, via actuation of Kagome members, the cantilevered end is raised a distance δ_A . The work per unit length done to raise this load scales as

$$W_P \approx P \delta_A = P \epsilon_A \ell \quad (28)$$

where ϵ_A is the typical actuation strain for a member near the clamped end. The energy per unit length stored as strain energy in the Kagome plate structure due to resistance to actuation scales as

$$W_A \approx kEA \epsilon_A^2 \quad (29)$$

where A is the member cross-sectional area and k is a small fraction of unity for structures with low internal resistance to actuation, such as those reported above.

The structure must be designed to be able to carry the load per unit length P . For an optimally designed structure, we anticipate that face yielding or buckling will be an active constraint, [10]. With σ_c as the critical stress in a Kagome member (set by either buckling or yielding), the member must be sized to satisfy a relation that scales as $\sigma_c AL \approx PL \ell$. Thus, to carry the applied load, the member cross-sectional area will be sized according to the scaling law

$$A \approx P \ell / \sigma_c \quad (30)$$

The maximum allowable actuation is also related to this critical stress σ_c according to

$$\epsilon_A \approx f \sigma_c / E \quad (31)$$

Here, f is the factor relating actuation strain and the maximum strain induced in the structure due to actuation as plotted for the

Kagome structures earlier in the paper. In most instances, the condition limiting actuation is likely to be yielding in bending, at least for the Kagome structures, but the possibility of buckling of members under compression must also be considered. Now calculate the ratio of the energy stored in the structure due to actuation to the amount of energy required to raise the load:

$$\frac{W_A}{W_P} \approx \frac{kEP\ell\epsilon_A^2/\sigma_c}{P\epsilon_A\ell} = \frac{k(E/\sigma_c)\epsilon_A^2}{\epsilon_A} = kf. \quad (32)$$

For the Kagome sandwich plates analyzed in Section 4, typical values of f are about 10, as the maximum induced bending strains in the Kagome plane are about 10% of the maximum actuation strain. Values of k depend upon the specifics of the actuation, but because of their low resistance to actuation they typically range from about 1/100 to 1/1000 for the Kagome structures. Thus, for such structures, the energy required to raise the applied loads will be 10–100 times the energy stored as strain energy in the structure. The sandwich plates subject to double curvature offer somewhat more internal resistance to actuation ($k \approx 1/40$), but values of f are also lower ($f \approx 2$) such that the energy stored in internal resistance is still relatively low, i.e., $W_A/W_P \approx 1/20$. In this fundamental sense, the Kagome plate structure offers minimal internal resistance to the actuation.

6 Concluding Remarks

Sandwich plates employing as the actuation plane a Kagome planar truss have been studied to assess their effectiveness and efficiency in the dual role of a load carrying structure capable of actuated shape changes. The advantage of the Kagome planar truss in this application is its in-plane stiffness and strength coupled with its low internal resistance to actuation. The sandwich plate offers more internal resistance than the isolated Kagome plane. Nevertheless, an actuated plate designed to carry specific loads can achieve a wide variety of shapes with relatively low expenditure of energy to overcome the internal resistance compared to the work expended in raising the loads. It remains to be seen from prototypes that are currently under construction, as well as from further theoretical work, just how large the actuated amplitudes can be and the range of modes shapes that can be produced. This is especially true for double curvature modes that require greater expenditure of energy to overcome internal resistance.

Acknowledgments

This work was supported by the grant Multifunctional Mechano-Electronic Materials (N00014-01-1-0523) and by the Division of Engineering and Applied Sciences, Harvard University.

Appendix

Periodic Displacement Boundary Conditions. Consider a periodic structure such as that shown in Fig. A1. With A as the reference periodic cell and $\mathbf{r}^{(i)}$ the vector from the origin in A to the i th node in A, we denote the displacements of the nodes in A as

$$\mathbf{u}_A^{(i)} = \mathbf{u}_0^{(i)}. \quad (A1)$$

Let B, C, and D be neighboring periodic cells, as shown in Fig. A1. We denote the displacements at the nodes in those cells as

$$\mathbf{u}_B^{(i)} = \mathbf{u}_0^{(i)} + \mathbf{u}_{BA} + \boldsymbol{\omega}_{BA} \times \mathbf{r}^{(i)} \quad (A2)$$

$$\mathbf{u}_C^{(i)} = \mathbf{u}_0^{(i)} + \mathbf{u}_{CA} + \boldsymbol{\omega}_{CA} \times \mathbf{r}^{(i)} \quad (A3)$$

$$\mathbf{u}_D^{(i)} = \mathbf{u}_0^{(i)} + \mathbf{u}_{DA} + \boldsymbol{\omega}_{DA} \times \mathbf{r}^{(i)} \quad (A4)$$

$$\mathbf{u}_D^{(j)} = \mathbf{u}_0^{(j)} + \mathbf{u}_{CA} + \boldsymbol{\omega}_{CA} \times \mathbf{r}^{(j)}. \quad (A5)$$

Combining (A4) with (A3) or (A5) with (A2) yields

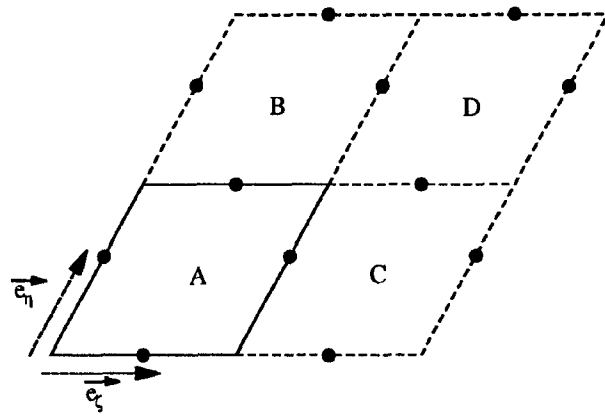


Fig. A1 A periodic structure. A, B, C, D are equivalent periodic cells. The dots correspond to nodes along the edges of the periodic cells. \mathbf{e}_x and \mathbf{e}_y are unit vectors aligned with the edges of the periodic cells.

$$\mathbf{u}_D^{(i)} = \mathbf{u}_0^{(i)} + \mathbf{u}_{BA} + \mathbf{u}_{CA} + (\boldsymbol{\omega}_{BA} + \boldsymbol{\omega}_{CA}) \times \mathbf{r}^{(i)}. \quad (A6)$$

Now consider the rotations at each node in A. Denote these as

$$\phi_A^{(i)} = \phi_0^{(i)}. \quad (A7)$$

Similarly for B, C, and D:

$$\phi_B^{(i)} = \phi_0^{(i)} + \omega_{BA} \quad (A8)$$

$$\phi_C^{(i)} = \phi_0^{(i)} + \omega_{CA} \quad (A9)$$

$$\phi_D^{(i)} = \phi_0^{(i)} + \omega_{BA} + \omega_{CA}. \quad (A10)$$

Now consider the edge joining cell A and cell B. With the displacements of the nodes along the top of A equal to the displacements of the nodes along the bottom of B:

$$\mathbf{u}_0^{(l)} = \mathbf{u}_0^{(i)} + \mathbf{u}_{BA} + \boldsymbol{\omega}_{BA} \times \mathbf{r}^{(i)}. \quad (A11)$$

Here, (l) is along the top of A and (i) along the bottom of B.

We can write $\mathbf{r}^{(l)} = \mathbf{r}^{(i)} + L_\eta \mathbf{e}_\eta$, where L_η is the length of the periodic cell in the \mathbf{e}_η direction.

Now, equate the displacements along the edge joining C and D:

$$\mathbf{u}_0^{(j)} + \mathbf{u}_{CA} + \boldsymbol{\omega}_{CA} \times \mathbf{r}^{(j)} = \mathbf{u}_0^{(i)} + \mathbf{u}_{CA} + \mathbf{u}_{BA} + (\boldsymbol{\omega}_{BA} + \boldsymbol{\omega}_{CA}) \times \mathbf{r}^{(i)}. \quad (A12)$$

Rearranging and simplifying (A12) leads to:

$$\mathbf{u}_0^{(j)} - \mathbf{u}_0^{(i)} = \mathbf{u}_{BA} + \boldsymbol{\omega}_{BA} \times \mathbf{r}^{(i)} - \boldsymbol{\omega}_{CA} \times L_\eta \mathbf{e}_\eta \quad (A13)$$

Comparison of (A13) with (A11) above yields:

$$\boldsymbol{\omega}_{CA} \times L_\eta \mathbf{e}_\eta = 0 \Rightarrow \boldsymbol{\omega}_{CA} = \omega_{CA} \mathbf{e}_\eta \quad (A14)$$

Now equate the displacements of nodes along the edge between cells A and C:

$$\mathbf{u}_0^{(j)} = \mathbf{u}_0^{(i)} + \mathbf{u}_{CA} + \boldsymbol{\omega}_{CA} \times \mathbf{r}^{(j)} \quad (A15)$$

Here, (J) is along the right of A and (j) along the left of C.

Now we can write $\mathbf{r}^{(j)} = \mathbf{r}^{(i)} + L_\zeta \mathbf{e}_\zeta$, where L_ζ is the length of the periodic cell in the \mathbf{e}_ζ direction.

Equating displacements of nodes along the edge between cells B and D yields

$$\begin{aligned} \mathbf{u}_0^{(j)} + \mathbf{u}_{BA} + \boldsymbol{\omega}_{BA} \times (\mathbf{r}^{(j)} + L_\zeta \mathbf{e}_\zeta) \\ = \mathbf{u}_0^{(j)} + \mathbf{u}_{CA} + \mathbf{u}_{BA} + (\boldsymbol{\omega}_{BA} + \boldsymbol{\omega}_{CA}) \times \mathbf{r}^{(j)}. \end{aligned} \quad (A16)$$

Rearranging and simplifying (A16) yields:

$$\mathbf{u}_0^{(j)} - \mathbf{u}_0^{(i)} = \mathbf{u}_{CA} + \boldsymbol{\omega}_{CA} \times \mathbf{r}^{(j)} - \boldsymbol{\omega}_{BA} \times L_\zeta \mathbf{e}_\zeta. \quad (A17)$$

Comparison of (A17) with (A15) with above yields

$$\omega_{BA} \times L_z \mathbf{e}_z = 0 \Rightarrow \omega_{BA} = \omega_{BA} \mathbf{e}_z. \quad (A18)$$

So, for edges parallel to \mathbf{e}_z , displacements are related by

$$\mathbf{u}_0^{(j)} - \mathbf{u}_0^{(i)} = \mathbf{u}_{BA} + \omega_{BA} \mathbf{e}_z \times \mathbf{r}^{(i)}. \quad (A19)$$

Now, write $\mathbf{r}^{(i)} = \zeta^{(i)} \mathbf{e}_z + z^{(i)} \mathbf{k}$ and note that \mathbf{k} is perpendicular to \mathbf{e}_z and \mathbf{e}_η .

Thus, we can write

$$\mathbf{u}_0^{(j)} - \mathbf{u}_0^{(i)} = \mathbf{u}_{BA} + \omega_{BA} z^{(i)} \mathbf{e}_z \times \mathbf{k}. \quad (A20)$$

Thus, for all pairs of points the same distance above the reference plane

$$\mathbf{u}_0^{(j)} - \mathbf{u}_0^{(i)} = \mathbf{u}_{BA} = \mathbf{u}_0^{(j+m)} - \mathbf{u}_0^{(i+m)}. \quad (A21)$$

Similar along the edges parallel to \mathbf{e}_η :

$$\mathbf{u}_0^{(j)} - \mathbf{u}_0^{(j)} = \mathbf{u}_{CA} = \mathbf{u}_0^{(j+m)} - \mathbf{u}_0^{(j+m)}. \quad (A22)$$

Now, compare the rotations. Setting equal the rotations at nodes along the edge joining cells A and B:

$$\phi_0^{(j)} = \phi_0^{(i)} + \omega_{BA} = \phi_0^{(i)} + \omega_{BA} \mathbf{e}_z. \quad (A23)$$

Equating rotations at nodes along the edge joining cells C and D:

$$\phi_0^{(j)} + \omega_{CA} = \phi_0^{(i)} + \omega_{BA} + \omega_{CA} \quad (\text{same as (A23)}). \quad (A24)$$

Finally, equating rotations at nodes along the edge joining cells A and C:

$$\phi_0^{(j)} = \phi_0^{(j)} + \omega_{CA} = \phi_0^{(j)} + \omega_{CA} \mathbf{e}_\eta. \quad (A25)$$

References

- [1] Hutchinson, R. G., Wicks, N., Evans, A. G., Fleck, N. A., and Hutchinson, J. W., 2003, "Kagome Plate Structures for Actuation," *Int. J. Solids Struct.*, **40**, pp. 6969–6980.
- [2] Hutchinson, R. G., and Fleck, N. A., 2003, in preparation.
- [3] Hyun, S., and Torquato, S., 2002, "Optimal and Manufacturable Two-Dimensional Kagome-Like Cellular Solids," *J. Mater. Res.*, **17**, pp. 137–144.
- [4] Guest, S. D., and Hutchinson, J. W., 2003, "On the Determinacy of Repetitive Structures," *J. Mech. Phys. Solids*, **51**, pp. 383–391.
- [5] Wicks, N., and Guest, S. D., 2003, "Single Member Actuation in Large Repetitive Truss Structures," *Int. J. Solids Struct.*, **41**, pp. 965–978.
- [6] Eshelby, J. D., 1957, "The Determination of the Elastic Field of an Ellipsoidal Inclusion, and Related Problems," *Proc. R. Soc. London, Ser. A*, **241**, pp. 376–396.
- [7] Strang, G., 1988, *Linear Algebra and its Applications*, Harcourt Brace Jovanovich, Orlando, FL.
- [8] Hibbit, Karlsson, and Sorensen, Inc., 2002, ABAQUS Version 6.3.
- [9] Timoshenko, S. P., and Gere, J. M., 1961, *Theory of Elastic Stability*, McGraw-Hill, New York.
- [10] Wicks, N., and Hutchinson, J. W., 2001, "Optimal Truss Plates," *Int. J. Solids Struct.*, **38**, pp. 5165–5183.

Part VII: Kagome plate structures for actuation



PERGAMON

International Journal of Solids and Structures 40 (2003) 6969–6980

www.elsevier.com/locate/ijssolstr

INTERNATIONAL JOURNAL OF
**SOLIDS and
STRUCTURES**

Kagome plate structures for actuation

R.G. Hutchinson ^a, N. Wicks ^b, A.G. Evans ^c, N.A. Fleck ^a, J.W. Hutchinson ^{b,*}

^a *Engineering Department, Cambridge University, Cambridge, UK*

^b *Division of Engineering and Applied Sciences, Harvard University, 29 Oxford Street Pierce Hall, Cambridge, MA 02138, USA*

^c *Department of Materials Engineering, University of California, Santa Barbara, CA, USA*

Received 21 October 2002

Abstract

A class of planar, pin-jointed truss structures based on the ancient Kagome basket weave pattern with exceptional characteristics for actuation has been identified. Its in-plane stiffness is isotropic and has optimal weight among planar trusses for specified stiffness or strength. The version with welded joints resists plastic yielding and buckling, while storing minimal energy upon truss bending during actuation. Two plate structures are considered which employ the planar Kagome truss as the actuation plane. It is shown that these plates can be actuated with minimal internal resistance to achieve a wide range of shapes, while also sustaining large loads through their isotropic bending/stretching stiffness, and their excellent resistance to yielding/buckling.

© 2003 Elsevier Ltd. All rights reserved.

Keywords: Trusses; Plates; Actuation; Buckling; Kagome

1. Introduction

A class of actuating plate structures is introduced, based on a planar truss having the Kagome weave pattern (Fig. 1). The two planar manifestations to be explored both consist of faces connected by a tetrahedral truss core (Fig. 2) with the following distinctions:

- (i) A Kagome plane and a solid skin,
- (ii) two Kagome faces.

The feature rendering the Kagome planar truss exceptional for actuation is that its members can be actuated (elongated or contacted) to achieve arbitrary in-plane nodal displacements with minimal internal resistance. This attribute arises because the infinite, pin-jointed version satisfies most of the requirements for static determinacy, permitting minimal elastic energy storage (in bending) even when the joints are welded. These benefits become apparent upon comparing with a highly redundant (isotropic) planar truss,

* Corresponding author. Tel.: +1-617-495-1000; fax: +1-609-258-1177.

E-mail address: hutchinson@husm.harvard.edu (J.W. Hutchinson).

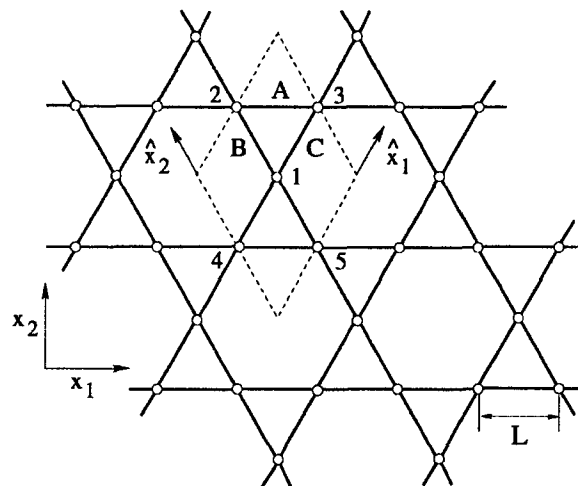


Fig. 1. Sketch of pin-jointed, planar Kagome lattice with member length L . Dashed lines give the boundaries of the primitive unit cell.

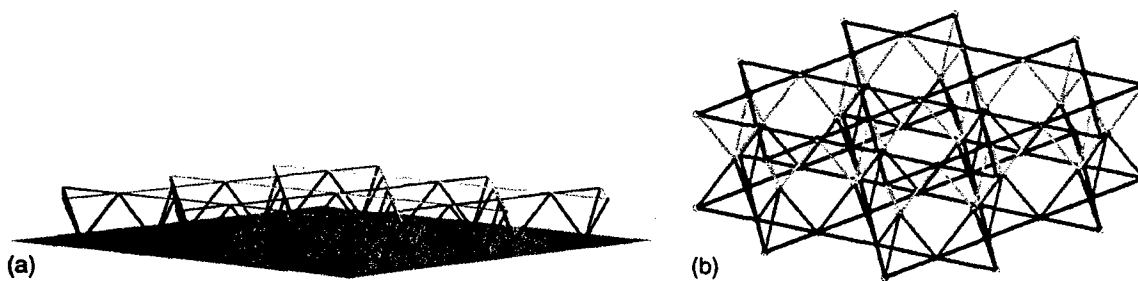


Fig. 2. Sandwich plates based on planar Kagome truss plates. (a) Sandwich with one Kagome truss face and a solid skin face and (b) sandwich with two Kagome truss faces.

exemplified by identical triangular units with equal length members. If such a truss replaces the Kagome in Fig. 2, axial deformation of the members would be required upon actuation, storing substantial energy. The Kagome truss is the only example known to us of an infinite planar truss amenable to assembly from repeat units having both isotropic stiffness and the properties desired for actuation.

The purpose of this paper is to introduce some important properties of the Kagome planar truss and to provide an overview of its role in actuating plate structures. More complete treatments will be given in subsequent papers. Several aspects of the performance of this configuration will be addressed.

- (i) A discussion of determinacy for infinite pin-jointed trusses with repeating units reveals that no such configuration can be both statically and kinematically determinate.
- (ii) The pin-jointed Kagome truss has kinematic mechanisms, but the weld-jointed version is resistant to premature failure by suppressing them and, moreover, inhibits premature failure by either plastic yielding or buckling.
- (iii) In combination with superior in-plane stiffness (Hyun and Torquato, 2002), these features render the Kagome planar truss an ideal structural unit for two-dimensional actuation.
- (iv) The actuation capability is revealed by analyzing the response of the plates in Fig. 2 at long wavelengths (relative to the truss member length).

2. Determinacy and the Kagome planar truss

The relevance of static determinacy to actuation of two- and three-dimensional truss structures has been appreciated for some time in connection with the design of space antenna and mirrors (Miura, 1984a,b; Rhodes and Mikulas, 1985; Mikulas et al., 1993). Because the forces in the members of a pin-jointed, statically determinate truss are determined by equilibrium alone, any member can be elongated or shortened without inducing forces in other members, at least to lowest order in the nodal displacements. Accordingly, the structure offers no resistance to actuation, yet, simultaneously, it is capable of carrying applied loads. With a focus on large actuated structures, we consider infinite plates of the kind shown in Fig. 2 where the truss part of the structure is comprised of identical repeating units. The effects of finiteness are discussed elsewhere. The first step considers infinite planar trusses with pinned joints.

2.1. Static and kinematic determinacy of infinite planar trusses with repeating units

Maxwell's necessary condition for static determinacy of a pin-jointed truss requires that the number of member forces equal the number of joint equilibrium equations. For an infinite planar truss, this criterion requires an average of four members converging at each joint. Note that the Kagome truss (Fig. 1) satisfies this condition, whereas a triangulated truss with repeating equilateral triangles has an excess of two members at each joint.

Kinematic determinacy for a truss satisfying the above condition requires that joint positions are uniquely determined by member lengths (no mechanisms) such that member lengths can be varied independently without incurring deformation of any members.

Additional conditions must be imposed to ensure static or kinematic determinacy of an infinite, pin-jointed planar truss. These are discussed by Guest and Hutchinson (2002) and applied to periodic trusses such as the Kagome truss. These authors show that infinite trusses built up from repeating units (planar or three-dimensional) cannot satisfy all of the conditions for both static and kinematic determinacy. That is, any such infinite truss that is statically determinate will necessarily have kinematic mechanisms. Conversely, any infinite truss that is kinematically determinate will have states of self-stress.

2.2. The Kagome planar truss: stiffness and uniform actuation strains

The infinite pin-jointed Kagome truss is neither statically nor kinematically determinate (Wicks, 2002) and yet it is capable of bearing arbitrary overall loads. In contrast, for the case of a finite Kagome truss, it is possible to add additional members to the boundaries in order to make it both statically and kinematically determinate.

Consider the infinite Kagome truss and assume that each member is identical with length, L , cross-sectional area, A , and Young's modulus, E . Further, suppose the truss is loaded at infinity such that the normal and tangential stress resultants per unit length acting on an edge perpendicular to the x_1 -direction are (N_{11}, N_{12}) ; similarly, the stress resultants on an edge perpendicular to the x_2 -direction are (N_{21}, N_{22}) , where $N_{21} = N_{12}$ and notation standard to plate theory is used. All bars with the same inclination carry identical loads. With three representative members denoted by A, B and C and for the truss orientation shown in Fig. 1, the forces are

$$F_A = (L/\sqrt{3})(3N_{11} - N_{22}), \quad F_B = 2L(N_{22}/\sqrt{3} - N_{12}), \quad F_C = 2L(N_{22}/\sqrt{3} + N_{12}) \quad (1)$$

The overall stiffness of the Kagome planar truss is isotropic such that the relation between the average in-plane strains and the overall stress resultants are given by

$$\varepsilon_{11} = S^{-1}(N_{11} - \nu N_{22}), \quad \varepsilon_{22} = S^{-1}(N_{22} - \nu N_{11}), \quad \varepsilon_{12} = S^{-1}(1 + \nu)N_{12} \quad (2)$$

with $S = EA/(\sqrt{3}L)$ and $\nu = 1/3$. The inverted relation is (with $\nu = 1/3$)

$$N_{11} = \frac{9}{8}S\left(\varepsilon_{11} + \frac{1}{3}\varepsilon_{22}\right), \quad N_{22} = \frac{9}{8}S\left(\varepsilon_{22} + \frac{1}{3}\varepsilon_{11}\right), \quad N_{12} = \frac{3}{4}S\varepsilon_{12} \quad (3)$$

Hyun and Torquato (2002) optimized the topology of infinite, planar isotropic truss-like structures in order to maximize stiffness for a given weight. They used an evolution algorithm coupled to a general plane stress analysis of the structure to arrive at an optimal geometry. The Kagome truss and the triangulated truss were found to be almost identical in stiffness per unit weight. When analyzed within the framework of pin-jointed trusses, the two geometries are precisely equally optimal, attaining the dilute limit of the Hashin and Strickman (1962) upper bounds.

It is an elementary exercise to relate the overall strains, $(\varepsilon_{11}, \varepsilon_{22}, \varepsilon_{12})$ to the actuation strains $(\varepsilon_A, \varepsilon_B, \varepsilon_C)$ of bars A, B and C, respectively. The overall strains can be achieved without inducing any stress in the members by actuating (i.e. elongating or contracting) the three sets of members according to

$$\varepsilon_A = \varepsilon_{11}, \quad \varepsilon_B = \frac{1}{4}\varepsilon_{11} + \frac{3}{4}\varepsilon_{22} - \frac{\sqrt{3}}{2}\varepsilon_{12}, \quad \varepsilon_C = \frac{1}{4}\varepsilon_{11} + \frac{3}{4}\varepsilon_{22} + \frac{\sqrt{3}}{2}\varepsilon_{12} \quad (4)$$

or

$$\varepsilon_{11} = \varepsilon_A, \quad \varepsilon_{22} = -\frac{1}{3}\varepsilon_A + \frac{2}{3}(\varepsilon_B + \varepsilon_C), \quad \varepsilon_{12} = \frac{1}{\sqrt{3}}(\varepsilon_C - \varepsilon_B) \quad (5)$$

When the joints are welded, bending in the members results in a small resistance to actuation. To estimate the magnitude, note that the strains induced by bending are of order, $(r/L)\varepsilon_A$, where ε_A is taken to be representative the actuation strain and $r = \sqrt{I/A}$ is the radius of gyration of the member, with I as the moment of inertia. Consequently, the elastic energy induced by actuation scales with $E(r\varepsilon_A/L)^2$ multiplied by the volume of truss deformed. The corresponding elastic energy-scaling factor for an actuated redundant truss is $E\varepsilon_A^2$. Thus, the energy stored in actuation of the Kagome truss is expected to be significantly lower than that in a redundant truss.

3. Mechanisms of the planar Kagome pin-jointed structure

It is instructive to determine the full set of possible collapse mechanisms for a pin-jointed planar Kagome structure of infinite extent. A systematic method has been developed to determine the competing collapse mechanisms for any pin-jointed periodic structure (Hutchinson and Fleck, 2002). The method builds upon the matrix methods of structural analysis pioneered by Pellegrino and Calladine (1986) and Pellegrino (1993), and the Bloch wave analysis for periodic continue by Triantafyllidis and Schnaidt (1993). An equivalent approach is to set up the governing set of finite difference equations for a periodic structure (e.g. Forman and Hutchinson, 1970). The main steps in the analysis are as follows:

- (i) The kinematic matrix for the unit cell is derived; this relates the bar elongations to the nodal displacements for all nodes and bars of the unit cell.
- (ii) For the given unit cell, the trial displacement field d_j^n of each node n at position \mathbf{x} is written as

$$d_j^n = p_j^n \exp(i2\pi \mathbf{k} \cdot \mathbf{x}) \quad j = 1, 2 \quad (6)$$

The harmonic function $\exp(i2\pi \mathbf{k} \cdot \mathbf{x})$ with wavevector \mathbf{k} , is modulated by an unknown periodic function p_j^n that repeats from one unit cell to the next. Substitution of the trial field (6) into the kinematic matrix for the unit cell leads to a reduced kinematic matrix for the unknown quantities p_j^n for the boundary and interior nodes.

- (iii) The possible collapse mechanisms are obtained by taking the bar elongations of the unit cell to equal zero, and by examining the null space of the reduced kinematic matrix for any chosen values of \mathbf{k} . The dimension of the null space equals the number of mechanisms for the assumed wavevector \mathbf{k} . In general, the null space is complex, and the real and imaginary parts of the displacement field d_j^n constitute independent mechanisms.

3.1. Application of matrix analysis to the planar Kagome pin-jointed structure

The full set of mechanisms for the pin-jointed planar Kagome structure have been calculated using the above matrix analysis. The Kagome structure is represented by the primitive unit cell as outlined by dotted lines in Fig. 1, with the local co-ordinates (\hat{x}_1, \hat{x}_2) aligned with the sides of the unit cell, and oriented with respect to the Cartesian reference frame (x_1, x_2) . Symmetry dictates the existence of three families of collapse mechanism, with one family characterized by the wavevector \mathbf{k} along the \hat{x}_1 -direction, one along the \hat{x}_2 -direction and the third along the x_2 -direction. It suffices to consider the canonical family of mechanisms associated with wavevectors along the x_2 -direction; the other two families can be obtained simply by rotating the Kagome structure with its canonical family of mechanisms by a clockwise or counter-clockwise rotation through 60° .

The canonical mechanisms are associated with $|\mathbf{k}|$ adopting the following values: $|\mathbf{k}| = \sqrt{3}/4L, \sqrt{3}/6L, \sqrt{3}/8L, \sqrt{3}/10L, \dots, 0$. For $|\mathbf{k}| = 0$, a single mechanism exists, and it can be characterized by the relative rotation of neighboring triangles, see Fig. 3a. This infinitesimal mechanism does not generate macroscopic strain, but the finite version of this mechanism does give rise to an equi-biaxial compressive strain. The mechanism for $|\mathbf{k}| = \sqrt{3}/4L$ resembles twinning of alternating sign along the x_2 -direction, as sketched in Fig. 3b. For intermediate values of $|\mathbf{k}|$, such as $\sqrt{3}/6L$, two independent collapse mechanisms exist (given by the real and imaginary parts of d_j^n); each collapse mechanism comprises discrete bands of deformation that are periodic along the x_2 -direction. For the sake of brevity, these additional collapse mechanisms are not shown, and the reader is referred to Hutchinson and Fleck (2002) for full details.

None of the infinitesimal collapse modes described above gives rise to macroscopic strain. This is consistent with the fact that the Kagome structure has a finite overall stiffness, as given by Eq. (3).

4. Strength of the planar Kagome structure with welded joints

When the joints of the Kagome planar truss are welded, the kinematic mechanisms identified above are suppressed. However, the issue remains as to whether the welded truss is susceptible to buckling in modes of similar shape to the mechanisms described above. This possibility is examined by performing a general

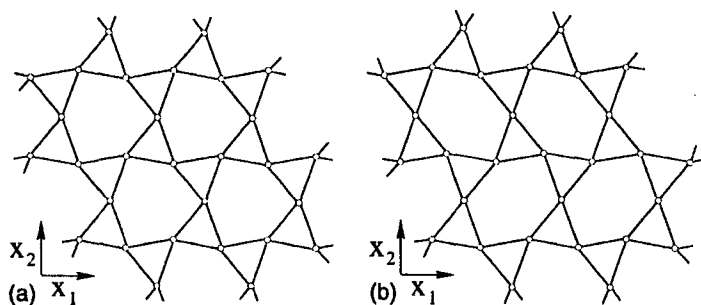


Fig. 3. Mechanisms of the planar Kagome truss. (a) $|\mathbf{k}| = 0$ and (b) $|\mathbf{k}| = \sqrt{3}/4L$.

bifurcation buckling analysis of the in-plane modes. As in the earlier sections, the length of each member is L , the modulus is E and the cross-sectional area is A . The moment of inertia of the members governing in-plane bending is I . We first consider conditions for plastic yielding of the truss and continue with a complete analysis of the in-plane elastic buckling modes.

4.1. Yield

It is straightforward to obtain analytic expressions for the plastic collapse strength of the Kagome truss by assuming that each member behaves in rigid-ideally plastic manner, with a yield strength σ_Y , and by neglecting the small effect of bending. The effective yield locus is found by setting the bar tensions defined in (1) equal to the fully plastic axial yield load $\pm A\sigma_Y$ with the following results:

$$\begin{aligned} N_{11} - N_{22}/3 &= \pm A\sigma_Y/(\sqrt{3}L) \\ N_{22} - \sqrt{3}N_{12} &= \pm \sqrt{3}A\sigma_Y/(2L) \\ N_{22} + \sqrt{3}N_{12} &= \pm \sqrt{3}A\sigma_Y/(2L) \end{aligned} \quad (7)$$

Note the special case with $N_{12} = 0$ defines a four-sided convex yield locus in the (N_{11}, N_{22}) plane as shown in Fig. 4. The relations (7) can be re-phrased in terms of the principal in-plane stresses (N_1, N_2) and the orientation of the principal directions with respect to the Kagome truss. Using this approach it can be shown that the Kagome truss is almost isotropic in its yield response (Hutchinson and Fleck, 2002).

4.2. Elastic buckling of the Kagome truss

Bloch wave theory can be used to obtain the elastic buckling strength of the welded Kagome truss subjected to arbitrary, macroscopic in-plane loading. Following Triantafyllidis and Schnaidt (1993), the first step is to determine the tangential stiffness matrix \mathbf{K} for the primitive unit cell (Fig. 1) at a given macroscopic stress. Let \mathbf{d} be the vector of virtual nodal displacements (two translations and one rotation per node), and \mathbf{f} be the work-conjugate vector of generalised forces (two direct forces and one moment per node). Then, a non-trivial solution is sought for the homogeneous system of equations $\mathbf{K}\mathbf{d} = \mathbf{f}$ where \mathbf{K} is the symmetric, tangential stiffness matrix of the primitive unit cell, in accordance with beam-column theory (see e.g. Livesley, 1975). One first forms the 15×15 matrix \mathbf{K} for the Kagome unit cell of Fig. 1 (five nodes each with three degrees of freedom, d.o.f.) with the axial bar forces determined by the macroscopic stress state using (1). Next, the generalised virtual displacement and force vectors \mathbf{d} and \mathbf{f} are given a Bloch wave representation similar to (6), and one thereby obtains a (9×9) reduced stiffness matrix \mathbf{K}_r . The governing equation for any buckling mode now reads $\mathbf{K}_r \mathbf{d}_r = \mathbf{0}$. Further reductions may be made if desired: e.g. one may “statically condense” internal d.o.f. such as those associated with joint 1 in Fig. 1. It is emphasized that the reduced stiffness matrix is a non-linear function of both the assumed pre-buckling stress state and the wavevector \mathbf{k} .

The buckling load of the welded Kagome truss is obtained by incrementing the macroscopic stress state (and thus the bar forces) along a given stress path, and by searching for a non-trivial solution of $\mathbf{K}_r \mathbf{d}_r = \mathbf{0}$ for all \mathbf{k} . This null space contains infinitesimal elastic buckling modes (in general, real and imaginary) analogous to the linear eigenvalue buckling analysis found in many commercial finite element codes (e.g. ABAQUS). At low loads the nullspace is trivial whereas at sufficiently high loads buckling is triggered and the nullspace is non-trivial.

The elastic buckling locus in the macroscopic (N_{11}, N_{22}) plane is shown in Fig. 4 for various strut slenderness ratios. In this plot the stress resultants have been normalized by $A\sigma_Y/L$, and, thus, the elastic buckling locus depends upon the magnitude of the yield strain, $\varepsilon_Y = \sigma_Y/E$. Whether elastic buckling or plastic collapse controls the in-plane strength of the truss depends upon the ratio $r/(L\sqrt{\varepsilon_Y})$, where

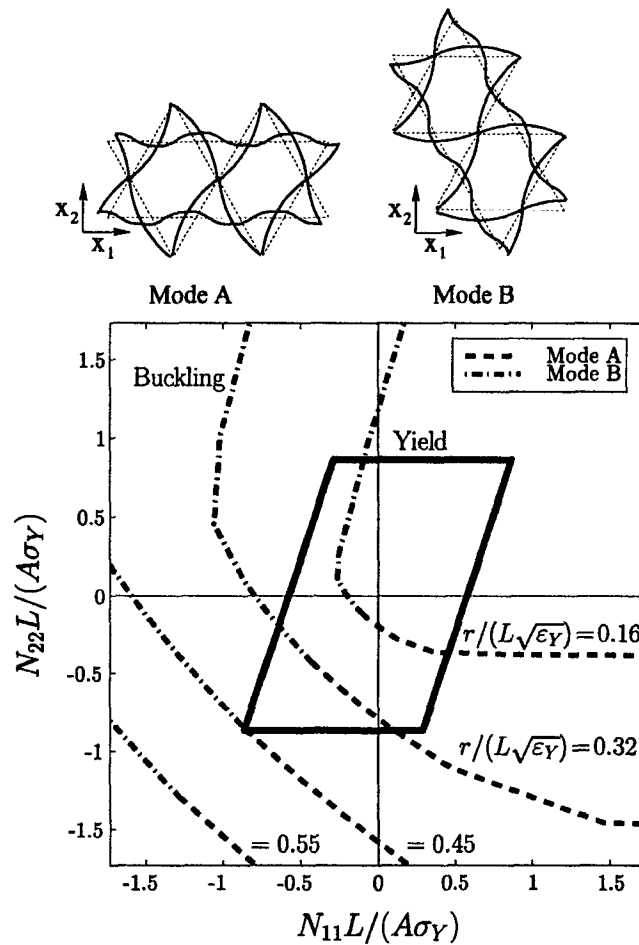


Fig. 4. The competition between elastic buckling and plastic collapse of the welded Kagome truss for selected values of slenderness ratio $r/(L\sqrt{\epsilon_Y})$.

$r \equiv \sqrt{I/A}$ is the radius of gyration of the cross-section. If $r/(L\sqrt{\epsilon_Y}) > 0.45$, plastic yielding occurs prior to elastic buckling for all combinations of N_{11} and N_{22} . For example, if $\epsilon_Y = 0.003$ then plastic yielding is operative if $r/L > 0.024$. In other words, only when its members are exceptionally slender will the welded Kagome truss be susceptible to elastic buckling.

In general, only two elastic buckling modes—modes A and B (Fig. 4)—are found to be of practical interest; all others occurred at higher loads. Mode A is associated with N_{22} -compression and the wavevector $|\mathbf{k}| = \sqrt{3}/4L$ (note similarity to Fig. 3b) while Mode B is associated with N_{11} -compression and is equivalent to Mode A rotated by 60° analogous to the above “canonical pin-jointed mechanism” discussion.

5. Two Kagome sandwich plates

The two sandwich plates considered in this paper are shown in Fig. 2. Actuation of members of the Kagome planar trusses is envisioned. For the plate having just one truss face, it is assumed that face will be actuated to achieve desired shapes of the solid face sheet. The Gaussian curvature of the desired shape must

be small, otherwise large actuation forces will be required to overcome stretching of the solid face. For the plate in Fig. 2b with two truss faces, each face will be actuated. This allows arbitrary shapes to be achieved with no restriction on the Gaussian curvature.

For the sandwich plate with a single truss plate, the core is comprised of tetragonal truss units connecting the nodes of the face to the solid face as shown in Fig. 2a. The spacing between the faces is H and the truss face sheet is characterized by (1)–(3). The solid face sheet has Young's modulus, E_f , Poisson's ratio, ν_f , thickness t_f , and stretching stiffness, $S_f = E_f t_f$. The sandwich plate has isotropic stretching and bending stiffnesses that can be readily derived. However, the expressions for these stiffnesses are algebraically lengthy. They simplify significantly if $\nu_f = \nu = 1/3$, in which case the plate stretching stiffness, \bar{S} , and bending stiffness, \bar{B} , under a single component of moment are given by

$$\bar{S} = S + S_f, \quad \bar{B} = \frac{H^2}{2} \frac{S^2 + S_f^2}{S + S_f} \quad (8)$$

The conventional plate bending stiffness, defined for curvature in only one direction, is $\bar{B}/(1 - \nu^2)$.

Second, consider the sandwich plate with two Kagome truss faces; the core comprises tetragonal truss units symmetrically positioned with respect to the mid-plane and connected to the face nodes as shown in Fig. 2b. Eq. (8) applies with S_f denoting the in-plane stiffness of the bottom face. If the two faces are identical, $\bar{S} = 2S$ and $\bar{B} = H^2 S/2$.

6. Long wavelength actuation of Kagome plates

For the plate having one solid face, the Kagome back plane is actuated to achieve the desired shapes (Figs. 2 and 5). For this case, the Gaussian curvature of the goal shape must be small, otherwise large actuation forces will be required to overcome stretching. Conversely, for the plate with two truss faces, both can be actuated to realize arbitrary shapes with no restriction on the Gaussian curvature. The aim is to achieve specified non-planar shapes defined by the transverse displacement field, $w^0(x_1, x_2)$, of the lower face sheet as closely as possible (Fig. 5). When the desired shape has wavelengths that are long compared to the length of the truss members, the analysis is elementary. The results will be presented below. The corresponding analysis for shorter wavelengths will be presented in a subsequent paper.

6.1. Relation between member actuation and average in-plane displacements and strains for long wavelength modes in the two-dimensional Kagome planar truss

Invoke a continuum description of the truss wherein the joints and members are imagined embedded within a planar membrane. Measure displacements and strains from the reference state of the undeformed membrane, and denote them in the usual way for a continuum by $u_\alpha(x_\mu)$ and $\varepsilon_{\alpha\beta} = (u_{\alpha,\beta} + u_{\beta,\alpha})/2$ where the Greek subscripts range from 1 to 2. The displacement of a truss node coincides with the displacement, u_α , of the membrane at that point, and the extensional strain, ε , of a member connecting neighboring nodes I and J is $\varepsilon = (u_\alpha(\vec{x}^I) - u_\alpha(\vec{x}^J))t_\alpha/L$ where t_α is the unit vector parallel to the member and directed from J to I . Equivalently, in the long wavelength limit the member strain can be expressed as $\varepsilon = \varepsilon_{\alpha\beta} t_\alpha t_\beta$ where the strain is evaluated at the member location. Denote the top Kagome face sheet by the superscript T . Then, an



Fig. 5. Desired shape to be achieved by actuation.

arbitrary in-plane displacement field, u_α^T , of the truss joints can be achieved by actuation of the members to undergo the extensional strain described above and derived from u_α^T , i.e. $\varepsilon^T = (u_\alpha^T(\bar{x}') - u_\alpha^T(\bar{x}''))t_\alpha/L$. Thus, the Kagome planar truss can be actuated to achieve any long wavelength, in-plane strain field, $\varepsilon_{\alpha\beta}^T = (u_{\alpha,\beta}^T + u_{\beta,\alpha}^T)/2$. Relations (4) and (5) can be used to obtain the member actuation strains from $\varepsilon_{\alpha\beta}^T$. If the Kagome truss plate had true pin joints, arbitrary member actuation would leave the truss unstressed. The welded-joint Kagome truss is capable of arbitrary actuation without substantial resistance, while at the same time being stiff and strong in all directions.

6.2. Actuation of a Kagome-backed truss plate for long wavelength shapes

The combination of qualities noted above make the Kagome truss a unique two-dimensional element for actuating either of the plate structures shown in Fig. 2. The passive bending behavior of each of the plates is isotropic and substantial, as is the stretching stiffness. Moreover, the sandwich plate has a high resistance to local buckling. Under the restriction of long wavelength actuation modes, it will be shown that the Kagome planar truss comprising the top face of the plate can be actuated to achieve any normal deflection shape of the bottom face sheet, provided that the deflection slopes are sufficiently small. As already noted, larger deflections are limited to those shapes for which the Gaussian curvature of the solid face sheet is small. For the plate having a Kagome planar truss for both faces, this restriction can be removed if both faces are actuated, as will be discussed in Section 6.3.

Let $\varepsilon_{\alpha\beta}^0$ be the in-plane strains of the virtual middle surface of the sandwich. Let $w^0(x_1, x_2)$ be the normal deflection of that surface with $\kappa_{\alpha\beta}^0$ as its curvature tensor, where $\kappa_{\alpha\beta}^0 = w_{,\alpha\beta}^0$. With $u_\alpha^0(x_\beta)$ as the in-plane displacements of the virtual middle surface, the in-plane strains are given by

$$\varepsilon_{\alpha\beta}^0 = \frac{1}{2}(u_{\alpha,\beta}^0 + u_{\beta,\alpha}^0) + \frac{1}{2}w_{,\alpha}^0 w_{,\beta}^0 \quad (9)$$

The compatibility equation for the middle surface strains is

$$\varepsilon_{11,22}^0 + \varepsilon_{22,11}^0 - 2\varepsilon_{12,12}^0 = G \quad (10)$$

where $G = \kappa_{12}^{0^2} - \kappa_{11}^0 \kappa_{22}^0$ is the Gaussian curvature of the middle surface. The formulation is limited to the same restrictions as von Karman nonlinear plate theory: small strains and moderately large out-of-plane rotations such that $|u_{,\alpha}^0| \ll 1$ and $|w_{,\alpha}^0|^2 \ll 1$. For a core with ample shear stiffness, the strains in the top and bottom faces can be expressed in terms of the middle surface strain and curvature using the classical Euler–Bernoulli hypothesis. This hypothesis states that material points lying on a normal to the undeformed middle surface remain on the normal to the deformed middle surface. For the top Kagome face this implies

$$\varepsilon_{\alpha\beta}^T = \varepsilon_{\alpha\beta}^0 - (H/2)\kappa_{\alpha\beta}^0 \quad (11)$$

while for the bottom face (Kagome or solid)

$$\varepsilon_{\alpha\beta}^B = \varepsilon_{\alpha\beta}^0 + (H/2)\kappa_{\alpha\beta}^0 \quad (12)$$

Let $w^0(x_1, x_2)$ be the desired shape of the plate. (Under the present restrictions for which (11) and (12) apply, both the top and bottom face sheets have the same normal deflection as the virtual middle surface.) The objective is to activate the top Kagome truss sheet to achieve $w^0(x_1, x_2)$ such that there is no stretching strain in the bottom face sheet. This ensures that any resistance to actuation is due only to bending and, therefore, relatively small. Imposing $\varepsilon_{\alpha\beta}^B = 0$, requires $\varepsilon_{\alpha\beta}^0 = -(H/2)\kappa_{\alpha\beta}^0$. Then, by (11), it follows that the top Kagome truss sheet must be activated such that $\varepsilon_{\alpha\beta}^T = -H\kappa_{\alpha\beta}^0$. Compatibility of the middle surface strains, $\varepsilon_{\alpha\beta}^0$, requires that (10) be satisfied. Since $\varepsilon_{\alpha\beta}^0 = -(H/2)w_{,\alpha\beta}^0$ satisfies $\varepsilon_{11,22}^0 + \varepsilon_{22,11}^0 - 2\varepsilon_{12,12}^0 = 0$ identically, it follows from (10) that the choice of shape $w^0(x_1, x_2)$ must be restricted to have zero Gaussian curvature, that is

$G \equiv \kappa_{12}^{02} - \kappa_{11}^0 \kappa_{22}^0 = w_{,12}^{02} - w_{,11}^0 w_{,22}^0 = 0$. (This condition can be relaxed for sufficiently small deflection slopes, as will be discussed later.)

Assuming $G = 0$, the nodal displacements in the top Kagome truss needed to achieve the strains $\varepsilon_{\alpha\beta}^T = -H\kappa_{\alpha\beta}^0$ are $u_\alpha^T = -Hw_{,\alpha}^0$ and the elongation (or contraction), ΔL , of a member with orientation specified by the unit vector t_α is

$$\Delta L = -HL\kappa_{\alpha\beta}^0 t_\alpha t_\beta \quad (13)$$

As discussed above, this displacement field can always be achieved by actuating members of the Kagome truss plane. Moreover, upon actuating to produce any shape of zero Gaussian curvature there are no induced stresses except those caused by truss bending. Additional loads applied to the sandwich plate induce both bending and stretching. The members and solid face sheet must be designed to carry those loads. The work of actuation is that required to displace the applied loads, plus the small internal energy stored in bending.

The condition on w^0 that $G = \kappa_{12}^{02} - \kappa_{11}^0 \kappa_{22}^0 = 0$ ensures that no stretch energy occurs in the face sheets. When the slopes of the desired shape, $w_{,\alpha}^0$, are restricted to be sufficiently small, the Gaussian curvature can be taken to vanish (since it is quadratic in $w_{,\alpha\beta}^0$), and the compatibility equation (10) can be linearized, with its right hand side vanishing identically. Then, any shape w^0 can be achieved by actuating the top Kagome truss, but some stretching energy will be induced if $G \neq 0$. The practical limits to the linear regime will depend on energy requirements for actuation and on buckling as well as plastic yielding constraints in the truss members and the solid face sheet.

6.3. Long wavelength actuation of both faces of a two-faced Kagome truss plate

If members of each face of the two-faced Kagome truss plate in Fig. 2 can be actuated, it is possible to achieve arbitrary shapes with no restriction on the Gaussian curvature of the desired shape. Given the desired shape, $w^0(x_1, x_2)$, take $u_\alpha^0 = -(1/2)Hw_{,\alpha}^0$ such that, by (9), $\varepsilon_{\alpha\beta}^0 = -(1/2)Hw_{,\alpha\beta}^0 + (1/2)w_{,\alpha}^0 w_{,\beta}^0$. (This choice necessarily satisfies (10).) Then, by (11) and (12), the strains that must be attained by actuation in the top and bottom faces are $\varepsilon_{\alpha\beta}^T = -H\kappa_{\alpha\beta}^0 + (1/2)w_{,\alpha}^0 w_{,\beta}^0$ and $\varepsilon_{\alpha\beta}^B = (1/2)w_{,\alpha}^0 w_{,\beta}^0$, respectively. These strains are achieved by actuating length changes of the members according to $\Delta L = L\varepsilon_{\alpha\beta} t_\alpha t_\beta$, as already discussed.

It is worth noting that, as specified, the scheme is not unique. To prescribe unique actuation of the members, both the in-plane displacements and the normal deflection must be prescribed. If the virtual mid-plane undergoes displacements (u_α^0, w^0) , $\varepsilon_{\alpha\beta}^0$ is given by (9). Then, by (11) and (12), the face sheets must be actuated to achieve (u_α^0, w^0) such that

$$\varepsilon_{\alpha\beta}^T = \frac{1}{2}(u_{\alpha,\beta}^0 + u_{\beta,\alpha}^0) - \frac{1}{2}H\kappa_{\alpha\beta}^0 + \frac{1}{2}w_{,\alpha}^0 w_{,\beta}^0 \quad \text{and} \quad \varepsilon_{\alpha\beta}^B = \frac{1}{2}(u_{\alpha,\beta}^0 + u_{\beta,\alpha}^0) + \frac{1}{2}H\kappa_{\alpha\beta}^0 + \frac{1}{2}w_{,\alpha}^0 w_{,\beta}^0$$

The displacements in the bottom face are $(u_\alpha^0 + (1/2)Hw_{,\alpha}^0, w^0)$. Thus, if the aim is to activate the top and bottom face sheets such that the bottom face sheet undergoes displacements (u_α^B, w^B) , this can be achieved without incurring stretching energy by substituting $w^0 = w^B$ and $u_\alpha^0 = u_\alpha^B - (1/2)Hw_{,\alpha}^0$ into the expressions just listed to obtain

$$\varepsilon_{\alpha\beta}^T = \frac{1}{2}(u_{\alpha,\beta}^B + u_{\beta,\alpha}^B) - H\kappa_{\alpha\beta}^B + \frac{1}{2}w_{,\alpha}^B w_{,\beta}^B \quad \text{and} \quad \varepsilon_{\alpha\beta}^B = \frac{1}{2}(u_{\alpha,\beta}^B + u_{\beta,\alpha}^B) + \frac{1}{2}w_{,\alpha}^B w_{,\beta}^B \quad (14)$$

with $\kappa_{\alpha\beta}^B = w_{,\alpha\beta}^B$.

In summary, a plate having actuated Kagome planar trusses for each face can achieve any desired displacement of the nodes of one of the faces, in-plane and out-of-plane. The resistance to actuation is due only to truss bending effects. A prescription for shapes having wavelengths that are long compared to the plate thickness is presented. This prescription applies to shapes with moderately large slopes, $|w_{,\alpha}^0|^2 \ll 1$. It can be extended to shallow shells in a straightforward manner.

7. Concluding remarks

The Kagome truss has been introduced as an actuating plane into a sandwich plate structure with the potential for achieving arbitrary non-planar shapes. The primary feature of the weld-jointed Kagome truss for actuation applications is its ability to deform as an effective medium with arbitrary in-plane strains against the minimal bending resistance of the joints. Other properties that make it especially effective for such applications are its isotropic stiffness, its substantial, near-isotropic in-plane yield strength, and its high local buckling strength. The sandwich plate with two Kagome truss faces can be actuated to achieve arbitrary displacements of the nodes of one face. The plate with only one face as a Kagome truss can be actuated to deform the solid skin to a desired shape. However, unless the Gaussian curvature of the desired shape is small, significant stretching forces will develop and the energy of actuation will be large.

When the actuation is limited to long wavelength modes surprisingly simple results pertain. Methods are being developed to cope with actuation into arbitrary shapes, including a detailed assessment of the stresses produced by both the actuation and by the applied loads to be displaced. Problems related to the potential for fatigue at welded joints will be addressed. More detailed results on the buckling strength will be published separately (Hutchinson and Fleck, 2002). Optimization of plates designed for specific actuation goals will also be performed in subsequent work.

Finally, we note that it has been possible to fabricate the panels described in Fig. 2 by using a procedure based on the CNC bending of perforated plates, followed by transient liquid phase bonding of the faces to the core. Tests on these structures are in progress to affirm the stiffness and strength, to ascertain the bending resistance of welded truss joints, and to establish limits on the realizable deformations imposed by fatigue.

Acknowledgements

This work was supported in part by the ONR Grant: Multifunctional Mechano-Electronic Materials and by Cambridge University, Harvard University and the University of California, Santa Barbara.

References

- Forman, S.E., Hutchinson, J.W., 1970. Buckling of reticulated shell structures. *Int. J. Solids Struct.* 6, 909–932.
- Guest, S.D., Hutchinson, J.W., 2002. On the determinacy of repetitive structures. *J. Mech. Phys. Solids* 51, 383–391.
- Hashin, Z., Strickman, S., 1962. On some variational principles in anisotropic and non-homogeneous elasticity. *J. Mech. Phys. Solids* 10, 335–342.
- Hutchinson, R.G., Fleck, N.A., in preparation.
- Hyun, S., Torquato, S., 2002. Optimal and manufacturable two-dimensional Kagome-like cellular solid. *J. Mater. Res.* 17 (1), 137–144.
- Livesley, R.K., 1975. *Matrix Methods in Structural Analysis*, second ed. Pergamon Press.
- Mikulas, M.M., Thorwald, G., Wada, B.K., 1993. Design considerations for doubly curved conformable trusses. Report JPL D-10528, Jet Propulsion Lab, Caltech, Pasadena, CA.
- Miura, K., 1984a. Design and operation of a deployable truss structure. In: *Proceedings of 18th Aerospace Mechanisms Symposium*, 2–4 May 1984, NASA Goddard Space Flight Center, Greenbelt, Maryland, NASA-CP-2311. pp. 49–63.
- Miura, K., 1984b. Variable geometry truss and its application to deployable truss and space crane arm. In: *Proceedings of 35th Congress of the International Astronautical Federation*, 7–13 October 1984, Lausanne, Switzerland, IAF-84-394.
- Pellegrino, S., 1993. Structural computations with the singular value decomposition of the equilibrium matrix. *Int. J. Solids. Struct.* 30, 3025–3035.
- Pellegrino, S., Calladine, C.R., 1986. Matrix analysis of statically and kinematically indeterminate frameworks. *Int. J. Solids. Struct.* 22, 409–428.
- Rhodes, M.D., Mikulas, M.M., 1985. Deployable controllable geometry truss beam. NASA Langley Research Center Report, NASA TM-86366.

Triantafyllidis, N., Schnaidt, W.C., 1993. Comparison of microscopic and macroscopic instabilities in a class of two-dimensional periodic composites. *J. Mech. Phys. Solids* 41, 1533–1565.

Wicks, N., 2002. Optimization and actuation of truss structures, in preparation.

**Part VIII: Minimum weight design of a high authority
flexural actuator based on electroelastomers**

**MINIMUM WEIGHT DESIGN OF A
HIGH AUTHORITY FLEXURAL
ACTUATOR BASED ON
ELECTROELASTOMERS**

L.H. Han^{*}, T. J. Lu^{*}

**^{*}Department of Engineering, University of Cambridge
Trumpington Street, Cambridge CB2 1PZ, UK**

A.G. Evans^{}**

^{}Materials Department, University of California
Santa Barbara, CA, USA, 93106**

NOMENCLATURE

B	Cantilever width	L_s	Solid length of spring
C_0	Permittivity of free space	L_0	Initial length of elastomer film in x direction
C_r	Dielectric constant of elastomer film	ΔL	Actuated length
d	Diameter of spring wire	N	Design Load
d_s	Diameter of SMA wire	N^*	Number of inactive coils
D	Mean coil diameter of spring	N_a	Number of active coils
D_0	Outside diameter of spring	N_{\min}	Minimum number of active coils
E_A	Young's modulus of SMA in austenite phase	n_{film}	Number of film layers
E_c	Young's modulus of core material	P	Electric field
E_e	Young's modulus of elastomer film	\bar{p}	Coil pitch
E_f	Young's modulus of facesheet material	p_e	Effective pressure in the thickness direction
E_M	Young's modulus of SMA in martensite phase	p'_e	Effective pressure in the thickness direction when the film is subject to an external force
F_{cr}	Euler buckling load	S_{es}	Endurance strength of spring wire
f_n	Natural frequency of spring	S_{ew}	Torsional fatigue strength of spring wire
G	Shear modulus	S_{us}	Ultimate shear strength of spring wire
H	Core thickness	S_{ut}	Ultimate tensile strength of spring wire
K	Spring constant	t_c	Thickness of core member
K_e	Effective length factor	t_e	Thickness of film layers
L	Cantilever length	t_f	Thickness of facesheet
L_{act}	Length of actuation element	V	Applied voltage
L_{free}	Free length of spring		

W_{spring}	Weight of spring	σ_Y^A	Yielding strength of SMA in austenite phase
W_{core}	Core weight	σ_Y^M	Yielding strength of SMA in martensite phase
W_{face}	Facesheet weight	τ	Shear stress
W_{film}	Film weight		
z_0	Initial thickness of elastomer film		
z	Final thickness of elastomer film		
α	Cross sectional area of film layers		
β	Corrugation angle		
θ	Helix angle of spring		
δ_0	Design requirement for tip deflection of cantilever		
Δ_{max}	Maximum compression of spring		
Δ_{min}	Minimum compression of spring		
ϵ_{r0}	Initial remaining strain		
ϵ_T	Actuation strain		
ϵ_{x0}	Pre-strain of film in the x direction		
ϵ_{y0}	Pre-strain of film in the y direction		
κ_s	Transverse shear factor		
λ	Half-length of corrugation pitch		
ω	Natural frequency of cantilever		
ρ_c	Core density		
ρ_f	Facesheet density		
ρ_{SMA}	SMA density		
ρ_s	Spring wire density		

Subscript

c	Core
f	Facesheet
e	Elastomer film
y	Yielding strength

ABSTRACT

A flexural actuator based on the operating principles of electro-elastomers has been designed and analyzed. The actuating element comprises multilayers of the electro-elastomer and a helical spring. The variables are the geometrical dimensions and the failure modes. A design that integrates this basic unit into a high authority flexural system has been analyzed. An optimization procedure has been devised and used to determine preferred designs. The analysis establishes the authority (product of end displacement and load to be lifted), at specified electric field by determining the minimum weight as a function of the actuation strain and the number of electro-elastomer layers, n_{film} . The dimensions of the constituents at the minimum weight emerge from the analysis. A comparison with a flexural actuator made using a one-way shape memory alloy reveals the performance advantages of the electro-elastomer system. An assessment of the variation in minimum weight with n_{film} has provided a basis for a future weight/cost trade-off analysis.

Keywords: Optimal design; Actuator; Electroelastomer; Shape Memory Alloy;
Minimum weight

1. INTRODUCTION

Recent articles have described high authority flexural actuators designed using structural concepts based on sandwich panels with corrugated cores (Wood et al., 1998; Pelrine et al., 2000; Lu et al., 2001, 2002). The concepts combine the mechanical duality of static determinacy with high bending stiffness. This combination facilitates systems capable of displacing large forces at low overall weight. However, the actuating mechanisms impose performance limitations. Actuators based on shape memory alloys (SMA) and electrostrictive polymers (ESP) have the following limitations.

- (i) The SMA actuated system only operates at low frequency and requires large amounts of power (Lu et al., 2001)
- (ii) The ESP system has excellent operating characteristics, but there are challenges in manufacturing the requisite number of polymer/electrode multi-layers (Lu et al., 2002).

The present article explores another actuation method, based on electro-elastomers, embodied within the same structural system. Such materials have large specific energy output and strain response, as well as high frequency and energy efficiency. For instance, acrylics (such as VHBTM 3910 from the 3M corp.) have demonstrated an actuation strain over 200%, with actuation stresses up to 7MPa and energy densities exceeding 3kJ/kg (Pelrine et al., 2000). For this material to realize high authority, it must be combined with a mechanical spring, to form an actuation element (Section 2).

In this article, the minimum weight flexural actuator capable of actuation by an electro-elastomer is designed, subject to all failure modes and prototypical constraints on geometry and voltage (Fig. 1). To illustrate the design, one end of the cantilever is clamped while the other is free. More complex bending and hinging modes can be envisaged and will be assessed in a subsequent study. The cantilever of length L is required to flex over a displacement δ_0 while sustaining a load N , which may vary with displacement and frequency. To realize low weight, the passive upper face and core are made from a high strength Al alloy. Multiple actuation elements are distributed between the nodes in the lower surface (Fig. 1). When a voltage is applied,

the actuator extends and the tip deflects to the required displacement. When the voltage is cut off, the actuator contracts and the structure recovers its original configuration. The system cycles at a frequency to be determined in the analysis.

The design objective is to minimize the overall weight of the actuation system. To realize this objective, the operations of the actuator must be characterized and the structural responses identified. Aspects of the latter are summarized in the Appendix. Note that the design places the actuator in compression when the load N is imposed (Fig. 1).

2. ELECTROELASTOMER ACTUATORS

The actuation element consists of a pre-compressed helical spring embedded within a concentric multi-layer of pre-stretched electro-elastomer with flexible electrodes (Fig. 2). When a voltage is applied, the actuator expands along its axis. The pre-compression in the spring allows the actuator to elongate while delivering appreciable force. The design embodies the choice of spring (material, diameter and so on) and the number of electro-elastomer layers, subject to voltage constraints. Ultimately, the design is performed in conjunction with that of an actuating system, as discussed in section 3.

For comparison, a one-way SMA actuator with helical springs acting as the pull-back mechanism is also evaluated (Fig. 3). Results of the minimum weight design for both actuators will be discussed in section 4.

2.1 Operating Principle

When a voltage, V , is applied to the electrodes within any segment of the electro-elastomer (Fig. 3), the electrostatic forces cause the film to compress in thickness (z -direction) and expand in area (Peltine et al., 1998; 2001). The effective pressure, p_e , exerted by the electrodes is:

$$p_e = C_0 C_r P^2 = C_0 C_r \left(\frac{V}{z} \right)^2 \quad (1)$$

where C_r is the dielectric constant of the elastomer; $C_0 = 8.85 \times 10^{-12} \text{ F/m}$ is the permittivity of free space; P is the electric field; and z is the film thickness. In

practice, the film is plastically pre-stretched to enhance the actuator performance and the electrical breakdown strength (Pelrine et al., 2000). If such a film with initial thickness z_0 is pre-strained ϵ_{x0} in the x direction and ϵ_{y0} in the y direction, its final thickness will be $z = z_0 / [(1 + \epsilon_{x0})(1 + \epsilon_{y0})]$. Since the elastomer is incompressible (Poisson's ratio 0.5), the effective longitudinal force is, $F_e = -0.5 p_e \alpha$, where α is the cross sectional area of the film layers. This force causes the actuation element to change its length by ΔL . If there is no external force, the spring is released from point A_0 to B_0 on Fig. 4. The blocking force when a voltage V is applied and the actuator is rigidly constrained is represented by $C_0 C$. The horizontal distance between A_0 and B_0 represents the stroke. If an external force F_N is applied, the work line $A_0 B_0$ displaces to AB .

The equilibrium state of the actuation element without the external force is given by,

$$E_e (\Delta L / L_0) \alpha + F_s = p_e \alpha / 2 \quad (2)$$

where L_0 is the initial length of the film, $F_s (= K \Delta L)$ is the spring force, with K the spring constant. The stroke of the actuation element is,

$$\Delta L = L_{act} \epsilon_T \quad (3)$$

Here ϵ_T is the stress-free strain of the actuation element, while $L_{act} = (1 + \epsilon_{x0}) L_0$ is the length of the element after the pre-stretch ϵ_{x0} caused by the spring. From Eq. (2) the actuation strain induced by an electric field P can be described by:

$$\begin{aligned} \epsilon_T &= \frac{1}{2} \frac{p_e \alpha}{(E_e \alpha / L_0 + K) L_{act}} \\ &= \frac{1}{2} \frac{C_r C_0}{(E_e + K L_0 / \alpha)(1 + \epsilon_{x0})} P \\ &= \frac{1}{2} \frac{C_r C_0}{(E_e + K L_0 / \alpha)(1 + \epsilon_{x0})} \left(\frac{V}{z} \right)^2 \end{aligned} \quad (4)$$

Note that the cross-sectional area of the layers $\alpha \approx \pi D_0 t_e$, with D_0 the outside diameter of the spring and $t_e = n_{film} z$ the total thickness of the n_{film} layers. The thickness z of an elastomer film upon deformation ϵ_x, ϵ_y in its planar area is

$$z = \frac{z_0}{(1 + \epsilon_x)(1 + \epsilon_y)} \quad (5)$$

When an external force F_N is applied, the strain ε_x is determined from the equilibrium state of the actuation element ($B'B_0$ in Fig. 4) as:

$$\varepsilon_x = \varepsilon_{x0} - \frac{F_N}{KL_0 + E_e \alpha} \quad (6)$$

Because the film is constrained in the y direction, ε_y is constant, ε_{y0} . To avoid buckling, the spring load must assure that the film is always in tension: $\varepsilon_x \geq 0$.

2.2 Spring Design (Juvinall et al., 1999)

The weight of the spring is given by:

$$W_{Spring} = \left[\frac{\pi^2}{4} \right] \rho_s d^2 D \left[\frac{N_a}{\cos \theta} + N^* \right] \quad (7)$$

where ρ_s is the density of the spring wire, D is the mean diameter of the spring, d is the coil diameter, and θ is the helix angle (the angle between the coils and the base of the spring). Here N_a and N^* are the number of active and inactive coils, respectively.

The helix angle θ is related to the coil-pitch \bar{p} (see Fig. 5) by: $\theta = \tan^{-1}(\bar{p}/\pi D)$. A closed-coil requires a small helix angle ($\theta \leq 15^\circ$), therefore $\cos \theta \approx 1$. For plates in contact with the end of the spring, $N^* = 2$. The number of active springs, N_a , is governed by the spring constant as: $N_a = Gd^4 / 8D^3 K$, with G the shear modulus of the wire, such that, from (7):

$$W_{Spring} \approx \left(\frac{\pi^2}{4} \right) \rho_s d^2 D \left[\frac{Gd^4}{8D^3 K} + 2 \right] \quad (8)$$

When the actuation strain ε_T is specified, the spring constant K can be determined by Eq. (4): whereupon, D , and d become the variables in the optimization problem.

2.3 Material Selection

High strength steel wires are the preferred material for lightweight springs (Ashby, 1992). Common steel wires have diameters 0.1-6.5mm. The *tensile strength* S_{ut} is a function of wire diameter d :

$$S_{ut} \cong A(d)^b \quad (9a)$$

with $A = 2.2$ GPa and $b = -0.163$ when d is measured in *mm*. The *shear strength* S_{us} is related to the ultimate tensile strength by:

$$S_{us} \cong 0.67 S_{ut} \quad (9b)$$

2.4 Maximum and Minimum Compression

The *maximum* compression of the spring occurs at the clamped end of the actuator. It is given by the sum of initial displacement $\Delta_{init} = L_{free} - L_{act}$ and the compression Δ_a induced by force F_N (due to external load N ; point A in Fig. 4):

$$\Delta_{max} = \Delta_a + \Delta_{init} = L_{free} - L_A \quad (10a)$$

$$\begin{aligned} \Delta_a &= \frac{F_N}{E_e \alpha + KL_0} L_0 \\ &= \frac{NL}{H(E_e \alpha + KL_0)} L_0 \end{aligned} \quad (10b)$$

$$F_N = \frac{NL}{H} \quad (10c)$$

$$L_{free} = \frac{E_e \alpha \varepsilon_{x0}}{K} + L_{act} \quad (10d)$$

$$L_A = L_{free} - \Delta_{max} \quad (10e)$$

When an external force is applied, the corresponding *minimum* (point B in Fig.4) is:

$$\Delta_{min} = L_{free} - L_B \quad (11a)$$

$$\begin{aligned} L_B &= L_A + 0.5 \frac{p'_e \alpha}{K + \frac{E_e \alpha}{L_0}} \\ &= L_A + 0.5 \frac{C_0 C_r}{\frac{KL_0}{\alpha} + E_e} \left(\frac{V}{z'} \right)^2 L_0 \end{aligned} \quad (11b)$$

$$z' = \frac{z_0}{(1 + \varepsilon_{xA})(1 + \varepsilon_{yA})} \quad (11c)$$

$$\varepsilon_{xA} = \frac{L_A}{L_0} - 1 \text{ and } \varepsilon_{yA} = \varepsilon_{y0} \quad (11d)$$

The realizable displacements are limited by *spring consolidation*. The usual recommendation is to provide a clash allowance of approximately 10% of the total spring deflection Δ_{max} at maximum working load, $\Delta_{solid} - \Delta_{max} \geq 0.1 \Delta_{max}$, or in non-dimensional form:

$$\frac{\Delta_{max}}{L} \leq 0.9 \left[\frac{L_{free}}{L} - \frac{L_s}{L} \right] \quad (12)$$

where $L_s = d(N_a + 3)$ for closed coil springs.

2.5 Failure Criteria

The limitation imposed by *yielding* of the spring can be expressed in non-dimensional form, as:

$$\frac{\tau_{\max}}{E_f} = 8\kappa_s \left[\frac{K}{\pi E_f L} \right] \frac{\Delta_{\max}}{L} \left(\frac{D}{L} \right) \left(\frac{L}{d} \right)^3 \quad (13)$$

where the transverse shear factor (Wahl, 1963), $\kappa_s = 1 + 0.5d/D$.

Buckling occurs if the ratio of spring displacement to free spring length L_{free} exceeds a critical value Δ_{crit}/L_{free} (Wahl, 1963):

$$c_1 \frac{\Delta_{crit}}{L_{free}} = 1 - \sqrt{1 - \left(c_2 \frac{D}{L_{free}} \xi \right)^2} \quad (14)$$

where, for steel, the constants are $c_1 = (1 + 2\nu)/(1 + \nu) = 1.23$ and $c_2 = \pi\sqrt{(1 + 2\nu)/(2 + \nu)} = 2.62$. The parameter ξ reflects the method of support. If both ends are guided axially, but free to rotate (like a hinged column), then $\xi = 1$. If both ends are guided, and prevented from rotating, then $\xi = 0.5$. Based on the maximum compression Δ_{\max} (Eq. (10)), the critical free length L_{crit} becomes:

$$L_{free} \leq L_{crit} = 0.5c_1 \Delta_{\max} \left[1 + \left(\frac{c_2 D}{c_1 \lambda \Delta_{\max}} \right)^2 \right] \quad (15)$$

Accordingly, when both ends of the spring are prevented from rotation, spring buckling will be avoided if

$$L_{free} \leq 0.615 \Delta_{\max} \left[1 + \left(4.5 \frac{D}{\Delta_{\max}} \right)^2 \right] \quad (16)$$

Torsional fatigue is dictated by the fully reversed endurance limit:

$$S_{es} = 0.5 \left[\frac{S_{ew} S_{us}}{S_{us} - 0.5 S_{ew}} \right] \quad (17)$$

where S_{ew} is the torsional fatigue strength, and S_{us} is the ultimate shear strength.

Surging must be avoided in high-speed cyclic applications. For this purpose, the natural frequency of the spring should be greater than about 12 times that of the applied forcing frequency f_{an} :

$$f_n \geq 12f_{an} \quad (18)$$

The fundamental natural frequency is,

$$f_n = \frac{2}{\pi N_a} \left(\frac{d}{D^2} \right) \sqrt{\frac{Gg}{32\rho}} \quad (19)$$

where ρ is the density of the spring material.

A lower limit on the *number of coils* must be imposed in order to obtain accuracy and control in manufacturing. A value of 3 is normally used as an absolute minimum, but a larger value can be selected to assure a small helix angle:

$$N_a = \frac{Gd^4}{8D^3K} \geq N_{\min} > 3 \quad (20)$$

3. DESIGN OF THE ACTUATING SYSTEM

The objective is to design an actuating system capable of realizing a specified performance (authority) at lowest possible overall weight, given by:

$$W = \rho_f L B t_f + \rho_c \left[\frac{L}{\cos \beta} \right] B t_c + N_m (W_{film} + W_{spring}) \quad (21)$$

where $W_{film} + W_{spring}$ is the weight of the actuation element (above) and $N_m = (L - \lambda) / 2\lambda$ is the total number of elements. The face thickness t_f / L , core member thickness t_c / L , core thickness H / L , number of layers n_{film} , actuation strain ϵ_r , mean coil diameter D / L and spring wire diameter d / L are the design variables. Failure mechanisms, spring behavior, and geometry constraints are considered.

The objective function in non-dimensional form is:

$$\Psi = \frac{W}{\rho_f B L^2} = w_{face} + w_{core} + w_{film} + w_{spring} \quad (22)$$

where

$$w_{face} = \frac{t_f}{L} \quad (22a)$$

$$w_{core} = \frac{1}{\cos \beta} \frac{\rho_c t_c}{\rho_f L} \quad (22b)$$

$$w_{film} = 0.5 \left(\frac{L}{H} \tan \beta - 1 \right) \frac{\rho_e}{\rho_f} \left(\frac{L_{act}}{L} \right) \frac{L}{B} \left\{ \pi \left(\frac{D}{L} + \frac{d}{L} \right) \frac{t_e}{L} + \pi \left(\frac{t_e}{L} \right)^2 \right\} \quad (22c)$$

$$w_{spring} = 0.5 \left(\frac{L}{H} \tan \beta - 1 \right) \frac{\pi^2}{4} \frac{\rho_s}{\rho_f} \left(\frac{d}{L} \right)^2 \left(\frac{D}{L} \right) \frac{L}{B} \left(\frac{N_a}{\cos \theta} + 2 \right) \quad (22d)$$

The weight minimization is subject to the following constraints:

Minimum deflection

$$1 - \left(\frac{1}{2} + \frac{1}{\epsilon_T} \right) \frac{H}{L} \left(1 - \cos \epsilon_T \right) \frac{L}{H} \frac{\delta_0}{L} + \frac{1}{3} \left[\frac{N}{E_f BL} \right] \frac{B}{L} \left(\frac{E_f L^4}{D_{eq}} \right) \frac{\delta_0}{L} + \frac{\delta_0}{L} \left[\frac{N}{E_f BL} \right] \frac{E_f L^2}{D_q} \leq 0 \quad (23a)$$

Face yielding

$$\frac{B}{L} \left(\frac{L}{t_f} \right) \left(\frac{L}{H} \right) \left[\frac{N}{E_f BL} \right] \frac{E_f}{\sigma_Y^f} - 1 \leq 0 \quad (23b)$$

Core yielding

$$\frac{1}{\sin \beta} \left[\frac{N}{E_f BL} \right] \frac{E_f}{\sigma_Y^c} \left(\frac{L}{t_c} \right) - 1 \leq 0 \quad (23c)$$

Core buckling

$$\frac{12}{\pi^2 \sin^3 \beta} \left[\frac{N}{E_f BL} \right] \frac{E_f}{E_c} \left(\frac{L}{t_c} \right)^3 \left(\frac{H}{L} \right)^2 \left(\frac{\pi^2 C_A + 2}{\pi^2 C_A + 4} \right) \left(\frac{\pi^2 C_B + 2}{\pi^2 C_B + 4} \right) - 1 \leq 0 \quad (23d)$$

There are multiple constraints for the actuating element:

Minimum number of coils

$$1 - \frac{1}{48(1+\nu)} \left[\frac{E_f L}{K} \right] \left(\frac{L}{D} \right)^3 \left(\frac{d}{L} \right)^4 \frac{E_s}{E_f} \leq 0 \quad (23e)$$

Limits on spring index

$$(D/L)(L/d)/20 - 1 \leq 0 \quad (\text{Upper}) \quad (23f)$$

$$1 - (D/d)(L/d)/4 \leq 0 \quad (\text{Lower}) \quad (23g)$$

Clash allowance

$$\frac{\Delta_{max}}{L} \leq 0.91 \left[\frac{L_{free}}{L} - \frac{d}{L} (N_a + 3) \right] \quad (23h)$$

Surging

$$1 - \frac{1}{6\pi N_a f_{an}} \frac{d}{D^2} \sqrt{\frac{Gg}{32\rho}} \leq 0 \quad (23i)$$

Spring compression

$$1 - \frac{L_{free}}{(1 + \epsilon_T) L_{act}} \leq 0 \quad (23j)$$

Structural integrity

$$1 - \frac{S_{es}(S_{us} - \tau_i)}{S_{es}(\tau_m - \tau_i) + S_{us}\tau_a} \leq 0 \quad (\text{fatigue}) \quad (23k)$$

$$8K_s \left[\frac{K}{\pi E_f L} \right] \left(\frac{\Delta_{max}}{L} \right) \frac{D}{L} \left(\frac{L}{d} \right)^3 \frac{E_f}{S_{ys}} - 1 \leq 0 \quad (\text{yielding}) \quad (23l)$$

$$\left[1 + \left[4.26 \frac{D}{\Delta_{max}} \left(\frac{D}{L} \right) \right]^2 \right]^{-1} \frac{L_{free}}{L} \left(\frac{L}{\Delta_{max}} \right) - 0.615 \leq 0 \quad (\text{spring buckling}) \quad (23m)$$

$$1 - \frac{L_A}{L} \frac{L}{L_0} \leq 0 \quad (\text{film buckling}) \quad (23n)$$

A MatLab program using the method of sequential quadratic programming (SQP) (Matlab, 1998) was implemented to find optimal solutions. Since the objective function has many local optima, an algorithm (Aird and Rice, 1977) based on systematic placement of points was implemented to generate starting points. Owing to manufacturing limitations on size and shape, the design parameters are often restricted to only integer (or discrete) values. For instance, design variables such as the wire diameter, corrugation angle, coil number and layer number are not continuous functions but discrete values. Therefore, finding the optimal design involves discrete programming. The SQP approach remains valid in such situations. Initially, it solves the problem by assuming continuous design variables. Then the discrete/integer values closest to the continuous optimum solutions are assigned and the design checked for feasibility using the backtrack programming method (Farkas, 1984). Through trial and error, the most feasible design closest to the continuous optimum is obtained.

4. OPTIMAL RESULTS

4.1 Optimization Procedure

Actuators made with a high strength aluminum alloy are chosen for the design examples. The material properties used are summarized in Table 1. The design parameters are listed in Table 2. The graphical method for optimization illustrates the design process (Fig. 6). The two examples use the face thickness, t_f/L , and core thickness, H/L , as co-ordinates. All of the parameters governing the actuation element have been fixed [$D/L, d/L, n_{film} = 5, \epsilon_T, \epsilon_{x0} = 500\%$ and $\epsilon_{y0} = 600\%$]. The maps have been constructed for a required end displacement, $\delta_0/L = 0.05$, and a specified load index, $\Pi = N/(E_f BL) = 1.33 \times 10^{-7}$. Two different values of the core member thickness have been used. For these cases, core yielding does not occur (it is a function of the external force and core thickness, independent of the two variables H/L and t_f/L used in Fig. 6). All of the parameters related to the actuation element depend only on the core thickness (independent of t_f/L), as indicated by the arrows along the abscissa. For the avoidance of spring yielding, film buckling and clash, the requirement is that the core thickness should *exceed* the indicated values. For these examples, the most stringent among these constraints is that due to clash, which imposes a minimum on H/L . Conversely, for the avoidance of spring buckling the core thickness must *be less than* the indicated value: whereupon, clash and spring buckling place bounds on the allowable core thickness.

Face yielding, deflection and core buckling must also be considered. It is apparent from the figures that the face yield requirement is confined to the lower left and is not a limitation. Limits are posed by the deflection constraint and by buckling of the core members. The curves representing the deflection constraint dictate the lowest allowable face thickness, as indicated on the figures. Core buckling imposes another upper limit on the core thickness. In case (a) involving the thinner core members, this limit supercedes that due to spring buckling, causing the allowable core thickness to be bound by core buckling and clash, as indicated by the permissible (shaded) domain on the figure. For case (b), with the thicker core members, the core buckling constraint displaces to larger levels of core thickness and spring buckling establishes the upper bound on the permissible domain.

It remains to ascertain which part of the permissible domain dictates the design point. This is achieved by superposing contours of constant weight. The most lightweight solution that resides within the permissible domain governs the design point, indicated by A in the figures. The optimum solutions are weight $w = 8.6 \text{ g}$, face thickness $t_f = 1.5 \text{ mm}$ and core thickness $H = 31.5 \text{ mm}$ for Fig. 6a, and weight $w = 8.6 \text{ g}$, face thickness $t_f = 1.4 \text{ mm}$ and core thickness $H = 25.6 \text{ mm}$ for Fig. 6b.

4.2 Design Examples

With Fig. 6 used to illustrate the issues that enter the optimization, a few examples are given to highlight the key considerations affecting the weight, fabrication and operating conditions. There are many different ways of posing the design problem. Here, we start by requiring that the end displacement be fixed at, $\delta_0 / L = 0.05$, and that compact transformers capable of operating at 5kV are available (Emco High Voltage, model Q50). The passive structure is made from a high strength Al alloy (Table 1).

To investigate the effect of actuation strain on the optimum design, three different values, 5%, 10% and 15%, are assigned to the design variable ϵ_T . The trends in the lowest weight and in the number of film layers n_{film} are plotted on Figs. 7a, b. The dimensions of the passive components, determined at the lowest weight designs are plotted as functions of the force to be lifted on Fig. 8. At actuation strains $\epsilon_T > 10\%$, when the loads to be lifted are large, the core thickness remains unchanged (Fig. 8c), because the corrugation angle, $\beta = 54.7^\circ$, must be maintained. Corresponding results for the spring are summarized on Fig. 9. While the coil diameter is relatively invariant with ϵ_T , especially at large forces (Fig. 9a), the spring diameter must be increased systematically as ϵ_T is increased (Fig. 9b). There are associated implications for the spring constant (Fig. 9c). It is emphasized that, for each load to be lifted, there is an explicit design solution (Figs. 7, 8, 9). Accordingly, if the design dictates a range of different loads, the design should be based on the largest and would be sub-optimal for all lower loads. In practical design, it remains to ascertain whether the dimensions satisfy minimum gauge or other fabrication limitations.

Note that increasing the actuation strain causes the face-sheet thickness to decrease (Fig. 8a) and the coil and wire diameters to increase (Figs. 9a,b), resulting in increased spring and decreased face-sheet weight. Consequently, at a fixed end load, there is an optimum actuation strain for the lowest weight. Repeating the analysis with the actuation strain as a design variable (Fig. 10) reveals that $(\epsilon_T)_{\text{optimal}} \approx 10\%$, regardless of the load to be lifted.

The attainable operational frequency (Fig. 11) increases as the load index is increased. Note that an actuator with the optimum actuation strain of about 10% can operate at a higher frequency than the actuator with a larger (15%) actuation strain, because of its lower weight and thicker face-sheet, which together provide a higher bending stiffness (Figs. 7a and 8a).

A major interplay to be addressed in a final optimization is that between weight and cost. The former is governed by the overall weight, described above, and the latter by aspects of the manufacturing related to the number of elastomer layers, n_{film} , needed to realize the weight objective. To assess some aspects of this interplay, the lowest weight is plotted as a function of the number of layers for a fixed end load of $10N$ and actuation strain, $\epsilon_T = 10\%$ (Fig. 12). For this example, the weight has a minimum when $n_{\text{film}} = 5$. This curve, combined with independent information about cost, could be used to elaborate this interplay.

There may be other limits imposed by breakdown, not specifically introduced in this optimization. All such information should be included in further optimization studies.

5. COMPARISON WITH SHAPE MEMORY ALLOY (SMA) ACTUATOR

A comparison is made with a bias spring one-way SMA actuator with similar geometrical configuration (Liang and Roger, 1992; Lu et al., 2001) (Fig. 3). The design of the passive structure remains the same. The SMA wire is resistively heated. When assembled with a helical spring, the recovery force generated by the shape

memory alloy compresses the spring. Then, when the wire is cooled, the stress induced in the SMA by the spring is designed to be large enough to enact the reverse transformation, causing the SMA wire to revert back to its initial length.

The design variables are the face-sheet thickness t_f/L , the thickness of the core members t_c/L , the SMA wire diameter d_s/L , the core thickness H/L , the mean coil diameter of spring D/L , the spring wire diameter d/L , the actuation strain ϵ_T and the remnant strain ϵ_{r0} . The design parameters are listed in Table 3. Other parameters are the same as those used for the elastomer actuator. The minimum weight as a function of the authority is plotted for both systems subject to the same design requirement, $\delta_o/L = 5\%$ (Fig. 13). Given the similarity in the achievable levels of authority, the choice between these two systems would be based on other considerations, especially power, frequency and cost.

6. CONCLUSION

A flexural actuation system based on the operating principles of electro-elastomers has been analyzed. An actuating element has been emphasized in which the primary variables are the geometrical dimensions and the failure modes. A design that integrates this basic unit into a high authority flexural actuation system has been explored. An optimization procedure has been devised and used to determine preferred designs.

The analysis establishes the authority (product of end displacement and load to be lifted), at specified electric field (5kV), by determining the minimum weight as functions of the actuation strain and the number of electro-elastomer layers. The dimensions of the constituents at the minimum weight emerge from the analysis.

A comparison with a one-way shape memory alloy system reveals that, for the same weight, full advantage can be taken of the power and frequency attributes of the electro-elastomer.

An assessment of the minimum weight against the number of electro-elastomer layers n_{film} provides a basis for a future weight/cost trade-off analysis.

APPENDIX

1. Failure Modes

Three failure modes may occur: face yielding, core yielding, and core buckling. *Face yielding* occurs when tensile stress in the face equals yield strength. To avoid face yielding at the clamped end:

$$\left[\frac{N}{E_f BL} \right] \frac{E_f}{\sigma_Y^f} \left(\frac{B}{L} \right) \frac{L}{t_f} - 1 \leq 0 \quad (A1)$$

where E_f is the Young's modulus. To avoid *core yielding*:

$$\frac{1}{\sin \beta} \left[\frac{N}{E_f BL} \right] \frac{E_f}{\sigma_Y^c} \left(\frac{L}{t_c} \right) - 1 \leq 0 \quad (A2)$$

Beam theory is adopted to study the *buckling of the core* (Weiernicki et al., 1991).

The Euler buckling load F_{cr} for the core is:

$$F_{cr} = \frac{\pi^2 E_c I_c}{(k_e L_c)^2} \quad (A3)$$

where $E_c I_c$ is the bending stiffness, and k_e is the effective length factor for column buckling, determined from structural steel design practice (Tall, 1974; Weiernicki et al., 1991) as:

$$k_e = \left[\frac{(\pi^2 C_A + 2)(\pi^2 C_B + 2)}{(\pi^2 C_A + 4)(\pi^2 C_B + 4)} \right]^{1/2} \quad (A4)$$

Here,

$$C_A = \frac{\sin \beta}{12H} \left[\frac{E_c B t_c^3}{\frac{3(EI)_{act}}{H} \tan \beta + \frac{E_c B t_c^3}{4H} \sin \beta} \right] = \left\{ \frac{3}{\cos \beta} \frac{(EI)_{act}}{E_f L^4} \frac{E_f}{E_c} \frac{L}{B} \left(\frac{L}{t_c} \right)^3 + 3 \right\}^{-1}$$

$$C_B = \left(\frac{E_c I_c}{L_c} \right) \left(\frac{1}{R_B} \right) = \frac{E_c B t_c^3 \sin \beta}{12H} \left[\frac{E_f B t_f^3}{4H} \tan \beta + \frac{E_c B t_c^3}{4H} \sin \beta \right]^{-1} = \left\{ \frac{36}{\cos \beta} \frac{E_f}{E_c} \left(\frac{t_f}{L} \right)^3 \left(\frac{L}{t_c} \right)^3 + 3 \right\}^{-1}$$

with

$$R_A = \sum \frac{3E_f I_f}{p_f} = 3 \left(\frac{2(EI)_{base}}{2\lambda} + \frac{E_c B t_c^3}{12L_c} \right) = \frac{3(EI)_{act}}{H} \tan \beta + \frac{\sin \beta E_c B t_c^3}{4H}$$

$$R_B = \sum \frac{3E_f I_f}{p_f} = 3 \left(\frac{2E_f B t_f^3}{12(2\lambda)} + \frac{E_c B t_c^3}{12L_c} \right) = \frac{E_f B t_f^3}{4H} \tan \beta + \frac{E_c B t_c^3}{4H} \sin \beta$$

In the above expressions, the equivalent stiffness of the actuation element consists of the stiffness of the spring (Wahl, 1963) and the electro-elastomer multi-layer, which can be described as:

$$(EI)_{act} = \frac{\pi E_e}{64} \left[(D + d + 2t_e)^4 - (D + d)^4 \right] + \frac{L_{free} E_s G d^4}{16N_a D(2G + E_s)} \quad (A5)$$

Failure can be avoided if the member stress σ_c arising from the applied force N is less than the critical stress $F_{cr} / B t_c$:

$$\frac{12}{\pi^2 \sin^3 \beta} \left[\frac{N}{E_f B L} \right] \frac{E_f}{E_c} \left(\frac{L}{t_c} \right)^3 \left(\frac{H}{L} \right)^2 k_e^2 - 1 \leq 0 \quad (A6)$$

To determine the *tip deflection*, the small constraining effect from the core is ignored. The stiffness of the electrodes is also neglected. The length change upon actuation, $\Delta L = \epsilon_r L$, causes the beam to bend upwards, with a tip deflection δ_1 given by:

$$\frac{\delta_1}{L} = \left(\frac{1}{2} + \frac{1}{\epsilon_r} \right) \frac{H}{L} \left(1 - \cos \epsilon_r \frac{L}{H} \right) \quad (A7)$$

The tip deflection δ_2 due to external force N applied at the free end is (Allen, 1969)

$$\frac{\delta_2}{L} = \frac{1}{3} \left[\frac{N}{E_f B L} \right] \frac{B}{L} \left[\frac{E_f L^4}{D_{eq}} \right] + \left[\frac{N}{E_f B L} \right] \frac{E_f L^2}{D_q} \quad (A8)$$

where D_{eq} and D_q are the equivalent flexural and transverse shear stiffness of the actuator, respectively: D_{eq} can be derived from simple beam theory (Zenkert, 1995):

$$D_{eq} = (E_e \alpha (1 + \epsilon_0) + K L_{act}) \left(\frac{H}{2} + e \right)^2 + \frac{1}{3} E_f B \left\{ \left(\frac{H}{2} - e + t_f \right)^3 - \left(\frac{H}{2} - e \right)^3 \right\}$$

where

$$e = \frac{1}{2} \frac{E_f B t_f (H + t_f) - (E_e \alpha (1 + \epsilon_0) + K L_{act}) H}{E_e \alpha (1 + \epsilon_0) + K L_{act} + E_f B t_f}$$

is the distance between the neutral axis of the actuation element and the center of core, D_q can be described as (Lu et al., 2001):

$$D_q = E_c B d_c \sin^2 \beta \cos \beta$$

Based on the overall deflection $\delta = \delta_1 - \delta_2$, the deflection constraint for the actuator is given by

$$\delta_f = \delta_1 - \delta_2 \geq \delta_0 \quad (\text{A9})$$

where δ_0 represents the minimum deflection that the actuator must attain to satisfy design objectives.

2. Natural Frequency

For a cantilever fixed at one end, the resonance frequency in bending is (Young, 1989):

$$\omega = \frac{k^2}{2\pi L^2} \left(\frac{D_{eq}}{m} \right)^2 \quad (\text{A10})$$

where $k=1.875$ for the first mode and 4.69 for the second mode, D_{eq} is the equivalent bending stiffness of the cantilever, and $m=W/L$ is the mass per unit length.

Acknowledgements

This work is supported by the DARPA MURI project on multifunctional materials.

References

- Aird T.J., and J.R. Rice, 1977. Systematic search in high dimensional sets, SIAM Journal on Numerical Analysis, 14, 296-312.
- Allen H.G., 1969. Analysis and Design of Structural Sandwich Panels. Pergamon Press, Oxford.
- Ashby M.F., 1992. Materials Selection in Mechanical Design. Pergamon Press, Oxford.
- Farkas J., 1984. Optimum Design of Metal Structures. Ellis Horwood Ltd., Chichester
- Juvinall R.C. and Marshek K.M., 1999. Fundamentals of Machine Component Design. Wiley, New York.
- Lu T.J., Hutchinson J.W. and Evans A.G., 2001. Optimal design of a flexural actuator, J. Mech. Phys. Solids, 49, 2071-2093.
- Lu T.J. and Evans, A.G., 2002. Design of a high authority flexural actuator using an electrostrictive polymer, Sensors and Actuators, A 99, 290-296.
- Liang C. and Rogers C.A., 1992. Design of shape memory alloy actuators, J. Mechanical Design, 114, 223-230.
- Matlab 5. 1998, Mathworks Inc.

- Pelrine R.E., Kornbluh R. and Joseph J.P., 1998. Electrostriction of polymer dielectrics with compliant electrodes as a means of actuation, *Sensors and Actuators, A* 64, 77-85.
- Pelrine R., Kornbluh R., Pei Q. and Joseph J., 2000. High-speed electrically actuated elastomers with strain greater than 100%, *Science*, 287, 836-839.
- Pelrine R., Sommer-Larsen P., Kornbluh R., Heydt R., Kofod G., Pei Q and Gravesen P., 2001. Applications of dielectric elastomer actuators, In: *Smart Structures and Materials 2001: Electroactive Polymers and Devices*, Proceedings of SPIE 4329, 335-349.
- Tall L., 1974. *Structural Steel Design* (2nd Ed.). The Ronald Press Co., New York.
- Wahl A.W., 1963. *Mechanical Springs* (2nd Ed.). McGraw-Hill Inc, New York.
- Weiernicki C.J., Liem P.E., Woods G.D. and Furio A.J., 1991. Structural analysis methods for lightweight metallic corrugated core sandwich panels subjected to blast loads, *Naval Engineering J.* 103, 192-203.
- Wood D., Burdess J.S. and Harris A.J., 1998. Actuators and their mechanisms in microengineering, *IEEE Engineering Science and Education Journal* 7(1), 19-27.
- Young W.C., 1989. *Roark's Formulas for Stress and Strain*. McGraw-Hill, New York.
- Zenkert D., 1995. *An Introduction to Sandwich Construction*. Warley, West Midlands.

Table1 Material parameters used in the example study

Material	Young's Modulus $E(GPa)$	Yield Strength $\sigma_y(MPa)$	Density $\rho(Kg / m^3)$
Aluminum Alloy 2014-T6	75	400	2790
VHB4910 Tape	3.10^{-3}	----	960
Polymer	2	40	1300
Music wire A228	210	-----	7800

Table 2 Design parameters used in the example study

Width B (m)	0.01
Length L (m)	0.1
Corrugation angle (β)	$\tan^{-1}\sqrt{2} = 54.7^\circ$
Minimum size of music wire (mm)	0.1
Minimum deflection δ_0 / L	5%
Pre-strain in x direction ε_{x0}	500%
Pre-strain in y direction ε_{y0}	600%
Applied voltage (kV)	5
Initial thickness of 3M VHB4910 tape (z_0) (mm)	1

Table 3 Design parameters of the SMA actuator

$E_A = 90\text{GPa}$	$E_M = 30\text{GPa}$
$\sigma_Y^A = 300\text{MPa}$	$\sigma_Y^M = 100\text{MPa}$
$\rho_{SMA} = 6500\text{kg/m}^3$	$\epsilon_{\max} = 6.7\%$

LIST OF FIGURES

- Fig. 1 The flexural structure with actuation elements
- Fig. 2 Operating principle of the dielectric elastomer actuator
- Fig. 3 Typical actuation element of an sma actuator
- Fig. 4 Typical work cycle of an actuation element
- Fig. 5 Typical helical compression spring
- Fig. 6 Two examples of the graphic method design:
(a) $D = 13mm, d = 1mm, t_c = 0.2mm$
(b) $D = 13mm, d = 1mm, t_c = 0.24mm$
- Fig. 7 (a) Minimum weight and (b) Number of layers plotted as functions of load index
- Fig. 8 The dimensions of the passive components of the actuation system at the lowest weight designs plotted as functions of load index $N / E_f BL$
- Fig. 9 The spring design parameters at the minimum weight designs
- Fig. 10 Optimum actuation strain plotted as a function of load index
- Fig. 11 Natural frequency of the actuator plotted as a function of load index
- Fig. 12 Effect of number of elastomer layers on the lowest weight
- Fig. 13 Minimum weight plotted as a function of authority: comparison between SMA and elastomer actuators

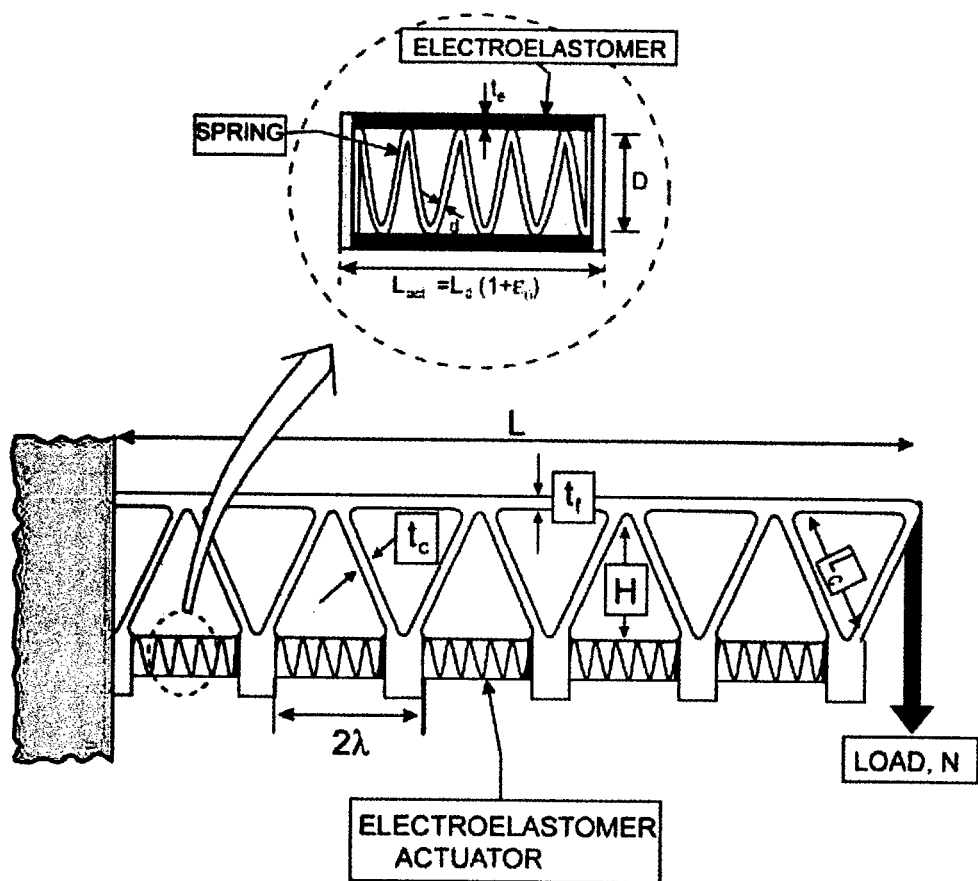


Figure 1

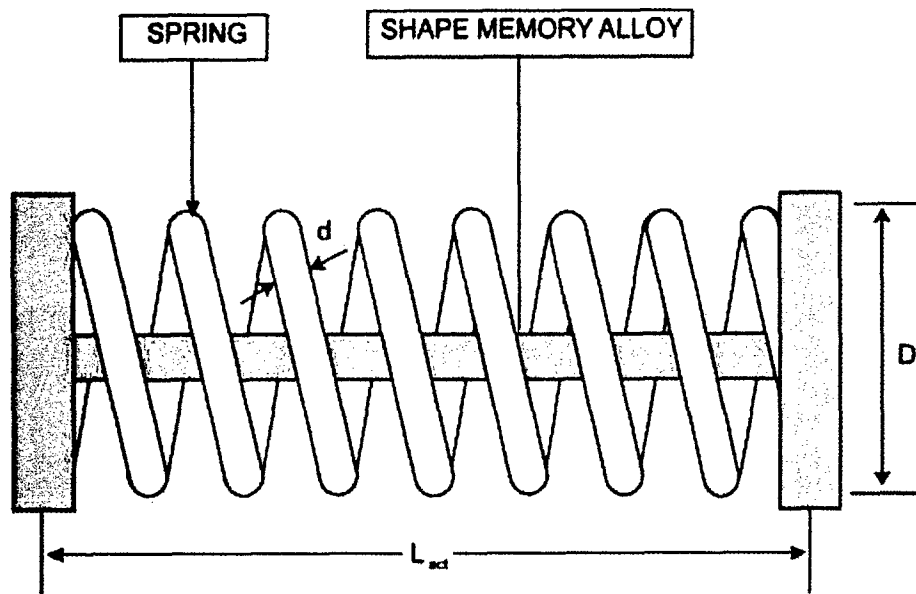


Figure 2

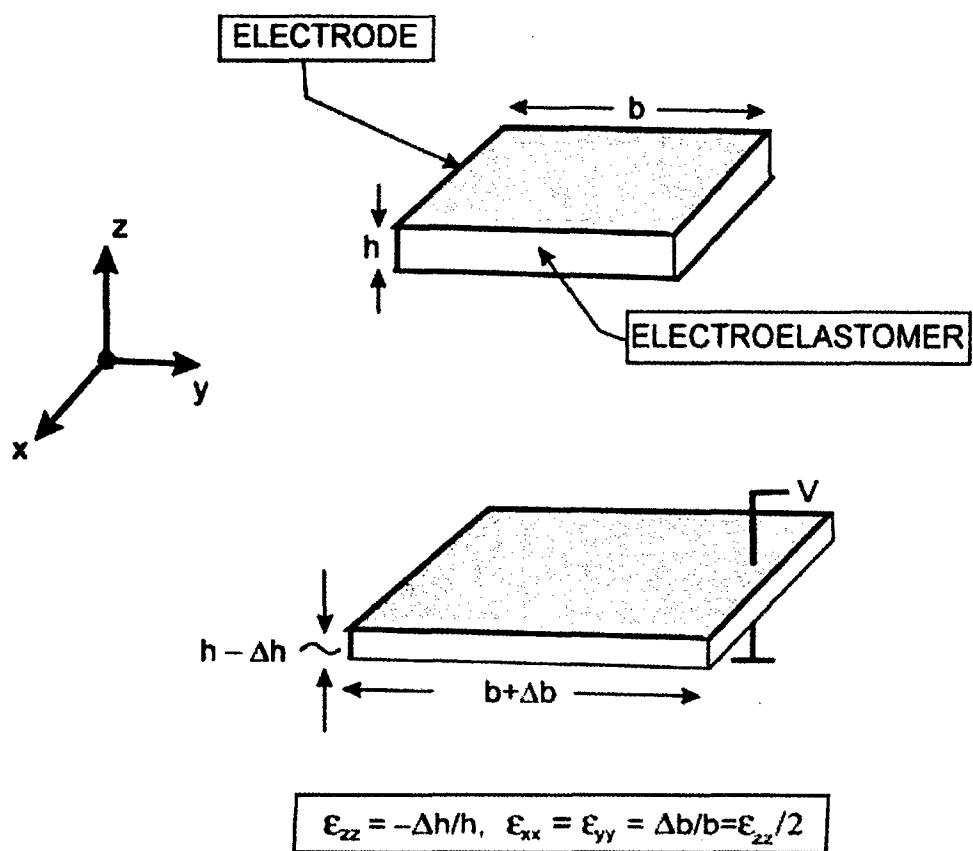


Figure 3

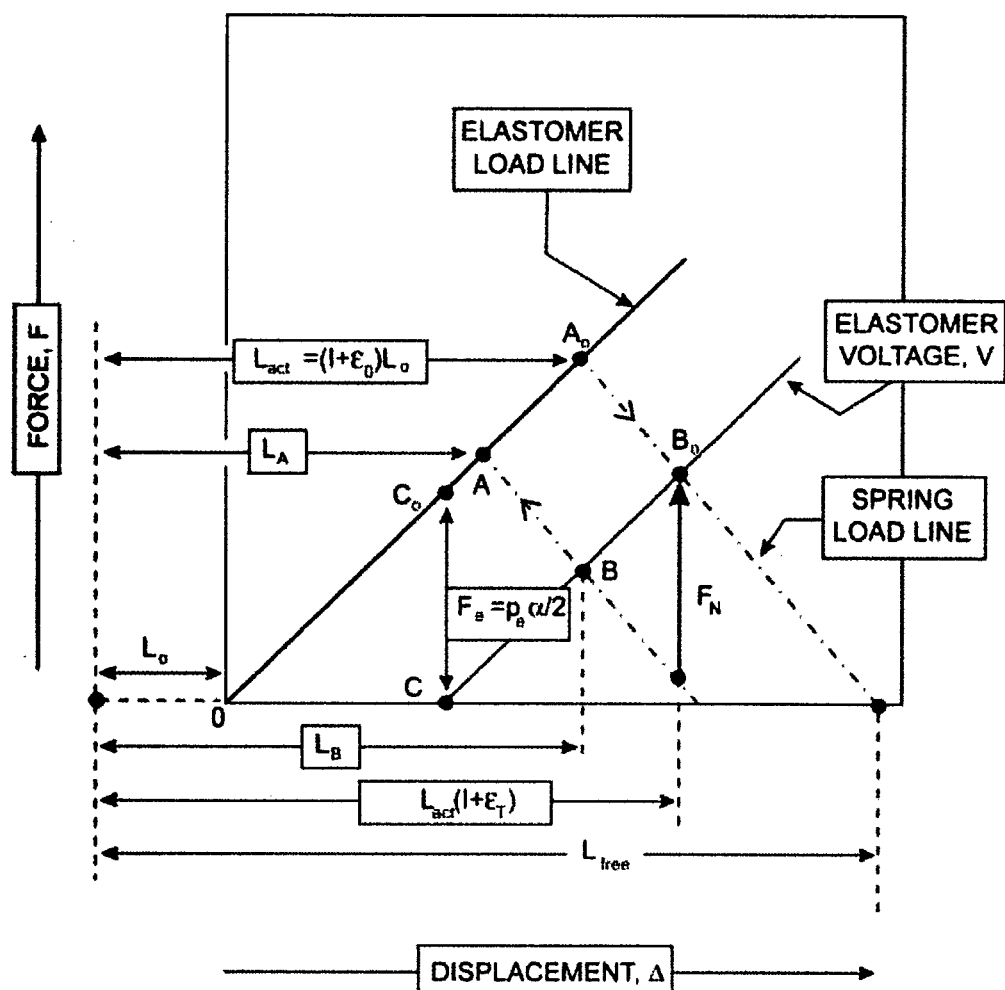


Figure 4

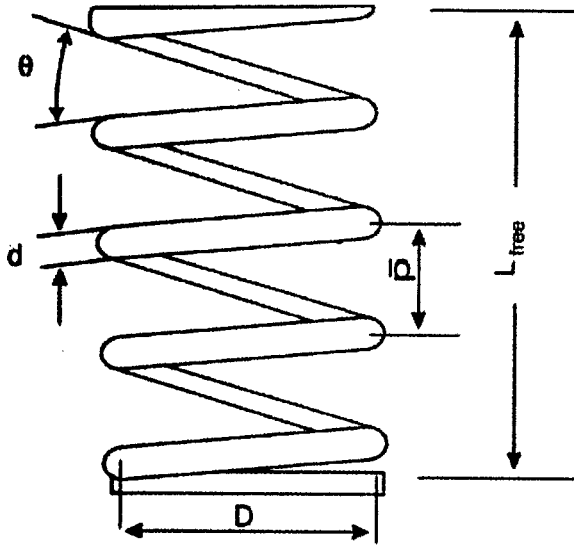


Figure 5

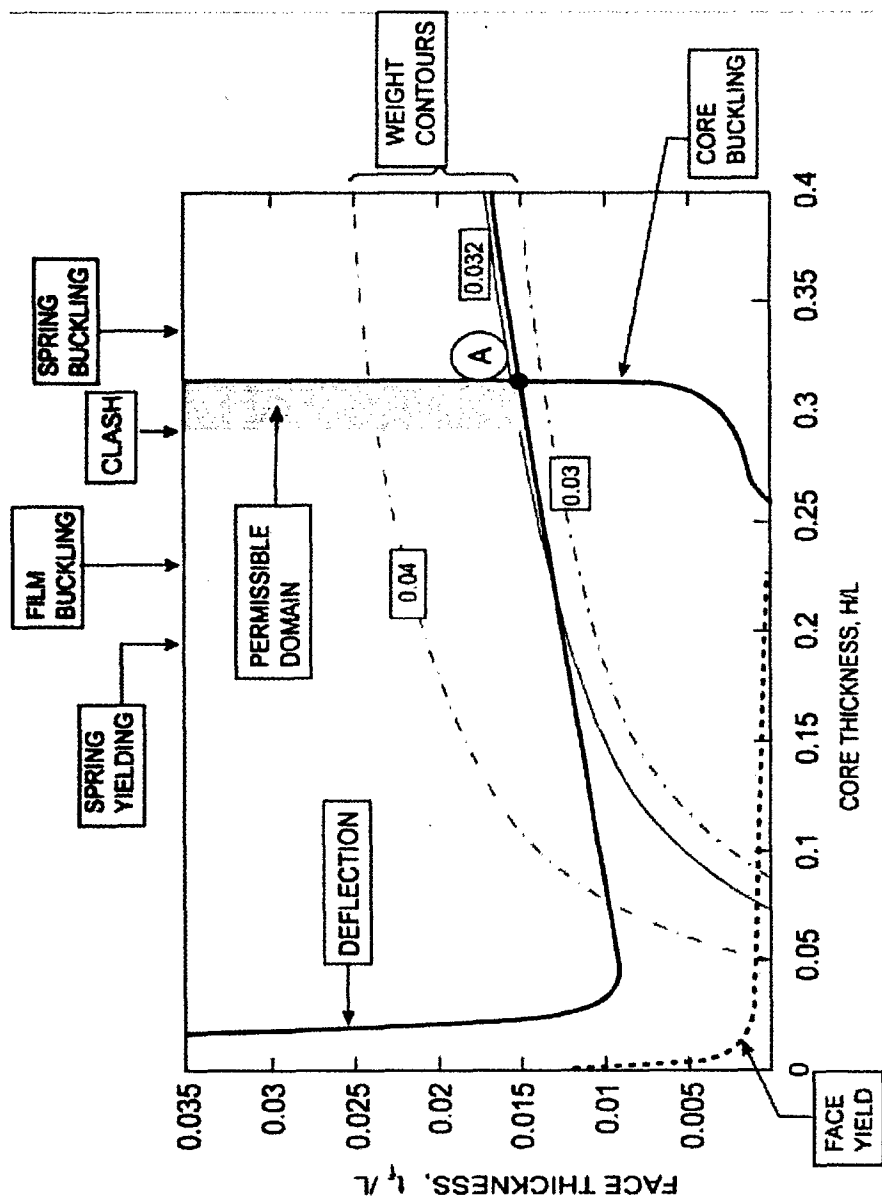


Figure 6a

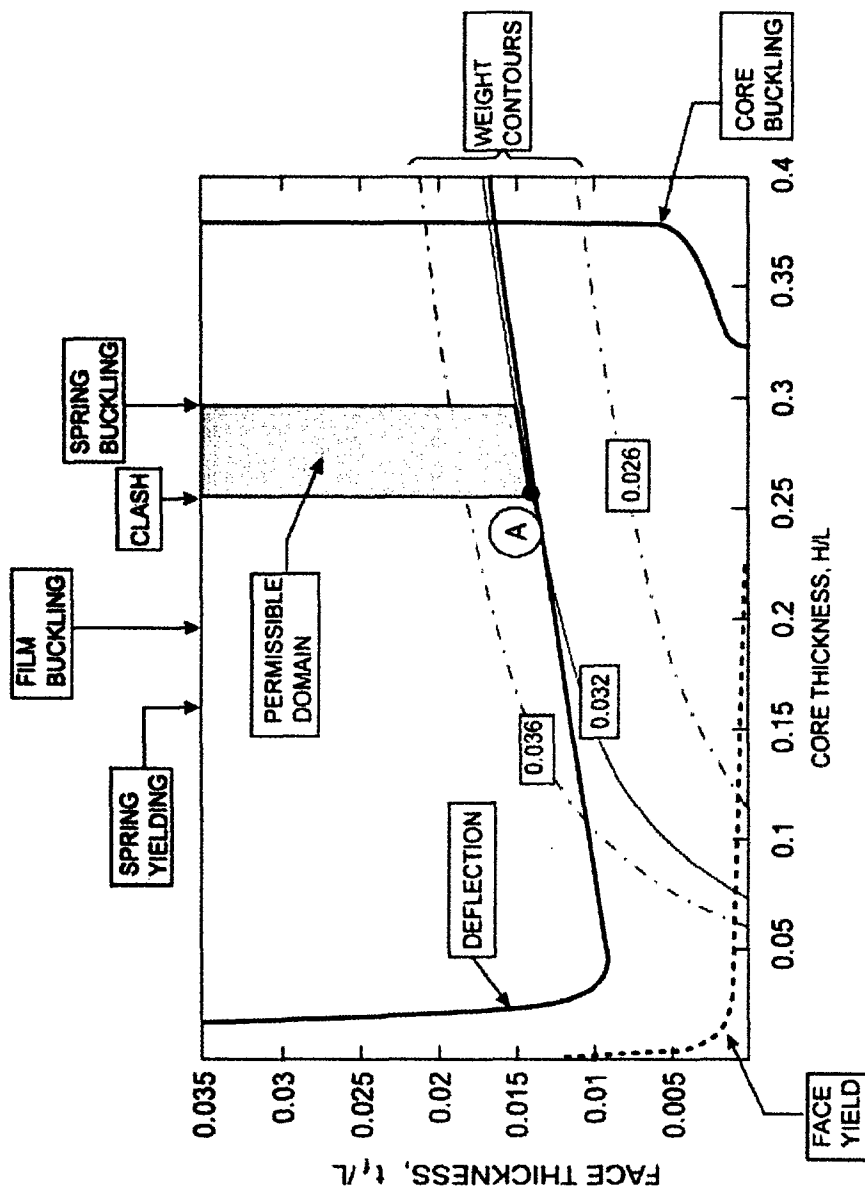


Figure 6b

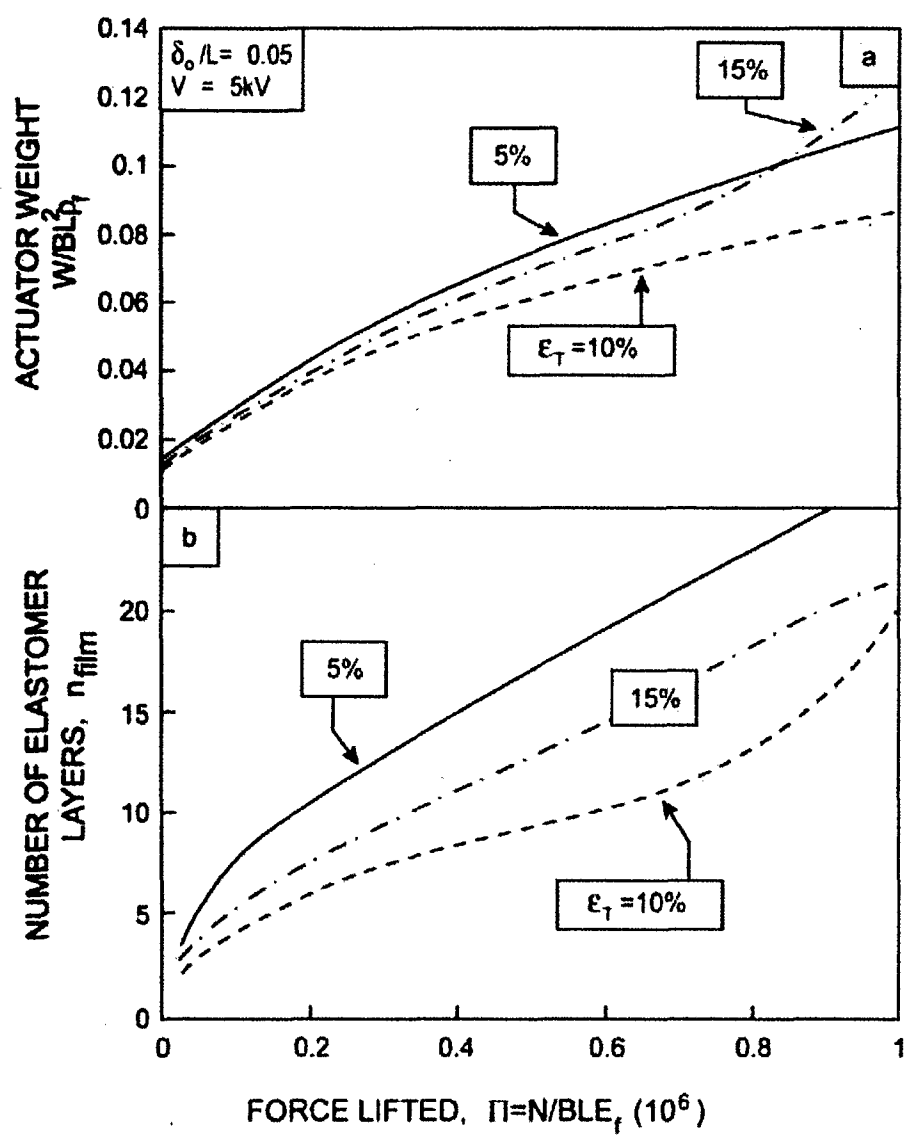


Figure 7

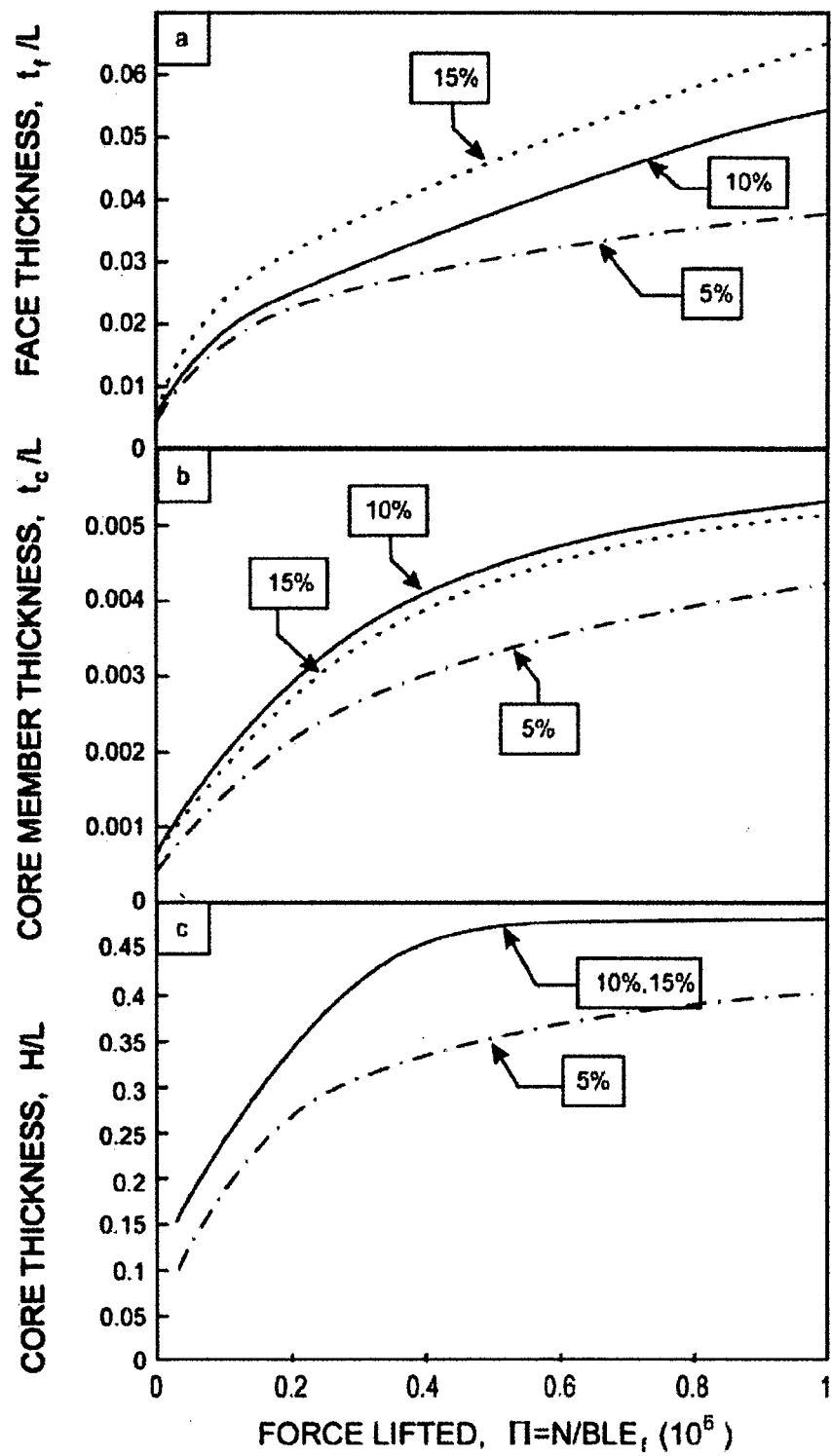


Figure 8

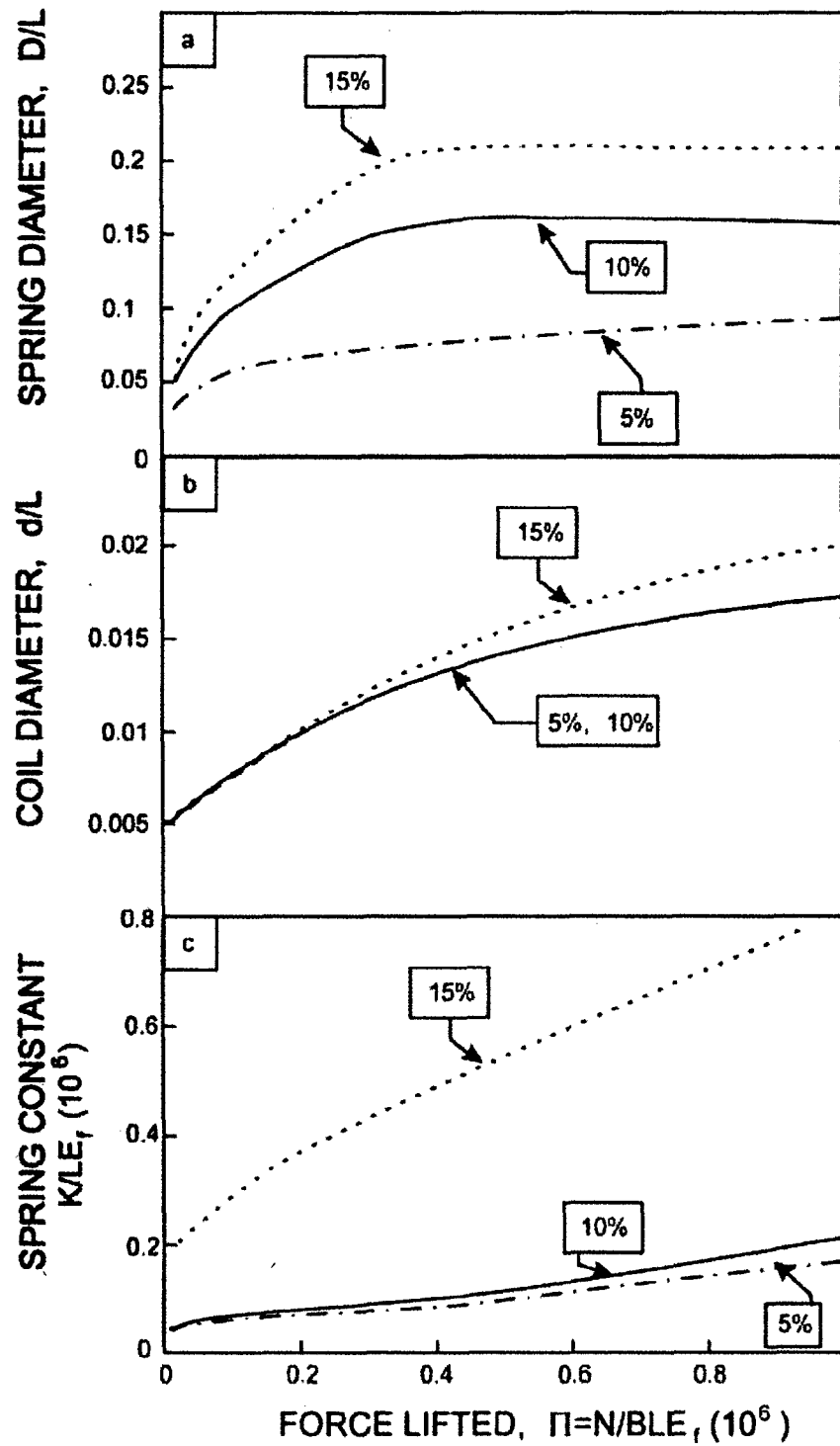


Figure 9

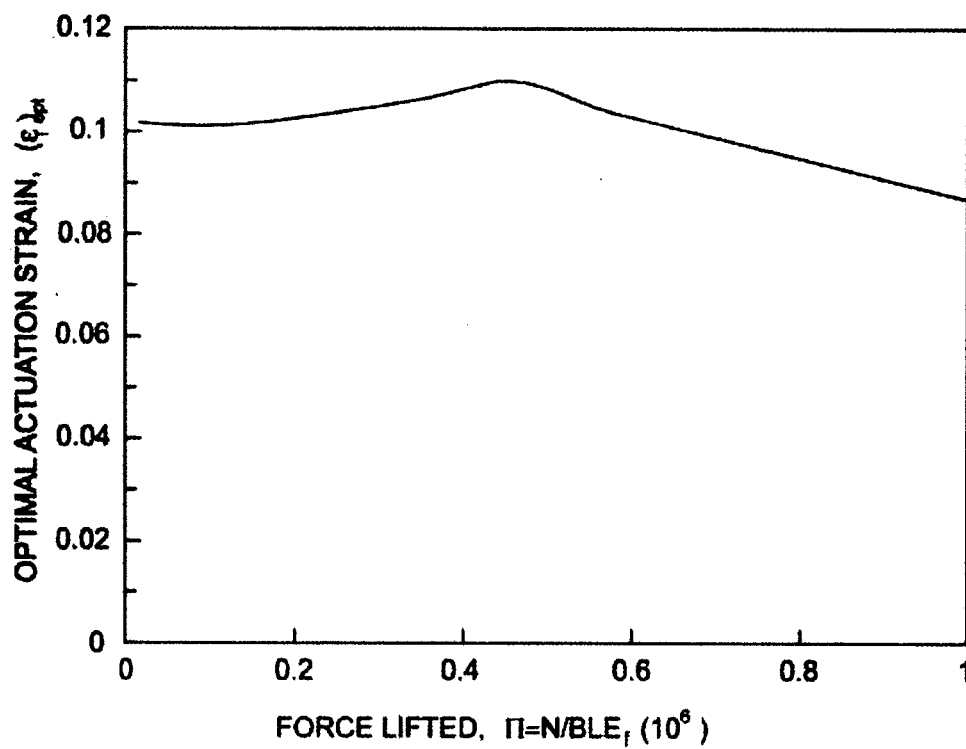


Figure 10

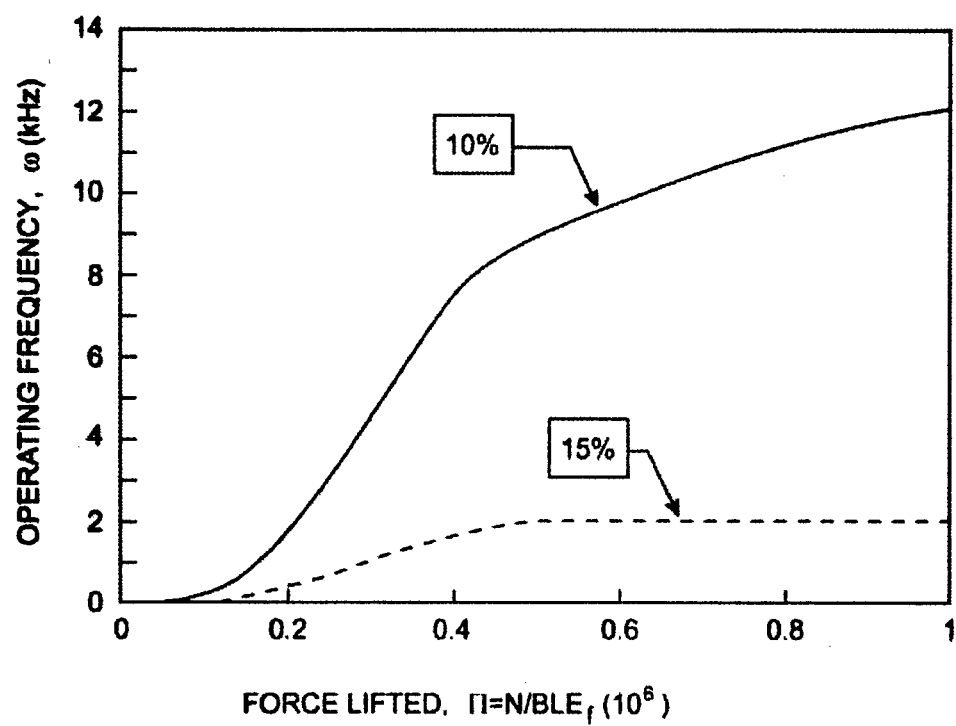


Figure 11

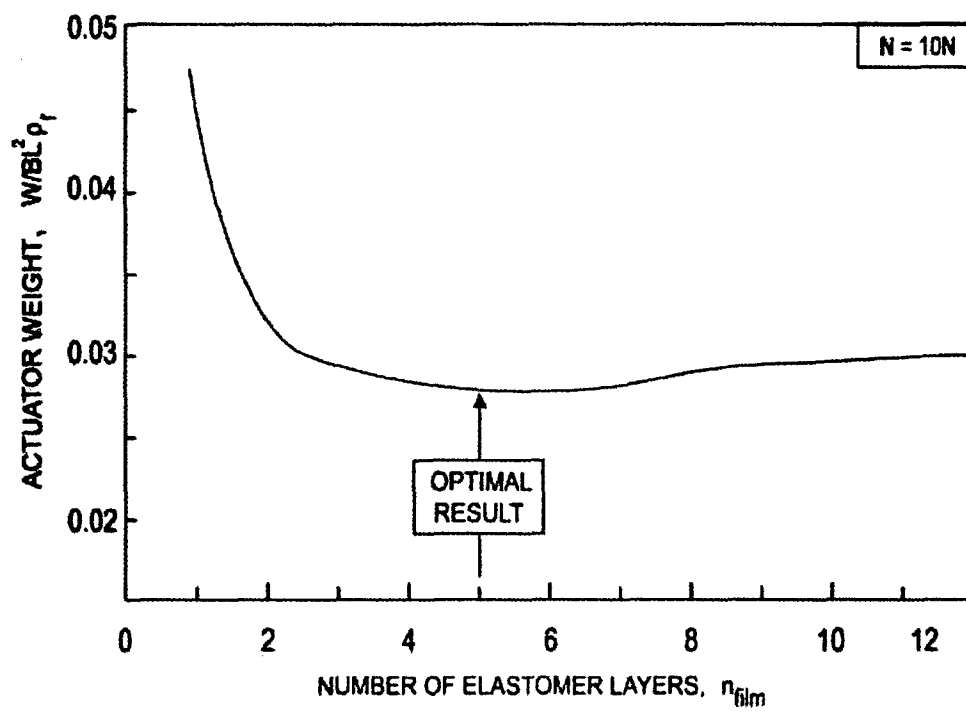


Figure 12

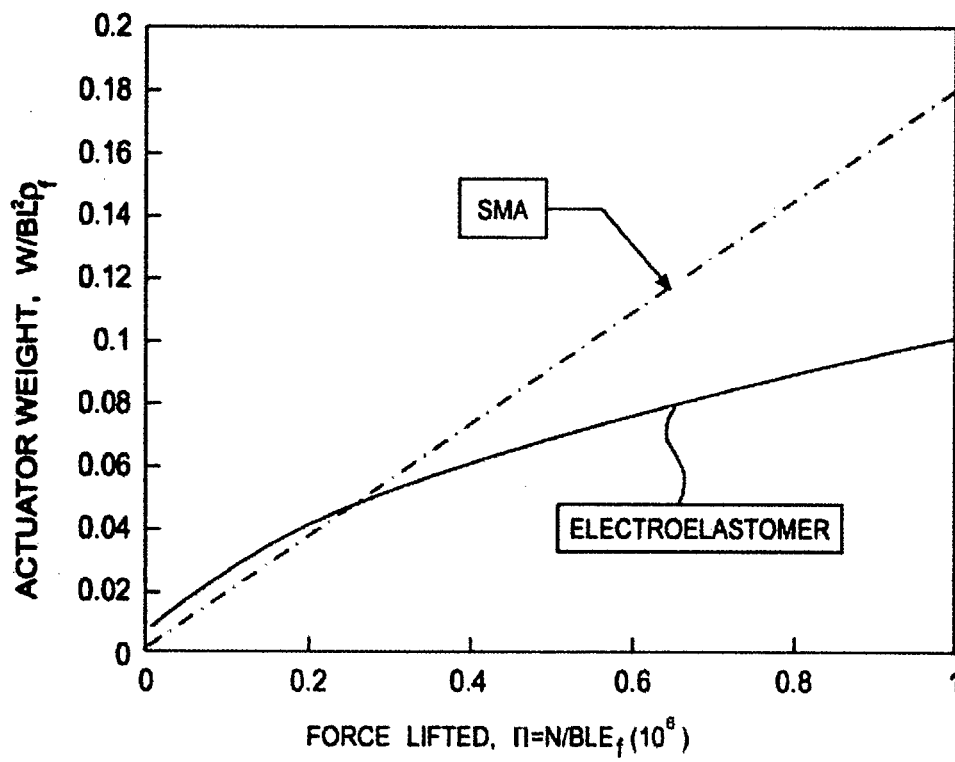


Figure 13

Part IX: Actuation of the kagome double layer grid.
**Part 1: Prediction of performance of the
perfect structure**

Actuation of the Kagome Double Layer Grid.

Part 1: prediction of performance of the perfect structure

D. D. Symons, R. G. Hutchinson and N. A. Fleck

Cambridge University Engineering Department, Trumpington St.,
Cambridge, CB2 1PZ, UK

Abstract

The Kagome Double Layer Grid is a sandwich-like structure, based on the planar Kagome pattern, which has properties that make it attractive for application as a morphing material. In order to understand the passive and active properties of the Kagome Double Layer Grid with rigid joints an analysis is made of the determinacy of the pin-jointed version. The number of internal mechanisms and states of self-stress of the finite pin-jointed structure are calculated as a function of the size of the structure. A statically and kinematically determinate version is obtained by relocating the internal nodes and by prescribing a set of patch bars around the periphery. The actuation performance of the rigid-jointed version is then explored theoretically by replacing a single bar in the structure by an actuator. The resistance to actuation is determined in terms of the stiffness and the allowable actuation strain as dictated by yield and buckling. The paper concludes with the optimal design of a double layer grid to maximise actuation performance.

Keywords: A: buckling; B: elastic-plastic material; structures; C: stability and bifurcation; morphing structures

1. Introduction

There is increasing interest in the development of morphing materials which are stiff to external loads yet can undergo large changes of shape upon actuation by lengthening (or shortening) some part of the material. One strategy for identifying useful morphing materials is to consider periodic, pin-jointed trusses. If the *pin-jointed* structure is both kinematically determinate (no internal mechanisms) and statically determinate (no internal states of self-stress), it will be stiff under passive (i.e. static and external) loads, but will become a mechanism when any bar is actuated. It is anticipated that the rigid-jointed version of a statically and kinematically determinate pin-jointed structure will inherit a morphing capability. This approach is different from current methods of topology optimization for morphing materials, see for example Bendsøe and Sigmund (2002). In the topology optimization of morphing materials, the ideal topology of compliant mechanism is generated by selective material placement in order to achieve an overall objective against a set of constraints. A systematic procedure for translating the compliant mechanism into an equivalent statically and kinematically determinate pin-jointed structures remains a research challenge.

The hunt for a periodic, statically and kinematically determinate 2D or 3D structure is a challenging task. Recently, Guest and Hutchinson (2003) have proved that no such infinite periodic structure exists. Hutchinson (2004) has shown, however, that the finite planar Kagome grid, with suitable patch bars on the periphery, is both statically and kinematically determinate, see Fig. 1a. In the present paper we consider the finite Kagome double-layer grid (KDLG) as shown in Fig. 1b, and we show that the pin-jointed version can be made to be both statically and kinematically determinate by perturbing the location of internal nodes and by prescribing a set of patch bars around the periphery. The double layer grid can exist as a flat plate, or can be distorted into a shell-like structure with single or double curvature. We leave to a subsequent study the analysis of the fully 3D Kagome structure, with the microstructure of Tridymite.

1.1. *The planar Kagome truss*

Consider the planar Kagome truss as sketched in Fig. 1a, with each truss bar made from a linear elastic solid of Young's modulus E_S . Hyun and Torquato (2002) have shown that the elastic, infinite version has in-plane effective properties which are close to optimal, and attains the upper Hashin-Shtrikman bound for a two-phase composite (where one phase is empty space). In the dilute limit, the in-plane Young's modulus E scales with the relative density of the cellular solid $\bar{\rho}$ according to

$$E = \frac{1}{3} \bar{\rho} E_S \quad (1)$$

and the Poisson's ratio is $\nu = 1/3$, see Hutchinson et al. (2003). Hutchinson (2004) has shown that the infinite pin-jointed structure has an infinite number of internal periodic collapse mechanisms, but none of these mechanisms produce macroscopic strain. This explains the paradox that the Kagome structure is stiff yet has internal collapse mechanisms.

1.2. *The Kagome Double Layer Grid*

Two alternative "sandwich" constructions can be derived from the planar Kagome truss, as has been proposed by Hutchinson et al. (2003). One scheme is to attach a single planar Kagome truss to a solid plate via a tetrahedral core; such a structure has been considered by dos Santos et al. (2004). The second is the "Kagome Double Layer Grid" (KDLG), comprising two planar Kagome trusses and a double layer tetrahedral core. The topology of the KDLG can be represented by an assembly of tetrahedra, with each tetrahedron defining the location of six neighbouring bars. In the actual structure, the faces of each tetrahedron do not exist: they are shown in Fig. 1b in order to help visualise the structure. The extensional stiffness and bending stiffness of the KDLG are high due to the fact that it behaves as a sandwich plate with planar Kagome grids as the faces. In this paper we explore the properties of the KDLG.

1.3. *Outline of the study*

The structure of the paper is as follows. First, linear algebra is used to investigate the properties of the finite pin-jointed KDLG. The number of internal mechanisms m and states of self-stress s is calculated as a function of the size of the structure. Second, a statically and kinematically determinate version is obtained by perturbing the location of internal nodes to thereby introduce asymmetry, and by prescribing a set of patch bars around the periphery. The actuation performance of the rigid-jointed version is explored by replacing a single bar by an actuator. The allowable actuation strain is dictated by yield and buckling of the KDLG. The paper concludes with a discussion of the effect of material properties and geometry upon actuation performance.

2. **Determinacy of pin-jointed structures**

It is envisaged that most practical realisations of the KDLG will have joints which have high rotational stiffness. However, the structural response can be informed by a consideration of the pin-jointed truss of identical topology. In this section a matrix analysis is performed on pin-jointed, rigid-bar KDLG structures in order to explore whether internal mechanisms and states of self-stress exist. To achieve this the equilibrium (or equivalently the kinematic) matrix of the rigid, pin-jointed structure is analysed using the methodology of Calladine (1978), Pellegrino and Calladine (1986) and Pellegrino (1993). The fundamental set of subspaces of the equilibrium matrix is obtained by a singular value decomposition procedure, implemented within the software package MATLAB (2002). These subspaces provide the states of self-stress and internal mechanisms.

2.1. *The search for a statically and kinematically determinate KDLG*

Maxwell's equation, as modified by Calladine (1978), for a finite pin-jointed truss of b bars and j joints is

$$s - m = b + c - dj \quad (2)$$

where s is the number of states of self-stress, m the number of mechanisms, c the number of constraints in the structure and d is the dimension of the problem (2 for a

planar structure, and 3 for a three-dimensional lattice). A statically and kinematically determinate structure has the property that $s = m = 0$, and we seek such a structure as the ideal topology for a morphing material.

The finite KDLG has a reduced connectivity at the periphery giving rise to mechanisms $m > 0$. Additional boundary bars can be added to remove these mechanisms; we refer to the finite structure with these additional bars as “patched”.

But there remains a problem. Both the unpatched and patched KDLG possesses $s > 0$ due to its symmetry about the mid-plane. This symmetry can be broken by moving the joints of the mid-plane: the resulting KDLG is referred to as “asymmetric”. For consistency, the KDLG is referred to as “symmetric” when it is symmetric about the mid-plane. We shall show that an asymmetric, patched KDLG gives us $s = m = 0$.

2.2. *Symmetric structure*

2.2.1 *States of self-stress*

Matrix analysis of “symmetric” KDLGs reveals that states of self-stress exist ($s > 0$) for KDLGs containing a sufficiently large number of bars. States of self-stress are combinations of bar tensions that are in equilibrium with zero external loads. Such states of self stress are undesirable for a morphing structure as they may be excited by the extension of any bar in the structure, thereby producing a high resistance to bar actuation.

The “7-hexagon” structure is the smallest symmetric KDLG that contains a state of self-stress ($s = 1$). The name “7-hexagon” indicates the number of whole hexagons visible in a plan view of the grid, and this structure with its attendant state of self-stress is shown in Fig. 2a. The colours indicate the magnitude of the axial force within each bar according to the legend. Absolute values are arbitrary, but the magnitude of the vector of bar forces has been normalised to give a maximum value of unity.

A singular value decomposition of the equilibrium matrix of the symmetric KDLG structure reveals that each state of self-stress has a mechanism associated with it. Each mechanism involves equal and opposite out-of-plane displacements of adjacent nodes on the faces of the KDLG, as sketched in Fig. 2b. These mechanisms of the

pin-jointed truss are reflected by unwanted compliant modes of deformation in the rigid-joint configuration.

Consider a plan view of a KDLG with n hexagons per side, see Fig. 3. The total number of hexagons, H , in a plan view of the double layer grid is

$$H = 3n^2 - 3n + 1 \quad (3)$$

The $H = 7$ structure ($n = 2$) contains a single state of self-stress. Larger structures contain additional states of self-stress; the number of these states equals the number of 7-hexagon units contained within the structure. A simple formula can thereby be derived, such that the number of states of self-stress for a KDLG comprising n hexagons per side is

$$s = 3n^2 - 9n + 7 \quad \text{for } n > 1 \quad (4)$$

These relationships are plotted in Fig. 3. The implication is that larger, symmetric, KDLG structures provide increasing resistance to actuation and will therefore be increasingly less suitable for actuation.

2.3. *Asymmetric structure*

The “symmetric” pin-jointed KDLG contains both states of self-stress and mechanisms. Consequently, it is not an ideal morphing material. Numerical experimentation using matrix analysis of the pin-jointed KDLG reveals that breaking the mid-plane symmetry of the KDLG removes the states of self-stress (and also removes the complementary mechanisms). This is done by moving the mid-plane nodes alternately up and down to produce an “asymmetric” KDLG, as illustrated in Fig. 4. This sequence of nodal re-positioning has the distinct advantage that it gives rise to a core which can be fabricated by folding.

2.4. *Patching scheme*

The finite asymmetric KDLG contains no states of self-stress ($s = 0$) and is therefore statically determinate. To make the structure kinematically determinate ($m = 0$) the remaining mechanisms must be “switched off” by a peripheral patching scheme.

We consider first a planar Kagome grid of n hexagons per side, and derive the required patching scheme. This grid contains $6n^2$ triangles, $b=18n^2$ bars, and $j=9n^2+3n$ joints. Recall that the finite, planar Kagome grid contains no states of self stress, $s=0$. Upon applying three constraints, $c=3$, to prevent rigid body motions, the number of mechanisms (and therefore the number of required patch bars) follows from the 2D version of Maxwell's equation

$$s - m = b + c - 2j \quad (5)$$

giving

$$m = 6n - 3 \quad (6)$$

Thus, for the planar 7-hexagon Kagome grid ($n=2$) we require 9 patch bars. There remains an arbitrary choice in the location of the patch bars, but the arrangement shown in Fig. 1a is systematic and straightforward to generate.

The same approach is used to obtain the required number of patch bars for the three dimensional KDLG. A KDLG with faces containing n hexagons per side has a total of $12n^2$ tetrahedra and therefore the number of bars is

$$b = 72n^2 \quad (7)$$

The number of joints is

$$j = 24n^2 + 6n \quad (8)$$

If we apply 6 constraints ($c=6$), to prevent rigid body motions the three dimensional form of Maxwell's equation

$$s - m = b + c - 3j \quad (9)$$

implies

$$m - s = 18n - 6 \quad (10)$$

For the asymmetric KDLG we have $s=0$ and therefore the required number of patch-bars is $18n-6$. The associated patching scheme is sketched in Fig. 1b. The scheme for the top and bottom faces and the mid-plane nodes closely resembles that sketched in Fig. 1a for the planar Kagome grid. Three additional patch bars complete the patching scheme and these bars connect the top and bottom layers of the KDLG.

2.5. Case study: the 7-hexagon KDLG

Consider the 7-hexagon KDLG; as noted above, this is the smallest KDLG which can contain a state of self-stress. The number of states of self-stress s and mechanisms m have been calculated for the patched and unpatched KDLG in both its symmetric and asymmetric forms. The results for the four topologies are summarised in Table 1.

The 7-hexagon unpatched KDLG comprises 48 tetrahedra, 288 bars, and 108 joints, as listed in Table 1. Now invoke Maxwell's equation, $s - m = b + c - 3j$, with 6 constraints ($c=6$) to remove all rigid body motions. We are left with $s - m = -30$ for both the symmetric and asymmetric geometries. A calculation of the rank of the equilibrium matrix gives ($s=1, m=31$) for the symmetric unpatched structure, and ($s=0, m=30$) for the asymmetric unpatched KDLG.

Now add 30 patch bars (9 for each of the top, mid and bottom planes, plus an additional 3) in an attempt to remove 30 mechanisms, and thereby give $s - m = 0$. A calculation of the rank of the equilibrium matrix gives $s = m = 6$ for the symmetric patched structure which means that we have not been successful in eliminating all internal mechanisms; in fact the symmetry is such that we have introduced six additional states of self stress. However, our attempt is successful in the asymmetric case and $s = m = 0$ for the asymmetric patched KDLG. It is concluded that only the asymmetric patched KDLG is statically and kinematically determinate.

Table 1

Comparison of the four versions of the 7-hexagon KDLG, $H = 7$, $n = 2$

Topology	b	c	j	s	m
Symmetric, no patches	288	6	108	1	31
Symmetric, patched	318	6	108	6	6
Asymmetric, no patches	288	6	108	0	30
Asymmetric, patched	318	6	108	0	0

3. Methodology for calculating the actuation properties of KDLG

Consider the replacement of any rigid bar in a statically and kinematically determinate pin-jointed structure by an axial actuator; the structure behaves as a mechanism with a single degree of freedom upon activation of the actuator. The mechanism involves extension of the actuator with all other bars remaining fixed in length. A matrix analysis of the pin-jointed structure will give the nodal displacements associated with this mechanism, see Pellegrino (1993). We shall address below the practical case of actuation of KDLGs with rigid joints¹. Actuation is resisted by elastic bending and stretching of the remaining passive bars and is limited by the onset of yield or elastic buckling at sufficiently large actuator displacements.

The relative contributions of stretching and flexural stiffness in a rigid-jointed truss depends upon the stockiness S of the constituent bars. Here, stockiness is defined as the ratio of the radius of gyration λ to the length L of the bar,

$$S = \lambda / L \quad (11)$$

with the second moment of area I of the bar related to its cross-sectional area A by

$$I = A\lambda^2 \quad (12)$$

The actuation stiffness, first yield load and elastic buckling load of rigid-jointed KDLGs are quantified below using a p-version of the finite element method, as implemented in the commercial software package Pro/Mechanica (2001). This program is limited to linear, elastic behaviour. Theoretical foundations of the p-method are discussed by Babuska et al. (1981) and Babuska and Szabo (1982). The constituent lattice members of the KDLG are treated as Timoshenko (shear flexible) beams while the joints are treated as rigid, but of vanishing volume. Each bar is

¹ In Part II of this study (Symons et al., 2004) Kagome Double Layer Grids have been manufactured by sheet metal forming and brazing. The face sheets are computer-numerical-control (CNC) laser-cut from mild steel sheet, the core sheets are laser-cut and folded from mild steel sheet to form the double-layer tetrahedral core, and the entire assembly is then spot welded or brazed together.

represented by a single variable-order element, and is considered to have a circular cross-section with a Poisson's ratio of 0.3.

Additional finite element calculations of the non-linear elastic-plastic response have been performed using the finite element program ABAQUS/Standard (HKS, 2003). The simulations used non-linear kinematics and the structures were discretised into five Euler-Bernoulli cubic order beam elements per bar.

In the simulations, the actuated bar is replaced by a slider mechanism which is rigid to shear and bending, but possesses zero axial stiffness. The slider is extended and the resistive force of the structure is determined in order to define the *actuation stiffness*. In addition, we calculate the actuator force for the onset of yield or buckling of any member, assuming linear elastic behaviour.

4. Actuation stiffness

4.1. *Effect of size of structure upon the actuation stiffness of symmetric, unpatched KDLGs*

Consider first the actuation of a symmetric, unpatched KDLG with rigid joints. In its pin-jointed form this structure has an increasing number of states of self stress with increasing size. Fig. 5a shows a plan view of five such structures. We investigate the actuation stiffness of each structure by replacing a single, central, bar in the bottom layer of the KDLG (as shown in bold in Fig. 5a) by a slider mechanism. The resistive force provided by the KDLG is calculated using the finite element program Pro/Mechanica. Displacement constraints are applied to three nodes adjacent to the actuated bar (as shown in Fig. 5a) in order to prevent rigid body motion.

The actuation stiffness k of the symmetric KDLG structures is plotted in the non-dimensional form kL/EA as a function of stockiness S of each member in Fig. 5b. The group kL/EA denotes the ratio of the passive stiffness k of the restraining structure to the axial stiffness EA/L of an individual bar. It is evident from Fig. 5b that the actuation stiffness of the 6-hexagon structure scales as S^2 : this implies that the actuation stiffness is dictated by bending of the members. This is consistent with the fact that the pin-jointed version of the 6-hexagon KDLG has no states of self-stress. In contrast, the pin-jointed 7-hexagon structure has a single state of self-stress;

consequently, the rigid-jointed version is stretching dominated and displays a constant value of kL/EA over a wide range of values of S .

An increase in size of the structure from 7 hexagons to 9 hexagons has very little effect upon the stiffness because no additional state of self stress is introduced in the pin-jointed version. The 10-hexagon pin-jointed structure, however, has two states of self stress and this endows the rigid-jointed version with a higher actuation stiffness. The trend of increasing stiffness with increasing number of states of self-stress in the parent pin-jointed structure continues: Fig. 5b shows that a 91-hexagon structure, with 61 states of self-stress, has the highest actuation stiffness.

4.2. Effect of the degree of asymmetry upon the actuation stiffness of unpatched KDLGs

It has been shown above that the states of self stress in the symmetric pin-jointed KDLG may be removed by moving the mid-plane nodes off the mid-plane. We now investigate the effect of this asymmetry upon the actuation stiffness of an unpatched KDLG.

Consider the smallest unpatched KDLG that, in pin-jointed form, contains a single state of self stress. This is the 7-hexagon structure. In order to explore the effect of size of asymmetric nodal displacement upon the actuation stiffness we consider the 7-hexagon, rigid-jointed KDLG in four states: symmetric, and asymmetric with a 1%, 5% and 15% asymmetry. The magnitude of asymmetry is the out-of-plane displacement of the mid-plane nodes normalised by the total thickness of the KDLG (that is, normalised by the distance between the two planar Kagome grids). For each of these four structures, the non-dimensional actuation stiffness kL/EA is plotted against stockiness S in Fig. 6.

The normalised actuation stiffness of the symmetric KDLG is almost insensitive to bar stockiness. Its behaviour is stretching controlled because of the state of self-stress in the pin-jointed version. In contrast, the 15% modified structure is bending controlled and its normalised actuation stiffness scales with S^2 . This is consistent with the fact that the state of self-stress in the pin-jointed version of the structure has been removed. The behaviour of the 1% and 5% modified structures is more complex. At small values of S the mode of deformation extends to the periphery of the structure

and the actuation stiffness scales as S^2 . However, for large values of S the actuation mode is local to the actuator, as discussed in the 2D planar case by Wicks and Guest (2004), and the actuation stiffness scales with S . In this regime, the contributions of axial and bending stiffness to the actuation stiffness become approximately equal.

4.3. *Effect of patch bars and asymmetry upon the actuation stiffness of KDLGs*

Recall that the finite, asymmetric, pin-jointed KDLG requires peripheral patch bars in order to make it kinematically determinate (no mechanisms). We shall now investigate the behaviour of rigid-jointed KDLGs in patched and unpatched, and symmetric and asymmetric realisations. The non-dimensional actuation stiffness of five prototypical structures is plotted in Fig. 7 as a function of bar stockiness.

The five structures are:

1. 91-hexagon, symmetric, patched KDLG, designated *91hex-S-P*
2. 91-hexagon, symmetric, unpatched KDLG, designated *91hex-S-U*
3. 91-hexagon, 15% asymmetric, patched KDLG, designated *91hex-15%-P*
4. 91-hexagon, 15% asymmetric, unpatched KDLG, designated *91hex-15%-U*
5. 7-hexagon, 15% asymmetric, patched KDLG, designated *7hex-15%-P*

A consideration of these five structures allows us to investigate the effect of asymmetry, patching and size of structure upon the actuation stiffness. The 91 hexagon arrangement has been selected as being sufficiently large to find practical application.

The *7hex-15%-P* KDLG is derived from a statically determinate pin-jointed structure and has an attractively low actuation stiffness, see Fig. 7. The actuation mode involves bending of the members and this gives rise to a quadratic dependence of kL/EA upon S . This is reminiscent of the actuation of a regular 2D hexagonal rigid-jointed framework as analysed by Wicks and Guest (2004).

The *91hex-15%-P* KDLG has a significantly higher actuation stiffness than the *7hex-15%-P* case. Here, actuation primarily involves bending of members in a boundary layer surrounding the actuated member. Remote from the actuator the displacement field is dictated by stretching of the members. This competition between local

bending and remote stretching gives rise to a characteristic decay length within the structure. Wicks and Guest (2004) have studied this in some detail for a 2D Kagome structure. A consequence is that kL/EA scales linearly with S , see Fig. 7. Note that the peripheral patch on the 91-hexagon asymmetric structure is needed in order for the outer bars to be stretching dominated. Without the patch (*91hex-15%-U*), the structure is bending dominated and kL/EA scales with S^2 .

Now consider the symmetric 91-hexagon KDLG (both *91hex-S-P* and *91hex-S-U*). The 61 states of self-stress in the pin-jointed version leads to the rigid-jointed variants behaving in a stretching manner with or without the patch. Consequently $kL/EA \approx 0.1$ and the structure has a high resistance to actuation.

It is concluded that the 91-hexagon, 15% asymmetric, patched KDLG (*91hex-15%-P*) is the version which is most likely to find practical application: its actuation stiffness is small, particularly at low values of stockiness S . It is demonstrated below that this structure also has an acceptable value of actuation strain before it buckles elastically or yields plastically. It is instructive to plot the out-of-plane deflected shape of the *91hex-15%-P* KDLG, see Fig. 8. The contour plots give the out-of-plane deflection of the top and bottom surfaces of the grid, for unit extension of the single central actuator. The amplitude of deflection and the spatial extent of the deflection zone both decrease with increasing bar stockiness S : compare the contour plot for $S = 0.07$ in Fig. 8a with the case $S = 0.5$ in Fig. 8b. We note in passing that the lower face of the plate deflects in similar manner to the top face, and the mode of deflection can be approximated to that of an ovalised blister.

5. Actuation limits of Kagome Double Layer Grids

We now investigate the actuation limit for each of the KDLG structures considered above. Actuation is limited either by elastic buckling or by the onset of yield of the structure. (The fatigue strength of a repeatedly actuated structure scales with the load for first yield, although an additional knock-down factor is required.) In the following sections the achievable actuation load and actuation strain are determined as a function of stockiness of each KDLG. Attention is focussed on the most promising morphing material in the form of the 91-hexagon asymmetric, patched structure

(91hex-15%-P). The sensitivity of achievable actuation strain to material choice and to the shape of cross-section is then addressed.

5.1. Elastic buckling

The lowest actuation buckling load P_b for each KDLG is calculated using the program Pro/Mechanica (2001) for the five structures detailed in section 4.3 and with stiffness response shown in Fig. 7. We anticipate that the buckling load is sensitive to the stockiness of all bars including the patch bars; in this study we make the arbitrary choice that all patch bars have the same stockiness as internal bars. It is instructive to normalise P_b by the Euler buckling load P_E for a pin-jointed strut of the same cross-sectional area and stockiness as that of the parent KDLG structure, $P_E \equiv \pi^2 EI / L^2 = EAS^2$. It is found that the normalised buckling load P_b / P_E for the five structures is only mildly sensitive to the magnitude of the stockiness S and lies within the range of 1.2 to 4.1 for values of S between 0.00025 and 0.05. No weak long-wavelength modes exist, and all structures investigated can bear a buckling load in excess of the Euler load for a pin jointed strut. This makes all of the structures promising for carrying high actuation loads.

The actuation strain at buckling ε_b is related to the buckling load P_b of the actuated structure by

$$\varepsilon_b = \frac{P_b}{kL} \quad (13)$$

where the actuation stiffness k has already been introduced. The actuation buckling strain for the five structures is plotted against S in Fig. 9a. The symmetric KDLGs (91hex-S-P and 91hex-S-U) are stretching dominated. Thus the buckling strain scales with S^2 . In contrast, the 7hex-15%-P and 91hex-15%-U are bending-dominated structures and have actuation stiffnesses which scale with S^2 (see Fig. 7); consequently, the buckling strain is insensitive to S at low values of S . The 91hex-15%-P KDLG shows intermediate behaviour due to the interaction of stretching and bending within it.

5.2. Onset of yield

Potential failure modes for a morphing structure include the onset of yield and fatigue failure. Consequently, strains should be kept within the elastic limit of the structure. The actuation load for the onset of first yield of any member P_y has been calculated using Pro/Mechanica (2001) for each of the five structures described in section 3.3. In general, first yield initiates in a single bar at a joint adjacent to the actuator.

The actuation strain at first yield ε_a is given by:

$$\varepsilon_a = \frac{P_y}{kL} \quad (14)$$

It is instructive to normalise ε_a by the material yield strain ε_y and to plot the normalised values against S , see Fig. 9b. The relative ranking of the five structures by the metric $\varepsilon_a/\varepsilon_y$ is the reverse of that noted in Fig. 7 for the normalised actuation stiffness kL/EA . This is due to the extreme sensitivity of actuation stiffness k to the type of structure. At low stockiness, $S < 0.001$, the achievable actuation strain for the stretching structures (*91hex-S-P* and *91hex-S-U*) is about twenty times ε_y . In contrast, for the bending structures, ε_a is two to three orders of magnitude that of ε_y . The ratio $\varepsilon_a/\varepsilon_y$ decreases monotonically with increasing S in all cases, and converges to $\varepsilon_a/\varepsilon_y = 1$ as S approaches about 0.3.

6. Optimal actuation strain

Yield and buckling are competing failure mechanisms, with yield dominating at high stockiness and buckling dominating for slender bars. The maximum possible actuation strain is achieved where the two failure modes coincide. It is of practical significance to explore how the achievable actuation strain can be maximised. Consider two strategies: changing the material and changing the shape of the bar cross-section. We restrict discussion to the practical case of the 91 hexagon, 15% asymmetric, patched KDLG (*91hex-15%-P*).

6.1. Effect of yield strain upon achievable actuation strain

The magnitude of the yield strain ε_y of the constituent bars has no effect upon the actuation strain for buckling ε_b . In contrast, the actuation strain for yield ε_a is directly proportional to ε_y and consequently the choice of material has a direct effect upon the achievable actuation strain. The actuation limit for yielding ε_a of the *91hex-15%-P* structure is plotted against S in Fig. 10a for the choices $\varepsilon_y = 0.1\%$, 0.3% and 1% . The figure includes the dependence of the buckling strain ε_b upon S . For a solid with $\varepsilon_y = 0.1\%$ the optimum stockiness is $S = 0.0035$ and the maximum actuation strain is only 1.8% . However, an increase in the value of ε_y to 1% leads to a maximum actuation strain of 7.5% at $S = 0.012$. We now investigate the non-linear behaviour of the KDLG at selected values of stockiness for a choice of yield strain (0.3%) which is representative of that for a medium strength alloy of steel, aluminium or titanium.

6.2. Post buckling and yield response

The post buckling and post yield response of KDLG structures has been calculated using the ABAQUS/Standard (HKS, 2003) non-linear finite element software. Typical load displacement responses are shown in Fig. 10b. The simulations assume non-linear kinematics, and each bar is represented by five Euler-Bernoulli cubic beam elements. The assumed material response is either elastic, or elastic-perfectly plastic with a yield strain $\varepsilon_y = 0.3\%$.

Figure 10b shows the actuation load versus strain response of the *91hex-15%-P* KDLG with selected values of stockiness ($S = 0.001, 0.007$ and 0.025). These values of S represent a slender, optimal and stocky KDLG, respectively, for the choice $\varepsilon_y = 0.3\%$. The actuation force P has been non-dimensionalised by the Euler buckling load P_E of a single pin-jointed strut of the same cross-sectional area and stockiness as that of the parent KDLG structure. The plot includes predictions for both elastic and elastic-perfectly plastic material responses.

The slender KDLG ($S = 0.001$) buckles elastically at an actuation strain of 0.004, and the post-buckling response remains elastic up to a large value of actuation strain of 0.1. In contrast, the stocky KDLG ($S = 0.025$) yields rather than buckles at an actuation strain of $\varepsilon_a \approx 3.9\varepsilon_y = 0.012$. The KDLG with optimal stockiness ($S = 0.007$) undergoes simultaneous elastic buckling and yield at an actuation strain of 0.04. It is anticipated that the coincidence of failure modes will make the structure imperfection sensitive, and this is explored below in a preliminary manner.

The effect of imperfection is investigated by repeating the non-linear finite element simulations on structures with a stochastic dispersion of nodal position. A MATLAB (Mathworks, 2002) routine is used to reposition randomly every finite element node of the structure. Since the ABAQUS finite element model uses five elements to describe each bar, the MATLAB routine introduces two types of imperfection: bar waviness and a misalignment of the bar joints. The magnitude of the random nodal displacement was chosen to be one third and two thirds of the bar radius. Predictions for a single stochastic realisation of each structure are given in Fig. 10c for the elastic-perfectly plastic material response. The figure gives the actuation load versus strain response of the *9Ihex-15%-P* KDLG with selected values of stockiness ($S = 0.001$, 0.007 and 0.025).

In all cases the presence of imperfections reduces the actuation stiffness. Since the most slender structure ($S = 0.001$) buckles in a symmetric elastic manner, imperfections give a negligible knock-down upon the buckling load and post-buckling (elastic) response. In contrast, the optimal structure ($S = 0.007$) and the stocky structure ($S = 0.025$) are imperfection sensitive. It is noted that the actuation strain corresponding to peak load is only mildly sensitive to imperfection in view of the fact that the actuation stiffness degrades with increasing imperfection. In the companion paper of this study (Symons et al. 2004), a more complete study is made of the role of bar waviness and joint misalignment upon the actuation stiffness, and comparisons are made with manufactured structures.

6.3. Effect of shape of bar cross-section upon achievable actuation strain

The actuation performance of the modified Kagome double layer grid can be improved somewhat with a change in bar cross section from that of a solid circular bar

to a hollow circular tube. For a bar of solid circular cross-section the radius of gyration is given by:

$$\lambda = D/4 \quad (15)$$

Now consider a circular hollow cross section bar of outer diameter D and inner diameter αD . The radius of gyration for this section is given by:

$$\lambda = \sqrt{\frac{1-\alpha^4}{1-\alpha^2}} \frac{D}{4} \quad (16)$$

Thus the ratio λ/D is greater for a hollow tube than for a solid circular bar.

The effect of cross-sectional shape upon the achievable actuation strain is plotted in Fig. 11a against S for hollow tubes ($\alpha = 0.9$ and 0.5) and for the solid-bar case ($\alpha = 0$), all for the *9Ihex-15%P* KDLG with the choice $\varepsilon_y = 1\%$. In the elastic buckling regime, the actuation strain for buckling is independent of α . However, when the achievable actuation strain is dictated by the onset of yield, the hollow bar outperforms the solid cross-section. This can be explained by the following scaling argument. Assume that the actuation strain scales with the bar curvature, with yield dictated by bar bending. The non-dimensional curvature at yield of a circular cross-section is

$$\kappa_y L = 2\varepsilon_y \frac{L}{D} = \frac{2\varepsilon_y}{S} \frac{\lambda}{D} \quad (17)$$

It is evident from (16) that λ/D increases with increasing α and therefore, *for the same stockiness S* , a hollow bar has a greater curvature at yield than a solid bar.

The achievable actuation strain is replotted from Fig. 11a as a function of relative density of the structure in Fig. 11b. Here, relative density is defined as the ratio of the density of the structure, upon treating it as a smeared-out continuum, to the density of the solid material. The figure reveals that a KDLG constructed from hollow bars can accommodate higher actuation strains than a KDLG constructed from solid bars for a relative density below approximately 0.01 (with the choice $\varepsilon_y = 1\%$). At relative densities above 0.01 the order switches and solid bars are superior.

7. Concluding remarks

A statically and kinematically determinate, pin-jointed, double layer grid has been developed, based upon the Kagome geometry. This structure contains no mechanisms or states of self stress and is thereby an ideal topology for a morphing structure; it can resist externally applied loads yet can be internally actuated with minimal resistance. This double layer grid also has a high bending stiffness as its faces comprise planar Kagome lattices. The rigid-jointed version inherits the properties of the pin-jointed version: it has high passive stiffness but can be actuated against a small internal resistance upon replacing a bar by an actuator. The achievable actuation strain, as limited by yield and buckling, has been explored as a function of bar stockiness and cross-sectional shape, and of the yield strain of the solid. It is shown that the achievable actuation strain attains a maximum value for an optimal value of bar stockiness due to the competition between buckling and yield. It is concluded that the Kagome Double Layer Grid is a promising topology for a morphing material. This motivates the companion paper (Symons et al, 2004); in the follow-on study, KDLG structures are manufactured and the measured actuation performances are compared with predictions including the role of imperfections.

Acknowledgments

The authors are grateful for financial support from a DARPA grant on synthetic multi-functional materials and wish to thank Profs. A G Evans, J W Hutchinson and M F Ashby for helpful discussions.

References

- Babuska, I., Szabo, B.A., 1982. On the rates of convergence of the finite element method. *International Journal for Numerical Methods in Engineering*, 18, 323-341.
- Babuska, I., Szabo, B.A., Katz, I.N., 1981. The p-version of the finite element method. *SIAM Journal of Numerical Analysis*, 18, 515-545.
- Bendsøe, M.P., Sigmund, O., 2002. *Topology optimization: theory, methods and applications*. Springer-Verlag, Berlin.
- Calladine, C.R., 1978. Buckminster Fuller's "tensegrity" structures and Clerk Maxwell's rules for the construction of stiff frames. *International Journal of Solids and Structures*, 14, 161-172.
- dos Santos e Lucato, S.L., Wang, J., Maxwell, P., McMeeking, R.M., Evans, A.G. 2004. Design and demonstration of a high authority shape morphing structure. *International Journal of Solids and Structures*, 41, 3521-3543.
- Guest, S.D., Hutchinson, J.W. 2003. On the determinacy of repetitive structures. *Journal of the Mechanics and Physics of Solids*, 51, 383-391.
- Hutchinson, R.G., 2004. *Mechanics of lattice materials*. PhD Thesis, University of Cambridge.
- Hutchinson, R.G., Wicks, N., Evans, A.G., Fleck, N.A., Hutchinson, J.W. 2003. Kagome plate structures for actuation. *International Journal of Solids and Structures*, 40, 6969-6980.
- Hyun, S. and Torquato, S., 2002. Optimal and manufacturable two-dimensional, Kagomé-like cellular solids. *Journal of Materials Research*, 7, 137.
- HKS, 2003. ABAQUS/Standard Version 6.3.1. Hibbit, Karlsson and Sorenson Inc., Providence, RI.
- MathWorks, 2002. MATLAB Version 6.5, The MathWorks Inc., 3 Apple Hill Drive, Natick, MA 01760-2098, USA.
- Pellegrino, S. 1993. Structural computations with the singular value decomposition of the equilibrium matrix. *International Journal of Solids and Structures*, 30, 3025-3035.
- Pellegrino, S., Calladine, C.R., 1986. Matrix analysis of statically and kinematically indeterminate frameworks. *International Journal of Solids and Structures*, 22, 409-428.
- PTC, 2001. Pro/MECHANICA Version 23.3. Parametric Technology Corporation, Needham, MA.
- Symons, D.D., Shieh, J., Fleck, N.A., 2004. Actuation of the Kagome Double Layer Grid. Part 2: Effect of imperfections on the measured and predicted actuation stiffness. Submitted to the *Journal of the Mechanics and Physics of Solids*.
- Wicks, N., Guest, S.D., 2004. Single member actuation in large repetitive truss structures. *International Journal of Solids and Structures*, 41, 965-978.

Figure Captions

Fig. 1 (a) Finite “patched” planar Kagome grid; (b) Topology of Kagome Double Layer Grid (KDLG) including patching scheme (faces of solid tetrahedra are absent in actual structure)

Fig. 2 (a) State of self-stress in symmetric 7-hexagon KDLG; (b) Complementary mechanism in a symmetric KDLG

Fig. 3 Number of hexagons and states of self-stress in symmetric KDLG topologies

Fig. 4 Modification scheme for the asymmetric KDLG

Fig. 5 (a) Plan views; (b) Actuation stiffness of various symmetric, unpatched, rigid-jointed KDLG structures

Fig. 6 Actuation stiffness of 7-hexagon, unpatched, KDLG structures with increasing asymmetry of mid-plane node position

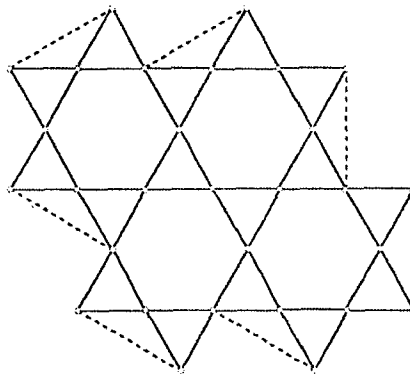
Fig. 7 Non-dimensional actuation stiffness of five KDLGs

Fig. 8 Contour plots of out-of-plane displacement of top (solid) and bottom (dotted) surfaces of *91-hex-15%-P* KDLG for unit extension of a single central bar: (a) $S = 0.07$; (b) $S = 0.5$

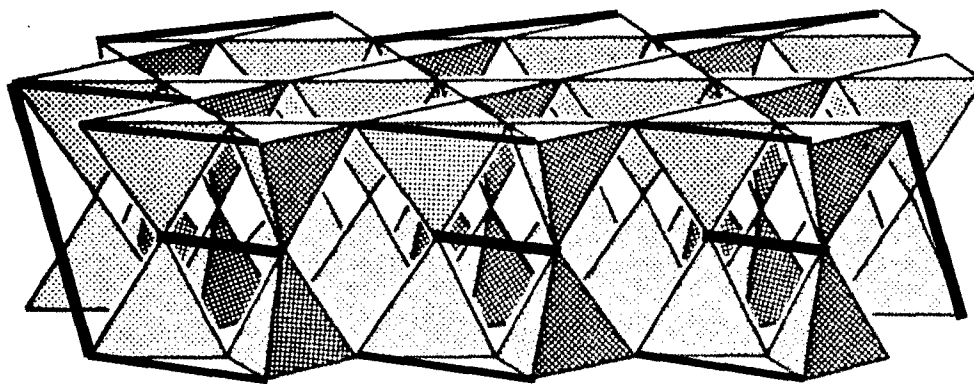
Fig. 9 (a) Actuation strain of five KDLGs limited by buckling; (b) by first yield

Fig. 10 (a) Achievable actuation strain for *91-hex-15%-P* KDLG limited by buckling or yield (for $\varepsilon_y = 0.1\%$, 0.3% and 1%); (b) Elastic and elastic-plastic and; (c) perfect and imperfect, load versus strain responses for *91-hex-15%-P* KDLGs of variable stockiness ($S = 0.001$, 0.007 and 0.025) with $\varepsilon_y = 0.3\%$

Fig. 11 (a) Achievable actuation strain (for $\varepsilon_y = 1\%$) for *91hex-15%-P* KDLG with solid or hollow bars as a function of stockiness; (b) as a function of relative density

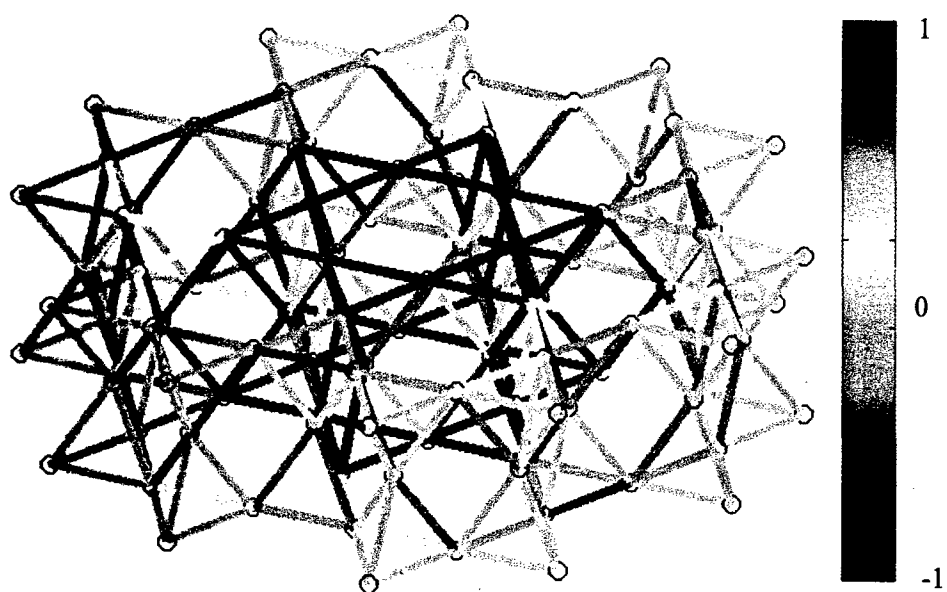


(a)

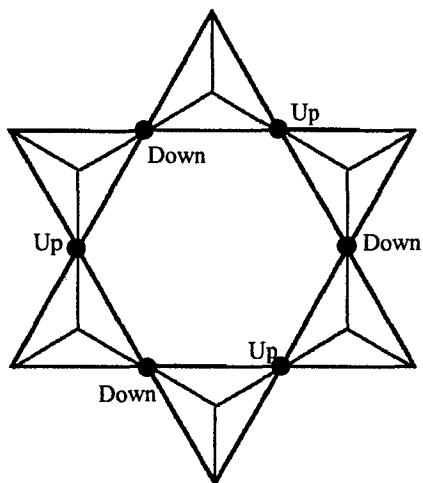


(b)

Fig. 1 (a) Finite "patched" planar Kagome grid; (b) Topology of Kagome Double Layer Grid (KDLG) including patching scheme (faces of solid tetrahedra are absent in actual structure)



(a)



(b)

Fig. 2 (a) State of self-stress in symmetric 7-hexagon KDLG; (b) Complementary mechanism in a symmetric KDLG

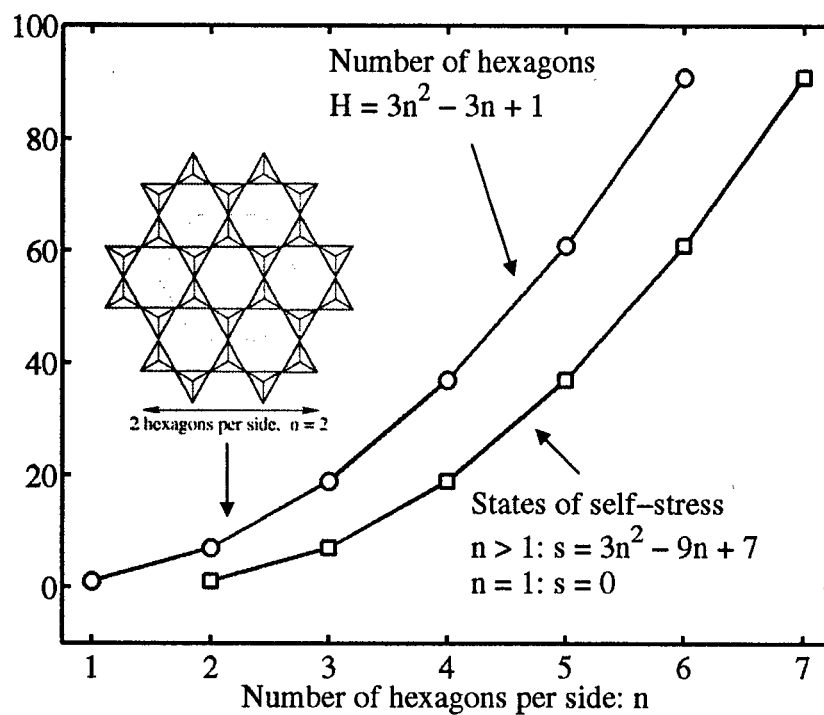


Fig. 3 Number of hexagons and states of self-stress in symmetric KDLG topologies

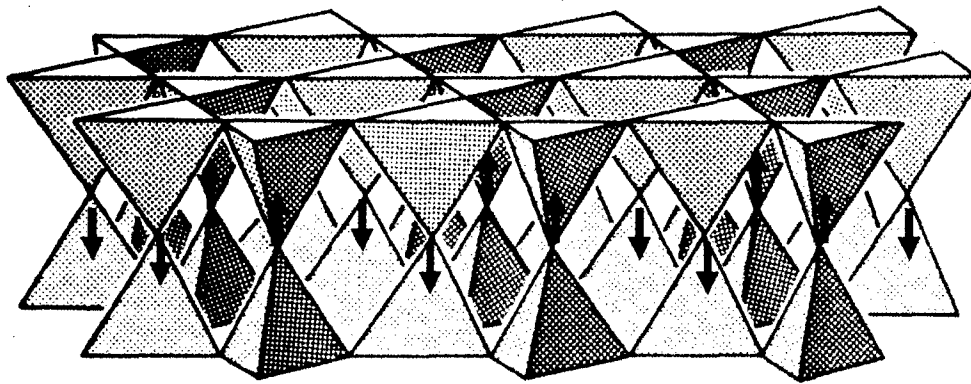


Fig. 4 Modification scheme for the asymmetric KDLG

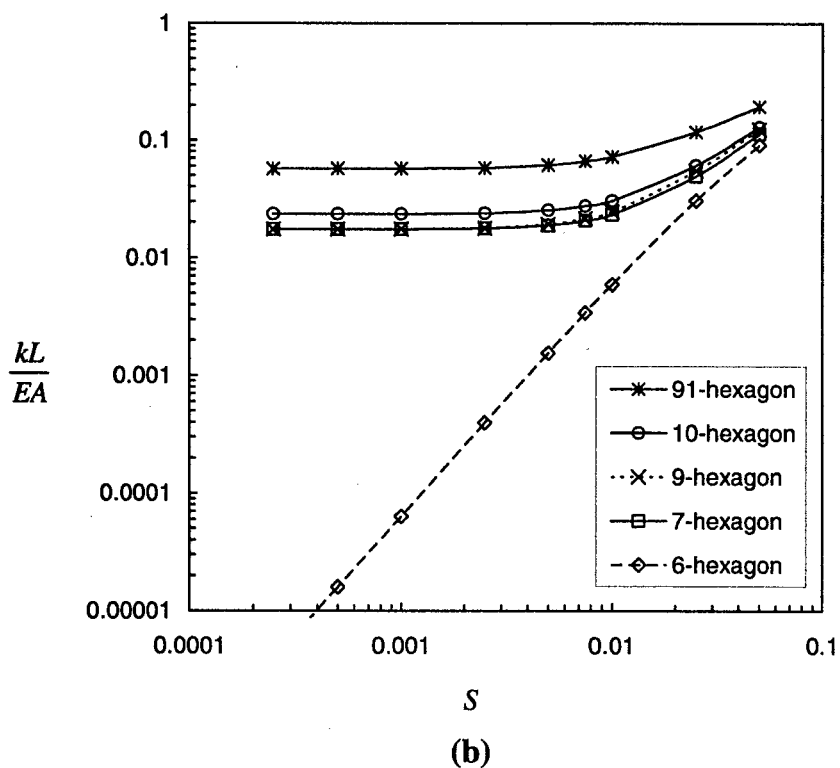
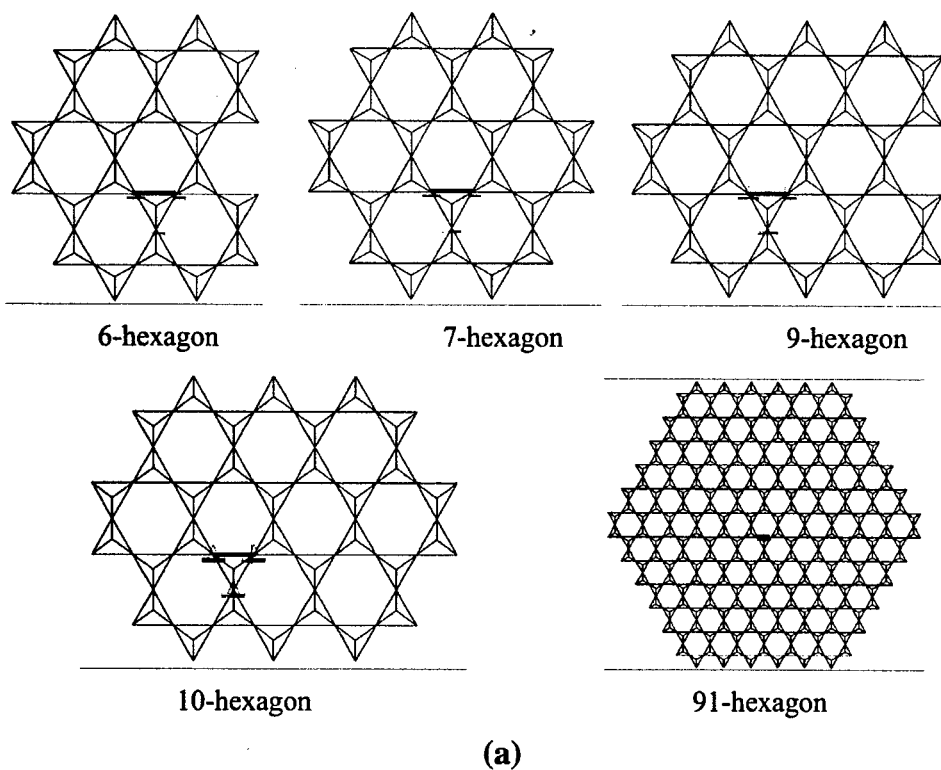


Fig. 5 (a) Plan views; (b) Actuation stiffness of various symmetric, unpatched, rigid-jointed KDLG structures

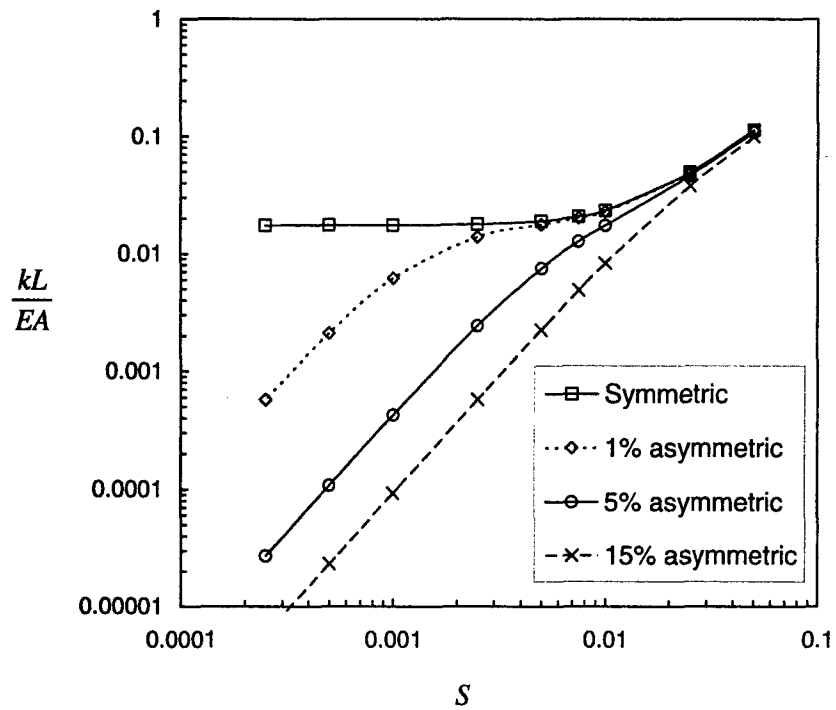


Fig. 6 Actuation stiffness of 7-hexagon, unpatched, KDLG structures with increasing asymmetry of mid-plane node position

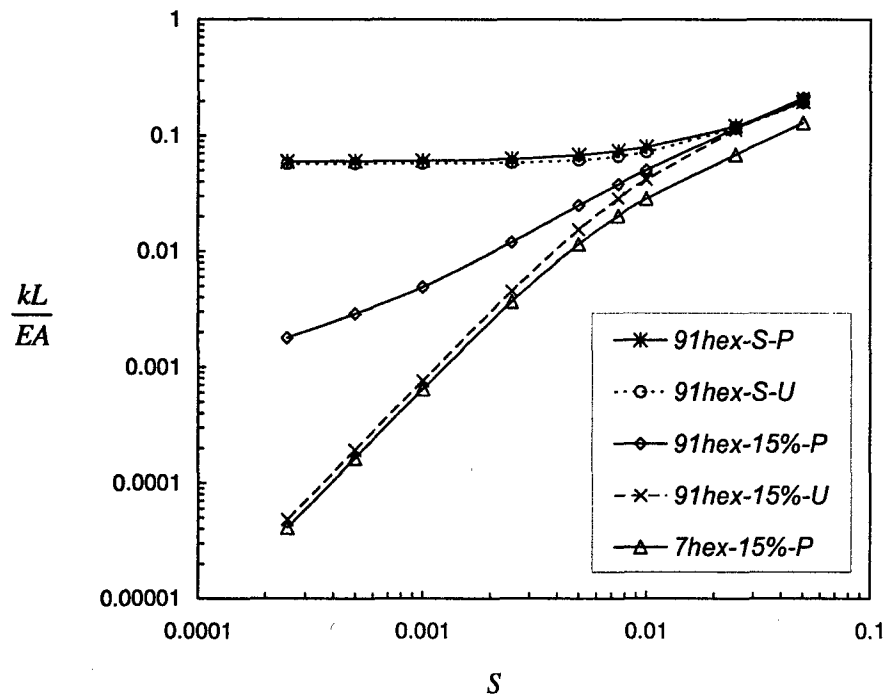
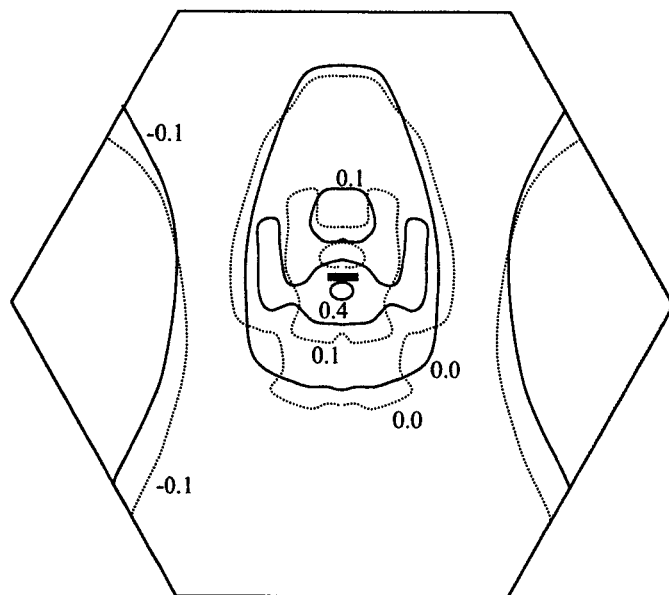
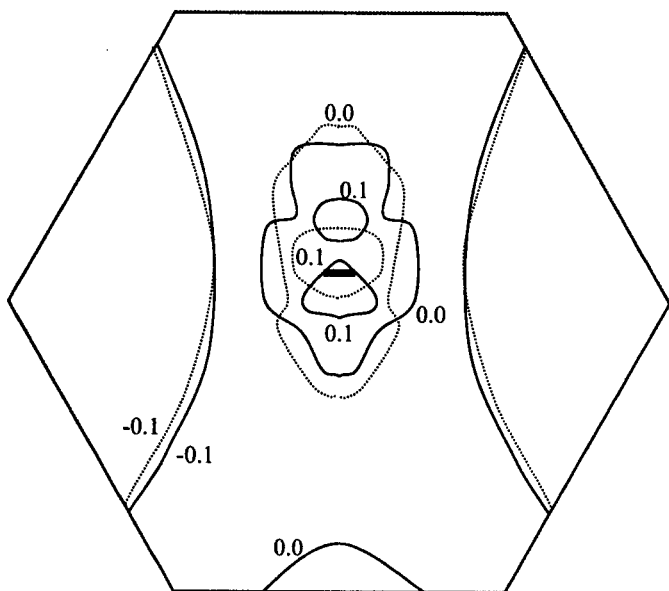


Fig. 7 Non-dimensional actuation stiffness of five KDLGs



(a)



(b)

Fig. 8 Contour plots of out-of-plane displacement of top (solid) and bottom (dotted) surfaces of *91-hex-15%-P* KDLG for unit extension of a single central bar: (a) $S = 0.07$; (b) $S = 0.5$

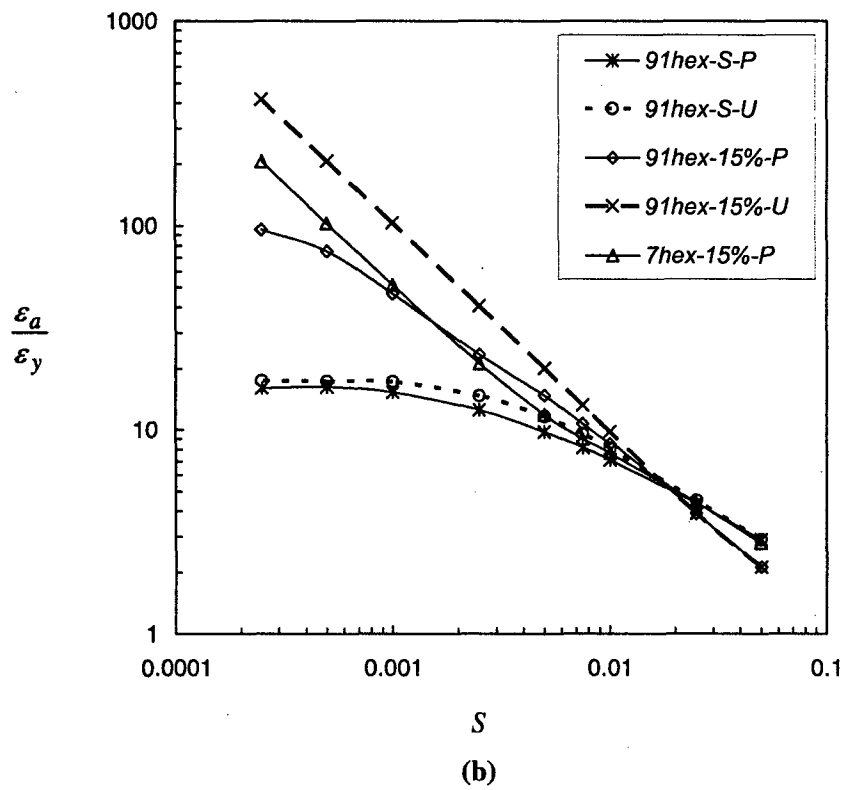
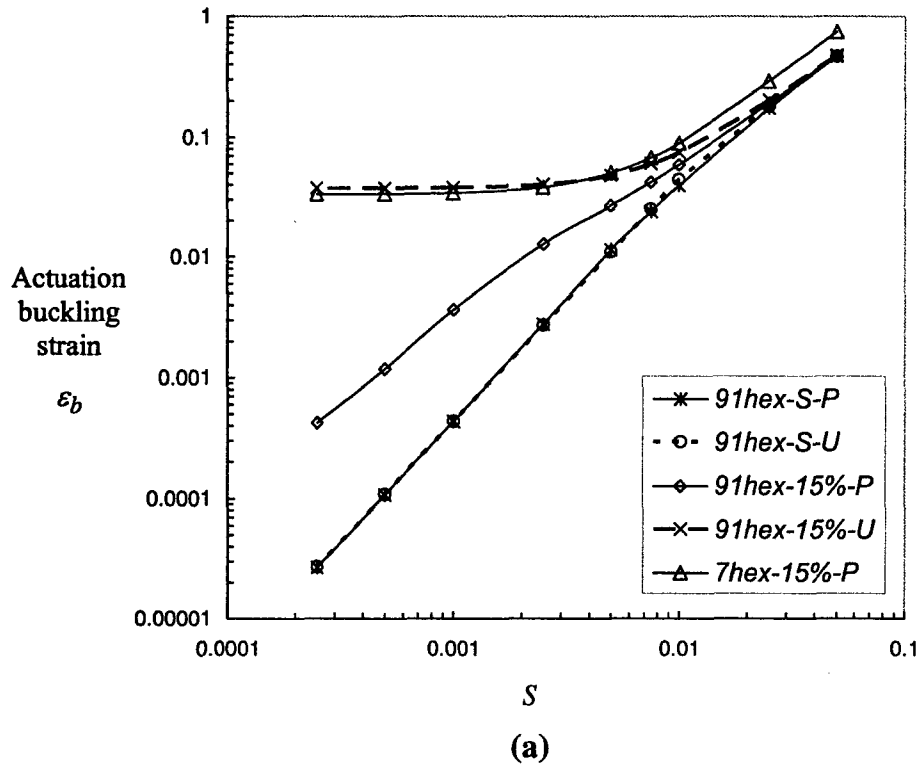
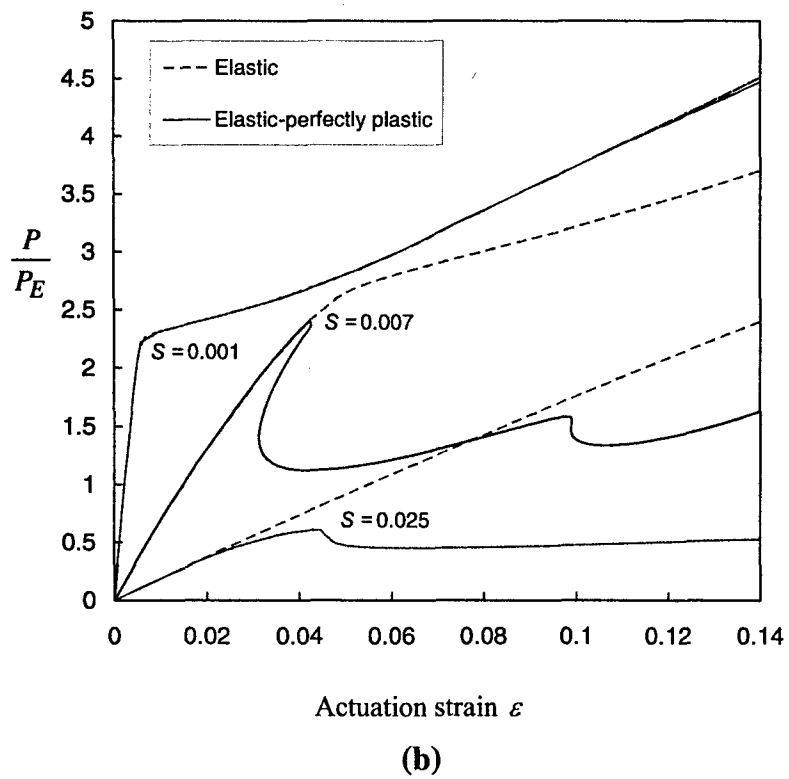
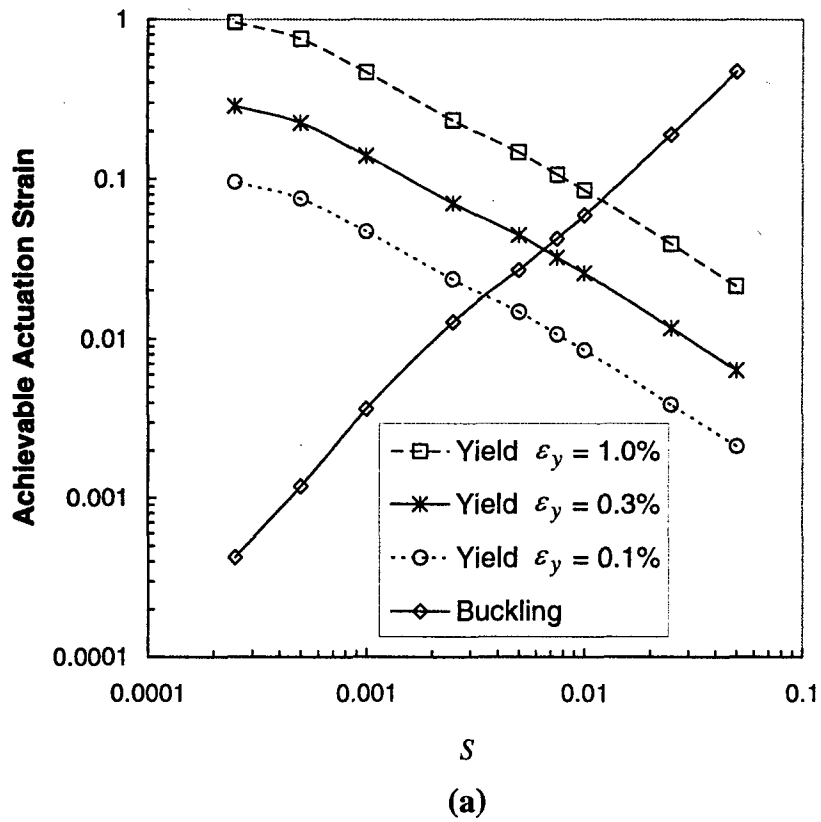
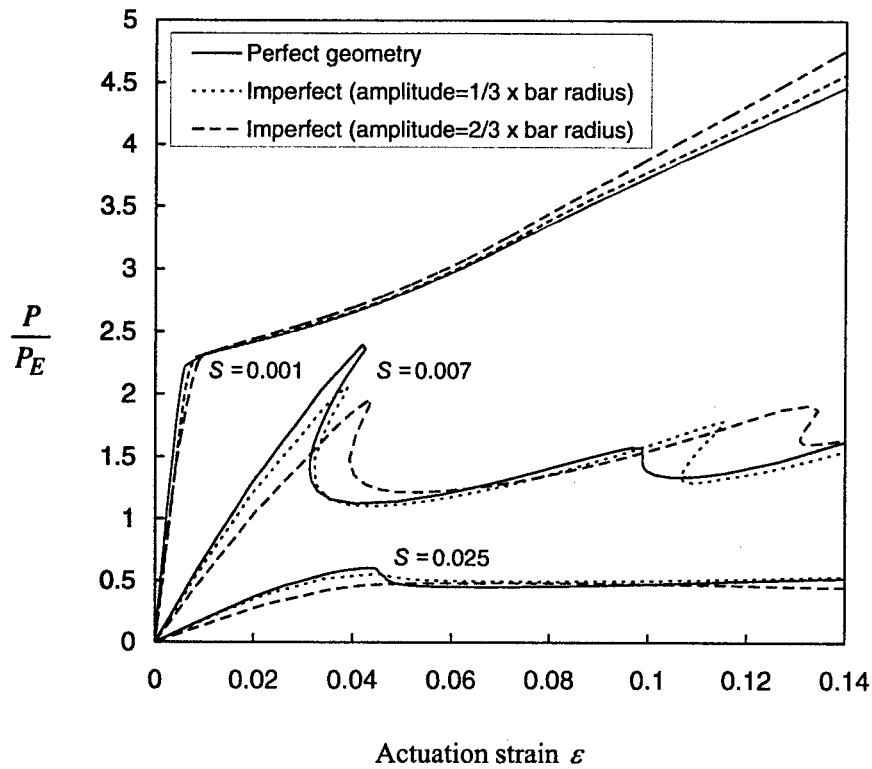


Fig. 9 (a) Actuation strain of five KDLGs limited by buckling; (b) by first yield





(c)

Fig. 10 (a) Achievable actuation strain for *91-hex-15%-P* KDLG limited by buckling or yield (for $\epsilon_y = 0.1\%$, 0.3% and 1%); (b) Elastic and elastic-plastic and; (c) perfect and imperfect, load versus strain responses for *91-hex-15%-P* KDLGs of variable stockiness ($S = 0.001$, 0.007 and 0.025) with $\epsilon_y = 0.3\%$

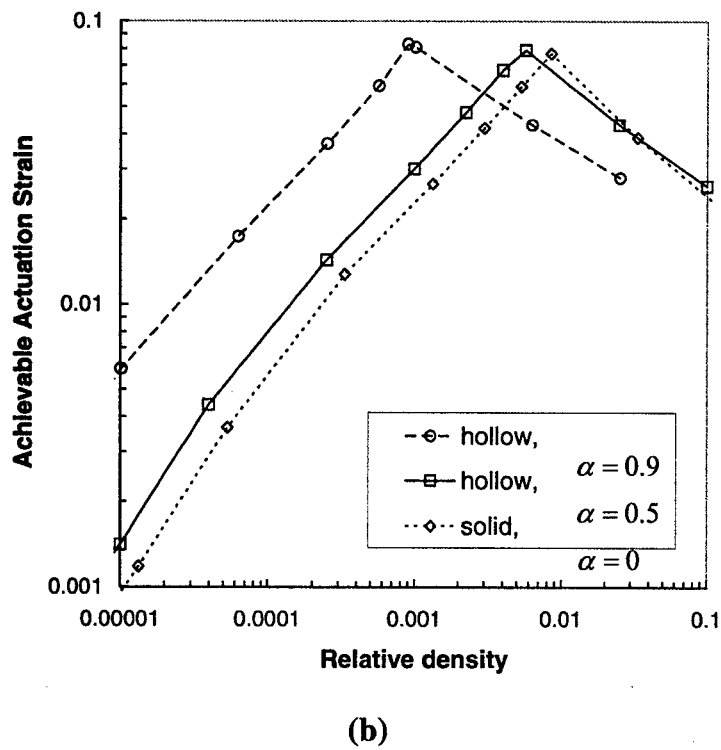
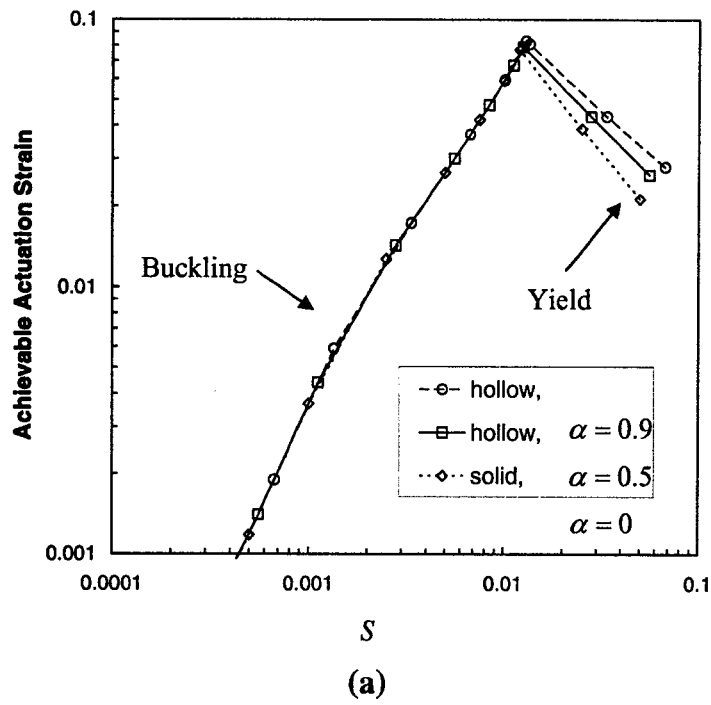


Fig. 11 (a) Achievable actuation strain (for $\varepsilon_y = 1\%$) for *9Ihex-15%-P* KDLG with solid or hollow bars as a function of stockiness; (b) as a function of relative density

Part X: Actuation of the kagome double layer grid.
**Part 2: Effect of imperfections on the measured and
predicted actuation stiffness**

Actuation of the Kagome Double Layer Grid. Part 2: Effect of imperfections on the measured and predicted actuation stiffness

D. D. Symons, J. Shieh¹ and N. A. Fleck

Cambridge University Engineering Department, Trumpington Street,
Cambridge, CB2 1PZ, UK

¹ now at Department of Materials Science and Engineering, National Taiwan University
1 Roosevelt Road, Sec. 4, Taipei, Taiwan

Abstract

The actuation stiffness of a set of steel Kagome Double Layer Grid (KDLG) structures with brazed joints is measured experimentally and compared with predictions by the finite element method. The predicted actuation stiffnesses for the perfect KDLGs much exceed the measured values, and it is argued that the low values of observed actuation stiffness are due to the presence of geometric imperfections introduced during manufacture. In order to assess the significance of geometric defects upon actuation stiffness, finite element calculations are performed on structures with a stochastic dispersion in nodal position from the perfectly periodic arrangement, and on structures with wavy bars. It is found that bar waviness has the dominant effect upon the actuation stiffness. The predicted actuation stiffness for the imperfect structures are in satisfactory agreement with the measured values assuming the same level of imperfection between theory and experiment.

Keywords: B: Elastic-plastic material; Structures; C: Finite elements; Mechanical testing; Morphing structures

1. Introduction

There is much recent interest in the development of morphing materials that are stiff to external loads yet can accommodate large changes in shape upon actuation by lengthening (or shortening) a portion of the material. Hutchinson et al. (2003) have proposed that the planar Kagome truss is a suitable two-dimensional microstructure for shape changing (morphing) application. The finite planar Kagome truss, with suitable patch bars on the periphery is both statically and kinematically determinate in its pin-jointed form. Consequently, it is a rigid topology, but becomes a single-degree-of-freedom mechanism if any bar is replaced by an actuator. The Kagome topology has the additional advantage that the elastic, infinite planar Kagome truss is isotropic and has an in-plane modulus which attains the upper Hashin-Shtrikman bound, see Hyun and Torquato (2002). Practical morphing materials have, by necessity, rigid (welded) joints. Wicks and Guest (2003) have shown that the rigid joint 2D Kagome truss provides a low resistance to actuation compared to a fully triangulated planar grid.

The Kagome Double Layer Grid (KDLG) is a sandwich construction comprising two planar Kagome trusses and a double layer tetrahedral core, see Fig. 1. The KDLG has been proposed by Hutchinson et al. (2003) and in Part I of this study (Symons et al., 2004) as a suitable microstructure for morphing plate structures. The plate extensional stiffness and plate bending stiffness of the KDLG are high due to the fact that it behaves as a sandwich plate with planar Kagome grids as the faces.

The infinite, periodic KDLG is neither statically nor kinematically determinate. However, Symons et al. (2004) have shown that the finite pin-jointed KDLG can be made to be statically and kinematically determinate by two modifications to its geometry. The structure is made asymmetric about its mid-plane (termed the asymmetric KDLG), and is given additional patch bars on its periphery, see Fig. 1. Consequently, the rigid jointed version of this *asymmetric patched KDLG* is a stiff, stretching dominated structure under passive external loading. Now consider the removal of any bar from the pin-jointed *asymmetric patched KDLG*; the structure behaves as a mechanism with a single degree of freedom. The rigid jointed version reflects this property: when one or more bars are elongated by suitable actuators, the rigid jointed structure resists this actuation by a

compliant deformation mode dominated by bar bending. The deformation mode reduces to an internal collapse mechanism in the pin-jointed limit. Thus, the asymmetric patched KDLG is an attractive topology for a morphing structure.

1.1. Imperfection sensitivity

Practical, as-manufactured structures contain geometric imperfections. These imperfections may influence both the passive and active structural response, and it is the aim of the present study to investigate the sensitivity of the actuation stiffness of the KDLG to imperfections.

The effect of imperfections upon the macroscopic stiffness and strength of a lattice material is dependent upon both the type of imperfection and the mode of deformation exhibited by the perfect pin-jointed parent structure. For example, the fully triangulated 2D lattice (with a connectivity of 6 bars per joint) is a highly redundant stretching structure in pin-jointed form. An imperfection in the form of a random perturbation in the position of nodes has only a minor effect upon the overall stiffness and strength. In contrast, an imperfection in the form of waviness of each bar dramatically reduces the macroscopic stiffness and strength due to the large knock-down in axial stiffness and yield strength of each bar.

The regular hexagonal honeycomb has a different imperfection sensitivity to that of the fully triangulated structure. Under in-plane hydrostatic loading the hexagonal honeycomb behaves as a stiff, stretching structure. However, on moving the nodes to form an irregular hexagonal honeycomb, hydrostatic loading causes the rigid jointed structure to deform in a much more compliant manner by the local bending of bars, see Chen et al. (1999, 2001). Similarly, the introduction of bar waviness degrades the structure from stretching-governed to bending-governed, for macroscopic hydrostatic loading, as reviewed by Chen et al. (1999). This behaviour is fundamentally different to that of the regular hexagonal honeycomb under in-plane deviatoric loading. Under deviatoric loading, the perfect structure deforms by bar bending, and the macroscopic

stiffness and strength are relatively insensitive to the introduction of geometric defects, in the form of bar waviness and nodal position.

In Part I of this study, Symons et al. (2004) explored theoretically the actuation response of finite perfect KDLGs. Upon actuation, the structure deforms by a combination of bar bending and stretching, and for such structures the significance of imperfections has not been resolved. In this paper, the predicted sensitivity of actuation stiffness to a random repositioning of nodes and to the degree of bar waviness are compared with measurements of actuation stiffness on fabricated KDLGs.

2. Introduction to the 7-hexagon KDLG

Symons et al. (2004) have studied the effect of the number of repeating unit cells within a pin-jointed KDLG upon the total number of collapse mechanisms and states of self-stress within the structure. They demonstrated that conversion of the infinite, periodic KDLG to a finite form requires the addition of peripheral patch bars in order to remove the collapse mechanisms associated with the reduced connectivity at the periphery. Their analysis of the static determinacy of the patched and unpatched finite structures revealed the existence of states of self-stress, unless the structure has a very limited number of unit cells (less than 7). For example, the symmetric-unpatched structure with 7 hexagons on each face contains a single state of self-stress, see Fig. 2a. Symons et al. (2004) showed that such states of self stress can be removed by breaking the symmetry of the structure about the mid-plane to produce a so-called *asymmetric version* of the KDLG. The 7-hexagon asymmetric-unpatched version is sketched in Fig. 2b.

In the present study, the actuation response of the 7-hexagon KDLG is measured and calculated for versions which are either symmetric (S) or asymmetric (A), and either patched (P) or unpatched (U). These four variants are labelled symmetric-unpatched (S-U), asymmetric-unpatched (A-U), symmetric-patched (S-P), and asymmetric-patched (A-P), and are catalogued in Fig. 2.

2.1. States of self-stress

The single state of self-stress in the pin-jointed S-U KDLG is triggered by the axial actuation of any bar associated with this state of self-stress. In contrast, the A-U KDLG, as shown in Fig. 2b, contains no states of self-stress, and provides no resistance when any bar is actuated. In rigid jointed form, a small resistance to actuation is anticipated due to bending of bars in the A-U grid, and a much larger resistance due to stretching of bars in the S-U grid.

2.2. Patching scheme

The A-U KDLG is statically determinate with no states of self-stress ($s = 0$), but it does contain $m = 30$ infinitesimal collapse mechanisms. To make the structure kinematically determinate ($m = 0$), yet remain statically determinate ($s = 0$), these 30 mechanisms are eliminated by a peripheral patching scheme, as shown in Fig. 2d. This patching scheme is applied to the top layer, mid-plane and bottom layer of the KDLG, with three additional bars.

Now consider the S-U KDLG. It contains a single state of self-stress ($s = 1$) and $m = 31$ mechanisms. The above patching scheme does not remove all mechanisms and the final count of states of self-stress and mechanisms for the symmetric-patched (S-P) grid is $s = 6$, $m = 6$ for the structure sketched in Fig. 2c. The number of mechanisms m and states of self-stress s for each of the above KDLG structures is summarised in Table 1.

Table 1

The four versions of the 7-hexagon KDLG

	Symmetric (S)	Asymmetric (A)
Unpatched (U)	S-U $s = 1, m = 31$	A-U $s = 0, m = 30$
Patched (P)	S-P $s = 6, m = 6$	A-P $s = 0, m = 0$

2.3. Actuation of the KDLG

Symons et al. (2004) have explored theoretically the actuation response of the four variants of the 7-hexagon KDLG by replacing one bar with an axial actuator. They considered rigid-jointed structures and determined the sensitivity of actuation response to the *stockiness* S of the bars, as defined by the ratio of the radius of gyration λ to the length l of the bar,

$$S = \lambda / l \quad (1)$$

The second moment of area I of the bar cross section can be expressed by

$$I = A\lambda^2 \quad (2)$$

in terms of the cross-sectional area A and radius of gyration λ of the bar. Symons et al. (2004) showed that the achievable actuation strain is limited by the elastic buckling and yielding of the bars, and has a maximum value at a stockiness of $S = 0.004$ to 0.1 , depending upon the assumed yield strain of the solid (ε_y in the range 0.1% to 1%).

3. Manufacture of KDLG structures

A single specimen of each of the four variants of 7-hexagon KDLG shown in Fig. 2 was manufactured by the assembly of two Kagome face sheets and two folded tetrahedral core layers. The struts of the core and faces were laser cut from a low carbon steel sheet using a CNC-controlled machine. The measured elastic-plastic uniaxial response of the steel sheet is given in Fig. 3a, measured at a strain rate of 10^{-3} s^{-1} . The low carbon steel has a measured Young's Modulus $E = 200 \text{ GPa}$ and a 0.2% offset yield strength of 200 MPa , giving a yield strain of 0.001 . The constituent bars of the KDLGs were manufactured to a length of 40.5 mm , a square cross-section of $1 \times 1 \text{ mm}$, and thereby a stockiness of $S = 0.007$. The previous study of Symons et al. (2004) shows that this value of stockiness is close to optimal for maximising the actuation strain, for the given value

of yield strain. The two core component sheets were cold pressed by a CNC-controlled folding machine into their three-dimensional form and were then assembled with the face sheets into the KDLG geometry. Two manual operations were used to bond together the structure: spot welding of the nodes, followed by reinforcement of the nodes by silver soldering with a gas flame and silver solder applied locally to each joint. Fig. 3b shows an example of a completed KDLG specimen: the S-U version.

The core geometry used in the construction of the asymmetric KDLG differs from that used for the symmetric KDLG, see Fig. 2. In the symmetric case, the nodes *on each face* of the folded tetrahedral core layers lie on the same plane, as in Fig. 2a and 2c. In the asymmetric case, the mid-plane nodes are perturbed in the through-thickness direction, as shown in Fig. 2b and 2d. The amplitude of the asymmetry of the nodes about the mid-plane of the asymmetric KDLG is equal to 14% of the total KDLG depth.

3.1. Measurement of imperfections in fabricated structures

A 3-axis co-ordinate measuring machine¹ was used to measure as-manufactured imperfections in the manufactured KDLG specimens. Imperfections in nodal position were measured in both the through-thickness and in-plane directions. Additionally, the degree of bar waviness was measured by measuring the co-ordinates of each bar at mid-span in relation to its two ends. The degree of imperfection was measured for each variant of KDLG, and was found to show little variation from one type of structure to the next. Consequently, the values of imperfection reported below are averaged over measurements taken on all four variants.

The root mean square (RMS) value of nodal displacement in the through-thickness direction from that of the perfect structure was measured to be 2.1mm. This imperfection is large relative to the bar cross-section of 1 x 1 mm, and is ascribed to the manual nature of the spot welding operation during specimen fabrication. The magnitude of the imperfection of nodal location in the plane of the KDLG is defined by the RMS value of

¹ An OMICRON A001 machine was used, with a sensor head tip radius of 0.5mm.

the radial displacement of each node from that of the perfect lattice. This measured RMS value of 0.23mm is much less than the out-of-plane value of 2.1mm, and the difference is ascribed to the fact that the Kagome face sheets were accurately cut by the CNC laser cutting machine. Finally, the RMS value of the amplitude w_0 of bar waviness was measured to be 0.55 mm.

4. Actuation of the fabricated KDLG structures

4.1. Test protocol

Each of the four KDLG structures was actuated by replacing a single bar of the central hexagon on one of the Kagome face trusses by an instrumented axial actuator. A screw-driven mechanical test machine was used as the actuator: the two nodes of the removed member were stretched apart in a direction parallel to that of the removed bar, using a pair of L-shaped loading fixtures (see Fig. 3b). The load was measured using the load cell of the test machine while the displacement of the two loading nodes was measured continuously by a laser extensometer. Five load-unload cycles were applied to each specimen, incrementing the peak load in 10N steps up to a maximum value of 50N, at a displacement rate of $10^{-2} \text{ mm s}^{-1}$.

4.2. Measurements of actuation response

The actuation force versus deflection responses are plotted in Fig. 4a for the two symmetric KDLGs, and in Fig. 4b for the two asymmetric KDLGs. Finite element predictions of the loading response are included to allow comparison; details of the finite element model are given later.

The initial measured stiffness of the structures decreases by a factor of 5 from most stiff to least stiff in the order S-P, S-U, A-P and A-U. The measurements confirm that symmetry and patch bars both contribute to the actuation stiffness. The symmetric patched (S-P) structure is essentially linear elastic over the applied load range (up to 50N). However, the less stiff KDLGs show increasing hysteresis with increasing load

level in their force-deflection responses, due to plastic deformation within the struts. For example, when the asymmetric unpatched (A-U) structure was loaded up to 50N (and 2.8 mm actuation) the residual deflection was 0.3mm.

5. Predicted actuation response

Actuation of the KDLG structures by extension of the single central bar has been simulated by finite element analysis. Recall that the position of the actuated bar in each 7-hexagon variant is shown in Fig. 2. The actuated bar is removed and pinned displacement constraints are applied so that the relative separation of the end nodes of the replaced bar is prescribed. The axial force between these two end nodes is calculated as a function of nodal separation. No rotational constraints are applied to any nodes other than those required to eliminate rigid body motion.

5.1. Prediction of actuation stiffness

Two commercially available finite element packages were used to calculate the initial actuation stiffness of the structures: Pro/Mechanica (PTC, 2001) and ABAQUS/Standard (HKS, 2003). Both the Pro/Mechanica and ABAQUS simulations assumed linear elastic, infinitesimal displacements in order to calculate the initial actuation stiffness. The struts comprise an isotropic elastic solid of Young's modulus 200 GPa and Poisson ratio 0.3.

Pro/Mechanica uses a p-version of the finite element method. Theoretical foundations of the p-method are given by Babuska et al. (1981) and Babuska and Szabo (1982). The basic idea is that the degree of interpolation function within each element can be adjusted to give any desired convergence accuracy. This method allows for automatic convergence by a multi-pass process: the element order is refined as required to give any desired solution accuracy, here taken to be 1% on actuation stiffness. The constituent bars of the KDLG were treated as single elements. Timoshenko (shear flexible) beams were employed with the joints treated as rigid nodes.

The element order in the ABAQUS program is controlled manually by the user. In the ABAQUS simulations a single "B33" 2-node cubic beam element was used for each

strut. The B33 element is an Euler-Bernoulli beam that does not allow for shear deformation. The actuation stiffnesses obtained by the two finite element procedures are compared in Table 2. The differences between the Pro/Mechanica and ABAQUS results are sufficiently small for us to conclude:

- (i) shear deformation is insignificant for these structures, and
- (ii) the ABAQUS calculations, based on a single element per bar with cubic interpolation, suffice for our purposes.

Table 2

Measured and predicted actuation stiffness of 7-hexagon KDLGs

		S-P	S-U	A-P	A-U
Pro/Mechanica	(N/mm)	174.18	87.46	72.08	21.72
ABAQUS	(N/mm)	174.21	87.48	72.17	21.75
% difference		0.019	0.022	0.12	0.17

5.2. Prediction of non-linear actuation response

The above calculations of actuation stiffness give no information on the effects of finite deformation and material non-linearity upon the response of the perfect structures. Leung et al. (2004) have shown that geometric softening occurs in actuated planar Kagome trusses due to finite deformation effects. It is clear from the observed hysteresis in actuation response that significant plastic deformation occurs in the KDLG structures. In order to determine whether the observed actuation response can be captured by a full non-linear finite element analysis of the perfect structure, additional ABAQUS predictions of actuation were made for the four KDLG variants, employing both geometric and material non-linearity.

The non-linear calculations were performed with 10 type B33 elements used to model each beam, in order to capture local non-linear effects. The measured elastic-plastic uniaxial response of the steel sheet was employed, recall Fig. 3a, with von Mises plastic flow theory and isotropic hardening. The finite element predictions of the loading and unloading actuation force versus displacement for the four perfect variants, loaded up to 50N, are included in Figs. 4a and 4b. The predictions for the symmetric (S-P and S-U) and the asymmetric-patched (A-P) structures give the same linear response as that obtained by the previous linear finite element analyses as summarised in Table 2. In contrast, the asymmetric-unpatched (A-U) KDLG gives pronounced non-linearity at loads exceeding 30N. The hysteresis present in the predicted response of the A-U structure is due to material non-linearity, and the linear unloading response indicated that finite deformation effects can be ignored.

5.3. Comparison of predicted actuation stiffness for perfect geometry with measured response

The measured initial stiffnesses are compared with finite element (FE) predictions in Table 3 and in Fig. 4. Only in the case of the asymmetric-unpatched (A-U) KDLG does the measured experimental actuation stiffness show good agreement with the FE prediction. The measured stiffness of the other three structures is significantly lower than the prediction.

Table 3

Comparison of measured and predicted initial actuation stiffness

	S-P	S-U	A-P	A-U
Measured	100 N/mm	49 N/mm	42 N/mm	20 N/mm
Prediction	174.2 N/mm	87.5 N/mm	72.2 N/mm	21.8 N/mm
Ratio	0.57	0.56	0.58	0.92

6. Predicted sensitivity to manufacturing imperfections

It has already been noted that the manufacturing method gives rise to geometric imperfections in the form of misplaced nodes and bar waviness. We proceed to predict the sensitivity of actuation stiffness to each type of imperfection, and to then compare the predicted actuation stiffnesses of the as-manufactured grids with the observed values.

6.1. Sensitivity of actuation stiffness to misplaced nodes

Recall from section 3.1 that the root mean square (RMS) value of nodal perturbation, in the direction normal to the plane of the KDLG, equals 2.1mm. The magnitude of the imperfection of nodal location within the plane of the KDLG has already been defined by the RMS value of radial displacement of each node from that of the perfect lattice; the measured RMS value for in-plane perturbation equals 0.23mm. The finite element method using the ABAQUS package is now used to predict first the effect of through-thickness nodal imperfection, and second the effect of in-plane nodal imperfection upon actuation stiffness.

A MATLAB (Mathworks, 2002) routine is used to displace randomly every node in the ABAQUS input file from that of the perfect structure, for any chosen amplitude of imperfection. The finite element model uses only a single beam element for each bar and so the bars remain straight after movement of the structural nodes. Ten structural realisations were constructed by the MATLAB routine for any given amplitude of imperfection in order to gauge the dispersion in actuation stiffness from one realisation to the next. The ten calculations were then used to deduce the mean and standard deviation².

Fig. 5a shows a plot of the mean and 95% confidence limits (\pm two standard deviations) of the actuation stiffness for the four 7-hexagon KDLGS versus the magnitude of nodal

² It would be preferable to perform additional simulations to give statistically significant results, but this was prohibitively time consuming.

movement in the through-thickness direction. Likewise, Fig. 5b shows a plot of the mean and 95% confidence limits of the actuation stiffness of the four KDLGS with increasing in-plane imperfection. In both plots the RMS value of nodal imperfection has been normalised by the bar length ($l = 40.5$ mm).

Take the two figures together, and consider first the mean values of the responses. Out-of-plane and in-plane imperfections have only a minor effect upon the actuation stiffness for the asymmetric KDLGs, but lead to a significant drop in actuation stiffness for the symmetric KDLGs. Recall that the pin-jointed symmetric structures contain a number of internal states of self-stress which are activated by bar actuation. Geometric imperfections break the symmetry of the structure and remove these states of self-stress in the pin-jointed version. Consequently, the actuation stiffness of the rigid-jointed symmetric grids are reduced.

It is further noted from Fig. 5a and 5b that the predicted actuation stiffness displays significant scatter from one structural realisation to the next: the spread in the 95% confidence limits increases with overall magnitude of imperfection for all topologies, with the largest dispersion evident for the patched structures. Such scatter is of practical concern and suggests the need for tight quality control in manufacture.

6.2. *Effect of bar waviness upon actuation stiffness*

Waviness of a bar leads to a reduction in its axial stiffness but to a negligible change of its bending stiffness. Consider a bar with pre-existing sinusoidal waviness of amplitude w_0 and wavelength l' . Assume that the bar length l spans an integral number of semi-wavelengths of waviness, such that $nl' = 2l$, where n is a positive integer. Then, the axial stiffness k of the bar is reduced by the factor $1 + \frac{1}{2}e^2$ in terms of the waviness normalised by the radius of gyration, $e \equiv w_0 / \lambda$. This knock-down in stiffness can be large. For example, consider a bar of 1mm square cross-section, and waviness of amplitude 0.6 mm. Then, e equals 2.1 and the axial stiffness of the bar is reduced from

$k = EA/l$ to $k = 0.31 EA/l$, where as before E denotes Young's modulus and A the cross-sectional area of the bar.

It is straightforward to model the effect of bar waviness upon the bar properties within a finite element model. Recall that the effect of bar waviness is to reduce the effective axial stiffness of a bar while leaving its bending stiffness unchanged. This can be achieved by reducing the cross-sectional area of the bar by the factor $(1 + e^2/2)$, while leaving the bending modulus EI unchanged. Finite element calculations of this type have been performed using the ABAQUS program: all bars in the KDLG are ascribed the same level of waviness, and the actuation stiffness is determined as a function of e for each of the four variants shown in Fig. 2. It is emphasised that the nodal positions are those of the perfect structure.

Fig. 6 contains a plot of the actuation stiffness of the four KDLG variants as a function of the non-dimensional bar waviness imperfection e . The A-U KDLG is bending dominated in its performance and is largely unaffected by bar waviness. In contrast, the S-P KDLG is stretching dominated and shows a large drop in actuation stiffness with increasing bar waviness. The A-P and S-U cases are intermediate.

6.3. Comparison of predicted and measured actuation stiffness for imperfect KDLGs

It remains to match the predicted actuation stiffness for the imperfect structures and the observed actuation stiffness for the four KDLGs. Recall from Table 3 that all KDLGs except for the A-U variant have an observed actuation stiffness of 56-58% that of the perfect structure. It is clear from Fig. 5a and 5b that imperfections in nodal position (both out-of-plane and in-plane) lead to only a small drop in mean value of actuation stiffness for the symmetric KDLGs and to a negligible change for the asymmetric KDLGs. The confidence limits in Fig. 5a and 5b reveal that nodal imperfections of the magnitude observed could not give rise to the knock-down observed for three of the structures. In contrast, bar waviness is a promising candidate for the source of the reduction in actuation stiffness: it is clear from Fig. 6 that bar waviness leads to a drop in stiffness for

the same three variants as that noted in Table 3. But is there quantitative agreement between predicted and measured actuation stiffness for the imperfect structures?

The predicted actuation stiffness is plotted against the measured stiffness for selected amplitudes of bar waviness in Fig. 7. It is seen that a non-dimensional amplitude of $e = 1.5$ ($w_0 = 0.43$ mm) provides reasonable agreement for all four variants of KDLG. This magnitude of waviness is in satisfactory agreement with the measured value of $e = 2.0$ ($w_0 = 0.55$ mm). It is concluded that the measured values of actuation stiffness can be explained in terms of as-manufactured bar waviness.

7. Concluding remarks

In this study, the sensitivity of the actuation performance of the Kagome Double Layer Grid (KDLG) to manufacturing defects is explored. The finite element simulations demonstrate that the observed knockdown in actuation stiffness due to imperfections is a consequence of bar waviness rather than the misplacement of nodes. It is also shown that the actuation stiffness of both the perfect and imperfect grids depend upon the detailed topology of the grids – whether symmetric or asymmetric, and whether patched or unpatched.

Insight into the differences in actuation stiffness from one variant of KDLG to the next is achieved by examining the pin-jointed parent structures. First, consider the symmetric-patched pin-jointed KDLG. In the absence of imperfections, it contains 6 states of self-stress, as detailed in Table 1. The extension of a bar by actuation triggers one or more of these states of self-stress, and the remaining structure resists actuation by the storage of elastic energy by bar stretching (and bending). The introduction of bar waviness leads to a sharp drop in the axial stiffness of the bars, and thereby to a drop in actuation stiffness, see Fig. 6. Alternatively, an imperfection in the form of a random movement of nodes removes the states of self-stress in the pin-jointed structure, and this is reflected by a reduction in actuation stiffness of the rigid-jointed version, recall Figs. 5a and 5b.

Second, consider the asymmetric-patched KDLG. In its pin-jointed form, with one bar removed, the patched structure A-P contains a single mechanism, and can be actuated

freely, with zero resistance by the surrounding structure. Random movement of nodes changes neither the number of states of self-stress (zero) nor the number of mechanisms (one), and consequently the rigid-jointed version has a negligible change in mean actuation stiffness with increasing nodal imperfection, see Figs. 5a and 5b. The moderate actuation stiffness of the rigid-jointed perfect version is due to the moderate level of stockiness of bars considered in this investigation. Consequently, the structure has some stretching resistance, and this is reduced by the introduction of bar waviness, see Fig. 6.

Finally, consider the asymmetric-unpatched (A-U) KDLG. The perfect, pin-jointed version with one bar removed has no states of self-stress but does possess 30 mechanisms. The random movement of nodes has no effect upon the number of states of self-stress and mechanisms, and consequently the actuation stiffness of the rigid-jointed version is insensitive to the repositioning of nodes, recall Figs. 5a and 5b. The rigid-jointed A-U KDLG deforms predominantly by bending of its constituent bars. Since the bending stiffness of a bar is almost insensitive to the presence of bar waviness the actuation stiffness is almost independent of bar waviness, as shown in Fig. 6. The actuation stiffnesses of the perfect and imperfect A-U grid are least of all the KDLG grids investigated, due to the fact that the structure is bending dominated.

Acknowledgements

The authors are grateful for financial support from a DARPA grant on synthetic multi-functional materials and wish to thank Profs. A G Evans and J W Hutchinson for helpful discussions.

References

- Babuska, I., Szabo, B.A., 1982. On the rates of convergence of the finite element method. *International Journal for Numerical Methods in Engineering*, 18, 323-341.
- Babuska, I., Szabo, B.A., Katz, I.N., 1981. The p-version of the finite element method. *SIAM Journal of Numerical Analysis*, 18, 515-545.
- Calladine, C.R., 1978. Buckminster Fuller's "tensegrity" structures and Clerk Maxwell's rules for the construction of stiff frames. *International Journal of Solids and Structures*, 14, 161-172.
- Chen, C., Lu, T.J., Fleck, N.A., 1999. Effect of imperfections on the yielding of two-dimensional foams. *Journal of the Mechanics and Physics of Solids*, 47, 2235-2272.
- Chen, C., Lu, T.J., Fleck, N.A. 2001. Effect of inclusions and holes on the stiffness and strength of honeycombs. *International Journal of Mechanical Sciences*, 43, 487-504.
- dos Santos e Lucato, S.L., Wang, J., Maxwell, P., McMeeking, R.M., Evans, A.G. 2004. Design and demonstration of a high authority shape morphing structure. *International Journal of Solids and Structures*, 41, 3521-3543.
- Guest, S.D., Hutchinson, J.W. 2003. On the determinacy of repetitive structures. *Journal of the Mechanics and Physics of Solids*, 51, 383-391.
- Hutchinson, R.G., Wicks, N., Evans, A.G., Fleck, N.A., Hutchinson, J.W. 2003. Kagome plate structures for actuation. *International Journal of Solids and Structures*, 40, 6969-6980.
- Hyun, S. and Torquato, S., 2002. Optimal and manufacturable two-dimensional, Kagomé-like cellular solids. *Journal of Materials Research*, 7, 137.
- HKS, 2003. ABAQUS/Standard Version 6.3.1. Hibbit, Karlsson and Sorenson Inc., Providence, RI.
- Leung, A.C.H., Symons D.D., Guest, S.D., 2004. Actuation of kagome lattice structures. 45th AIAA/ASME/ASCE/AHS/ASC Structures, Structural Dynamics and Materials Conference, Palm Springs, CA 19-22 April 2004.
- MathWorks, 2002. MATLAB Version 6.5, The MathWorks Inc., 3 Apple Hill Drive, Natick, MA 01760-2098, USA.
- Pellegrino, S. 1993. Structural computations with the singular value decomposition of the equilibrium matrix. *International Journal of Solids and Structures*, 30, 3025-3035.
- Pellegrino, S., Calladine, C.R., 1986. Matrix analysis of statically and kinematically indeterminate frameworks. *International Journal of Solids and Structures*, 22, 409-428.
- PTC, 2001. Pro/MECHANICA Version 23.3. Parametric Technology Corporation, Needham, MA.
- Symons, D.D., Hutchinson, R.G., Fleck, N.A., 2004. Actuation of the Kagome Double Layer Grid. Part I: prediction of performance of the perfect structure. Submitted to *Journal of the Mechanics and Physics of Solids*.

Wicks, N., Guest, S.D., 2004. Single member actuation in large repetitive truss structures. *International Journal of Solids and Structures*, 41, 965-978.

Figure Captions

Fig. 1 Topology of Kagome Double Layer Grid (KDLG) showing asymmetric modification and patching schemes (the solid tetrahedra are representative only, in the real structure the faces are absent).

Fig. 2 Orthographic projections of four KDLG 7-hexagon variants: (a) symmetric-unpatched (S-U); (b) asymmetric-unpatched (A-U); (c) symmetric-patched (S-P); (d) asymmetric-patched (A-P).

Fig. 3 (a) Uniaxial stress-strain curve of low carbon steel; (b) 7-hexagon-S-U KDLG specimen (bar length = 40.5 mm) and loading arrangement.

Fig. 4 Predicted and measured load versus displacement response of (a) symmetric; (b) asymmetric KDLG specimens. The finite element predictions, labelled FE, assume finite deformations and an elastic-plastic material response.

Fig. 5 Actuation stiffness of KDLGs with (a) out-of-plane; (b) in-plane nodal imperfection (mean and 95% confidence limits). The measured actuation stiffness is given on the right-hand side for comparison.

Fig. 6 Effect of bar waviness on actuation stiffness.

Fig. 7 Measured actuation stiffness of KDLG specimens plotted against predicted stiffness for bar waviness imperfection $e = 0, 0.5, 1$ and 1.5 .

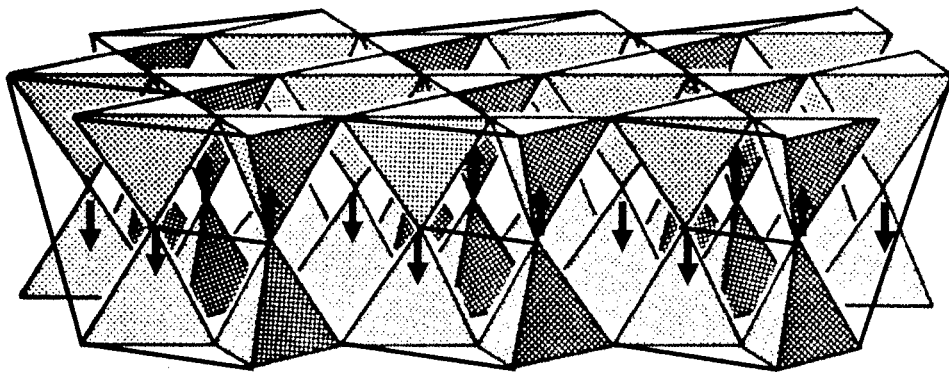
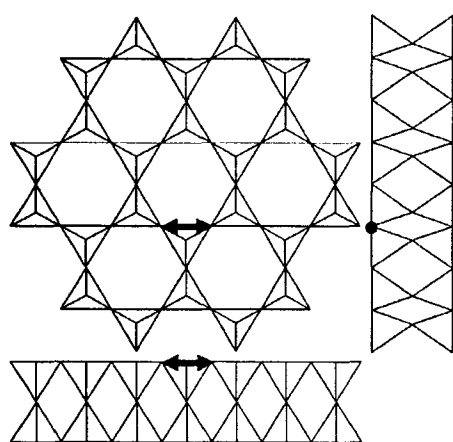
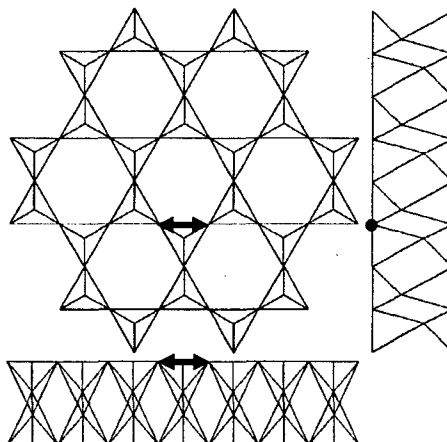


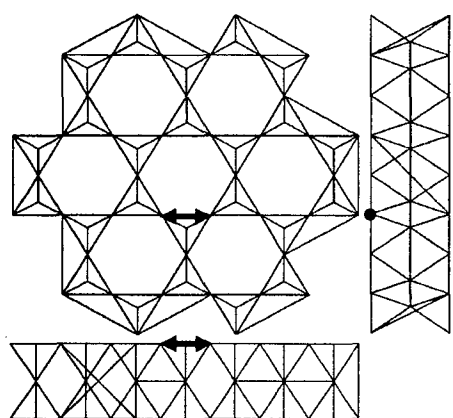
Fig. 1 Topology of Kagome Double Layer Grid (KDLG) showing asymmetric modification and patching schemes (the solid tetrahedra are representative only, in the real structure the faces are absent).



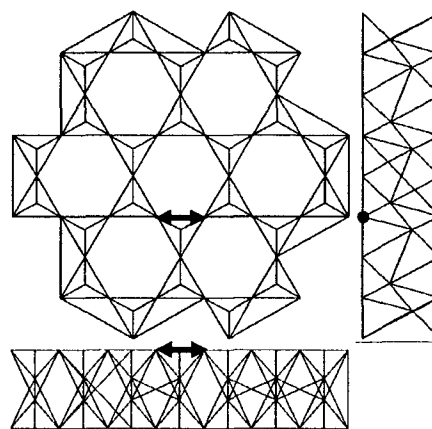
(a)



(b)

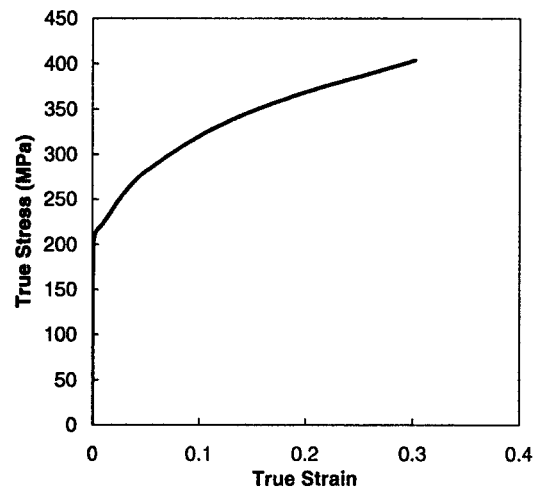


(c)

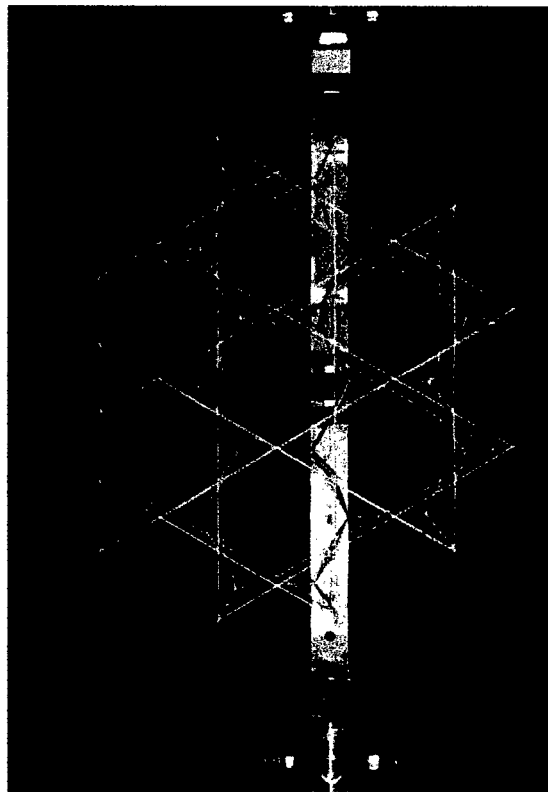


(d)

Fig. 2 Orthographic projections of four KDLG 7-hexagon variants: (a) symmetric-unpatched (S-U); (b) asymmetric-unpatched (A-U); (c) symmetric-patched (S-P); (d) asymmetric-patched (A-P).

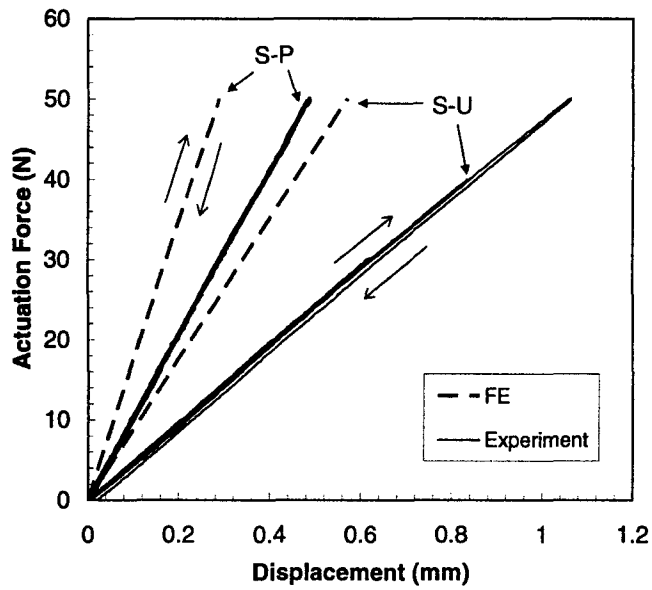


(a)

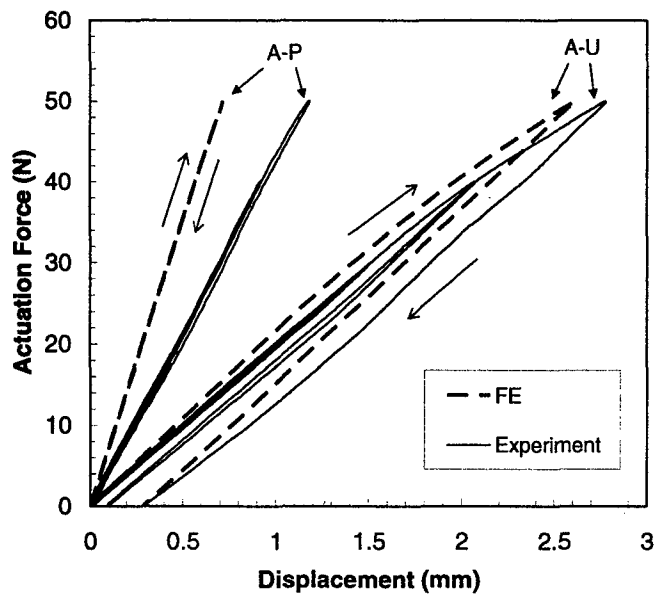


(b)

Fig. 3 (a) Uniaxial stress-strain curve of low carbon steel; (b) 7-hexagon-S-U KDLG specimen (bar length = 40.5 mm) and loading arrangement.

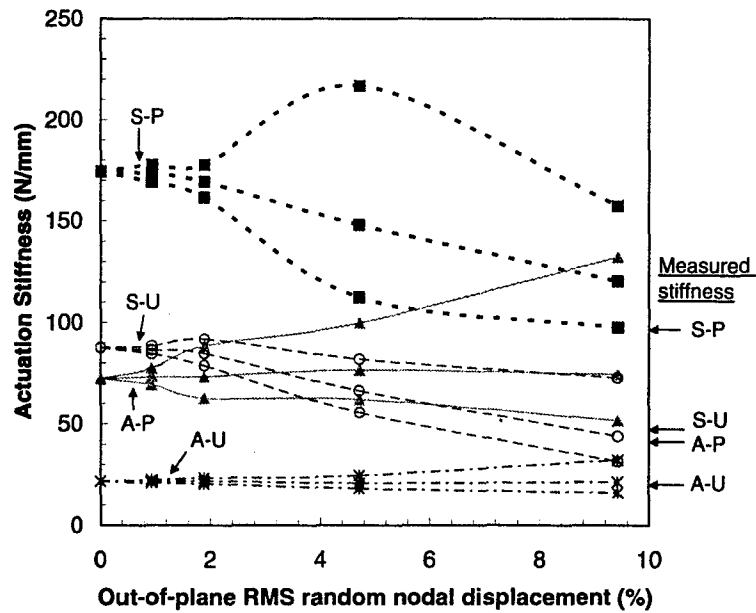


(a)

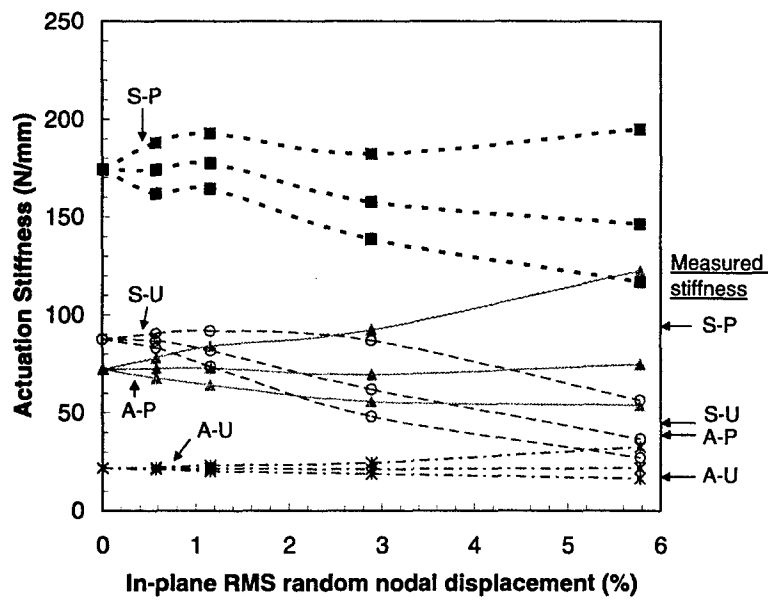


(b)

Fig. 4 Predicted and measured load versus displacement response of (a) symmetric; (b) asymmetric KDLG specimens. The finite element predictions, labelled FE, assume finite deformations and an elastic-plastic material response.



(a)



(b)

Fig. 5 Actuation stiffness of KDLGs with (a) out-of-plane; (b) in-plane nodal imperfection (mean and 95% confidence limits). The measured actuation stiffness is given on the right-hand side of the plots, for comparison.

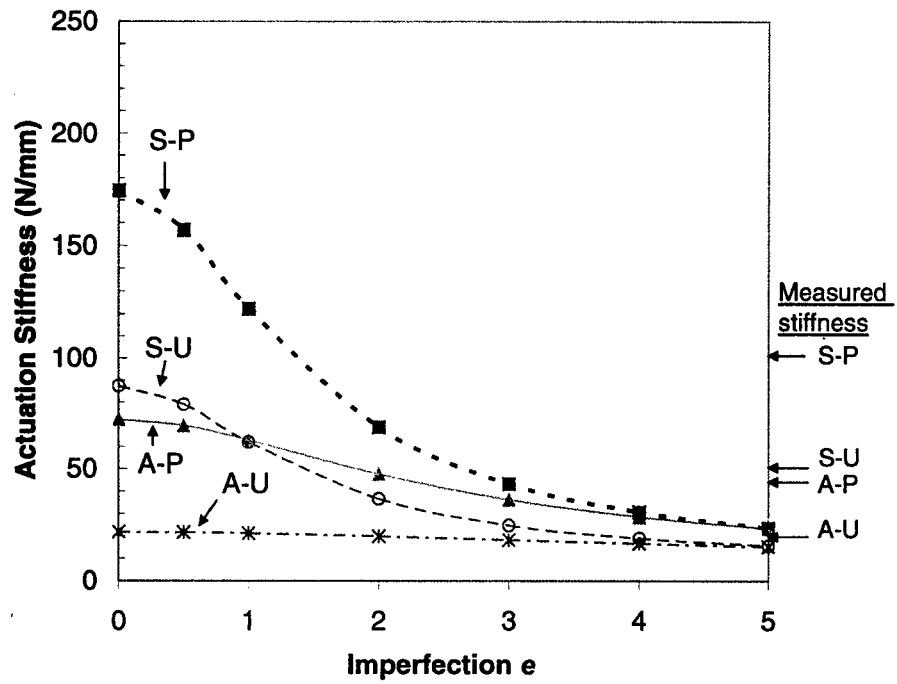


Fig. 6 Effect of bar waviness on actuation stiffness.

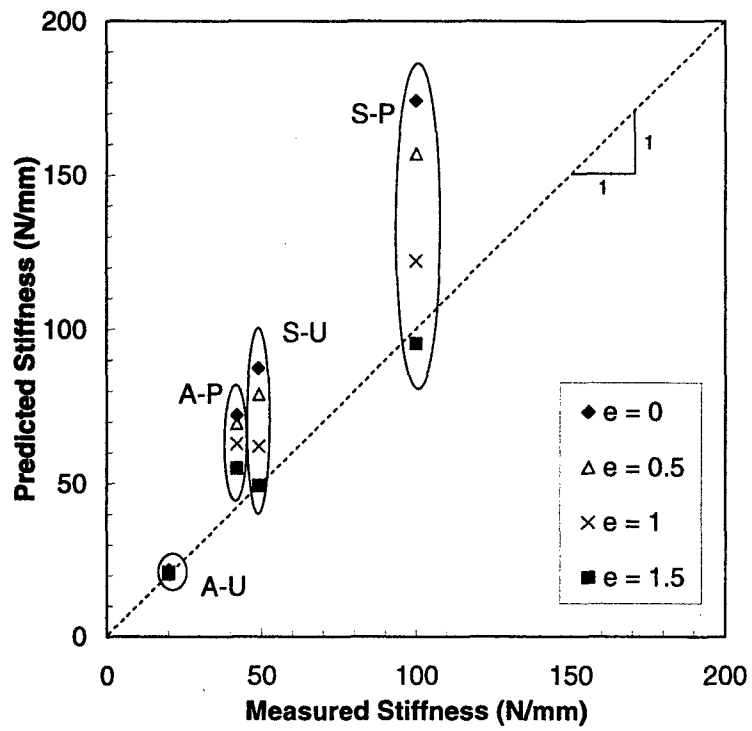


Fig. 7 Measured actuation stiffness of KDLG specimens plotted against predicted stiffness for bar waviness imperfection $e = 0, 0.5, 1$ and 1.5 .